

Title	A family of multi-functional phosphorescent bioprobes based on the PtPFPP scaffolding moiety
Authors	Zanetti, Chiara
Publication date	2023
Original Citation	Zanetti, C. 2023. A family of multi-functional phosphorescent bioprobes based on the PtPFPP scaffolding moiety. PhD Thesis, University College Cork.
Type of publication	Doctoral thesis
Rights	© 2023, Chiara Zanetti. - https://creativecommons.org/licenses/by-nc-nd/4.0/
Download date	2025-09-13 04:23:03
Item downloaded from	https://hdl.handle.net/10468/15941

Ollscoil na hÉireann, Corcaigh
National University of Ireland, Cork



**A family of multi-functional
phosphorescent bioprobes based on the
PtPFPP scaffolding moiety**

Thesis presented by

Chiara Zanetti

for the degree of

Doctor of Philosophy

University College Cork

School of Biochemistry and Cell Biology

Head of School: Prof. Justin McCarthy

Supervisors: Prof. Dmitri B. Papkovsky, Prof. Anita R. Maguire

2023

Table of contents

List of abbreviations.....	7
Abstract.....	9
Chapter 1: Literature review.....	11
1.1. Introduction to biological roles of oxygen.....	11
1.2. Methods for O ₂ detection.....	12
1.3. Principles of quenched-phosphorescence O ₂ sensing technique.....	17
1.3.1. Measurement of O ₂ and quantitative relationships.....	19
1.3.2. Sensor calibration.....	20
1.4. Detection and O ₂ sensing modalities.....	21
1.4.1. Intensity-based measurements.....	21
1.4.2. Lifetime-based measurements.....	23
1.4.3. O ₂ imaging.....	25
1.5. O ₂ sensitive dyes / phosphors.....	26
1.5.1. Transition metal complexes.....	29
1.5.2. Metalloporphyrins.....	31
1.6. Sensor materials.....	34
1.6.1. Solid-state sensors.....	34
1.6.2. Soluble probes.....	37
1.6.3. Particulate sensors.....	38
1.6.4. Metal–organic frameworks (MOFs).....	39
1.6.5. Intracellular O ₂ sensing and cell targeting strategies.....	40
1.7: Core biological applications of optical O ₂ sensing and measurement platforms.....	44
1.7.1. Mitochondrial respiration.....	44
1.7.2. Mammalian cellular respiration.....	45
1.7.3. Bacterial respiration.....	49
1.7.4. Tissue models.....	51
1.7.5. Measurements <i>in vivo</i> and <i>ex vivo</i>	51
1.8. PtPFPP dye and its chemical modifications.....	52
1.9. Conclusions and project objectives.....	54
Chapter 2: Materials and methods.....	56
2.1. Materials.....	56
2.2. Methods.....	56

2.2.1. Synthesis and purification of PtPFPP derivatives.....	56
2.2.2. Spectral and photophysical characterization.....	57
2.2.3. Cell culture, staining and toxicity assessment	58
2.2.4. OCR measurements	59
2.2.5. Internalization via glucose transporters (GLUTs) using BAY-876.....	60
2.2.5. Bacterial respirometric and turbidimetric assay procedures	60
2.2.6. Bioimaging.....	61
2.2.7. <i>E. coli</i> microscopy.....	61
2.3. Data processing.....	62
Chapter 3: Design, synthesis, and characterization of the new PtPFPP	63
hetero-substituted derivatives	63
3.1. Introduction	63
3.2. Rational design of PtPFPP-based phosphorescent probes	65
3.2.1. 3:1 Hetero-substituted derivatives	65
3.2.2. 2:2 Hetero-substituted derivative.....	66
3.3. Chemical synthesis and characterization of new derivatives and intermediates.....	68
3.3.1. Chemical synthesis, NMR and MS of Pt1Glc ₁	68
3.3.2. Chemical synthesis, NMR and MS of PtcPEG ₃ 1Glc.....	70
3.3.3. Chemical synthesis, NMR and MS of PtmPEG ₃ 1Glc	72
3.3.4. Chemical synthesis, NMR and MS of PtCA ₃ 1Glc	73
3.3.5. Chemical synthesis, NMR and MS of Pt1Glc ₂ (trans)	76
3.3.6. Chemical synthesis, NMR and MS of PtmPEG ₂ 1Glc ₂ (trans)	77
3.3.7. Chemical synthesis, NMR and MS of Pt1Glc ₄	80
3.3.9. Chemical synthesis, NMR and MS of PtcPEG ₄	85
3.3.9. Chemical synthesis, NMR and MS of PtmPEG ₄	87
3.4. Photophysical and O ₂ -sensing properties of the new compounds.....	93
3.4.1. <i>trans</i> -di-substituted derivatives of PtPFPP	96
3.5. Conclusions	98
Chapter 4: Cell staining behaviour of the new derivatives in mammalian cell cultures.....	99
4.1. Cellular uptake and toxicity of the 3:1 Derivatives	99
4.2. Cellular uptake and toxicity of the <i>trans</i> - 2:2 derivative	106
4.3. Microscopy analysis of intracellular distribution.....	109
4.4. Involvement of GLUTs transporters in probe uptake	112
4.5. Conclusions	115
Chapter 5: Applications of the new probes with bacterial cell cultures.....	116
5.1. Introduction	116

5.2. Performance of the small molecule probes in respirometric bacterial assays using complex media.....	117
5.2.1. Selection and general comparison of the O ₂ probes.....	118
5.2.2. Basal and maximal phosphorescent signals of the probes in the <i>E. coli</i> assays	120
5.2.3. Full respiration profiles of <i>E. coli</i> produced with the different media and probes	122
5.2.4. Analysis of individual media components for interferences	126
5.2.5. Analysis of blank signals and spectroscopic effects of the media	128
5.3. Staining ability of the probes with <i>E. coli</i> cells.....	132
5.4. Overall comparison and ranking of the probes	133
5.5. Conclusions	135
OVERALL DISCUSSION	137
Appendix	142
Thesis outcomes	147
Bibliography	148

Declaration

This is to certify that the work I am submitting is my own and has not been submitted for another degree, either at University College Cork or elsewhere. All external references and sources are clearly acknowledged and identified within the contents. I have read and understood the regulations of University College Cork concerning plagiarism and intellectual property.

Signed: Zanetti Chiara



Zanetti Chiara

Date: 14/12/2023

Acknowledgements

I would like to express my deepest and sincere gratitude to my supervisor Professor Dmitri Papkovsky for his invaluable expertise, guidance, and support.

Many thanks to Professor Anita Maguire for her collaboration and precious feedbacks for the chemical part of my project.

A special thanks goes to my co-worker Dr. Rafael Gaspar for his precious knowledge and constant support. Thanks to Dr. Alexander Zhdanov for his training and help with the biological part of my project. Thanks to Dr. Nuala Maguire, and Ciara Tyner for their kindness and support. Most sincere thanks to Dr. Denis Lynsh for his precious help with NMR training and MS analysis.

These four years would have been a lot less fun without all my office mates Emer, Liang, Rajannya, Dominic, and Sophia.

Finally, I want to thank my family, friends, and boyfriend Marcin for their constant encouragement, emotional support, and for always believing in me.

List of abbreviations

[O₂] - Oxygen concentration

¹Σg⁺ and ¹Δg - Singlet oxygen states

³Σg⁻ - Triplet oxygen state

ACN – Acetonitrile

AntiA – Antimycin A

ATP – Adenosine triphosphate

BCP – Bromocresol purple

BOLD MRI - Blood oxygen level-dependent magnetic resonance imaging

CA – Cysteamine

Cps – count per second

DMF – Dimethylformamide

E. coli – Escherichia coli

ECAR – Extracellular acidification rate

EGTA - Ethylene glycol tetraacetic acid

EPR - Electron paramagnetic resonance

ETC – Electron transport chain

FA – Formic acid

¹⁹F MRI - Fluorine-19 magnetic resonance imaging

FRET – Förster resonance energy transfer

Glc – Glucose

H₂O₂ – Hydrogen peroxide

Hb – Deoxy-hemoglobin

HbO₂ – Oxy-hemoglobin

HIF – Hypoxia inducible factor

IC – Intracellular

iCa²⁺ - intracellular calcium

IcO₂ – Intracellular oxygen probe

IFE – Inner filter effect

LED – Light emitting diode

LT – Lifetime

MEFs – Murine embryonic fibroblasts

MeOH – Methanol

MQw – MilliQ water

NIRS – Near infra-red spectroscopy

O₂ - Molecular oxygen

OCR – Oxygen consumption rate

OxPhos – Oxydative phosphorylation

PDT - Photodynamic therapy

PEG – Polyethylene glycol

PET - Positron emission tomography

pO₂ – Partial pressure of O₂

RLD – Rapid lifetime dtermination

ROS - Reactive oxygen species

rSO₂ - Regional oxygen saturation

SARs – Structure activity relationships

S_n - Excited singlet states

SpO₂ - Oxygen saturation

T₁ - Excited triplet state

TCSPC – Time correlated single photon counting

TEA – Triethylamine

TEAA - Triethylammonium acetate

TFA – Trifluoroacetic acid

TRF - Time-resolved fluorometry

TVCs - Total aerobic viable counts

Abstract

Accurate monitoring of O₂ levels is crucial for understanding the growth, differentiation, and function of individual cells and tissues. While phosphorescence-based oxygen sensing offers great potential for such investigations, current probes still show limitations in terms of their bio-distribution and analytical performance. New improved O₂ probes are highly needed.

In this project we synthesized a family of new hetero-substituted phosphorescent derivatives of Pt(II)-tetrakis(pentafluorophenyl)porphyrin (PtPFPP) dye, through click-modification of its *para*-fluorine atoms with 1-β-D-thio-glucose, neutral (mPEG) and carboxy (cPEG) thiol-PEGs, named as PtmPEG₃1Glc and PtcPEG₃1Glc respectively, or cysteamine (CA), named PtCA₃1Glc. Derivatisation with 2-thioethyl-β-D-glucopyranoside was also performed to evaluate the effects of alternative SH-Glucose structures on cellular uptake, obtaining the corresponding 2Glc derivatives. The new probes comprise one cell-targeting moiety and three polar moieties, forming a hydrophilic shell. We also synthesized the di-glucosilated-di-PEGylated derivative, named as PtmPEG₂1Glc₂ (*trans*), in which 1-thio-β-D-glucose (1Glc) and thio-methyl-polyethylene-glycol (mPEG) moieties were covalently attached to PtPFPP in *trans*- position. Tetra-substituted derivatives Pt1Glc₄, Pt2Glc₄, PtmPEG₄ and PtcPEG₄ were also synthesised and characterized for benchmarking.

The chemical synthesis and purification procedures were optimized for all the new derivatives to achieve high reaction yields and scalability, and new chemical structures were confirmed by HR-MS and NMR. Then, the most promising derivatives were assessed for their spectral properties and cell penetrating ability in 2D mammalian cell cultures using time-resolved fluorescence (TRF) on a standard plate reader, and confocal microscopy in PLIM mode (phosphorescence lifetime imaging). Probes' ability to function as either cell permeable or impermeable was found to depend on polarity, molecular charge, size, and substitution position of the bioconjugate.

Notably, the hetero-substituted tri-PEGylated (PtcPEG₃1Glc, PtmPEG₃1Glc) and tetra-PEGylated (PtcPEG₄, PtmPEG₄) derivatives showed reduced cell internalization compared to the 3:1 cysteamine (PtCA₃1Glc) derivative and 4:1 glycosylated probe (Pt1Glc₄). This finding opens possibilities for their extracellular applications.

In contrast, PtmPEG₂1Glc₂ (trans), demonstrated efficient cell staining and suitability for intracellular oxygen sensing (IcO₂) in murine embryonic fibroblast (MEFs) cells. Moreover, biocompatibility studies indicated no significant cytotoxicity for all probes at any tested concentrations, except for PtCA₃1Glc which caused reduced cell viability at concentrations above 10 μM.

The chemical modifications did not alter absorption and emission spectra of the PtPFPP moiety but reduced its brightness and lifetimes. Some of the PEGylated derivatives showed tendency to aggregate in biological media. PtmPEG₄ and Pt1Glc₄ were also evaluated in microbial respirometric assays with *Escherichia coli* (*E. coli*) cells, however due to the lack of shielding, their performance in complex media was not as good as the macromolecular MitoXpress probe and the nanoparticle based NanO₂ probe.

Overall, our new phosphorescent bioprobes, particularly the hetero-substituted structures, extend the library of extracellular and intracellular probes for monitoring and imaging O₂ in mammalian cell cultures. They are compatible with standard TRF plate readers and PLIM microscopes, making them promising candidates for physiological studies with cells. The established structure-activity relationships (SARs) will also help to develop new probe structures for future studies.

Chapter 1: Literature review

1.1. Introduction to biological roles of oxygen

Molecular Oxygen (O_2) is one of the most important analytes in many fields including industrial process control, microbial safety, food science (1), environmental monitoring (2), biomedical research and clinical diagnostics. With respect to cell biology and tissue physiology, O_2 is involved in many critical cell and tissue functions, which makes it an informative marker of metabolic status, viability, and presence of aerobic organisms. O_2 is fundamental for energy production in the form of adenosine triphosphate (ATP) in the mitochondria, it is an important signalling molecule (3), and substrate for numerous enzymatic reactions (4).

Mammalian cells and tissues are programmed to function at physiological O_2 levels (basal oxygenation state) to perform effectively all their specific function (5). Tight regulation of O_2 delivery and consumption is necessary to maintain a balance between energy production and formation of potentially toxic metabolites (6). Up to 95% of the O_2 in the body is normally utilized for aerobic ATP generation through the electron transport chain (ETC) and oxidative phosphorylation (OxPhos) pathway in the mitochondria. O_2 is the final electron acceptor and ultimately gets fully reduced into water. However, another important outcome of the O_2 reduction is the production of reactive oxygen species (ROS), via non-specific electron transfers to the O_2 , producing superoxide anion ($\cdot O_2^-$), which is quickly converted into hydrogen peroxide (H_2O_2) and then hydroxyl radical ($\cdot OH$). Under homeostatic conditions, ROS are degraded by enzymatic (e.g. superoxide dismutase - SOD) and non-enzymatic (glutathione S-transferase - GST) scavenger systems (7) which prevent cellular damage. At the same time, ROS and especially H_2O_2 , function as important signalling molecules (8) and are involved in the activation of antioxidant defences, cell repair and proliferation (3). An imbalance between O_2 supply and demand can lead to pathophysiological states such as inflammation, metabolic disorder, cancer, ischemia, and stroke (9). In particular, a sharp decrease in cellular O_2 concentration develops a state of tissue hypoxia which results in reduced ATP production, excessive ROS generation, and may ultimately lead to cell death (10). O_2 concentration can therefore

be used as an indicator of genetic adaptation in response to hypoxic conditions (11). At the molecular level, changes in cellular oxygenation are transduced to the nucleus altering gene expression via the hypoxia-inducible transcription factor (HIF). The HIF protein regulates the transcription of hundreds of genes involved in adaptation of the cell to hypoxia (12). HIF has an O₂-regulated HIF-1 α subunit, and a constitutively expressed HIF-1 β subunit (13). At low O₂, HIF-1 α degradation gets inhibited, causing its dimerization with the β subunit and translocation to the nucleus, where it ultimately activates transcription of many genes involved in metabolic adaptation to low O₂ availability, angiogenesis and erythropoiesis to increase O₂ delivery (6). Mammalian cells are indeed able to produce energy in anaerobic conditions through glycolysis paired with reduction of pyruvate into lactate, allowing the survival of stressful conditions and changing environment. However, maladaptive responses can also develop and lead to tissue remodelling, cell dysfunction, and uncontrolled cellular growth (5, 14). Therefore, quantification of O₂ in cells, tissues and other biological samples is of high value for researchers, to gain insights into cellular metabolism, oxygen delivery, responses to stimuli, changes in gene expression and cell signalling. Knowledge and precise control of tissue oxygenation can also aid our understanding of molecular mechanisms of many common disease states (15, 16) associated with cell and tissue hypoxia (e.g. cancer, stroke, inflammation, metabolic disorders), and development of new therapeutic treatments (e.g. photodynamic (17), chemo-, radio- and monoclonal antibody therapy (18, 19)).

1.2. Methods for O₂ detection

From the chemical and analytical points of view, O₂ is a small, non-polar gaseous molecule with paramagnetic characteristics. Its solubility in water is moderate and influenced by temperature, pressure, and salinity (20). It can diffuse quickly across cell membranes and different cell compartments (11). Direct detection of O₂ is limited by its poor photophysical characteristics (10). Its intrinsic absorption is characterized by a broad intense band at 145 nm and a very weak band at 760 nm (21). Direct determination of O₂ was attempted (22) using its deep UV absorption band, however, poor sensitivity and interferences from other gaseous compounds were found.

Therefore, traditional methods for quantification of dissolved O₂ relied on sampling and offline analysis by chemical methods, such as the Winkler titration (23), pressure-based techniques (24, 25), gas chromatography (26). However, to meet the growing demand for continuous monitoring, non-invasive measurements and in situ analysis of O₂ in complex biological samples, new detection platforms have been developed (10), mainly based on electrochemical and optical methods (Table 1.1).

The *Winkler method* allows for the indirect determination of dissolved oxygen in water samples via iodometric titration. During the test, an excess of manganese(II) salt, iodide (I⁻), and hydroxide (OH⁻) ions are introduced into a water sample, resulting in the formation of a white precipitate of Mn(OH)₂. This precipitate undergoes oxidation by the oxygen present in the water, transforming into a brown precipitate. Subsequently, the solution gets acidified using a strong acid which converts the iodide ions (I⁻) into iodine (I₂). The quantification of dissolved oxygen directly correlates with the titration of iodine using a thiosulfate solution. It is accurate and precise and still used today as a reference technique. It has been modified to improve sensitivity and semi-automated but still is not suitable for online measurements and can only be applied to simple 'clean' samples (27, 28).

In the 1950s the *Clark electrode* (29), which operates on the principle of polarography, was introduced. It contains a Pt-coated cathode and an anode (Ag/AgCl), immersed into an electrolyte solution (KCl) that communicates with the sample through an O₂ permeable membrane. The current created by the reduction of O₂ molecules at the polarized electrode is measured and correlated to O₂ concentration in the sample (27, 28). Clark electrode, regarded as one of the first sensors, has enabled the precise and continuous measurement of dissolved O₂ in various samples, including blood and tissues. This robust and reliable method is still considered as the gold standard for measuring tissue O₂ (30). However, it is invasive, consumes the analyte, it is subject to drifts, electrical and chemical interferences and it does not work reliably at low O₂ levels (sensitivity limited to micromolar (μM) levels of dissolved oxygen in aqueous solutions) (21, 31).

Table 1.1: Summary of instrumental methods for O₂ detection/quantification

Technique (Ref.)	Detection principle	Applications	Advantages	Limitations
Winkler method (32)	Iodine titration	Indirect dissolver O ₂ determination in water samples	Precise Sensitive (trace amounts)	Non-portable Not user friendly Indirect
Clark O₂ electrode - Polarographic-type (29)	Electrochemical measurement of dissolved [O ₂] (redox reaction at the electrode)	Blood and tissue oxygenation via point measurements	Real-time Simple setup Accurate Widely used	Invasiveness Frequent calibration High maintenance Consumes the analyte Low sensitivity
Pulse oximeter (33, 34)	Differential absorption of HbO ₂ and Hb	Monitoring of arterial SpO ₂ (and heart rate)	Non-invasive Easy to use Continuous Widely used	Optical interferences Signal artifacts
NIR spectroscopy (35-37)	Non-pulsatile oximetry	Monitoring of cerebral oxygenation and rSO ₂	Regional monitoring Continuous Non-invasive	Low S/N Optical interferences Motion artifacts
Pimonidazole Hypoxia staining (38, 39)	Immuno-histochemistry of redox dye	Visualize tissue hypoxia	Selective for hypoxic cells Widely used	Indirect Irreversible Not real-time Low sensitivity
¹⁹F MRI (40)	Paramagnetic relaxation of the ¹⁹ F nuclei	Tumours pO ₂ imaging O ₂ dynamics	Sensitivity Quantitative High affinity High S/N	Indirect Injectable Low detection limit (dosage)
BOLD MRI (41, 42)	Paramagnetic Hb signal	Intravascular /tumoral pO ₂ Detection of pO ₂ fluctuations	Real-time High spatial resolution Non-invasive	Qualitative Signal interferences
EPR probes (15, 43)	Paramagnetic O ₂ effect on EPR probe signal	Direct tissues pO ₂ measurements	Sensitivity Inert Real time Continuous	Implantation needed Spatial resolution
PET (44, 45)	Radiolabeled Markers (redox reaction or direct measurements)	Imaging of tumour hypoxia and brain oxygenation	Specificity and sensitivity Whole-body imaging	Radiations Spatial resolution Perfusion-limited
Phosphorescence quenching (5, 46-49)	Phosphorescence quenching of exogenous probes by dissolved O ₂	Intra- or extra-cellular O ₂ sensing and imaging	Direct Quantitative Highly sensitive Flexible applications (samples, modalities, and platforms)	Possible cito- and phototoxicity Photobleaching

Optical techniques for biological O₂ sensing represent a large and important group, which has emerged as an alternative to conventional methods (50). They take advantage of the interaction of light with endogenous or exogenous indicator molecules, or special oxygen-sensitive chromophores, that alter their photophysical characteristics in response to changes in oxygen levels (51).

In 1975, *pulse oximetry* was introduced (34), which is a non-invasive biomedical technique that allows continuous monitoring of oxygen saturation (SpO₂) levels of arterial blood. Its working principle relies on the different absorption characteristics of oxygenated hemoglobin (HbO₂, 640 nm) and deoxy hemoglobin (Hb, 940nm), present in the blood. Two LEDs emit light at these specific wavelengths, which passes through thin tissues such as the fingertip or earlobe, and a photodetector determines the amount of transmitted light and calculates the SpO₂ (33). The pulse oximeter was introduced in clinical settings during the '80s and remains essential nowadays in emergency situations, routine and intensive care, anesthesiology, and home care. However, it is not applicable to other sample types and often suffers from optical interferences, motion and signal artifacts (33).

Near infrared spectroscopy (NIRS), which became popular in the '90s, relies on the same photophysical principle as the pulse oximeter, but quantifies HbO₂ based on the amount of attenuated light that reaches the photodetector. Its advantage is that HbO₂ absorbs much more light in the near-IR than Hb, which allows hemoglobin saturation to be measured in a more targeted fashion (37). In medical settings, it is used to monitor regional cerebral oxygen saturation (rSO₂) (52) and metabolism, but was also applied to skeletal muscle (53), spinal cord (54) and other tissues (36, 55). Limitations mostly concern the thickness of the superficial tissue, optical interferences by other chromophores absorbing in the same region, e.g. myoglobin, and changes in the sample volume (35).

Several spectroscopic and imaging techniques have been developed to obtain quantitative and qualitative visualisation of hypoxic regions(56). They use injectable contrast agents – such as bio reducing 2-nitroimidazole analogues suitably labelled, or perfluorocarbons. For example, *pimonidazole* is used to selectively stain hypoxic areas in tumoral or ischemic tissues with subsequent visualization of its reduced form

by immunohistochemistry (38). When the oxygen tension is below 10 mmHg, pimonidazole is reduced by the enzyme 2-nitro-reductase, making it capable of binding to thiol-containing proteins. However, hypoxia could take place also at higher pO_2 (38, 39).

The Fluorine-19 Magnetic Resonance Imaging (^{19}F MRI) technique, introduced in the 1970s (40), employs biocompatible fluorinated contrast agents which can indirectly detect concentration changes of several chemical species, including O_2 . The interaction of these compounds with the F atoms shifts their detectable signal (paramagnetic relaxation effect), and this can be used for measurements of tumour oxygenation and quantitative imaging of pO_2 at low oxygen levels (57, 58). Another type of MRI technique is the *Blood oxygen level-dependent MRI (BOLD)* (42), which is utilized to study brain activity without any injectable contrast agent (41). Its detection principle relies on the ability of the diamagnetic HbO_2 (little to no susceptibility to magnetic fields) to change into the paramagnetic Hb (slight attraction to the magnetic field) during brain metabolic consumption, generating a decreased MRI signal intensity. It is a highly sensitive technique, however it does not determine absolute pO_2 (59), and it is subject to blood flow and volume fluctuations (60).

Electron paramagnetic resonance (EPR) oximetry is another spectroscopic and imaging technique that allows for precise and repeated measurements of tissue oxygenation (15). It takes advantage of the paramagnetic nature of O_2 which alters the relaxation rates of oxygen-sensitive paramagnetic materials. These exogenous EPR probes are implanted (particulates) in a specific area of the body or injected (soluble probes), to allow imaging of tissues, organs, or the full body. The magnitude of the effects on the EPR signal are correlated to the oxygen concentration $[O_2]$ in the vicinity of the paramagnetic material (43). It is a highly sensitive technique, however measurements are limited to the point of implantation and the sampling area, and it is not widely available due to lack of expertise and instrumentation. It is not yet established for use in humans (61).

Positron Emission Tomography (PET) is a highly specific and sensitive technique for imaging of tumour hypoxia, with the ability to access intracellular oxygenation (45). It employs radiotracer probes, such as nitroimidazole derivatives labelled with the positron-emitting radionuclide fluorine-18, which are intravenously injected and

subsequently accumulated in hypoxic tissues where they get gradually reduced and irreversibly trapped in the cells. One drawback of this technique is that the radiotracer diffusion is driven by tissue perfusion, thus its accumulation in the hypoxic tissue could be hindered (45). Alternatively, ^{15}O can be inhaled or introduced via ^{15}O -labeled water into the body (62), to determine brain oxygenation and metabolism (44).

However, our focus is the group of optical techniques for biological O_2 sensing based on photoluminescent materials that are quenched by O_2 . Quenched-phosphorescence O_2 sensing techniques were pioneered by David Wilson (46, 63) and D.W. Lübbers (47), and then underwent significant advancements in their sensor chemistries, measurement methods, and instrumentation (11, 21, 64). This, in turn, has enabled many new analytical tasks and applications (65).

1.3. Principles of quenched-phosphorescence O_2 sensing technique

Quenched-phosphorescence O_2 sensing is a versatile optical technique for O_2 sensing. It provides direct, reversible, real-time detection and continuous monitoring of O_2 concentration in chemical and biological samples. Its mechanism relies on specific molecules, called phosphors, which upon light excitation undergo intersystem crossing from their excited singlet states (S_n) into triplet state (T_1) and then produce long-lived emission called phosphorescence (Figure 1.1) (64, 66, 67). In the presence of O_2 , the phosphorescence emission is quenched by dynamic collisions between sample O_2 molecules and excited triplet states (T_1) of the luminophore, resulting in their radiation-less deactivation (21, 68). This process is described by the modified Perrin-Jablonski diagram (Figure 1.1).

The exact mechanism of oxygen quenching is not completely understood. It is generally accepted that when an excited triplet state luminophore molecule collides with a ground-state dioxygen molecule ($^3\Sigma_g^-$ triplet state), the T_1 state undergoes radiation-less transition to the ground state (S_0), while $^3\Sigma_g^-$ is converted into singlet oxygen states $^1\Sigma_g^+$ and $^1\Delta_g$ ($^1\text{O}_2$). The process occurs due to the similar but lower energy of the singlet oxygen orbitals which facilitates the spin-allowed energy

transfer from the luminophore's T_1 state to the quencher (64, 66). The production of 1O_2 is an indication of the energy transfer mechanism. However electron transfer was also demonstrated (69).

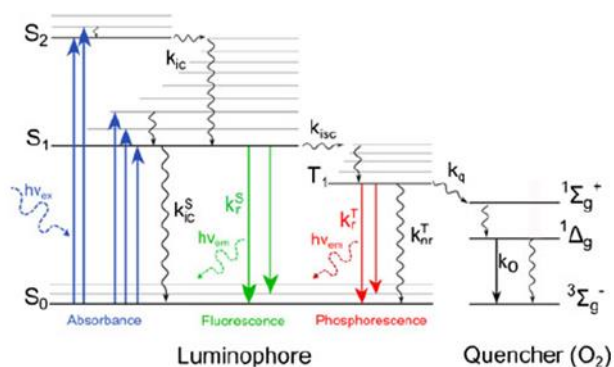


Figure 1.1: Perrin-Jablonski diagram, adopted from (64).

After its formation, the short-lived $^1\Sigma_g^+$ state undergoes fast transition into $^1\Delta_g$, which has a life span of several microseconds (70). During this period, $^1\Delta_g$ mostly relaxes to the ground triplet state ($^3\Sigma_g^-$), by radiation-less energy dissipation or by emitting weak fluorescence, thereby regenerating the quencher (66). At the same time, the $^1\Delta_g$ state is very reactive and can interact with adjacent molecules (e.g. lipids, DNA, proteins) and also generate other ROS and nitric oxide derivatives (71). These processes of photosensitisation and photo-consumption of O_2 , and corresponding photo-toxicity and photo-oxidation reactions of the luminophore with sample components are of significant concern in O_2 sensor development and application.

The good selectivity of the O_2 sensing technique is because O_2 is an abundant molecule and present at high concentrations compared to other potential quenchers, such as halogenated compounds (chlorine, iodine, and bromine), nitric oxides (NOx), olefines and quinones, nitro compounds and sulphur dioxide (SO_2), which are also rarely present in biological matrices. Interference from gases such as CO_2 , N_2 or H_2 is negligible, as well as from bioorganic molecules like nucleic acids, saccharides, proteins. Only tryptophan moiety can undergo Förster resonance energy transfer (FRET) with UV-absorbing phosphors (21).

1.3.1. Measurement of O₂ and quantitative relationships

Sample O₂ quenches the emission intensity (or quantum yield) and lifetime (or decay time, which is defined as the average time that a luminophore spends in the excited state before returning to the ground state) of the phosphor, in a concentration dependent manner (67). The relationship between these parameters and O₂ concentration is described by the Stern-Volmer equation:

$$\frac{I_0}{I} = \frac{\tau_0}{\tau} = 1 + k_q * \tau_0 * [O_2] = 1 + K_{sv} * [O_2] \quad (1.1)$$

Where I_0 , I are the emission intensities and τ_0 , τ are the lifetimes in the absence or presence of [O₂], respectively, k_q is the bimolecular quenching rate constant and K_{sv} is the Stern-Volmer quenching constant (67). τ is an intrinsic property that is independent of the concentration of the luminophore itself. For this reason, lifetime measurements are generally preferred over intensity for sensing applications (11). From eq. 1.1, the [O₂] can be quantified as follows:

$$[O_2] = (\tau_0 - \tau) / (\tau * K_{sv}) \quad (1.2)$$

$$[O_2] = (I_0 - I) / (I * K_{sv}) \quad (1.3)$$

The Stern-Volmer quenching constant ($K_{sv} = k_q * \tau_0$) is influenced by several parameters such as diffusion rate constant (72), temperature (T) and viscosity (η). Higher T slightly decreases the luminescence QY and the τ , but it increases the k_q (21). For dynamic quenching, higher T and lower η promote O₂ quenching as they facilitate the diffusion of the quencher to the luminophore (73). Since O₂ is a relatively mild quencher, to achieve optimal sensitivity, phosphors with relatively long decay of emission and moderate quenchability at ambient oxygen of approximately 2-to-5 times of their τ_0 should be used (74).

The Stern-Volmer constant, K_{sv} , reflects the sensitivity of the luminophore to O₂, the dynamic range and limit of detection (LODs) of a sensor (21). LOD is defined as the minimal concentration of the analyte that can be detected with statistical significance by a specific analytical procedure. In the case of optical sensing based on phosphorescent quenching, the LOD is driven by the initial slope of the SV plot (K_{sv}), by the sensitivity of the instrument used to collect the signal. Practically, it is

determined by the concentration of analyte yielding a signal to noise ratio (S/N) of 3/1 (75). By proper choice of the phosphor and the polymer, different analytical ranges can be achieved to suit the application requirements. Most sensors have been tuned to cover the sensitivity range from 0 to 40 kPa with LOD of about 0.5 Pa (21). Spectral characteristics, phosphorescent intensity signal, QY and lifetime of the T_1 are all determinants of the dynamic range of the O_2 sensor, which can also be tuned (76). At low O_2 the curve is almost linear and has the highest slope, whereas at higher pO_2 the slope decreases, so as the sensitivity and precision (Figure 1.2) (19).

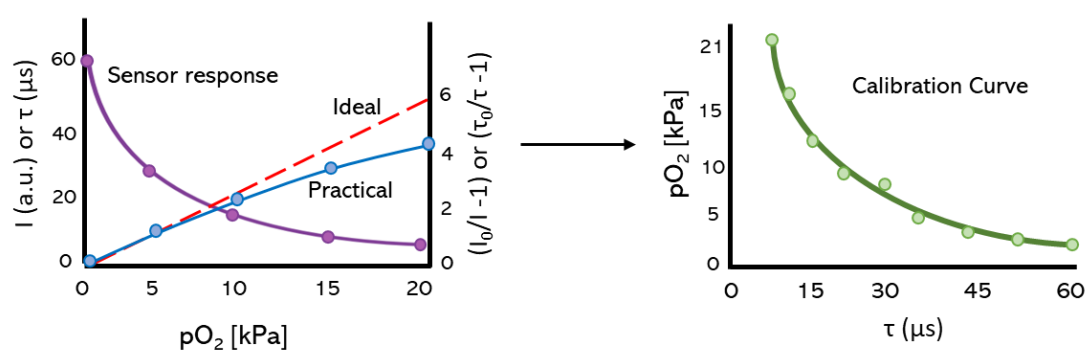


Figure 1.2: Plot of the luminescence intensity or decay time quenched by oxygen and the corresponding ideal and practical Stern–Volmer plots. Image modified from(21). Example of calibration curve obtained by measuring the lifetime of a phosphor at different known $[O_2]$ between 0 and 21 kPa.

1.3.2. Sensor Calibration

To accurately quantify sample $[O_2]$, sensor calibration needs to be established. This involves measuring the sensor I or τ at a set of known O_2 concentrations (standards), constructing a calibration curve based on the collected datapoints and fitting them with an appropriate mathematical function to produce the calibration equation, specific to each sensor material (65, 74). Each measurement should be carried out under stable pressure, temperature, and probe concentration, within 0 and 21 kPa. It is especially important to obtain accurate calibration and determine τ_0 in the absence of O_2 , as small experimental error in this range results in big errors in the calibration. Zero O_2 concentration in liquid samples can be achieved by bubbling O_2 -free gas (21), or using O_2 scavengers such as sodium sulfite or glucose/glucose oxidase (48).

Measured data and O₂ calibrations are often plotted as I₀/I or τ₀/τ vs [O₂] (or partial pressure pO₂). For an homogeneous dispersion of the phosphor (ideal case), a linear relationship (SV plot) between I or τ and [O₂] is produced, with the slope equal to K_{sv}, as shown in Figure 1.2 (64, 67). This is generally satisfied in solution systems, where all indicator molecules exist in a homogenous environment and produce single exponential emission decays (77) which allow for simple one- or two-point calibrations.

However, many O₂-sensitive probes produce curved plots, indicating heterogeneity. This is common for solid-state sensors (78) with complex interactions between the indicator and the polymeric matrix (77), which result in a downward curvature requiring multipoint calibration (78, 79). This non-linearity is due to different micro-environment of phosphor molecules producing different K_q and τ values (80). In such cases, alternative models should be used, such as the two-site model which assumes the existence of two populations of phosphor molecules and microenvironments (78).

According to eqn. 1.2 and 1.3, O₂ can be quantified by measuring sensor intensity or lifetime signal. Intensity measurements are more prone to drift, unstable calibration and measurement errors, whereas O₂ sensing based on luminescence lifetime measurements provides more stable calibration and better performance (74).

1.4. Detection and O₂ sensing modalities

1.4.1. Intensity-based measurements

Steady-state luminescence intensity measurements with an O₂ sensitive material is a simple and straightforward method to quantify O₂ concentrations in a sample (I = f[O₂]). The material is excited at its optimal absorption wavelength producing *emission signal* at a *different (longer) wavelength* (Figure 1.3 A). However, Intensity signal is influenced by the phosphor concentration and photobleaching (64), measurement geometry, scattering of light and autofluorescence from complex biological samples (81). The signal can also be affected by detector and light source

fluctuations. All this causes drifts in the calibration and sensor signals (74) and makes the O₂ measurements unstable, inaccurate and not truly quantitative (10).

Ratiometric intensity measurements can overcome some of the above limitations of intensity based sensing (81-83). This sensing scheme, in addition to the oxygen sensitive phosphor, uses a reference dye which is oxygen insensitive (Figure 1.3 B). The intensity signals of the two dyes are measured at two different wavelengths and the O₂ concentration is derived from their ratio $[O_2] = f(I_s/I_{ref})$ (84). *Dual wavelength emitters* (85, 86), i.e. one indicator dye with well resolved fluorescence and phosphorescence emission bands, have also been reported. However they are hard to design (72).

A more reliable type of intensity measurement is *time-resolved (or time-gated) fluorometry* (TRF) (Fig 1.3 C), which can effectively suppress the optical background while retaining specific long-lived luminescent signal, thus increasing the S:N ratio. In TRF, the sample is excited by a short pulse of light, and after a delay time interval the luminescent signal is collected. This way, short-lived autofluorescence and scattered light cannot interfere with the measurement (11, 21). Since the excitation pulse should be shorter than the sensor emission decay, the TRF mode is usually applied to luminophores with micro- or milli-second lifetimes.

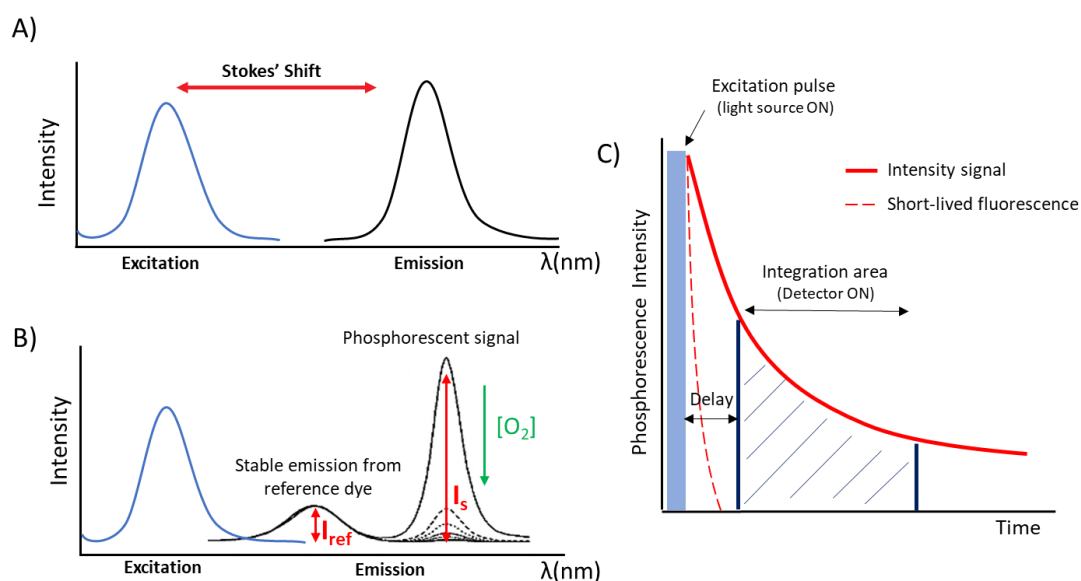


Figure 1.3: Intensity-based detection modes. A) Steady-state intensity measurements at one wavelength. B) Ratiometric intensity measurement: emission spectra measured at different $[\text{O}_2]$ concentrations using an oxygen sensitive indicator dye and an O_2 insensitive reference dye (fluorescent or phosphorescent). C) TRF intensity measurements.

1.4.2. Lifetime-based measurements

Generally, *lifetime-based measurements* are preferred as τ is an intrinsic parameter of the phosphor, not affected by the dye concentration or photobleaching, measurement geometry, light source and detector fluctuations, sample matrix, etc. Moreover, lifetime-based measurements are particularly useful for determination of O_2 in complex biological samples with high autofluorescence, light scattering or intrinsic absorbance (i.e. inner-filter effect), and in intracellular O_2 sensing in which the exact quantity of probe after cellular uptake is hard to determine and replicate (87). Phosphorescence lifetimes can be measured in frequency domain or in time domain, also known as phase and pulsed fluorometry techniques, respectively.

Frequency-domain fluorometry uses sinusoidally modulated excitation of the phosphor and measures phase shift of its emission, which is dependent upon the O_2 concentration. Knowing the modulation frequency and phase shift, lifetime (LT) can be calculated (21, 84) (Figure 1.4 A). Limitations of this method are that it is indirect,

sensitive to scattering and autofluorescence, and it requires multi-frequency measurements to devise complex emission decays.

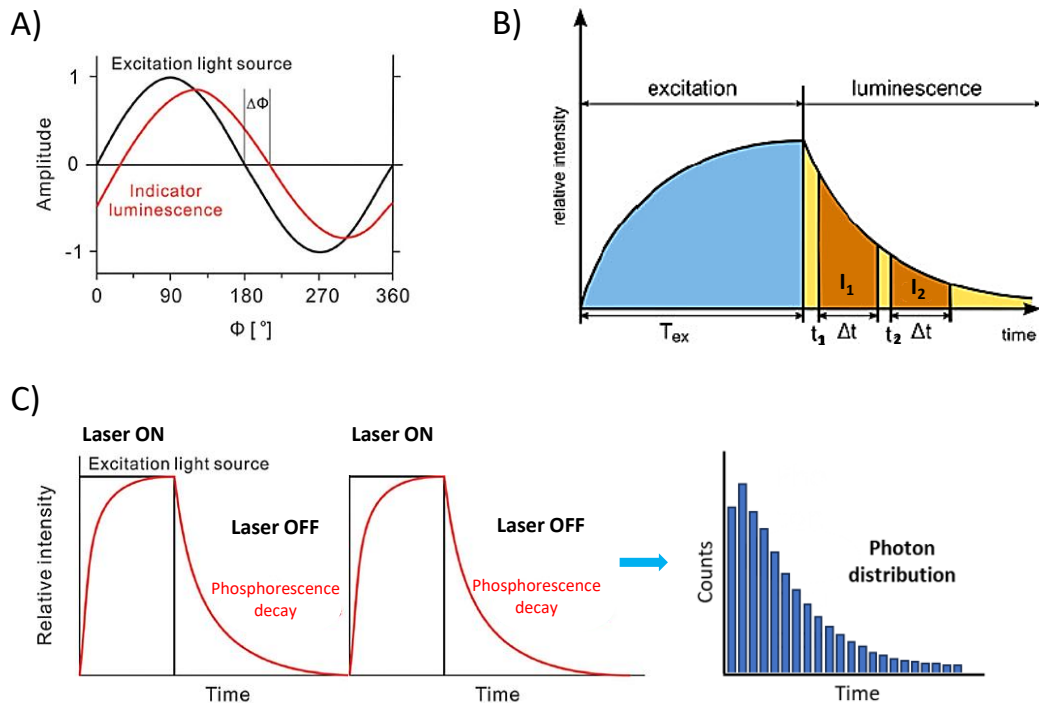


Figure 1.4: Examples of lifetime based measurements using A) frequency domain fluorometry, B) rapid lifetime determination (RLD) (84), or C) time-correlated single photon counting (TCSPC) (21).

Time-domain fluorometry can be performed in a number of formats: a) rapid lifetime determination (RLD); b) multi-point measurements of the decay by binning method; c) time-correlated single photon counting (TCSPC). A simplified version of the time-domain LT measurements is the RLD (88, 89): two TRF intensity signals are measured at two delay times (t_1 and t_2) following the excitation pulse, lifetime is then calculated as:

$$\tau = \frac{t_2 - t_1}{\ln \frac{I_1}{I_2}} \quad (\text{eq.1.4})$$

The RLD is used in screening applications of O_2 sensing on commercial microplate readers, which support this mode and provide high stability of LT measurements and quantitative calibration-free O_2 sensing. However, RLD does not account for complex

decays of the sensor material, but rather determines changes in apparent lifetime (21). As a result, its accuracy in lifetime determination is not as good as for the classical methods (90) (Figure 1.4 B).

Time-correlated single photon counting (TCSPC) technique uses short excitation pulses with higher repetition rate, with collection of emitted photons with a high-gain photomultiplier. The arrival time for each detected photon is determined and then correlated with the excitation pulse, generating a distribution of emitted photons over time. The resulting decay curve is subsequently fitted (91, 92) (Figure 1.4 C) with a mono- or multi-exponential decay function and lifetime is calculated (21).

While the time- and phase-domain techniques provide essentially the same information, the TCSPC technique is direct, and it provides absolute LT values. TCSPC also allows measurements of low fluorophore concentrations and low quantum yields (92).

1.4.3. O₂ imaging

Imaging of O₂ has gained increasing importance for the study of 2-D and 3-D biological objects and of intra- and extra-cellular O₂ distribution. *Luminescence imaging* can be performed in lifetime or intensity mode. Fluorophores, due to their short lifetimes (0.1-10 ns) and small Stokes' shifts, are affected by scattering and autofluorescence of endogenous emitters. When using triplet emitters (phosphors) with large Stokes' shifts (>100 nm) and long lifetimes (up to ms), the short-lived background fluorescence and scattered light can be separated by collecting the signal after a time delay. Such intensity-based measurements were explored for imaging of subcellular structures and oxygen distribution (63). However, they are often unsuitable for quantitative analysis due to high rate of dye photobleaching under intense excitation of the sample, and fluctuation in delivery efficiency of the probe and its uneven distribution (93). Ratiometric probes can overcome some of these issues, however, lifetime-based measurements are the most efficient and stable.

Generating images in fluorescence lifetime scale (ns range) is called fluorescence lifetime imaging microscopy (FLIM) (94), while phosphorescent lifetime imaging microscopy (PLIM) operates with μs -ms lifetimes. These techniques made it possible to use the lifetime not only to study the fluorophore / phosphor microenvironment with regards to $[\text{O}_2]$, pH, and many ions, but also as a function of biological parameters such as proteins interactions, and detection of fluorescence resonance energy transfer (FRET), and much more (94).

The most efficient and accurate way for FLIM/PLIM acquisition is by laser-scanning confocal microscopy paired with a TCSPC detector – a high-speed photon counting PMT (Photomultiplier Tube). This technique allows precise lifetime recording. Using point illumination through a pinhole located in the focal plane of the lens, this ensures that only the focused luminescence is detected, providing high level of resolution and depth of acquisition- (94). Alternatively, phase modulation technique or wide field microscope paired with a time-gated camera (intensity measurements using multiphoton excitation) can be utilized, to speed up image acquisition, or extend sample area (95). However, the combination of the axial resolution provided by the confocal scanning and the efficiency of data acquisition via TCSPC makes it the most robust and precise method to determine the lifetime, despite the slower acquisition rates (94).

1.5. O_2 sensitive dyes / phosphors

The chemical nature of the dye defines most of the characteristics of the oxygen sensitive material, such as spectral characteristics, luminescence efficiency and general quenchability. However, the quenching medium is another important factor as it defines O_2 solubility and diffusion rate and the dye microenvironment (74).

According to the Jablonski diagram (see above, Fig. 1.1), an efficient phosphor for O_2 sensing is expected to have: i) high absorption of excitation light ($S_0 \rightarrow S_n$); ii) efficient intersystem crossing process ($S_1 \rightarrow T_1$), iii) high yield of excited triplet states T_1 ; iv) high yield of phosphorescence emission ($T_1 \rightarrow S_0$); v) little to no fluorescence

emission ($S_1 \rightarrow S_0$); vi) high biocompatibility and stability to photodegradation; vii) low chemical and photo-toxicity.

The brightness and photostability of the chosen dye determine the sensitivity and precision of O_2 measurements, and should be taken into account for each specific measurement task. High brightness allows fast signal acquisition time, along with the relatively short luminescence decay time ($<1 \mu s$). On the other hand, decay times in the ns range allow faster image acquisition (84). For intensity-based measurements, photostability of the dye is essential to reduce signal drifts (96). For efficient O_2 imaging in living cells and tissues, deep light penetration and low levels of energy irradiation are preferred (97). This can be accomplished using near-IR indicators that can be excited by red light ($> 600 \text{ nm}$), or with an infrared multi-photon laser (98). Spectral compatibility with light sources, photodetectors, and other optical components is also important: most optical detection systems in laboratory settings are optimized for indicators within the visible range, typically emitting light at 550-700 nm (84).

The most widely used for O_2 sensing are the metal-ligand complexes which include transition metal complexes, mainly Ruthenium(II) (48, 87, 99-101) and Iridium(III) (97, 102-105), and Pt(II) and Pd(II) metalloporphyrins (106-112) (Figure 1.5) (Table 2).

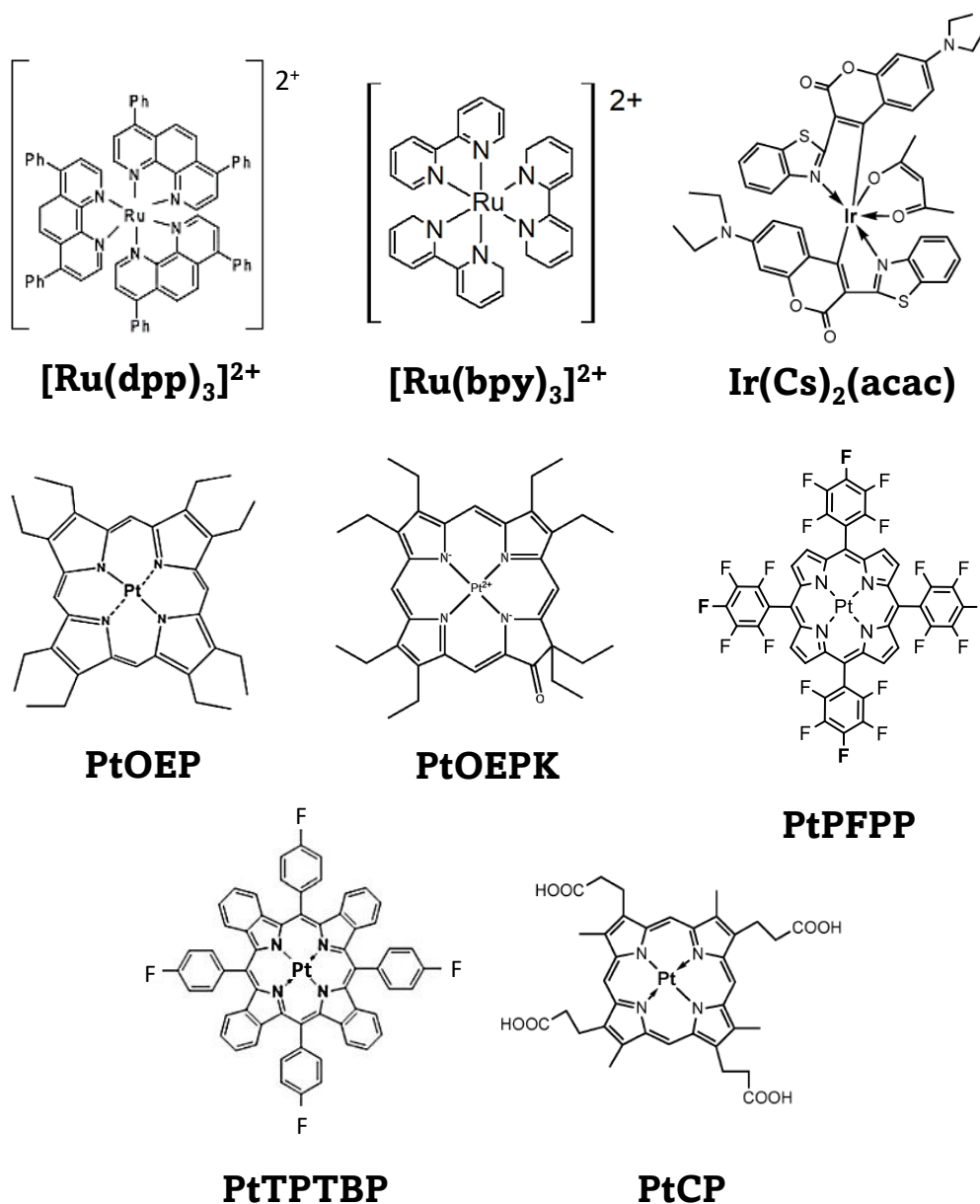


Figure 1.5: Examples of the most common O₂-sensitive dyes. Structures obtained from (5, 10, 48, 113). [Ru(dpp)₃]²⁺ - Ru(II)-tris(diphenylphenantroline) chloride; [Ru(bpy)₃]²⁺ - ris(bipyridine)ruthenium(II) chloride; Ir(Cs)₂(acac) - Ir(III)-(benzothiazol-2-yl)-7-(diethylamino)-coumarin acetylacetonate; PtOEP - Pt(II)-octaethylporphyrin; PtOEPK - Pt(II)-octaethylporphine ketone; PtPFPP - Pt(II)-tetrakis(pentafluorophenyl) porphine; PtTPTBP - Pt(II)-tetraphenyltetrabenzoporphyrin; PtCP - Pt(II)-coproporphyrin.

The photochemistry of a particular chromophore is dependent upon relaxation of its excited state. In particular, spin and symmetry of the ground and excited states, as

well as energy gap between them and presence of intermediate states are all important factors that influence the lifetime of the excited state (114).

Table 2. Spectral and photophysical characteristics of common phosphors used in biological oxygen sensing

Indicator dye (Ref)	Solvent (v/v)	λ_{max} Abs (nm)	λ_{max} Em (nm)	ϵ ($\text{M}^{-1}\text{cm}^{-1}$)	τ_0 (μs)	QY	Quenching medium
[Ru(dpp) ₃] ²⁺ (100)	EtOH:MeOH (4:1)	463	618	28,600	6.4	0.37	Dendrons Xerogels PAA PEBBLEs
[Ru(bpy) ₃] ²⁺ (101)	EtOH:MeOH (4:1)	450	630	14,300	1.15	0.089	SiO ₂ NP Zeolites
Ir(Cs) ₂ (acac) (102)	CHCl ₃	472	563	92,000	11.3	0.54	RL-100 NP EC PMMA
PtOEP (105, 115)	C ₆ H ₅ CH ₃	382	649	214,000	75	0.41	Doped PS Silica glass PDMS
PtOEPK (112)	CHCl ₃	398	758	86,200	60	0.12	PS
PtCP (116)	Phosphate buffer	380	650	120,000	52	0.23	PS
PtTFPP (117)	CH ₂ Cl ₂	390	648	323,000	60	0.088	Soluble RL-100 NP PS/ PS-PVP
PtTPTBP (108)	C ₆ H ₅ CH ₃	430 612	773	190,000 135,000	30	0.35	PS

n.b: Quantum yield (QY) and lifetime τ_0 values refer to deoxygenated solution.

PAA= Polyacrylamide, PS= polystyrene, PDMS= polydimethyl siloxane, PVP= polyvinyl pyrrolidone.

1.5.1. Transition metal complexes

Their long-lived luminescence arises from metal-to-ligand charge transfer (MLCT). This mechanism involves the electronic transfer from the metal d orbital to a delocalized π^* antibonding orbital of the ligand, after the absorption of excitation light photon (Figure 1.6). This causes the metal to oxidize and the ligand to reduce (118). Thus the efficiency of this photophysical behaviour is strictly dependent on the ligand ability to act as electron acceptor (114). What is formed is the luminescent excited triplet state ³MLCT which can be efficiently quenched by O₂ (119).

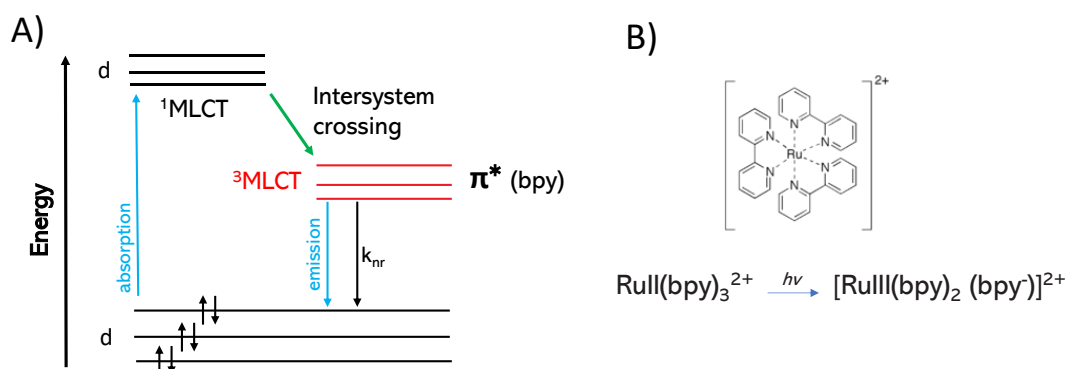


Figure 1.6: A) Jablonski diagram (modified from (67)) describing the photochemistry of metal-ligand complexes. Upon light absorption, the complex undergoes intersystem crossing to the MLCT triplet excited state which then decays via radiative and non-radiative pathways. B) Chemical structure of Ru(II)(bpy)₃²⁺ and its metal-ligand complexation reaction (67).

Such emissive MLCT states are often observed in complexes containing Ru(II), Os(II) and Ir(III) as central metals. These transition metals possess a unique d⁶ electronic configuration that produces strong metal-ligand interactions and high luminescence efficiency (118). Dyes that exhibit long decay times are more suitable for O₂ sensing due to the increased likelihood of collisional quenching. Thanks to their favourable spectral characteristics, transition-metal complexes have commonly been employed as oxygen sensors. They are hydrophilic cationic species characterized by the transition metal (strong oxidant) and ligands such as bpy⁻ or dpp⁻ (strong reductant). These ionic complexes are paired with counterions such as Cl⁻ or ClO₄⁻ (67). The latter produces lipophilic dyes suitable for incorporation in hydrophobic polymer matrices.

Ru(II) dyes exhibit good photostability and brightness, broad absorption bands in the visible range (400-480 nm), and relatively short lifetimes (0.5-5 μs). Their moderate sensitivity to O₂ requires appropriate polymeric matrices, while short lifetimes allow faster signal acquisition rates in lifetime measurements and fluorescence imaging using a pulsed excitation source with a high repetition rate (65, 120). Commonly used Ru(II) based oxygen-sensitive dyes include Ru(II)-tris(bipyridine) chloride - [Ru(II)(bpy)₃]²⁺ and Ru(tris-4,7-diphenyl-1,10-phenanthroline) chloride -

$[\text{Ru(II)(dpp)}_3]^{2+}$. The latter is the brightest among the polypyridyl complexes and its lifetime is longer (6.4 μs) (48). Moreover, due to its high lipophilicity it has mostly been used embedded into nanoparticle structures (81). One more hydrophilic analogue is the Ru-tris-phenanthroline chloride - $[\text{Ru(phen)}_3]^{2+}$, which was used for imaging of O_2 distribution in the liver (121).

Cyclometallated Ir(III) complexes, such as the coumarin complex $\text{Ir(Cs)}_2(\text{acac})$ (102), $\text{Ir(btp)}_2(\text{acac})$ also referred as BTP (122) are characterized by medium-range lifetimes under deoxygenated conditions (1-20 μs) (90), moderate brightness, compatibility with light emitting diodes (LEDs) (97), and good chemical stability. Their large k_q and shorter lifetimes, provide high signal acquisition rate (in TCSPC mode), thus allowing for monitoring of fast processes. Moreover, their emission wavelength can be efficiently tuned by changing the ligand structure (123). For example, coumarin complexes are characterized by higher absorptivity in the visible range, higher QY and thus high brightness compared to Ru(II) polypyridyl dyes, and reduced temperature-sensitivity. By modifying the nature of the coumarin ligand it is possible to fine-tune the spectral characteristics and O_2 sensitivity. Moreover, by embedding these probes into polystyrene the dynamic range is significantly improved, however, their reduced photostability limits any long term usage (102). More recently, several iridium(III) BTP complexes have been synthesized and applied for intracellular and in vivo O_2 sensing (124). They display excellent emission tunability, higher QY than Ru(II) dyes and efficient intracellular localization, with specific subcellular compartment accumulations dependent upon their molecular structure (120).

1.5.2. Metalloporphyrins

For metalloporphyrins, the primary mechanism for phosphorescence quenching is thought to be the resonance energy exchange, which produces singlet oxygen ($^1\text{O}_2$) (68). The rate constant for this process, has been estimated as $k_q = 1/9 k_d$, where k_d represents the diffusion rate constant for the formation of the metalloporphyrin-oxygen complex. The statistical spin factor of 1/9 suggests that only one out of the

nine possible spin states of the complex corresponds to both products in the singlet state (48, 68, 125).

Metalloporphyrins are among the most common and versatile indicators for O₂ sensing, especially platinum(II), palladium(II) porphyrins and related structures. Their triplet excited state is efficiently quenched by O₂ in solutions, as well as in O₂-permeable solid-state materials (126). Examples are complexes of coproporphyrin (CP), octaethylporphyrin (OEP), and *meso*-tetraphenylporphyrin (TPP) (Figure 1.5). These dyes exhibit distinct absorption spectra with a sharp Soret band around 380-420 nm, having molar absorption coefficients (ϵ) of 100,000 – 300,000 M⁻¹cm⁻¹. They also have smaller Q bands in the visible range of 500–550 nm, and give bright phosphorescent emission in the red region between 630–700 nm (72). Their unquenched phosphorescence lifetimes range 50-1000 μ s. Pd(II) complexes demonstrate 3 - 10 times longer lifetimes (0.5 – 1 ms) than their Pt(II) counterparts (20-100 μ s) due to an increased spin-orbit coupling of the heavy metals. While Pd-porphyrins are more useful for sensing of O₂ traces (84), Pt(II) complexes have higher emission quantum yields and molar absorption coefficients, producing brighter room temperature phosphorescence and smaller Stokes' shifts. Their phosphorescence lifetime range (20-80 μ s) and spectral bands in the visible area are well suited for physiological O₂ sensing applications and ensures sensitive monitoring and compatibility with laboratory detection systems (10, 21).

The red-emitting, hydrophilic *tetra-carboxylic Pt(II) coproporphyrin I (PtCP)* has been extensively used as highly sensitive phosphorescent labels in bioaffinity assays(106, 127). Thanks to its moderate chemical and photo stability and long phosphorescent lifetime, its derivatives for intracellular delivery have been synthesized and optimized (128, 129).

Another popular O₂ sensing dye is the hydrophobic *Pt(II) meso-tetrakis-(pentafluorophenyl)porphyrin (PtTFPP)* (84). It is characterized by medium range lifetime (60 μ s) and quantum yield (QY) of 0.088 (in deoxygenated CH₂Cl₂) at room temperature. Its Soret band peaks at 390 nm and two Q bands at 504 and 538 nm,

with emission maxima at 647 nm and a shoulder at 710 nm (130). Its crystal structure reveals a nearly planar porphyrin core (β -pyrrolic macrocycle coordinated with a Pt(II) atom in the centre) with orthogonal pentafluorophenyl rings which do not result in any significant perturbation of the structure compared to the free base tetraphenyl porphyrin (H₂TPP) (130). Its high photostability is due to the electron-withdrawing effect of the perfluorophenyl *meso*-substituents which decrease the electron density of the porphyrin core and make the dye more resistant towards oxidation by singlet oxygen (117, 131). To further reduce photodegradation, a series of metalloporphyrins that incorporate halogen substituents was also synthesized (132, 133). Some heavy halogen atoms like bromine, however, causes a substantial decrease in QY and lifetime. In contrast, fluorine is a much better choice to improve photostability thanks to its electron-withdrawing effect (21).

The β -substituted *octaethylporphyrins*, *PtOEP* and *PdOEP*, display high quantum yields (~ 0.5) and long lifetimes (75 μ s for PtOEP and 770 μ s for PdOEP) (109, 115). Due to their hydrophobicity and tendency to photodegradation, they have been mostly used in solid state sensors, particularly PtOEP immobilized in polystyrene (PS) (30, 134-136) or polydimethylsiloxane (PDMS) (136). PtOEP-PS was one of the first materials demonstrated in LT based O₂ sensors.

Excitation in the red part of the spectrum limits interferences coming from light scattering and autofluorescence. For this reason new NIR-emitting phosphors have become increasingly attractive, especially for biological and medical applications. Thus, *Pt(II) and Pd(II) octaethylporphin- ketones* (PtOEPK and PdOEPK) and *lactones* (*PtTFPPL*, *PdTFPPL*) are characterized by a pronounced bathochromic shift of the Soret band (red-shift) and stronger Q bands (137). These dyes, synthesized via oxidation of the OEP or TFPP core, respectively, show strong absorption Q band in the 570-600 nm region, although their NIR emission (~ 750 nm) is less bright than for their precursors (64, 84). The dyes also have improved photostability, due to the modification of the tetrapyrrole macrocycle (112).

Other NIR-emitting tetrapyrrole dyes are the complexes of *benzoporphyrins*, particularly the fluorinated Pt(II)-tetraphenyltetrabenzoporphyrin (PtTPTBP) (108) and its Pd(II) analogue (138). They are π -extended porphyrins, with aromatic structures attached to the porphyrin core which cause the bathochromic shift (21, 139). These *meso*-substituted derivatives are highly photostable, exhibit emission bands at 700-800 nm, high QY, strong Soret, and Q bands excitable with red or blue LEDs or lasers (64, 140). These dyes have demonstrated their superiority in solid-state sensors over the other phosphors.

1.6. Sensor materials

An O₂-sensitive material typically consists of an oxygen-sensitive dye (phosphor) embedded in an appropriate quenching medium. Liquid probes are directly added to the sample, which is usually aqueous media. Whereas a solid support is required for solid-state sensors for hosting the phosphorescent material in the form of a thin film coating (65, 74). The sample oxygen diffuses from the medium to the phosphorescent material, which generates a luminescent response determined by the O₂ concentration (10).

The main types of sensor materials are *solid-state sensors* and *water-soluble probes*, sensor *nanoparticles* (NPs) and *metal organic frameworks* (MOFs) structures lying in between (64, 65). In general, solid-state sensors are better suited for long-term applications, real-time and continuous monitoring of changes in oxygen levels in large samples, and absolute [O₂] measurements. Whereas water-soluble probes are better suited for screening applications (e.g. drug safety, cell analysis, respirometry), localized oxygen measurements at the microscale level, kinetic measurements of oxygen gradients within specific cell compartments, and live cell microscopy (74).

1.6.1. Solid-state sensors

This category typically consists of a lipophilic O₂-sensitive phosphor, immobilized in a hydrophobic polymer acting as the quenching medium, and applied as a thin film coating of a suitable support material. The solubility and chemical compatibility of

the indicator with the polymer is fundamental to avoid dye aggregation (48). The choice of polymer depends on the dye quenchability by O₂. Here short decay times of the dye can be compensated with a higher O₂ solubility and permeability (74) to achieve optimal sensitivity to O₂ (141). Physical-chemical stability (adhesion to the solid support) and biocompatibility (142) of the sensor are also important. Commonly used polymer matrices for O₂ sensors include PS, polycarbonates, fluorinated polymers, co-polymers, silicones, sol-gels, PVC and hydrogels (10). Dye encapsulation in polymeric matrices also provides shielding effect for solid-state O₂ sensors, which normally have well defined and stable working characteristics, quenching properties and O₂ calibration, reduced quenching interferences and unwanted interactions with sample components. For easier handling and faster response, sensor precursor (a cocktail in an organic solvent) can be deposited as a thin film coating on a solid support, and subsequently dried forming a solid-state sensor (143). The common formats are *sensor membranes, inserts, planar films, dots on plastic substrates (microplates, vials), on optical fibre tips or in microfluidic devices.*

Typical sensor support materials include a polyester film (Mylar[®]) (144, 145), glass slides, microporous membranes (146), bottom of a microwell or a microscopy dish, inner surface of a cuvette (10). The sample is placed in direct contact with the sensor coating, and the optical signal is collected by contactless measurements with an external detector.

The sensing layer can also be deposited directly on the tip of an optical fibre (147-151). Such optodes are characterized by high sensitivity, low maintenance, accuracy, and reliability. They are chemically inert, non-toxic, allow remote sensing with high spatial resolution and access to locations of the body that are hard to reach (21). Commonly, the polymer and the indicator dye are dissolved in an appropriate organic solvent to produce a “sensor cocktail” (50). The cocktail is subsequently spotted onto the solid support and dried to evaporate the solvent. Spin coating or dip-coating (152) techniques are also commonly employed. Such solvent-based incorporation does not fully prevent migration of the dye from the coating into the sample or support material (143). To prevent that, covalent linkage of the dye molecules to the

polymer, via appropriate functional groups, can be used (153-155), however the costs of sensor fabrication increase. More recently, the spot-crazing technique was developed, which is based on the impregnation of a polymeric film with the dye, using a crazing solvent (156). This causes the formation of nanopores which entraps the dye molecules, generating sensors with near-optimal sensitivity to O₂ (157).

Another type of solid-state sensors is the extrudable O₂ sensors fabricated via the hot melt extrusion technique. This manufacturing technology is especially common for the processing of plastics, as well as some advanced pharmaceutical formulations. It entails the pumping of an amorphous solid dispersion through an extruder, characterized by one or two rotating screws, at high temperatures, obtaining a final product of uniform shape. An example of dispersion is characterized by cross-linked polymeric microsphere impregnated with a phosphorescent dye dispersed in a low density polymer such as polyethylene or polylactic acid (extrudable polymers) (158). This formulation has been specifically designed for food packaging applications. This fabrication process allows uniform dispersal of the phosphorescent material, without incurring dye solubility or aggregation issues. 3D printing has been extensively employed for the manufacturing of devices (i.e. microfluidic cells) that use indicators for biochemical or chemical sensing. Recently it was applied for the manufacture of filaments containing the indicators themselves. The first 3D printable, optical O₂ indicator was produced by combining the extrusion technique to obtain an homogeneous dispersion of PtPFPP-coated silica microparticles into a filament containing the indicator, followed by 3D printing of the indicator dot onto a solid support (159). Extrusion-based 3D printable sensors are reproducible and easily scalable, allowing for large production of low cost O₂ indicators.

Solid-state sensors are reliable and robust, have good operational stability, are relatively inexpensive, do not contaminate the sample, and allow accurate and repetitive measurements and continuous monitoring of O₂ in various samples, experimental settings, and applications. However, for biological applications solid-state sensors are limited by their fixed structure and location, hydrophobicity of the polymer coatings, potential cyto- and photo-toxicity effects (11, 74).

1.6.2. Soluble probes

Water soluble probes are not attached to any surface, instead they are directly added to aqueous samples acting as quenching medium. They distribute across the whole sample and are quenched by dissolved O₂. Such probes provide flexibility in terms of sample type and size, platform, and measurement task. They can be used in complex biological samples such as cultured cells, and 3D tissue-models (organoids and spheroids), with the ability to penetrate the cells and stain intracellular compartments, or to perform extracellular O₂ measurements (5, 160).

However, soluble O₂ probes are more prone to quenching interferences by sample components, binding to surfaces and sample components, photobleaching, especially at low concentration (74). Different kinds of soluble O₂ probe structures have been developed, for intravital, extra-cellular and intra-cellular sensing, and macroscopic and microscopic imaging of O₂.

The first type is *small molecule probes*, comprising hydrophilic derivatives of PtCP (161) and PtTFPP (160), or complexes of Ru(II) (162) and Ir(III) (163) dyes. Their advantages are ease of synthesis, and tuning for exclusion or efficient uptake by cells and distinct localization in subcellular compartments. These attributes make them suitable for intracellular oxygen measurements (90). However, due to their large and hydrophobic aromatic core, they tend to non-specifically bind proteins and cell surfaces, and migrate within the sample. Their interaction with biological substances needs to be considered: the lack of protection from the environment makes such probes susceptible to interferences. Due to these interactions or non-homogeneous distribution within the cell or tissue, small molecule O₂ probes often produce complex phosphorescence decays or unstable Ksv and calibration (65).

Some of these issues can be partly solved by binding or covalent linkage of the reporter dye to hydrophilic macromolecular carriers such as proteins (serum albumin) or PEG, to produce *supramolecular probes* (126). This increases the solubility of the probe, stabilises its O₂ sensitivity and calibration, and makes the probe cell-impermeable. An example of such a probe is MitoXpress (127), a

monofunctional derivative of BSA-PtCP (106) which has convenient spectral characteristics (UV-Vis range, and large stoke's shift), high brightness and relatively long lifetimes. MitoXpress is compatible with widely available detection instrumentation - multi-label plate readers with TRF and RLD capabilities. It is routinely used for extracellular and intracellular lifetime-based O₂ sensing, although intracellular measurements require additional transfection reagents for the probe (88).

Another type is the cell-impermeable *dendron-coated probes* developed by Vinogradov (164, 165), in which the metalloporphyrin core is modified with hyperbranched polymers (polyglutamic acid and poly(arylglycine) dendrons) and then with poly-ethylene glycol (PEG) chains. These probes were designed specifically for intravitreal and interstitial O₂ measurements in the brain and in solid tumours (164). The peripheral modifications allow tuning of optical and physical properties, quenchability by O₂, linearization and stabilisation of calibrations (65). The dendritic chains also create a protective and biocompatible environment (166) which 'shields' the dye, ensures predictable diffusion of O₂ to the phosphor (167), improved hydrophilicity and solubility in aqueous media without aggregation at high concentrations (90). Moreover, the dendrimeric structures have the ability to fold in aqueous environment, creating an O₂ diffusion barrier, which allows for precise control over the sensitivity and dynamic range (168).

1.6.3. Particulate sensors

Micro- and nanoparticle sensors (NPs) have gained popularity thanks to their high brightness and tunability. They combine the phosphor protection by the polymeric matrix, with the flexibility and minimal invasiveness of the small particle size (21, 72). Fabrication procedures for such sensor nanobeads include emulsion polymerization of the monomer mixed with the dye (169-171), or precipitation of amphiphilic polymers by solvent displacement (172), which forms core-shell nanostructures (173). This latter method does not require surfactants or other additives, and it allows uniform distribution of the dye. The polymeric matrix can either covalently bind

phosphor molecules, or non-covalently trap them (physical entrapment) within nanoparticles during their formation. Since sensor NPs are usually used with aqueous samples, hydrophobic dyes are usually incorporated in the hydrophobic core of the NP structures, to prevent dye leaching during measurements or storage, while the external hydrophilic shell provides stability in aqueous solutions and cell penetration abilities. Moreover, the indicator should be soluble in the polymer to prevent its aggregation.

One example of a NP probe for sensing and imaging applications is PEBBLE - Probe encapsulated by biologically localized embedding (174), it is obtained by non-covalent incorporation of the dye by microemulsion polymerization generating spherical particles with submicron size (175, 176). PEBBLEs were used for intracellular small analyte sensing, often formulated with a second dye for ratiometric measurements. Several luminescent NPs for intra and extracellular O₂ sensing, and imaging have been reported in the literature (148, 169, 177-180).

1.6.4. Metal–organic frameworks (MOFs)

MOFs gained attention during the past decade due to their structural and functional tunability. They have been used in chemical (as catalytic substrates) and biomedical applications (as drugs or imaging agents, photodynamic therapy), and in optochemical sensing. MOFs are self-assembling materials produced by mixing metal-containing nodes/clusters and organic linkers, which constitute the building units. This class of crystalline materials has high porosity and internal surface area(181), which allow high load of cargo and its effective transport through the framework channels. More recently nanoscale MOFs (nMOFs) have been explored for biomedical applications. They enable intracellular sensing, multi-functionalization for cargo co-delivery, with temporal and spatial control of cargo release by tuning of the framework stability in physiological environments (synergistic combination therapies) (182). A number of luminescent MOFs have been synthesised using phosphorescent organic linkers (183, 184) or by encapsulation of ionic phosphors in the MOF structure (185, 186). Despite the recent discovery of intracellular delivery of MOFs, there is still limited understanding of their possible biological interactions, cell penetration

mechanisms and cargo release in the cell (187). With regards to cellular oxygen sensing, only a few luminescent nMOFs have been designed to incorporate within their framework oxygen sensitive materials such as porphyrins (183), and metal-ligand complexes (188), for intra and extracellular applications.

1.6.5. Intracellular O₂ sensing and cell targeting strategies

Intracellular sensing has always been an important task for O₂ sensors. It can be achieved using fibre optic sensor consisting of a tapered glass tip that can be directed inside the cell. However, such an invasive device and methodology cause perturbation of the biological sample and damage to the cell.

Many existing phosphorescent based O₂ probes are not able to penetrate the cells on their own. Thus, negative charges present on the small molecule dye or NP sensors prevent the interaction with cell membrane (also negatively charged) and subsequent translocation. Cationic probes tend to have good cellular penetration (189) and water solubility (177, 190), but often show prominent cyto- and photo- toxicity due to nuclear accumulation and DNA binding (191).

A number of *instrumental techniques* have been developed such as microinjection (192), or more invasive techniques of cell permeabilization and electroporation (193). Some NP O₂ sensors and probes, which are intrinsically cell-impermeable, can be brought into the cells by facilitated delivery methods. Thus, projectile delivery with a 'gene gun' was successful for PEBBLES (81), and transfection reagent Lipofectamine - for MitoXpress probe (194), although such techniques are still stressful for the cell. *Facilitated loading* can be achieved using transfection reagents such as EndoPorter (195) or Escort III (196) which increase endocytosis, as demonstrated in conjunction with the cell impermeable probe MitoXpress. However this method was slow, with rather poor efficiency and inconsistent across cell lines (190).

On the other hand, the use of dedicated oxygen-sensitive molecular probes or NP sensors with intrinsic cell-penetrating ability is more efficient, versatile, and cell-friendly approach. However, design of high-performance intracellular probes is challenging and currently available O₂ probes still have many limitations.

For intracellular (IC) probes, high cellular uptake efficiency and specific sub-cellular localization are necessary (97). Moreover, the probe has to remain within the cell and in a designated compartment for sufficient time to allow optical measurements without causing significant cyto- and phototoxic harm (190). The signal should also be strong, stable, with high S/N ratio and optimal sensitivity to O₂ (197).

This can be achieved via *chemical modification of peripheral functional groups* with substituents such as primary amino or aliphatic hydroxyl groups (124, 198), low molecular weight PEG, sugars (160, 199, 200) or hydrophobic ethyl ester groups (190) or lipophilic cations (198). Although for most phosphors there is a need to increase water solubility for better cell penetration, and lower non-specific binding, excessive hydrophilicity of the phosphor could negatively impact its uptake efficiency and O₂ sensitivity. Thus derivatization with more lipophilic groups or ligands might be necessary (162, 201).

Introduction of a suitable biological “delivery vector” is an effective strategy to increase cellular uptake and tune subcellular localization. For example, phosphorescent probes based on *cell penetrating peptides (CPP)*, which are part of the family of supramolecular structures, allow facilitated intracellular delivery (202). Such vectors usually consist of polyarginine (128) or proline-rich peptides (natural batenecin peptide or synthetically designed)(203), synthetic TAT-derived peptides (trans-activator of transcription) (203) small positively charged polypeptides, capable of crossing the cell membrane while carrying a much bigger cargo. They are conjugated to hydrophilic derivatives of the phosphor to allow its passive loading, retention and improve its sensing properties. Some examples are described in Table 3. Of note, several derivatives of PtCP conjugated with TAT-derived peptide (129), batenecin 7 fragment (203) and poly-arginine peptides (128) were synthesized, achieving efficient intracellular staining and application for measurement of O₂ dynamics. These derivatives show specific subcellular localization: cytoplasmic (PEPPO, PtCPTE-CFR9) or nuclear (PEPP3). Mitochondria specific O₂ probes were also proposed, mostly based on Ir(III) complexes. The first was BTP-Mito (198) containing a triphenylphosphonium (TPP) cationic group which facilitates mitochondrial accumulation. Other Ir(III) complexes with π -extended electronic system (NIR

emission), were also developed bearing 5-amino-1,10-phenanthroline ligands (204). Moreover, a nuclear targeted O₂ probe based on an Ir(III)ppy derivative bearing a DNA intercalator ligand (tetra-pyridophenazine), was synthesised for nuclear staining and hypoxia monitoring (185).

Other than traditional chemical modifications, facilitated uptake of metalloporphyrins can be achieved via their covalent attachment to a suitable macromolecular carrier. Thus, *metallochelatase coupling* employs a modified nitrilotriacetic acid (NTA) ligand coordinated with a metal ion (i.e. Ni²⁺, Zn²⁺, Co²⁺, or Cu²⁺) which can coordinate certain amino acid residues, usually oligo-histidine sequences. This technique is used for recombinant protein capturing, purification, and fluorescent labelling (205, 206). Metallochelatase coupling of phosphorescent porphyrins was also reported: PtCP and PtPFPP bearing Zn²⁺ NTA moiety were used to label small peptides (His- and Arg-containing CPP - His₆-Gly₂-Arg₆ amide), fluorescent protein for ratiometric measurements (EGFP via N-terminal His₆-tag), and self assembling virus-like nanoparticles (ELPCP with N-terminal His₆-tag). Best intracellular uptake and retention of optimal photophysical characteristics were observed with the PtPFPP-NTA coordinated with histidine containing peptide(207). Three different free-base porphyrins containing the Lysine-NTA ligand were examined. Although doubts were raised regarding their cellular uptake and chemical stability (208), this promising approach requires chemical tuning and further refinement.

CPPs, PEGs, targeting moieties and derivatization with charged molecules are all strategies that can also be employed for surface modification of NP structures, to enhance their cell permeabilization, and/or protection from interfering components(s) (160). Especially successful NP for IC O₂ sensing have been synthesised using the positively charged polymer RL-100 which provides fast IC staining, high brightness, efficient shielding and minimal cytotoxicity (177, 209).

Currently, CPP-based O₂ probes and core-shell polymeric and cationic nanoparticles of hydrophobic dyes, are the most effective designs to obtain cell permeable probes with reliable intracellular sensing characteristic for mammalian cells. Some examples of available O₂ probes are summarized in Table 3.

Table 3. Examples of available phosphorescent O₂ probes.

Probe (Ref)	Phosphor and Format	Detection modality	Application
<i>Extracellular</i>			
MitoXpress – PtCP conjugate with BSA (106)	Supramolecular SM	TRF, RLD	Assessment of cell bioenergetics (OCR).
Oxyphor R2 (164)	PdTCPP Dendrimer	FLIM	Monitor microvascular and interstitial pO ₂
Oxyphor G2 (164)	PdTCPTBP Dendrimer	Wide field, FLIM	<i>In vivo</i> O ₂ distribution in subcutaneous tumour
Oxyphor 2P (210)	PtTAPIP Dendrimer	Two-Photon PLIM	Deep-Tissue Longitudinal Oxygen Imaging
<i>Intracellular</i>			
MitoXpress with EndoPorter facilitated uptake (88)	PtCP-BSA conjugate - supramolecular SM	TRF, RLD	Cell oxygenation and OCR Quantitative Metabolic responses
PEPPO (203)	PtCPTe- modified bactenecin 7 peptide fragment SM-CPP	TRF, RLD FLIM	Cellular oxygenation
PtCPTe-CFR9 (129)	PtCPTe-TAT derived peptide SM-CPP		Quantitative analysis
PEPP3 (128)	PtCP(PFP) ₄ -polyArginine SM-CPP		Metabolic responses
PEPP3 (128)	PtCP(PFP) ₄ -polyArginine SM-CPP		Specific sub-cellular localization
MitoImage™ NanO2 (177)	PtPFPP embedded in RL-100 NP	Single Photon FLIM TRF, RLD	Changes in oxygenation, imaging, quantitative IC[O ₂] measurements
BTP-Mito (198)	Ir(III) BTP – TPP+ complex SM	Lifetime-based	Mitochondria targeted O ₂ sensor
MitoImage™ MM2 (178)	PtPFPP-PFO embedded in RL-100 NP	Single or Two Photon FLIM / Ratiometric Intensity	Live-cell fluorescence imaging: cell oxygenation and changes in O ₂ concentration/respiration
ST-PtTFPP (211)	PtPFPP Core-shell NP (Hydrophobic styrene core and hydrophilic NIPAM shell)	Lifetime-based	Quantitative O ₂ measurements and O ₂ mapping in living cells and tissues
MitoImage™ NanO2 IR (212)	PtBP in RL-100 hydrogel NP	Single Photon FLIM	Imaging of real-time oxygenation within specific brain regions
R-Uio (183)	PtDBP-RITC nMOF	Ratiometric Intensity	Intracellular O ₂ sensing

n.b: SM = small molecule; NP = nanoparticle; CPP= cell penetrating peptides

1.7: Core biological applications of optical O₂ sensing and measurement platforms

Initially, optical oxygen sensing was directed towards the biomedical, bioenergetic and toxicological studies of simple macroscopic samples such as perfused tissues or suspension cells (intravital and *ex vivo* studies). With the technological advancements, more complex systems can now be analysed such as adherent cells, respiring organs and tumoral tissues, 3D models which mimic physiological conditions *in vivo*, and on a micro-scale level such as isolated mitochondria or single cells (160).

The main parameters that can be monitored for biological respiring samples are: (i) oxygenation state of the sample, (ii) O₂ consumption rate (OCR), (iii) localised O₂ gradients and their spatial distribution, (iv) dynamics of O₂ fluctuations due to cell treatment or changes in cell function(65). These parameters serve as indicators for assessing cell viability, developmental stage, metabolic responses, pathological conditions, and toxicity effects.

1.7.1. Mitochondrial respiration

Mitochondria are the main producers of ATP via OxPhos and consumers of O₂ via the Electron Transport Chain (ETC). Thus, they are fundamental for the study of cellular patho-physiological processes i.e. apoptosis and autophagy, generation of ROS, Ca²⁺ signalling, and cellular homeostasis (213). These organelles can be isolated from cells and tissues while retaining their essential functions (214). Phosphorescence quenching based respirometric screening assays have been applied to assess mitochondrial function, drug-related toxicity, gather mechanistic insights into respiration states, drugs activity, and study of processes associated with OxPhos (215).

However, this method has limitations, particularly its lack of relevance to the whole cell context. It tends to overestimate the effects of drugs that cannot easily penetrate cell membranes and reach mitochondrial components. Additionally, it does not take into account the specific transport mechanisms, tissue specificity, or effects on other

metabolic pathways that characterize each drug (216). These limitations can be addressed by analysing whole cells.

1.7.2. Mammalian cellular respiration

The traditional assessment of drug induced mitochondrial toxicity relied on the polarographic technique using O₂-electrode. This low throughput respirometric assay measures the O₂ consumption using ADP containing medium to identify mitochondrial inhibitors, and ADP free medium to identify uncouplers (10, 216, 217). On the other hand, OCR assays based on phosphorescence quenching technique, offer higher throughput and automation.

Mammalian cell cultures offer a reliable platform for studying cellular processes by closely simulating the physiological environment. They enable researchers to consider interactions with neighbouring cells, transport of essential nutrients, influence of regulatory networks and compensatory mechanisms, metabolic and signalling pathways, and other secondary factors within the cells (218). Furthermore, it is possible to examine non-mitochondrial oxygen consumption in this context (219). Dedicated detection methods have been developed to monitor respiration in cell populations using a TRF plate reader, while examination of single cells and heterogeneous tissue samples require 2D and 3D O₂ imaging techniques, particularly PLIM microscopy (5).

Assessment of absolute OCR values is carried out in a sealed environment such as an hermetically sealed cuvette or stirred chamber (220) (Figure 1.7A, B). However, for high throughput respirometric analysis, comparison of relative OCR values is often sufficient for the assessment of cell bioenergetics, metabolism, and toxicity. In such cases, the vessel does not require complete sealing. A partial seal of the sample generates a barrier for atmospheric O₂ back-diffusion, thus promoting the formation of O₂ gradients in the medium with cells (221). Examples of such high-throughput miniaturized setups include standard microtiter plate formats with solid-state sensor coatings (222) or extracellular soluble probes (166, 221) which allow the measurement of average OCR and O₂ concentrations, on standard or customised

fluorescent readers, including those equipped with gas control (4, 11) (Figure 1.7C). This setup allows for multiplexed measurements of ECAR (the rate of conversion of pyruvate into lactic acid, a measure of glycolysis), combined with the OCR data, to give a detailed assessment of cell bioenergetics and their alteration upon drug treatment (162).

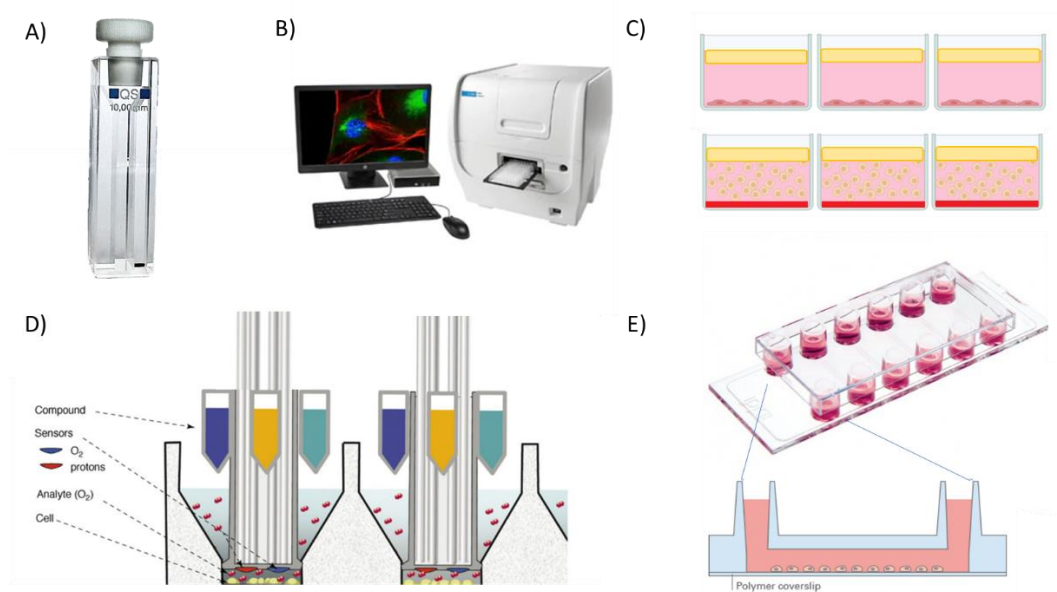


Figure 1.7: Common OCR measurements setups. A) Hermetically sealed quartz cuvette with Teflon stopper. B) BioTek (Agilent) Cytation 5 Cell Imaging Multimode Reader equipped with atmospheric control. C) Microwells sealed with oil, with either adherent cells (or suspension) and soluble probe, or suspension cells and sensor coating. D) Seahorse XF Analyser for OCR and ECAR measurements on adherent cells (222). E) A six channel μ -Slide for parallel flow assays (Ibidi.com).

One setup developed by Luxel Bioscience, is a 96/384-well plate with a partial seal obtained by adding heavy mineral oil on top of the liquid sample (approximately 100 μ L) at the start of the measurements (223). The signal of the O₂ probe is correlated with the O₂ concentration and relative OCRs of resting cells, or after drug treatment (221). The changes in oxygenation are detected by the extracellular soluble probe MitoXpress which is measured on a TRF plate reader by the RLD method (LT-based sensing), at one excitation and one emission wavelength. This is a convenient and

flexible format of O₂ respirometry for many types of mammalian cells (suspension and adherent) and bacteria (Figure 1.8. A,D), which can process large numbers of samples (1). The favourable photophysical characteristics of the MitoXpress probe allow its multiplexing, without any crosstalk, with a lanthanide fluorescent pH-probe, for parallel measurements of ECAR in the same sample. MitoXpress probe can also be used in other fluorescent cell-based assays (10), however oil-sealed wells only allow for end-point measurements, impeding repeated treatments (224).

This problem is solved by the platform developed by Seahorse Bioscience, also known as Seahorse XF Analyser (222) (Figure 1.7D). It is specifically designed for repeated high-sensitivity analysis of OCR in samples with adherent mammalian cells. It uses special 24/96 well microplates with moving pistons, the tips of which contain solid-state O₂ and a pH sensor coating. The pistons, when introduced into assay wells create sealed microchambers (200 nm height) with high cell-to-media volume ratio. This allows for a highly sensitive, rapid (few minutes) and simultaneous measurement of absolute OCR and extracellular acidification rate (ECAR). Moreover, the system allows multiple measurements with additions of stimulators, inhibitors or substrates via automated drug injection ports during the experiment (4). However, it is poorly suited for bacterial cells, relatively expensive due to the presence of solid-state sensors, has complex detection optics, is subject to sensor cross-talk and unstable calibrations, complex data processing, and it operates in intensity-based sensing mode (1, 225).

Perfusable plastic biochips can operate with suspension or adherent cells, and with 3D cell/tissue models such as multicellular spheroids and organoids. They have microchannels where test cells are seeded with a micropipette, limiting O₂ diffusion by the O₂-impermeable plastic body and by the length of the narrow channel (Figure 1.7E). Such biochips provide reproducible, rapid and sensitive measurements, and compatibility with both plate readers and fluorescence microscopy detection modalities (226). They also allow reperfusion of the sample and repetitive analysis with multiple treatments (227).

Thus, multi-parametric OCR/ECAR platforms have been developed for cell-based mitochondrial toxicity screening. These platforms have been validated with several commercial compounds on whole cells, showing comparable data (221, 228, 229).

OCR is a direct indication of the mitochondrial respiratory activity and thus reports on the bioenergetic status of the cell (10). Cell respiration, measured via oxygen consumption rate (OCR), is sensitive to metabolic changes, thus can be used to study cellular responses to drug action, *drug-induced toxicity*, *cell bioenergetics* using inhibitors or uncouplers of mitochondrial respiration, and adaptation to hypoxia (202) (Figure 1.8. A). Many drugs target mitochondria, leading to reduced aerobic metabolism and cell death (228). Consequently, drug toxicity and safety evaluation increasingly rely on OCR measurements with relevant cell models.

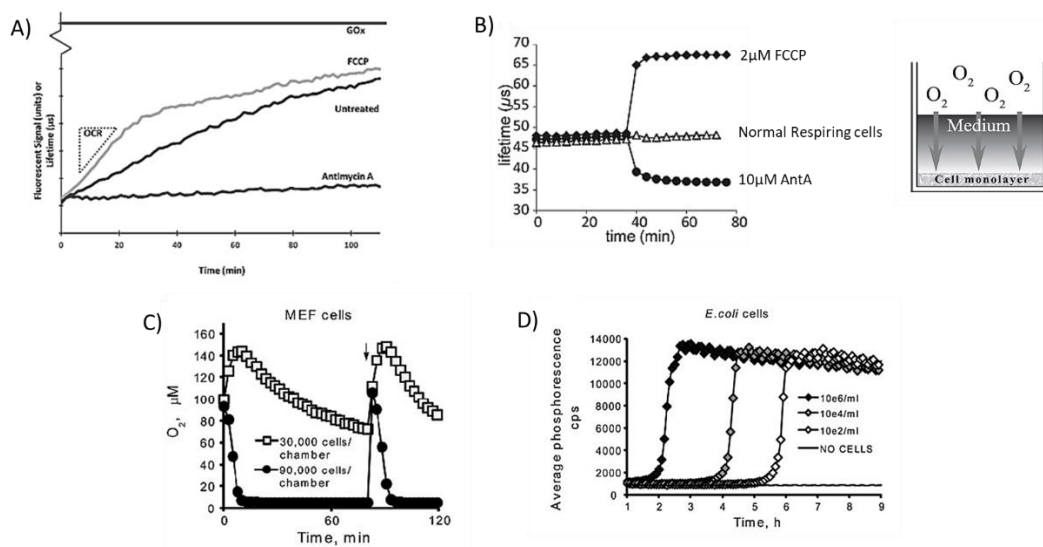


Figure 1.8: Respiration profiles obtained with different cells and measurement platforms. Cellular respiratory responses to mitochondrial uncoupler (FCCP) and mitochondrial inhibitor (Antimycin A) obtained A) with the extracellular probe MitoXpress with partial oil seal (Agilent.com) or B) with icO₂ probe NanO₂ in open well (177). C) O₂ consumption profiles for MEF cells grown at different densities in a microfluidic chip, upon sequential medium reoxygenation steps. D) Typical respiration profiles of bacterial cells seeded at different densities, measured using MitoXpress oxygen probe and a TRF reader in phosphorescent intensity mode. (C, D obtained from (11)).

Standard OCR measurements with respiring cells in screening assays do not account for heterogeneous O₂ distribution in tested samples, local gradients, and their dynamics. These parameters can be addressed by measuring O₂ in unsealed samples under steady-state conditions (10). In this setup, cellular O₂ consumption is balanced by diffusion of ambient air O₂ back into the sample (177) (Figure 1.8B). Intracellular O₂ sensing has been applied for study of *in situ* oxygenation and subcellular O₂ distribution, cell metabolism and responses to metabolic stimulation. In fact, due to the mitochondrial consumption of O₂ and its passive diffusion from the atmosphere, local gradients are formed which can be monitored via kinetic O₂ measurements or imaging of the icO₂ probe (5).

A real-time method carried out on open microtiter plates, allows monitoring of cell oxygenation upon metabolic stimulation, by measuring the signal from the icO₂ probe which corresponds to the transition of the sample to a new steady state (88, 129, 177, 230, 231) (Figure 1.8. B). For *metabolic studies*, resting and uncoupled cells are measured to determine basal and maximal respiration respectively, while glycolytic fluxes are assessed by ECAR measurements. In these conditions, there are several parameters that can interfere with cell oxygenation such as temperature, viscosity, and height of the medium, atmospheric pO₂ as well as sample geometry, which need to be kept constant. Finally, in this setup addition of effectors in the course of the experiment and during monitoring is possible.

1.7.3. Bacterial respiration

Aerobic bacteria require O₂ to sustain their metabolic processes. When compared to mammalian cells, typical aerobic bacteria exhibit significantly faster proliferation rates (approximately 30 minutes compared to the 24-48 hours observed in mammalian cells) (232). Typical growth profiles produced by aerobic bacterial cultures exhibit a lag phase, an exponential growth, and a stationary phase caused by substrate consumption, followed by death. Measurement of bacterial cell respiration by optical oxygen respirometry allows the monitoring of microbial growth and metabolism, effects of antimicrobial treatments, presence of microbial

contamination, and food spoilage. It is a high throughput analysis method that has been employed in the food and pharmaceutical industry, biomedical research, and environmental science (10).

The O₂ probe optical signal increases over time in response to the change in the oxygenation from air saturated to deoxygenated conditions caused by the bacterial growth. This produced the typical sigmoidal profiles (phosphorescent intensity (RFU) or lifetime (μs)) (233, 234) (Figure 1.8D). The O₂ signal allows determination of sterility or presence of bacterial load and provides information about the growth rate and their metabolic activity. By using a predetermined calibration equation, it is possible to count the number of bacteria in the sample (total aerobic viable counts (TVCs)), making this method a valuable alternative to tedious standard agar plating counting methods. Specifically, the microbial count of the original sample as CFU/g or mL is determined by the time taken to reach the signal threshold. It also allows calculation of doubling times and predictive analysis of bacterial species and determination of EC50 values (235).

Several platforms are commercially available for high throughput analysis of microbial growth. A standard micro-respirometry platform uses MitoXpress probe (Luxcel/Agilent) added directly to liquid samples containing *E. coli* and measured in standard 96/384-well plates on a benchtop time-resolved fluorescence (TRF) reader (234, 235). As described above, this method was initially developed for mammalian cell cultures (236) and then extended to bacterial cells (237), and is regarded as the golden standard in micro-respirometry. Based on the same approach are the BD Biosensor plates from Beckton Dickinson which employ a solid state sensor film at the bottom of each well to detect microbial oxygen consumption- (238). More recently a new swab testing portable platform was developed based on disposable plastic tubes containing a solid-state sensor coating (NIR Pt-benzoporphyrin) deposited inside a handheld reader such as Optech (Mocon/Ametek) or Firesting-GO₂ (Pyroscience GmbH) for signal redout (239).

1.7.4. Tissue models

Organotypic 3D tissue models mimic the *in vivo* micro-anatomy, organ functions, cell-cell interactions, and factors like limited nutrient supply and O₂ availability. Examples include multi-cellular spheroids, cellular aggregates, tissue slices, organ explants, and artificial tissue. Such models are commonly used in drug screening, hypoxia research, and developmental biology, and mapping of O₂ levels in these models is important. The use of cell-penetrating phosphorescent probes allows monitoring of oxygenation in real-time, and their multiplexing with other cell biomarkers and fluorescent probes allows detailed understanding of cellular and tissue physiology at the subcellular level (65). Phosphorescence imaging techniques, such as confocal PLIM microscopy, are particularly advantageous when examining complex heterogeneous samples. PLIM can provide detailed 2D and 3D maps of O₂ concentrations and can even reveal O₂ gradients near and within individual cells (5). Wide-field microscopy only allows for semi-quantitative or point measurements of O₂ and does not facilitate detailed 3D visualization of O₂ distribution.

Examples of efficient O₂ imaging probes are the nanoparticulate MM2 (178) and NanO₂ (177). While these nano-sensors effectively penetrate cells in 2D and 3D cultures, they face challenges for whole-body *in vivo* imaging due to phagocytosis induced by their positive charge (240, 241), as well as suboptimal excitation wavelengths (blue shifted). Valuable alternatives are the dendron coated probes obtained by subsequent modification by polyethylene glycol (PEG) arms. PEGylation prolongs circulation in the bloodstream enabling imaging of intravascular O₂ gradients or assessing tumour oxygenation (242). However, these probes are cell-impermeable and unsuitable for intracellular oxygen measurements (93).

1.7.5. Measurements *in vivo* and *ex vivo*

Quenched phosphorescence O₂ sensing has been extensively used for *in vivo* measurements of O₂, mainly employing extracellular, cell-impermeable probes injected intravenously in live animals. Intravital oxygen probes, featuring light-harvesting antennae and a PEGylated shell, allowed the study of cerebral vasculature, neuronal activity, tumour oxygenation, microcirculation, muscle

physiology, and retinal oxygen tension. PEGylation prolongs circulation in the bloodstream enabling imaging of intravascular O₂ gradients (221). These probes have also been employed for tomographic imaging at the macroscopic level.

1.8. PtPFPP dye and its chemical modifications

PtPFPP, like most O₂ sensitive dyes, is hydrophobic and cannot be solubilized and used in biological aqueous media. To enable this, PtPFPP can be incorporated in solid state polymeric sensors (131, 243), encapsulated inside the NP structures (177, 244), or micelles formed by amphiphilic block or graft copolymers or hydrogels (245-247). The dye can be left unmodified or covalently linked to the sensor matrix (248, 249). At the same time, the four liable para-fluorine atoms of PtPFPP allow nucleophilic aromatic substitution with nucleophiles such as amines, thiols or alcohols by click-modification (250-252) (Figure 1.9). This way, PtPFPP can be modified with peripheral substituents that improve hydrophilicity (253-256), modulate the photophysical properties and cell targeting (257, 258), enhance cell internalization (160, 202), or provide a scaffold for further chemical modification (207, 259, 260). Moreover, such small molecule structures enable covalent coupling with silica gel (155) or polymeric materials such as polystyrene (131) to prevent dye migration and leaching from the sensor matrix(251). Phosphorescent properties of PtPFPP and its derivatives are compatible with standard plate readers, so they can be measured in TRF and RLD modes for sensing O₂ in respiring cells and samples.

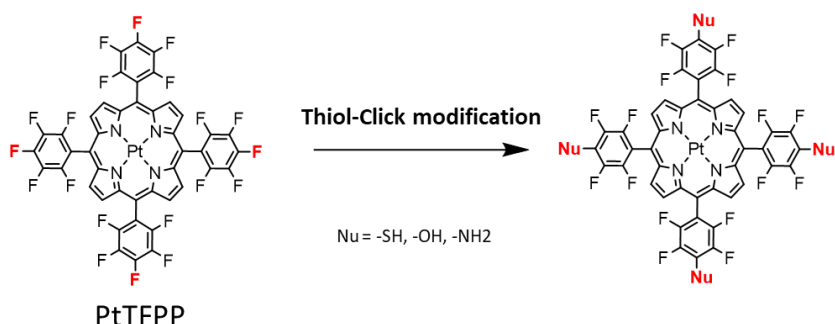


Figure 1.9: Scheme of nucleophilic substitution of the *p*-fluorine atoms via click-modification.

The nucleophilic substitution can be achieved sequentially producing mono- di- tri- or tetra- substituted derivatives in different configurations. Relevant examples include the monosaccharide derivatives with thio-galactose (PtGal₄) and thio-glucose (PtGlc₄) moieties (160). Both tetra-substituted derivatives were found to provide efficient intracellular staining of mammalian cells in 2D cultures, and in-depth staining of multicellular 3D micro-tissue models. It is worth noting that carbohydrate derivatives of porphyrin dyes were seen to enhance cancer cell targeting in photodynamic therapy (PDT). Glycoconjugation not only improved cell recognition and uptake, but also enhanced water solubility of the drug (200, 261, 262).

Such chemical modifications also hold promise for intracellular delivery of sensing materials. In contrast with the highly photo- and cyto-toxic PDT agents, the PtGlc₄ and PtGal₄ probes did not show any significant impact on cell functionalities such as ATP production, or total acidification rate. This was correlated to the different cell types, probe concentration and time of illumination (160).

As mentioned in section 1.6.5. PtPFPP was also employed to produce metal chelate NTA derivatives coordinated with histidine containing peptide which enhanced cellular uptake of such probe (207). Also in this case, the conjugates were obtained via the amino group available on the lysine derivative of NTA.

1.9. Conclusions and project objectives

O₂ is one of the most important physiological parameters involved in governing cellular respiration, metabolism, and homeostasis. Measurement of O₂ concentration and OCR provides new insights into cellular processes, facilitating a comprehensive understanding of normal and pathological states of the cell and responses to various treatments.

Among the techniques available for O₂ measurement, the phosphorescence quenching method has many advantages. Based on the ability of phosphorescent sensors and probes to respond reversibly to O₂, this versatile optical technique has established itself and also enabled the development of many new applications, which include minimally invasive measurement systems with high spatial and temporal resolution. It helps to elucidate the dynamics of O₂ transport in microenvironments, aiding the understanding of tissue oxygenation in disease states. From cellular and tissue-level analyses of free O₂ to the monitoring of oxygen gradients in complex biological matrices, both in vivo and in vitro, this technique has demonstrated its value in biomedical research.

Overall, optical O₂ probes and NP sensors are well established, providing a range of analytical tasks, and non-invasive, continuous, and precise monitoring of dissolved free O₂ in various samples including live respiring cells. Among the numerous oxygen-sensitive materials, phosphorescent Pt(II) porphyrin probes have emerged as useful and efficient tools for many applications. They provide robust quantification, and high-resolution imaging of O₂ levels in various mammalian cell lines and tissue models. These phosphors exhibit versatility across the different O₂ imaging and sensing platforms, and compatibility with common detection platforms available in research laboratories.

As our understanding of cellular and subcellular processes becomes more refined, the demand for more precise and informative oxygen measurements continues to rise. Thus, there is a need to develop new target-specific phosphorescent probes,

particularly for intracellular delivery and use. Fine tuning of the chemical and photophysical characteristics of existing structures can produce new probes with improved selectivity, effective penetration of cellular membranes and localization in specific subcellular compartments. Moreover, it can also enable multiplexed sensing and multi-functional sensor technologies, while maintaining ease of use and low cost.

Based on the above analysis of literature and state of the art in the areas of optical oxygen sensing and its applications, the main objectives of the project were:

- 1) Synthesize a new panel of hetero-substituted hydrophilic derivatives of PtPFPP for biological O₂ sensing applications.
- 2) Characterize their photophysical properties and cell staining ability.
- 3) Study their SAR: evaluate their applications as IC or EC O₂ sensing probes for cell bioimaging and respirometric bioassays on mammalian and bacterial cells, and compare them to existing soluble O₂ probes.

Chapter 2: Materials and methods

2.1. Materials

PtPFPP dye was from Frontier Scientific (Inochem Ltd, Lancashire, UK), 1-thio- β -D-glucopyranoside (1Glc) sodium salt and 2-Thioethyl- β -D-glucopyranoside (2Glc) were from Carbosynth Ltd (Berkshire, UK). *O*-(2-Carboxyethyl)-*O'*-(2-mercaptoethyl) heptaethylene glycol (cPEG-SH), *O*-(2-Mercaptoethyl)-*O'*-methyl-hexa(ethylene glycol) (mPEG-SH), 2-(Boc-amino)ethanethiol (Boc-CA), and BAY-876 were from Sigma-Aldrich. MitroTracker Green and Calcein Green were from Invitrogen. Cellular ATP assay CellTiter-Glo, was from Promega (Madison, WI). BCA Protein Assay kit was from Thermo Fisher Scientific (Rockford, IL). MitoXpress[®]-Xtra was from Agilent (Santa Clara, CA, USA). All the other probes were synthesized in our lab: NanO2 - as described in (106, 177). Nutrient Broth (NB) was obtained from Fisher Scientific Oxoid (Dublin, Ireland), selective and differentiating media specific for *E. coli* including the MacConkey (MC), Rapid Coliform ChromoSelect (RCC), M-Lauryl Sulfate (MLS), and Minerals Modified Glutamate (MMG) broths, were prepared as previously described(263). Heavy mineral oil was obtained from Cargille Laboratories. Solutions were prepared from sterile Milli-Q water (Millipore, Carrigtwohill, Ireland) or sterile DMSO (Sigma-Aldrich). All the other reagents and solvents were from Sigma-Aldrich.

2.2. Methods

2.2.1. Synthesis and purification of PtPFPP derivatives

Thiol-click modifications of the PtPFPP scaffold were performed according to the modified methods (160, 251). Briefly, the corresponding thiol-containing reagent was incubated with PtPFPP in DMF/methanol at 2:1 – 10:1 molar ratio in the presence of 10-molar excess of triethylamine (TEA) base, at 40 °C, under constant stirring. Reactions were monitored on an 1100 Series analytical HPLC (Agilent) on a YMC-Actus Triart C18, 150 x 4.5 mm I.D RP column (Gilson), using a 30 min or 40 min gradient 0→100% of acetonitrile in aqueous 0.1% trifluoroacetic acid (TFA) and a flow rate of 0.63 mL/min. Synthetic mixtures were then quenched with equivalent amount

of Trifluoroacetic acid (TFA), dried on a Rotavapor RII rotary evaporator system with a CVC 3000 vacuum pump (Vacubrand) to remove DMF and redissolved in 1-2 mL of MeOH or ACN or a mixture of the two solvents. Preparative purification was performed on a RP-HPLC PLC2250 (Gilson), using a YMC-Actus Triart C18, 150 x 20 mm I.D. RP column (Gilson), the same solvent mixture in a 40 min gradient and flow rate of 18.9 mL/min. Fractions containing the purified derivatives were then dried, weighed and aliquoted using a 5301-vacuum concentrator (Eppendorf). Their chemical structures were confirmed by NMR and QToF-MS.

2.2.2. Spectral and photophysical characterization

UV-Vis absorption spectra (range of 350-600 nm) were recorded on a HP8453 diode-array spectrophotometer (Agilent) in phosphate buffered saline (PBS) alone, or PBS with 5% fetal bovine serum (FBS), or PBS containing 0.1% Triton X-100. Corresponding molar extinction coefficients (ϵ) were calculated according to the Beer-Lambert law: $A = \epsilon lc$, where A is absorption, l is a path length and c is the known concentration of the probe.

Phosphorescent emission spectra (excitation range 300-600 nm and emission range 600-750 nm) and lifetime values were measured on a Cary Eclipse fluorescence spectrometer (Agilent) at room temperature or at 37 °C, under air-saturated and deoxygenated conditions (5 mg/mL KH_2PO_4 , 5 mg/mL Na_2SO_3). Lifetime values were obtained using OriginPro and multi-exponential fit.

NMR spectra were obtained on a AV300/400/600 MHz Bruker spectrometer, with chemical shifts related to residual deuterated solvent (ppm).

High-resolution mass spectrometry (HR-MS) analysis of purified PtPFPP derivatives was carried out in a XEVO G2 QToF mass spectrometer (Waters Corporation). Samples were injected by direct infusion after dissolving them in 70:30 ACN:H₂O (0.3% formic acid (FA) for positive mode, 30 mM triethylammonium acetate (TEAA) for negative mode). Ionization was performed with a capillary voltage of 2.5 kV and cone voltage of 40 V in a mass range of 400 to 3500 m/z. Source temperature and desolvation temperature were set at 120 °C and 450 °C respectively, cone gas flow was 50 L/hr and desolvation gas at 800 L/hr.

2.2.3. Cell culture, staining and toxicity assessment

Murine embryonic fibroblast (MEF), human colon carcinoma (HCT116) wild-type and $SCO_2^{-/-}$ mutant cells, and Rat pheochromocytoma (PC12) cells obtained from the ATCC (Manassas, VA, USA) were cultured as described before (128, 177, 264). Cell staining experiments were assessed on a TRF reader Victor2 (PerkinElmer), at 37 °C measuring phosphorescence intensity and lifetime signals.

MEFs cells were cultured on a 75 cm² flask until 80-100% confluence, in DMEM medium high glucose [4.5 g/L D-Glc] supplemented with 10% fetal bovine serum (FBS), 1 mM L-glutamine, 10 mM HEPES, and 1% (100 µg/mL) penicillin and streptomycin (P/S). For the staining efficiency experiments cells were grown on a 96 well plate for 24 h seeded at a concentration of 30,000 cells/well in 200 µL/well, to reach 100% confluence, then incubated with different probe concentrations (5, 10, 20, and 40 µM) for 3 h or 18 h, washed twice and measured in respiration medium serum free (phenol Red free DMEM (Sigma D5030) medium supplemented with 1 mM L-glutamine, 10 mM glucose, 1 mM sodium pyruvate, 20 mM HEPES and 10% FBS, pH 7.2). Phosphorescent intensity signals were monitored at 37 °C on a multi-label plate reader in TRF mode for approximately 40 minutes.

Cell permeability was also assessed using HCT116 WT and $SCO_2^{-/-}$. Cells were cultured in McCoy's medium supplemented with 10% FBS, 2 mM L-glutamine and P/S, seeded in a collagen IV coated 96 well plate at 20,000 and 30,000 cells/well, respectively. Cells were grown on a 96 well plate for 36 h to reach 100% confluence, and then incubated with probes for 3 h, washed three times and phosphorescent signals were monitored as described above. BCA protein assay was used to evaluate total protein content in cell lysates obtained from HCT WT and $SCO_2^{-/-}$ seeded on a collagen coated 6 well plate at 400,000 and 600,000 cells/well, respectively, and grown for 36 h. BCA data was used to normalize intensity signals of the two cell lines.

CellTiter-Glo ATP kit was used to measure probe toxicity on MEF cells via changes in their total ATP, following manufacturer instructions.

2.2.4. OCR measurements

Respirometry experiments upon cell stimulation using intracellular probes were carried out on an open plate as previously described (264). MEF cells were seeded at 35,000 cell/well in 200 μ L of medium and grown for 30 hours to reach high confluence (>100%). Cells were loaded with intracellular oxygen probes at 5 μ M working concentration, dissolved in 100 μ L of complete DMEM (Glc(+)) with 10% FBS, replacing the growth medium, and incubated for 18 h. Cells were washed three times with DMEM respiration medium (serum free) containing 10 mM glucose or 10 mM galactose, and measured for 20 min on a time-resolved fluorescence microplate reader Victor2 (Perkin-Elmer) to reach temperature equilibration. The calcium (Ca^{2+}) chelator ethylene glycol tetraacetic acid (EGTA) was then added at 2.5 mM and the plate was measured for further 60 min. Subsequently, antimycin A (AntiA) at 5 μ M was added and intensity recorded for further 30 min. TRF emission intensity measurements were taken in Gal(+)/Glc(-) respiration medium (serum free) with or without with 1 h incubation time prior signals monitoring (256, 264). Negative controls were treated with vehicle alone.

OCR measurements using extracellular probes were carried out on a sealed plate, as previously described (264). PC12 cells were cultured using RPMI 1640 medium supplemented with 5% FBS, 10% Horse serum, 10mM HEPES, and 100 μ g/mL P/S, pH 7.2. Cells were trypsinised, resuspended in respiration medium (DMEM Glc(+), serum free), and counted. Aliquots containing 250,000 cells/well in 100 μ l volume, mixed with final probe concentration (PtcPEG₄ and PtcPEG₃1Glc at 5 μ M) were seeded on a 96 well plate in triplicates and treated with carbonyl cyanide 4-(trifluoromethoxy) phenylhydrazone (FCCP) (0.25 μ M) – mitochondrial uncoupler, and antimycin A (Ant A) (2.5 μ M) – mitochondrial inhibitor, separately. Controls without cells and with untreated/non-stained cells were also included and used to correct sensor signals for any drifts unrelated to cellular fluxes. Each well was sealed with 200 μ L of mineral oil. Cells suspended in 100 μ L of respiration medium containing MitoXpress®-Xtra O₂ probe were also prepared as standard reference.

2.2.5. Internalization via glucose transporters (GLUTs) using BAY-876

MEF cells were seeded on a 96 wp at a density of 30,000/well and grown for 24 h in standard growth medium (DMEM, containing Glc 10 mM and 10% FBS). Cells were treated for 1 h with BAY-876 at 10 μ M to inhibit GLUT1 transporters. For staining in Glucose free medium, cells were previously starved for 2 h in glucose free DMEM in the presence of 10% FBS. After 1 h inhibition, the probes were added to the wells in the presence of the inhibitor. After 3 h staining, cells were washed, and emission intensity signals were measured on a plate reader in TRF mode.

To confirm the ability of BAY-876 to inhibit GLUT1 at the selected concentration, cells were starved for 2 h in glucose free medium, then simultaneously treated with BAY-876 at 10 μ M and rotenone at 5 μ M. Prior to measurements cells were incubated for 1 h at 37°C in the presence of 10 mM glucose (activation of GLUT1). After 30 min cells were washed in respiration medium and ATP levels measured using the assay kit.

2.2.5. Bacterial respirometric and turbidimetric assay procedures

Escherichia coli (*E. coli*) cells, strain NCIMB 11943, obtained from the School of Microbiology, University College Cork, were stored at -80 °C in LB broth containing 80% glycerol. Working stock of *E. coli* was prepared by overnight incubation in NB, as described in (263). From this fresh stock, 1:10 serial dilutions were prepared in NB and each selective media and mixed with working dilutions of MitoXpress (0.3 μ M), NanO2 (0.3 μ M), Pt1Glc₄ (3 μ M), PtmPEG₄ (3 μ M) to produce final *E. Coli* concentrations of 10⁴, and 10⁶ CFU/mL. Then 200 μ L aliquots of each solution were dispensed in triplicates into wells of a 96 well-plate (Sarstedt). Solutions of the probes in sterile media without bacteria (negative controls) and *E. coli* dilutions in media without oxygen probe were also prepared, dispensed on the plate, and measured as blank signals. Sample wells were then sealed with 70 μ L of mineral oil and the plate was placed in a Victor4 (PerkinElmer) reader equilibrated at 37 °C and monitored in time-resolved fluorescence (TRF) mode for 10 h measuring signals in each well every 5 min in kinetic mode.

Absorbance/light scattering signals were measured on Victor2 reader for the plate with *E. coli* dilutions in the different media (no probe) and negative controls (media, no cells), using 600 nm and 450 nm filters and the same temperature and kinetic mode as for TRF measurements described above.

2.2.6. Bioimaging

MEF cells were seeded on petri dishes (3.5 cm) at 200,000 in DMEM, grown for 24 hours, then loaded with oxygen probes at different concentrations (5, 10, 20 or 40 μ M) in DMEM and incubated for 18 h. The cells were washed three times with fresh medium containing only 1% HEPES and counterstained with Calcein Green at 1 μ M for 30 min. Medium was then replaced with complete medium and the cells were imaged (160) on a confocal TCSPC-PLIM microscope (Becker & Hickl) using an immersion lens adapter at 63x magnification objective, and recorded using the SPCImage software (Becker & Hickl). A 488 nm laser was used for the excitation of Calcein Green probe, and a 405 nm laser in PLIM mode was used for PtPFPP based O₂ probes(160, 256).

Co-staining with Mito Tracker Green (MTG) at 50 nm for 1 h (excited using 488 nm laser), and probes at 10 μ M for 18 h, were also evaluated recording images using the 20x magnification immersion lens.

2.2.7. *E. coli* microscopy

E. Coli was diluted in NB to 10⁶ in the presence of the final working concentration of the probe and plated on a 96 well plate for 3 h incubation at 37 °C (static conditions and protected from the light). Cell suspensions were collected into one vial/probe and centrifuged at 3,000 rpm for 10 min. Supernatant was removed and pellets were resuspended in approximately 100 μ L of NB containing at the final probe working concentration. Small aliquots were dispensed on a Millicell® disposable hemocytometer and analyzed using a confocal microscope at room temperature (excitation with a 405 nm laser, and 40x magnification lens).

2.3. Data processing

For all TRF measurements, instrument settings were the following: excitation filter - 340 nm, emission filter - 642 nm, two delay times 25 μ s and 50 μ s for small molecular probes, or 30-70 μ s for all other probes, and gate time - 100 μ s (for each delay). Phosphorescence lifetime values (LT) were calculated using the formula for rapid lifetime determination (RLD): $LT=(t_1-t_2)/\ln(I_1/I_2)$, where t_1 and t_2 are the delay times and I_1 and I_2 the corresponding intensity signals (88). The resulting LT values were plotted over time to produce respiration profiles for each well, media and probe controls.

Data analysis. All results were obtained from average values produced by at least three biological replicates, with standard deviations expressed as error bars. To ensure consistency, all the experiments were performed in technical duplicates or triplicates.

Chapter 3: Design, synthesis, and characterization of the new PtPFPP hetero-substituted derivatives

3.1. Introduction

Phosphorescent O₂-sensing probes facilitate the monitoring of oxygenation state and O₂ consumption rates (OCR) of biological samples containing live respiring cells and tissues and linking these parameters to vital biochemical processes and cellular responses to stimuli (10, 21, 65). To date, several types of such O₂ probes have been developed and applied for the measurement and imaging of O₂ concentration and OCR. Initially, intravascular and intravital O₂ probes were developed for use in live animals (164, 167, 210), followed by extracellular probes for *in vitro* diagnostics and cell-based assays (127). More recently, intracellular O₂ probes with cell-penetrating ability have been introduced (88, 120, 178). Dual pH/O₂ sensing probes have also been described (224). Many of these probes and applications can be used on standard detection platforms. The key component in all these probes is the phosphorescent indicator moiety that determines their O₂-sensing and photophysical properties.

Solubility of the probe in biological samples is essential to prevent aggregations or non-specific binding to macromolecules present in media or biological fluids, however most O₂ sensing dyes tend to be too hydrophobic. Rational design of the chemical structure should be based on the knowledge of the biochemical mechanisms that are involved in intracellular delivery, through testing and optimizing with different cell lines and more complex samples. This approach, with detailed study of the SARs, has enabled the synthesis of a new generation of O₂ sensing probes. Pt(II)-tetrakis(pentafluorophenyl) porphyrin (PtPFPP) (Figure 1.5) is an attractive indicator dye for O₂-sensing assays, as it possesses high brightness and photostability, optimal sensitivity to oxygen, convenient spectral characteristics, availability, and affordable cost. Because of this, PtPFPP is widely used in various

polymeric solid-state O₂ sensors (131) and nanoparticle based probes (dispensable aqueous reagents) (177, 178). However, high hydrophobicity and water insolubility prevent its direct use with cells and biological samples as a soluble O₂ probe. The latter limitation can be overcome by synthesizing derivatives of PtPFPP and tuning their physico-chemical characteristics, such as hydrophilicity, molecular charge, and functional groups. The relatively simple and efficient click-modification of PtPFPP via its pentafluorophenyl moieties with thiol- and amine-containing reagents (160, 207, 250-252) facilitates this work. Moreover, the very stable S-glycosidic bond in these compounds prevents their degradation in biological environments (259, 261, 265). Conjugates of free porphyrins with saccharide moieties were studied previously, mainly for their photosensitizing activity and possible use in photodynamic therapy (PDT) (262) or as biomimetics for carbohydrates recognition (266-268). Their cell recognition and labelling were studied with a particular focus on drug conjugates with more specific and targeted delivery (259). While saccharide moieties improve the water solubility of porphyrin molecules (261), their PEGylation was also known to reduce unwanted non-specific interactions and cellular uptake (167). Short PEG fragments (between 400 and 8000 MW) were shown to improve water solubility and bioavailability (serum life), reduce activation of the immune system, and facilitate receptor binding (253, 269) and accumulation of porphyrin sensitizers in tumours (270).

In this study, we applied the above knowledge to produce new O₂ probes for both intracellular and extracellular use and study their specificity, recognition, and interaction with cells (via GLUT transporters). Specifically, we describe a panel of hydrophilic hetero-substituted phosphorescent oxygen probes produced by click-modification of the four pentafluorophenyl moieties in the PtPFPP scaffold with different thiols.

3.2. Rational Design of PtPFPP-Based Phosphorescent Probes

3.2.1. 3:1 Hetero-substituted derivatives

To address the issues with the current probes and better understand their underlying mechanisms of action, we have decided to synthesize a panel of different hydrophilic PtPFPP derivatives and evaluate them comparatively in aqueous media and biological samples containing live cells. Specifically, we initially synthesized a panel of six hetero-substituted derivatives of PtPFPP with two different glucose moieties (1-thio- β -D-glucopyranoside - 1Glc and 2-thioethyl- β -D-glucopyranoside - 2Glc), two different PEG (*O*-(2-carboxyethyl)-*O'*-(2-mercaptoethyl) heptaethylene glycol - cPEG-SH and *O*-(2-mercaptoethyl)-*O'*-methyl-hexa(ethylene glycol)- mPEG-SH), and with a cysteamine moiety (2-(Boc-amino)ethanethiol - Boc-CA). We then purified each derivative and studied their biocompatibility and SARs by testing them on mammalian cell cultures. All these compounds contain one biochemical moiety responsible for the interaction with cells or cell surface receptors (i.e., plasma membrane, glucose transporters (GLUTs)) and three chemical moieties providing a hydrophilic shell and variable molecular charges (due to carboxy-PEG, cysteamine, methoxy-PEG moieties). Several symmetrical tetra-substituted derivatives were also synthesized and used for comparison and benchmarking. The general structure and derivatization chemistries of the new bioprobes are shown in Figure 3.1.

We anticipated that such bifunctional PtPFPP derivatives will show improved hydrophilicity and more predictable and tuneable cell internalization behaviour, due to their mono-glycosylation, variable molecular charge, and surface chemistry. The phosphorescence of these molecular structures can also be altered by substitution, particularly their intensity and lifetime signals in aqueous solutions and biological media. Altogether, this can generate a new family of intracellular or extracellular O₂-sensing probes for biological applications and provide more detailed information about their SARs.

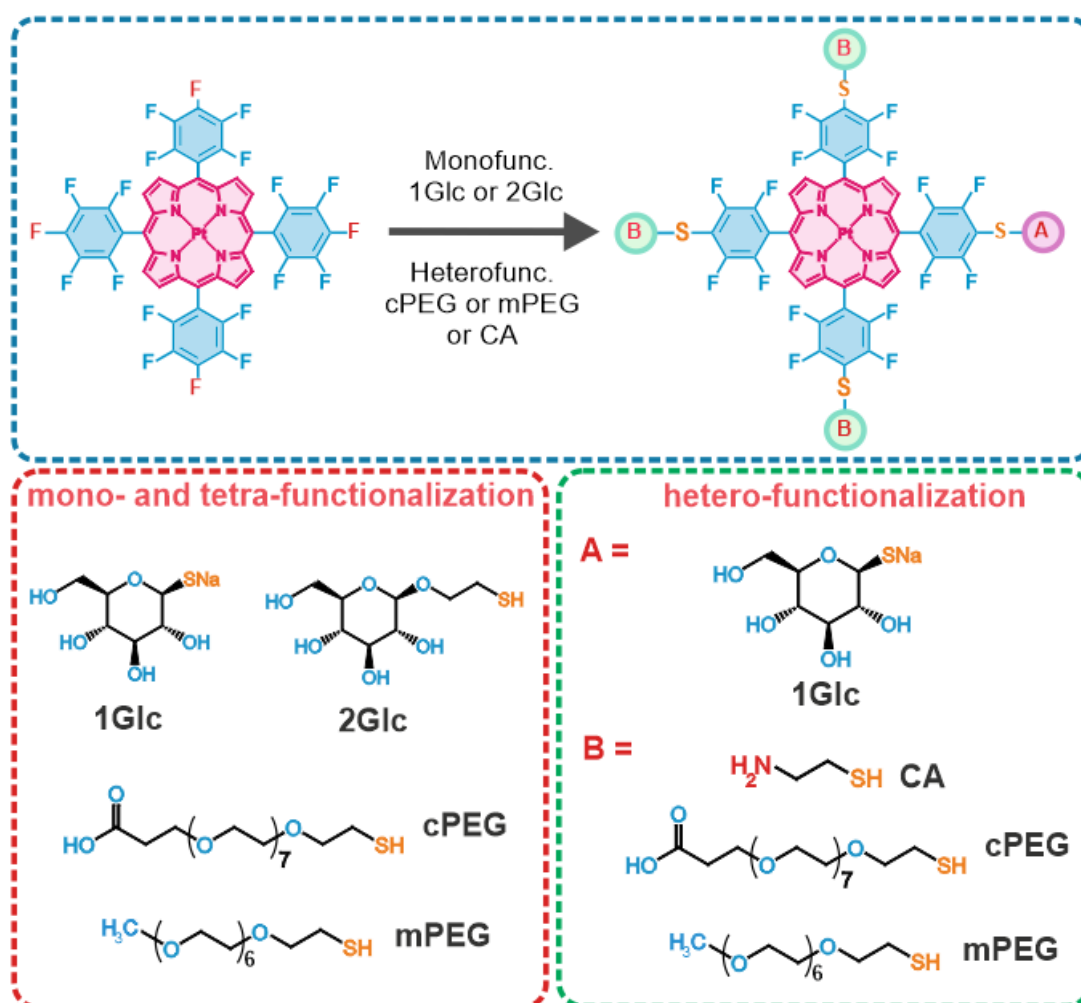


Figure 3.1: General structures of PtPFPP derivatives produced by click modification with thiols and the schemes of the mono- and hetero-substitution (top panel). The thiols used for the mono- and hetero-functionalization are also shown (bottom panels).

3.2.2. 2:2 Hetero-substituted derivative

Following up with the previous section, we decided to further study the effect of symmetric di-glycosylation (using 1-thio-glucose, 1Glc) and di-PEGylation (using the neutral methoxy-PEG, mPEG) in *trans*- position on the PtPFPP scaffold. In fact, previous studies in the PDT field, demonstrated the superiority of the *trans*-conformation for cellular uptake and subsequent cytotoxicity when exposed to light (271, 272). However, our research is aimed at producing intracellular O₂ probes that exert minimal cytotoxicity. Thus, we synthesized one new hetero-substituted

derivative of PtPFPP via two-step click chemistry (251, 252). The final compound PtmPEG₂1Glc₂ (trans) (Figure 3.2) has two thio-glucose and two thio-PEG moieties covalently attached in *trans*- position (Figure 3.2). Such substitutions produce a corona shell of PEG chains which improves the hydrophilicity and solubility in aqueous media and allows biological applications. The glycosylation provides cell targeting and internalisation, while PEGylation provides protection against non-specific interactions (253). Particularly, we opted for the neutral short PEG (mPEG-SH) to avoid any repulsive or attractive effects with the cell membrane. We also purified and analysed the *trans*-di-glycosylated Pt1Glc₂ (trans) intermediate (272) to compare its biocompatibility and cell staining with the corresponding *trans*-PEGylated derivative.

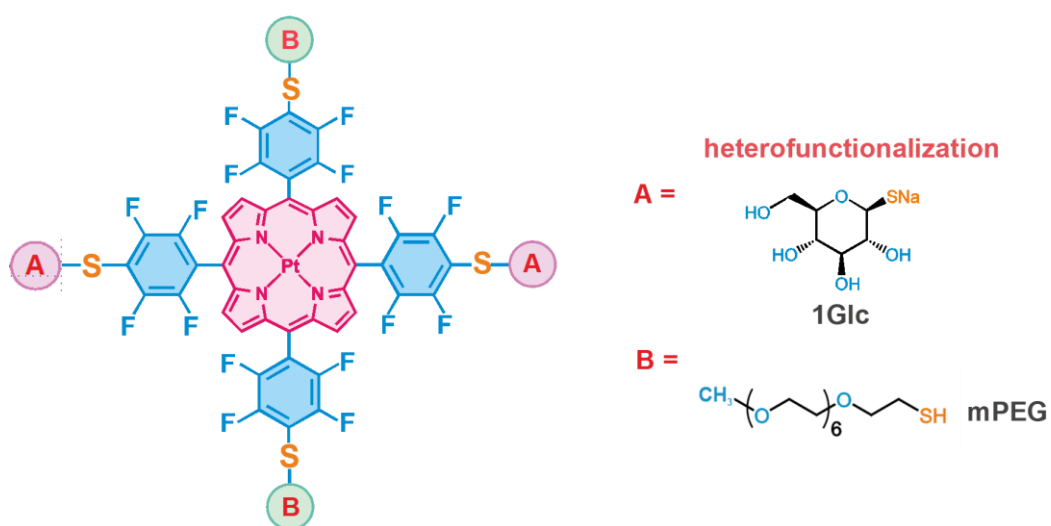


Figure 3.2: General structure of the 2:2 *trans*- hetero-substituted derivative of PtPFPP and chemical structures of the thiols used in the two-step bioconjugation reaction.

3.3. Chemical synthesis and characterization of new derivatives and intermediates

The click modification of the pentafluorophenyl moiety with thiols is known to proceed easily and “cleanly” (252). Therefore, the tetrafunctional PtPFPP is expected to produce five possible products: one mono-, two di- (*cis*- and *trans*-), tri-, and tetrasubstituted derivatives (Figure 3.4). By optimizing the reaction conditions, one can also achieve decent yields of mono-substitution at low molar ratios or almost quantitative yields for tetrasubstituted derivatives at 4–10 molar excess of the thiol. Thus, mono-glycosylation of PtPFPP with 1Glc or 2Glc thiols at a 1:2 molar ratio in DMF or MeOH containing TEA produced key intermediates (Pt1Glc₁ and Pt2Glc₁) with yields of ~40%.

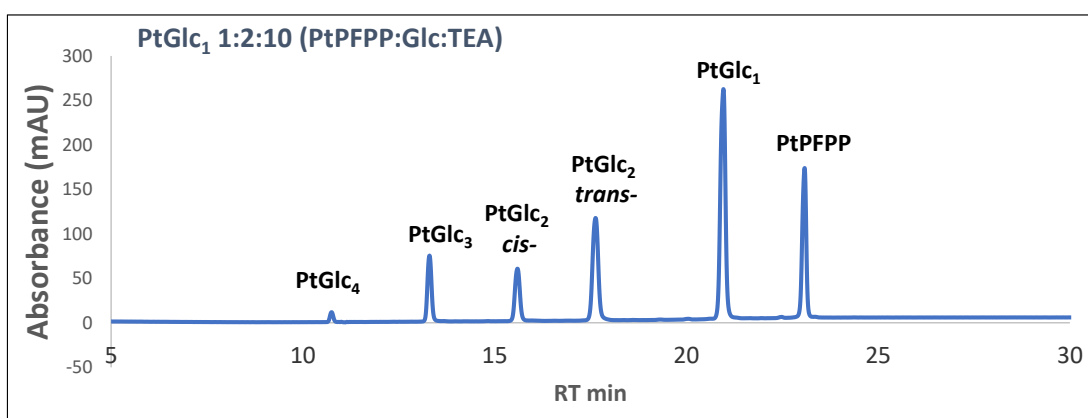


Figure 3.4: RP-HPLC chromatogram of the products of the glucosylation bioconjugation of PtPFPP. Pt1Glc₁ (target compound) is eluted at 20.96 min retention time (RT) using a 40 min gradient 0 → 100% ACN/water 0.1% TFA.

All the derivatives and intermediates were synthesised as describe in (256).

3.3.1. Chemical synthesis, NMR and MS of Pt1Glc₁

PtPFPP (0.585 mg, 500 nmol) dissolved in 1.2 mL of DMF, with 1-thio-β-D-glucose sodium salt (0.218 mg, 1 μmol) dissolved in 0.3 mL of MeOH containing TEA (1.63 μL, 10 μmol) for 5 h at 40 °C, monitored by analytical RP-HPLC (0.27 mg, **yield 39.8%**) (Figure 3.3). **Purity (HPLC): 99.6%**. QToF high resolution mass spectrometry: m/z for C₅₂H₂₄F₁₉N₅O₆PtS⁻ ([M+CH₃CN+H₂O]⁻) caclcd 1402.07994, found 1402.0421. ¹H NMR

(300 MHz, CDCl₃, CHCl₃=7.28 ppm) δ ppm= 3.75-4.17 (6H, m, 2',3',4',5',6'a,6'b-GlucH), 5.2 (1H, d, J = 8.8 Hz, 1'-GlcH), 8.73-8.82 (8H, m, β-pyrroleH). ¹⁹F NMR (300 MHz, CDCl₃) δ ppm= -132.00 (2F, dd, J_{1,2}= 25.68, 12.53, *meta*- 3,5-PhFGlc), -135.72 (2F, dd, J_{1,2}= 24.82, 11.92, *ortho*- 2,6-PhFGlc), -136.42,-136.65 (6F, m, *meta*- 3,5-PhF), -151.05,-151.37 (3F, m, *para*- 4-PhF), -161.1,-161.4 (6F, m, *ortho*- 2,6-PhF). UV-vis (DMF, path length = 1 cm, 25°C): λ(nm) = 390, 538, 505.

Full HR-MS and ¹H, ¹⁹F NMR spectra can be found in (256).

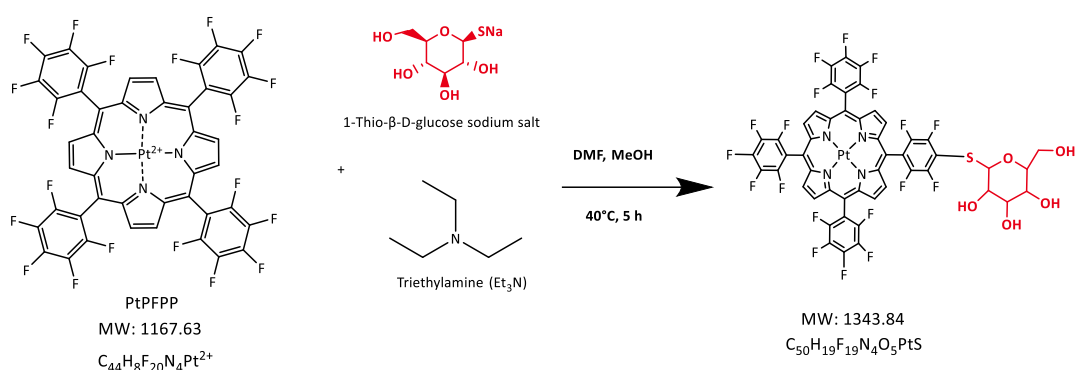


Figure 3.3: Graphical representation of the chemical reaction and structure of the final products for the synthesis of Pt1Glc₁.

The chromatogram in Figure 3.4. reveals all the main products in the reaction mixture, with the target 1:1 compound producing the main well-resolved peak (Pt1Glc₁ eluted at 20.96 min RT), which is easy to separate from the other products. The sequential derivatization of PtPFPP with Glc moieties also shows stepwise increase in hydrophilicity, with sharp, well-resolved, and easily identifiable peaks on RP-HPLC chromatograms. This facilitates synthesis scale-up and purification of target compounds, which in our case was achieved by preparative RP-HPLC.

Pt2Glc₁ was synthesized likewise using 2-thioethyl-β-D-glucopyranoside (0.240 mg, 1 μmoles) obtaining 0.31 mg of final product - **yield: 44.42%** (256) .

By scaling up the synthesis followed by preparative HPLC purification, compounds Pt1Glc₁ and Pt2Glc₁ were produced in a pure form, in ~5 to 10 mg quantities each. The hetero-substituted derivatives were synthesized by excessive thiolation of

mono-substituted intermediates Pt1Glc₁ and Pt2Glc₁ with anionic hepta- or neutral hexa-poly(ethylene glycols) cPEG-SH and mPEG-SH, respectively. In these cases, almost quantitative yields were achieved (~98% and ~94% respectively).

3.3.2. Chemical synthesis, NMR and MS of PtcPEG₃1Glc

The mono-glycosylated compound (Pt1Glc₁) (0.67 mg, 500 nmol) dissolved in 100 μ L of DMF was incubated with cPEG7-SH (2.3 mg, 5 μ mol), in the presence of TEA (1.63 μ L, 10 μ mol) for 5h at 40 °C, then purified by RP-HPLC (1.296 mg, **yield 97.5%**) (Figure 3.5). **Purity (HPLC): 92.7%**. QToF mass spectrometry: m/z for C₁₀₇H₁₂₈F₁₆N₄O₃₅PtS₄²⁻ ([M-2H]²⁻) caclcd 1327.8328, found 1328.1399. **¹H NMR** (600 MHz, (CDCl₃, CDCl₃ = 7.2 ppm) δ ppm = 2.47-2.51 (6H, m, CH₂-COOH), 3.3-3.96 (108H, m, O-(CH₂)₅₁ and 2',3',4',5',6'a,6'b-GlcH), 5.05 (1H, d, J=8.22 Hz, 1'-GlcH), 8.43 (8H, d, J=16.61 Hz, β -pyrroleH). **¹⁹F NMR** (300 MHz, CD₃OD) δ ppm = -131.84,-131.97 (2F, m, *meta*- 3,5-PhFGlc), -133.41,-133.58 (6F, m, *meta*- 3,5-PhFPEG), 136.72,-136.85 (2F, m, *ortho*- 2,6-PhFGlc), 137.04,-137.24 (6F, m, *ortho*- 2,6-PhFPEG). **¹³C NMR** (600 MHz, CDCl₃, CHCl₃ = 75.99) δ ppm = 33.28 (S-CH₂), 33.81 (COOH-CH₂), 65.43 (6'-GlcC), 69.04-69.86 (PEG-C chain and 4'-GlcC), 72.94 (2'-GlcC), 77.31 (3'-GlcC), 79.22 (5'-GlcC), 84.47 (1'-GlcC), 106.13 (mesoC), 115.73 (1-PhC), 118.3 (4-PhC), 130.01 (β -pyrroleC), 139.97 (α -pyrroleC), 144.19-146.64 (3,5-PhC and 2,6-PhC), 173.30 (-C=OOH). UV-vis (DMF, path length = 1.0 cm, 25 °C): λ (nm) = 393, 538, 506. FL (c = 0.2 μ M, DMF, path length = 1.0 cm, λ_{ex} = 390 nm, 25 °C): λ (nm) = 649, 703.

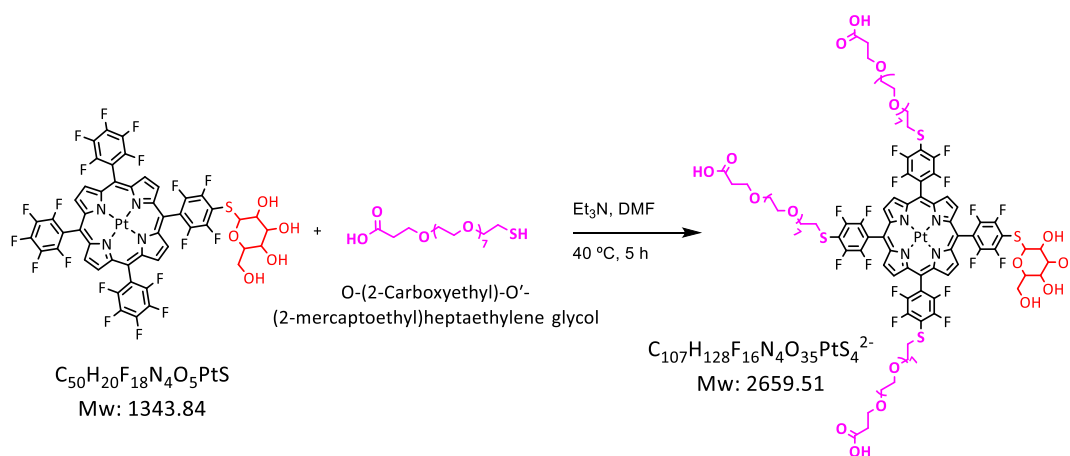
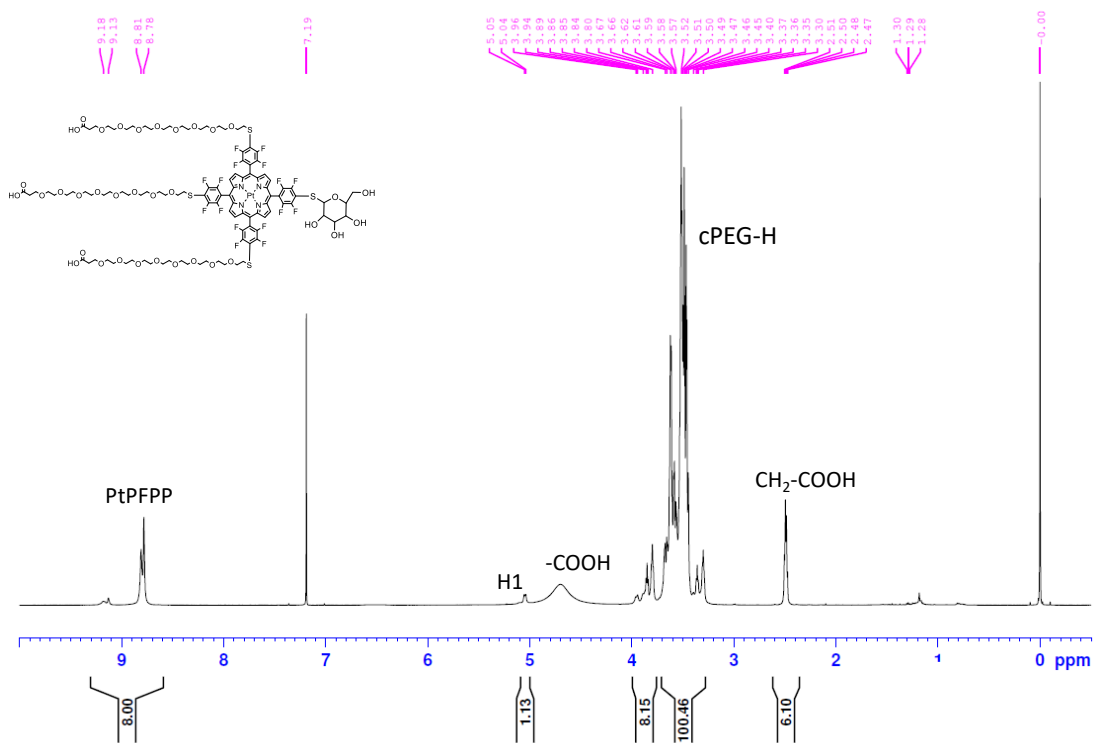
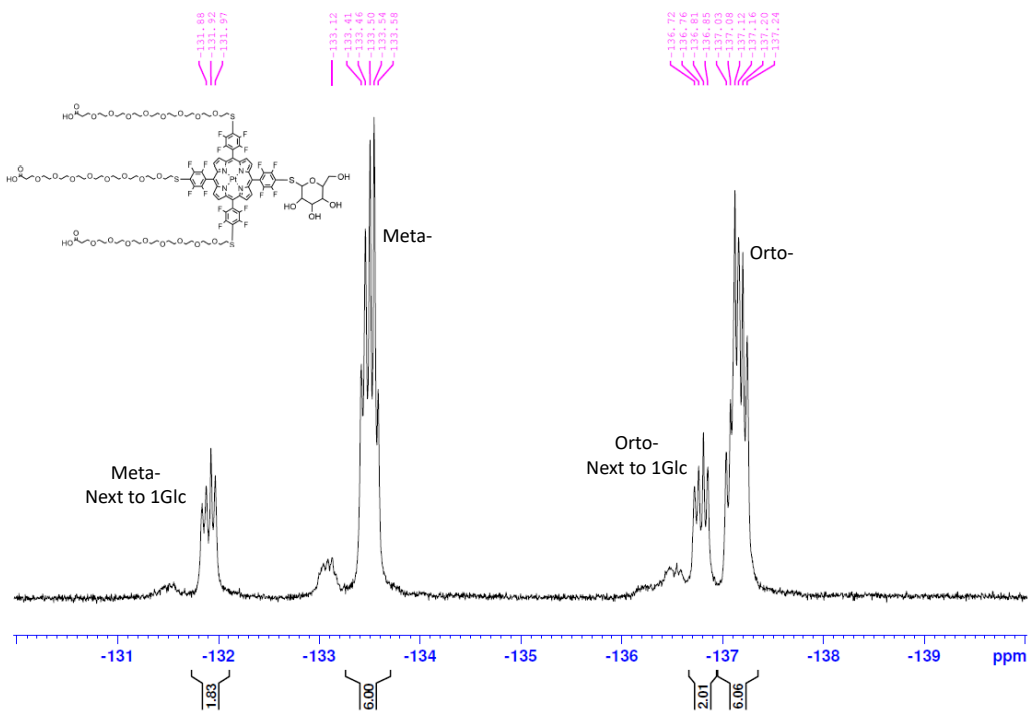


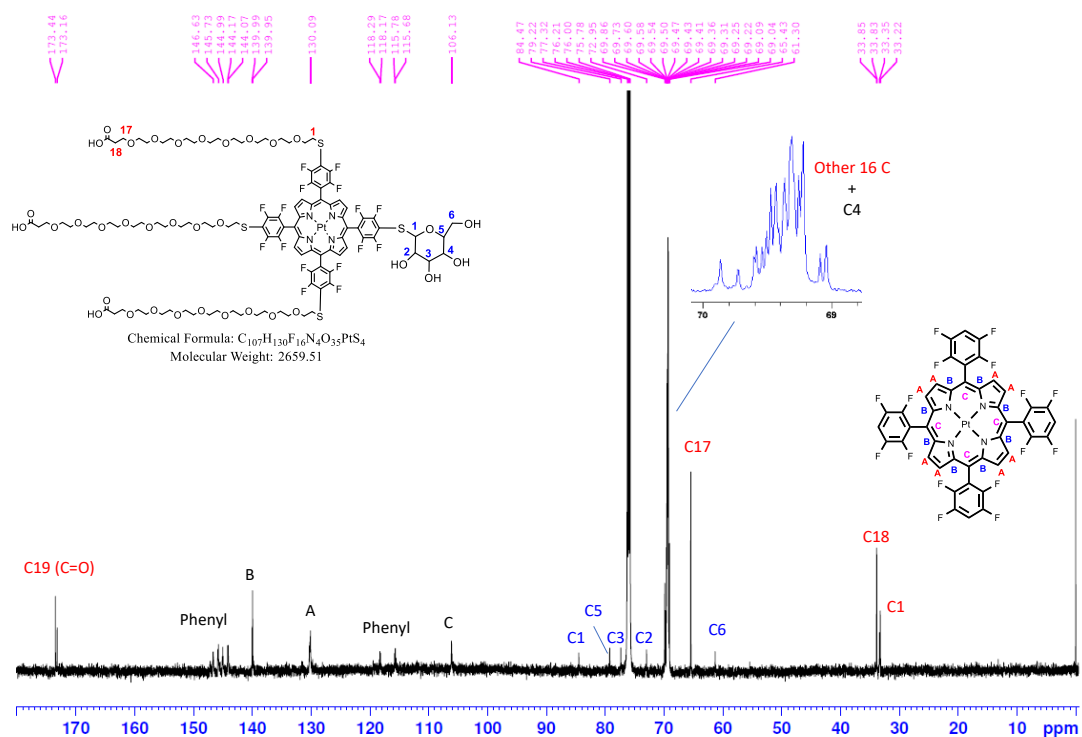
Figure 3.5: Graphical representation of the chemical reaction and structure of the final product for the synthesis of PtcPEG₃1Glc.



Spectrum 1: ¹H NMR PtcPEG₃1Glc in CDCl₃ (600 MHz)



Spectrum 2: ¹⁹F NMR PtcPEG₃1Glc in CDCl₃ (300 MHz)



Spectrum 3: ^{13}C NMR PtcPEG₃1Glc in CDCl₃ (600 MHz)

PtcPEG₃2Glc, was synthesized likewise reacting the mono-glycosylated compound Pt2Glc₁ (0.69 mg, 500 nmoles) dissolved in 100 μl of DMF were incubated with cPEG7-SH (2.3 mg, 5 μmoles) obtaining 1.27 mg of final compound - **yield 93.91%**. Purity (HPLC): 93.89% .

3.3.3. Chemical synthesis, NMR and MS of PtmPEG₃1Glc

The mono-glycosylated compound (Pt1Glc₁) (7 mg, 5.2 μmol) was dissolved in DMF (1.486 mL), and was incubated with mPEG7-SH (9.27 mg, 26 μmol), in the presence of TEA (7.25 μL , 52 μmol) for 5 h at 40 $^{\circ}\text{C}$, then purified by RP-HPLC (7.97 mg, **yield 65.15%**) (Figure3.6). **Purity (HPLC):** 84.2%. QToF mass spectrometry: m/z for C₉₅H₁₁₄F₁₆N₄O₂₆PtS₄²⁺ ([M + 2H]²⁺) cacl'd 1176.7993 found 1176.6803. **^1H NMR** (600 MHz, (CDCl₃, CDCl₃ = 7.26 ppm) δ ppm = 3.34 (9H, d, -CH₃), 3.39-3.47 (6H, m, S-CH₂), 3.49-3.76 (72H, m, O-(CH₂)₃₆ and 2',3',4',5'-GlcH), 3.92-4.03 (8H, m, S-CH₂-CH₂ and 6'a,6'b-GlcH), 5.02 (1H, d, J=8.6 Hz, 1'-GlcH), 8.85 (8H, s, β -pyrroleH). **^{19}F NMR** (300 MHz, CD₃OD) δ ppm = -131.54,-131.68 (2F, m, *meta*- 3,5-PhF-Glc), -133.4,-133.60 (6F, m, *meta*- 3,5-PhF-PEG), 136.29,-136.43 (2F, m, *ortho*- 2,6-PhF-Glc), 136.94,-137,13

(6F, m, *ortho*-2,6-PhF-PEG). ^{13}C NMR (600 MHz, CDCl_3 , $\text{CHCl}_3 = 77.04$) δ ppm = 34.39 (S- CH_2), 59.9 (- CH_3), 62.67 (6'-GlcC), 70.37-71.88 (PEG-C chain and 4'-GlcC), 73.89 (2'-GlcC), 78.27 (3'-GlcC), 80.19 (5'-GlcC), 85.78 (1'-GlcC), 107.0 (mesoC), 116.72 (1-PhC), 119.38 (4-PhC), 131.13 (β -pyrroleC), 140.9 (α -pyrroleC), 145.13-147.28 (3,5-PhC and 2,6-PhC). UV-vis (DMF, path length = 1.0 cm, 25°C): $\lambda(\text{nm}) = 393, 538, 505$.

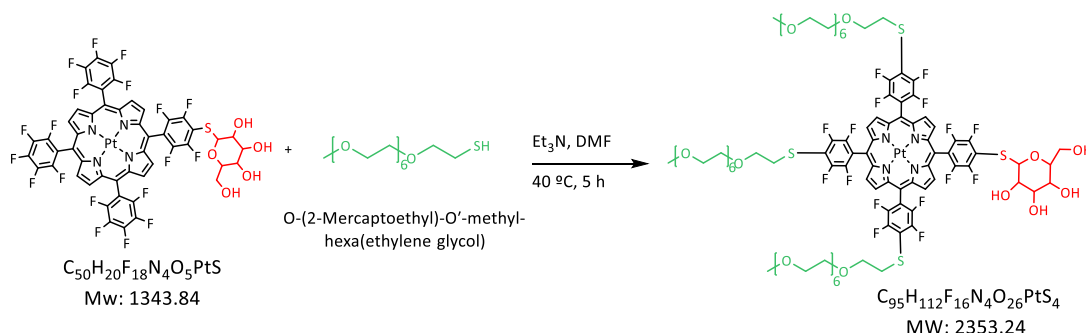


Figure 3.6: Graphical representation of the chemical reaction and structure of the final product for the synthesis of Pt(mPEG)₃Glc.

^1H , ^{19}F , ^{13}C NMR can be found in the appendix (Spectrum S1, S2, S3 of the appendix)

3.3.4. Chemical synthesis, NMR and MS of PtCA₃Glc

The synthesis of the cationic cysteamine (CA) derivatives of PtPFPP required the use of protected Boc-CA (since the CA amino group can also react with the pentafluorophenyl moiety (260), purification of the target hydrophobic product by RP-HPLC, subsequent deprotection with HCl, and final purification by RP-HPLC.

The mono-glycosylated Pt1Glc₁ (15.76 mg, 11.7 μmol) was dissolved in 3.348 mL of DMF and incubated for 2 h at 40 °C with 2-(Boc-amino)ethanethiol (22.5 μl , 93.6 μmol) in the presence of TEA (16.3 μl , 117 μmol). This was followed by TEA neutralisation with 1 molar equivalent of HCl and purification by RP-HPLC (11 mg, yield 52%). Deprotection was carried out by dissolving the dried product in 2 mL of acetonitrile: methanol (3:2) containing 1 M HCl and overnight stirring at 55 °C. The acid was then neutralized by 1 molar equivalent of TEA at room temperature, the reaction was then concentrated and the residue dissolved in MeOH for purification (6.52 mg, **yield 36.8%**) (Figure 3.7). **Purity (HPLC): 98.8%**. QToF mass spectrometry:

m/z for $C_{56}H_{40}F_{16}N_7O_5PtS_4^{3+}$ ($[M+3H]^{3+}$) caclcd 506.044279, found 506.0499. **1H NMR** (600 MHz, CD_3OD , $CH_3OH = 3.33ppm$) δ ppm = 3.43-3.56 (16H, m, $S-CH_2-CH_2$ and $4',2',3',5'-GlcH$), 3.76 (1H, dd, $J_{1,2} = 12.1, 6.56$, $6'-GlcH$), 4.02 (1H, dd, $J_{1,2} = 11.88, 1.84$, $6'-GlcH$) 5.17- 5.22 (1H, m, $1'-GlcH$), 9.11-9.17 (8H, m, β - pyrroleH). **19F NMR** (300 MHz, CD_3OD) δ ppm = -134.87 (2F, dd, $J_{1,2} = 24.45, 11.70$, meta- 3,5- PhFGlc), -135.27, -135.40 (6F, m, meta- 3,5-PhFCA), 139.29, -139.42 (6F, m, ortho- 2,6- PhFGlc), 140.62 (2F, dd, $J_{1,2} = 24.32, 11.73$, ortho- 2,6-PhFCA). **13C NMR** (600 MHz, CD_3OD , $CH_3OH = 49.0$) δ ppm = 33.01 (N- CH_2), 40.79 (S- CH_2), 63.11 ($6'-GlcC$), 71.74 ($4'-GlcC$), 75.96 ($2'-GlcC$), 79.74 ($3'-GlcC$), 82.77 ($5'-GlcC$), 86.68 ($6'-GlcC$), 108.28 (mesoC), 115.76 (1-PhC), 121.83 (4-PhC), 132.74 (β -pyrroleC), 142.7 (α -pyrroleC), 146.85-149.62 (3,5-PhC and 2,6-PhC). UV-vis (DMF, path length = 1.0 cm, 25°C): λ (nm) = 393, 538, 506. FL ($c = 0.2 \mu M$, DMF, path length = 1.0 cm, $\lambda_{exc} = 390$ nm, 25 °C): λ (nm) = 649,703.

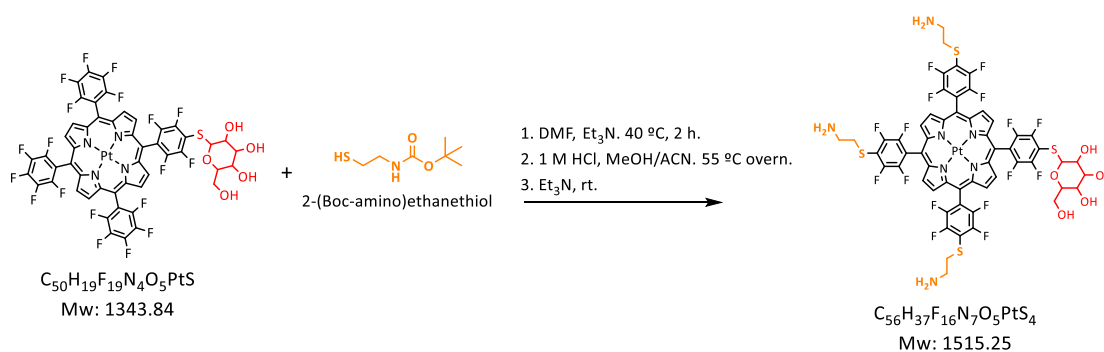
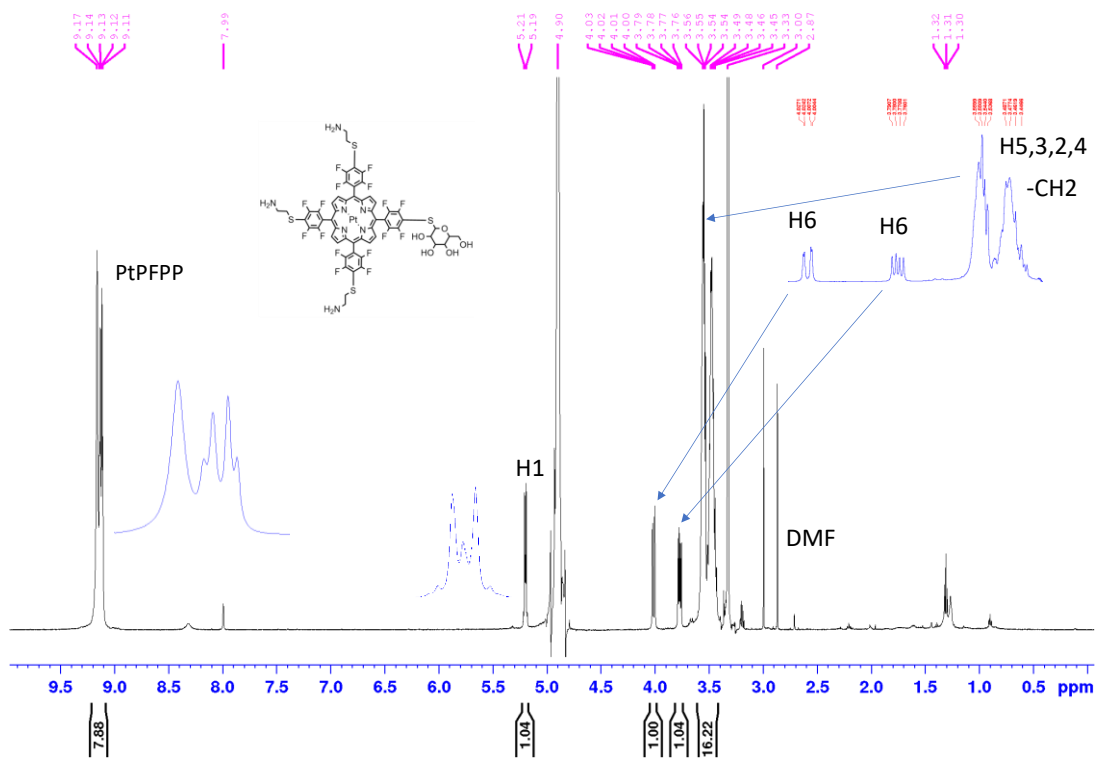
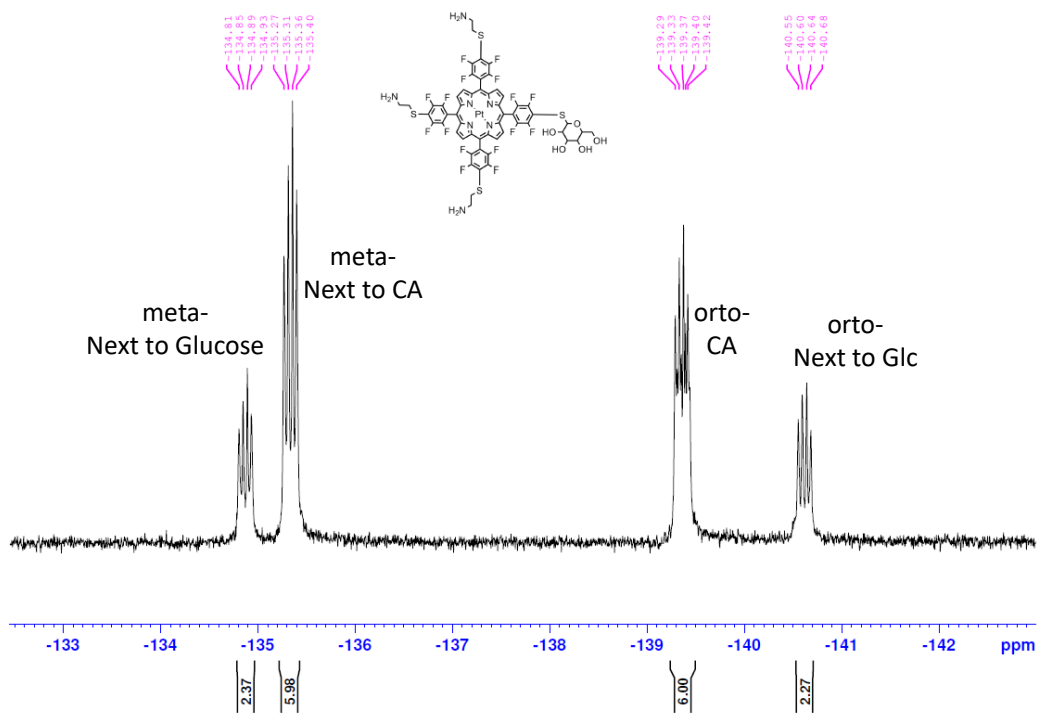


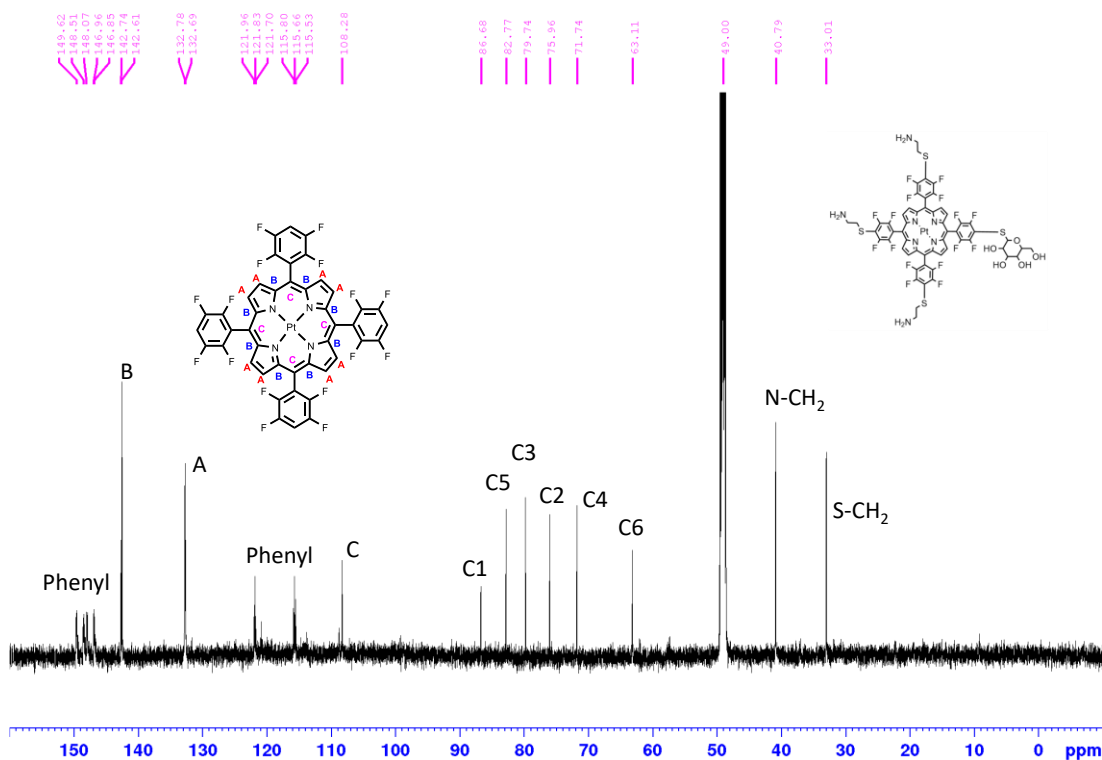
Figure 3.7: Graphical representation of the chemical reaction and structure of the final product for the synthesis of PtCA₃1Glc.



Spectrum 4: ¹H NMR of PtCA₃1Glc in CD₃OD (600 MHz)



Spectrum 5: ¹⁹F NMR of PtCA₃1Glc in CD₃OD (300 MHz)



Spectrum 6: ^{13}C NMR of PtCA₃1Glc in CD₃OD (600 MHz)

PtCA₃2Glc was synthesized likewise using the mono-glycosylated Pt2Glc₂ (0.69 mg, 500 nmoles) obtaining 0.282 mg, **yield 35.18%**. Purity (HPLC): >99%.

3.3.5. Chemical synthesis, NMR and MS of Pt1Glc₂ (trans)

PtTFPP (15 mg, 12.85 μmol) was dissolved in 9 mL of DMF, mixed with thio-glucose sodium salt (5.61 mg, 25.7 μmol) in 3.85 mL of MeOH, in the presence of TEA (17.9 μL , 128.5 μmol), incubated for 2 h at 40 °C. The reaction was quenched using TFA, and followed by preparative RP-HPLC purification (4.23 mg, **yield 21.7%**)(Figure 3.8).

Purity (HPLC): >99%. QToF mass spectrometry: m/z for C₅₆H₂₉F₁₈N₄O₁₀PtS₂⁻ ([M - 1H]⁻) caclcd 1518.0691, found 1518.0786. **^1H NMR** ((CD₃)₂CO, 300 MHz, (CH₃)₂OD = 2.07 ppm): δ ppm = 3.47-3.65 (8H, m, 4'2'3'5'-GlcH), 3.76 (2H, dd, J_{1,2} = 11.8, 6.7, 6'a-GlcH), 4.02 (2H, dd, J_{1,2} = 11.64, 2.17, 6'b-GlcH), 5.24 (2H, d, J = 8.7 Hz, 1'-GlcH), 9.21-9.32, (8H, m, β -pyrroleH). **^{19}F NMR** ((CD₃)₂CO, 300 MHz): δ ppm = -134.2,-134.4 (4F, m, meta- 3,5-PhFGlc), -135.95 (4F, dd, J_{1,2}=22.6, 7.15, ortho- 2,6-PhFGlc), -140.3,-140.47 (4F, m, meta- 3,5-PhF), -155.3 (2F, t, J = 19.75, para- 4-PhF), -164.2,-164.4 (4F, m, ortho- 2,6-PhF). UV-Vis (c = 5 μM , DMF, path length = 1 cm, 25 °C): $\lambda(\text{nm})$ = 391

(1.4), 538 (0.12), 505 (0.1). FL ($c = 0.25 \mu\text{M}$ in DMF, path length = 1 cm, $\lambda_{\text{ex}} = 400 \text{ nm}$, $25 \text{ }^\circ\text{C}$): $\lambda(\text{nm}) = 649$.

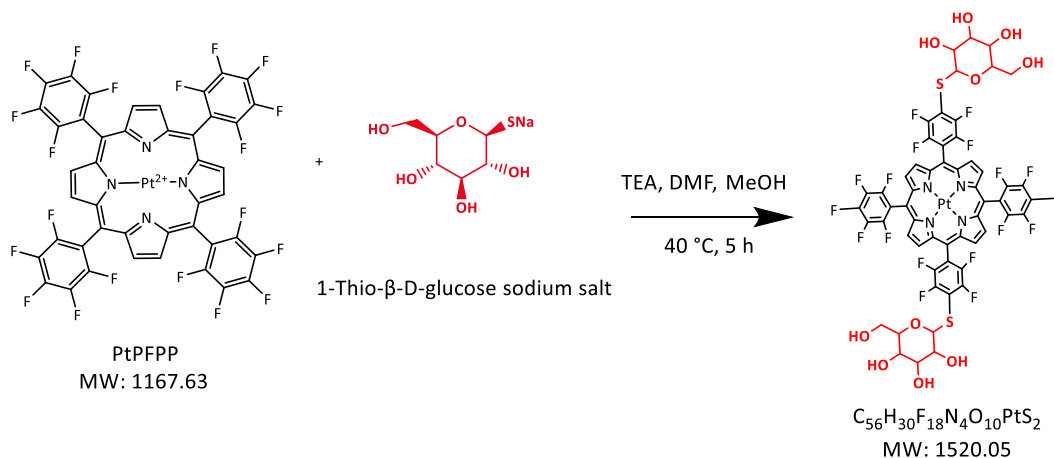


Figure 3.8: Graphical representation of the chemical reaction and structure of the final product for the synthesis of Pt1Glc₂ (trans).

¹H and ¹⁹F NMR can be found in the appendix (Spectrum S4, S5).

3.3.6. Chemical synthesis, NMR and MS of PtmPEG₂1Glc₂ (trans)

Pt1Glc₂ (trans) (8.64 mg, 5.7 μmol) was dissolved in 1.9 mL of DMF, mixed with methyl-thiol-PEG (10.13 mg, 28.4 μmol), in the presence of TEA (7.9 μL , 57 μmol), incubated overnight at 40 $^\circ\text{C}$. The reaction was quenched using TFA and followed by preparative RP-HPLC purification (6.14 mg, yield **49.12%**) (Figure 3.9). **Purity (HPLC): >99%**. QToF mass spectrometry: m/z for $\text{C}_{86}\text{H}_{90}\text{F}_{16}\text{N}_4\text{O}_{28}\text{PtS}_4^{2-}$ ($[\text{M} - 2\text{H}]^{2-}$) *calcld* 1094.7116, *found* 1095.3245. **¹H NMR** (CD_3OD , 600 MHz, ($\text{CH}_3\text{OD} = 3.33 \text{ ppm}$): $\delta(\text{ppm}) = 3.16$ (6H, s, CH_3), 3.25-3.3 (22H, m, $\text{O}-(\text{CH}_2)_{11}$), 3.39-3.71 (38H, m, $\text{O}-(\text{CH}_2)_{15}$ and 2',3',4',5'-GlcH), 3.77 (2H, dd, $J_{1,2} = 12.02$, 6.46, 6'a-GlcH), 3.93 (4H, t, $J = 5.85$, $\text{CH}_2\text{CH}_2\text{S}$ -), 4.01 (2H, dd, $J_{1,2} = 11.82$, 2.0 Hz, 6'b-GlcH), 5.2 (2H, t, $J = 4.6 \text{ Hz}$, 1'-GlcH), 9.09-9.13 (8H, m, β -pyrroleH). **¹⁹F NMR** (CD_3OD , 400 MHz): $\delta \text{ ppm} = -134.8$, -134.9 (4F, m, meta- 3,5-PhFGlc), -135.74 (4F, dd, $J_{1,2} = 24.71$, 11.78, meta- 3,5-PhFPEG) -140.3,-140.55 (8F, m, ortho- 2,6-PhFGlc and 2,6-PhFPEG). **¹³C NMR** (CD_3OD , 600 MHz, $\text{CH}_3\text{OH} = 47.6$): $\delta(\text{ppm}) = 34.2$ (S- CH_2), 57.5 (CH_3), 61.7 (6'-GlcC), 69.6-70.3 (PEG-C chain), 71.0 (4'-GlcC), 71.24 ($\text{CH}_3\text{O}-\text{CH}_2$), 74.6 (2'-GlcC), 78.34 (3'-GlcC), 81.4 (5'-GlcC), 85.27 (1'-GlcC), 107.2 (mesoC), 113.84-119.47 (1-PhC and 4-PhC), 131.3 (β -

pyrroleC), 141.2 (α -pyrroleC), 145.3-148.02 (3,5-PhC and 2,6-PhC). UV-Vis (c = 5 μ M, DMF, path length = 1 cm, 25 $^{\circ}$ C): λ (nm) = 393 (1.19), 538 (0.12), 506 (0.12). FL (c = 0.25 μ M in DMF, path length = 1 cm, λ_{ex} = 400 nm, 25 $^{\circ}$ C): λ (nm) = 650.

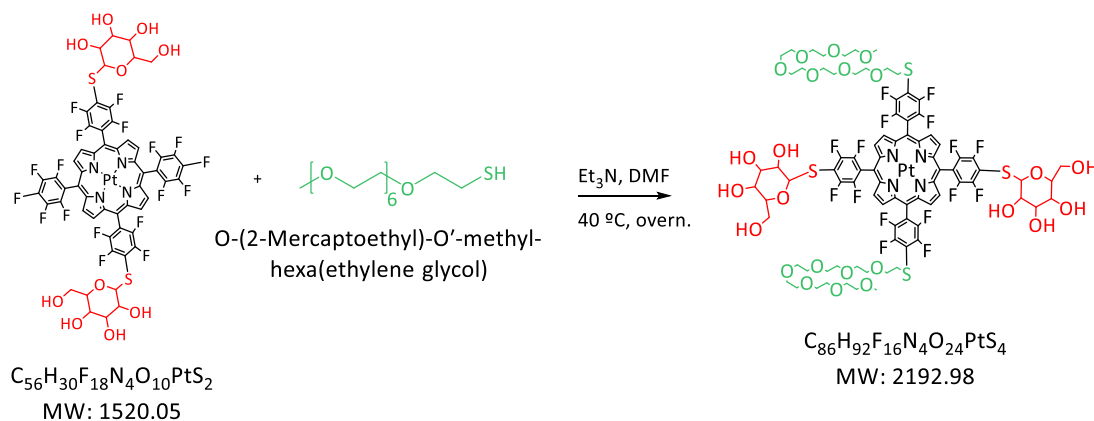
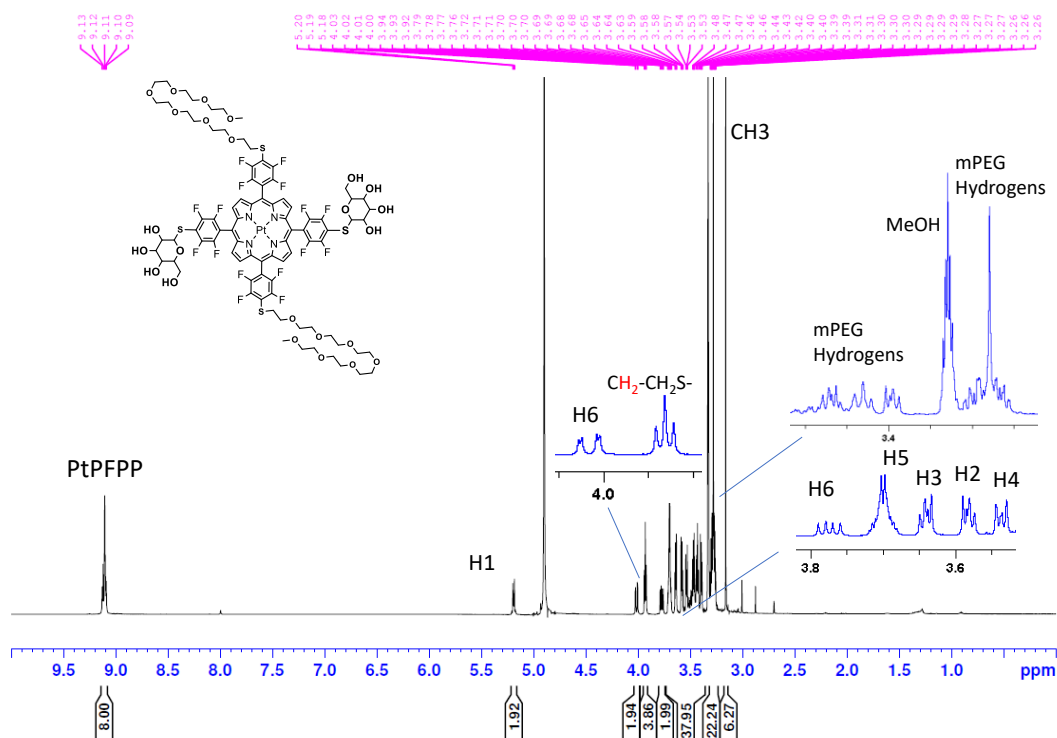
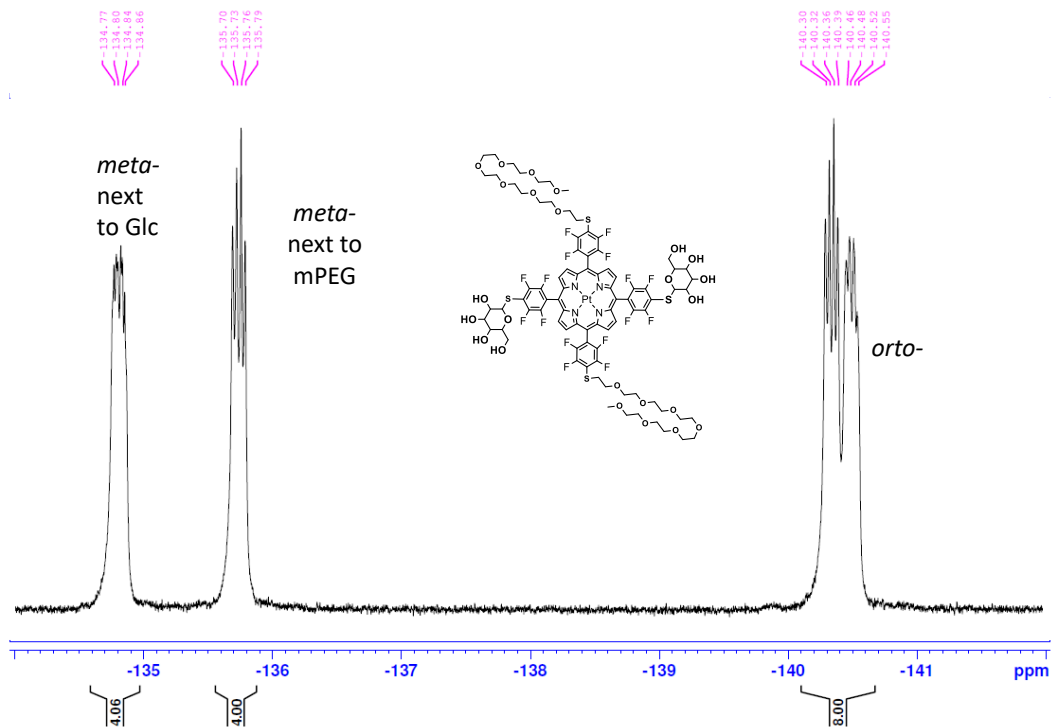


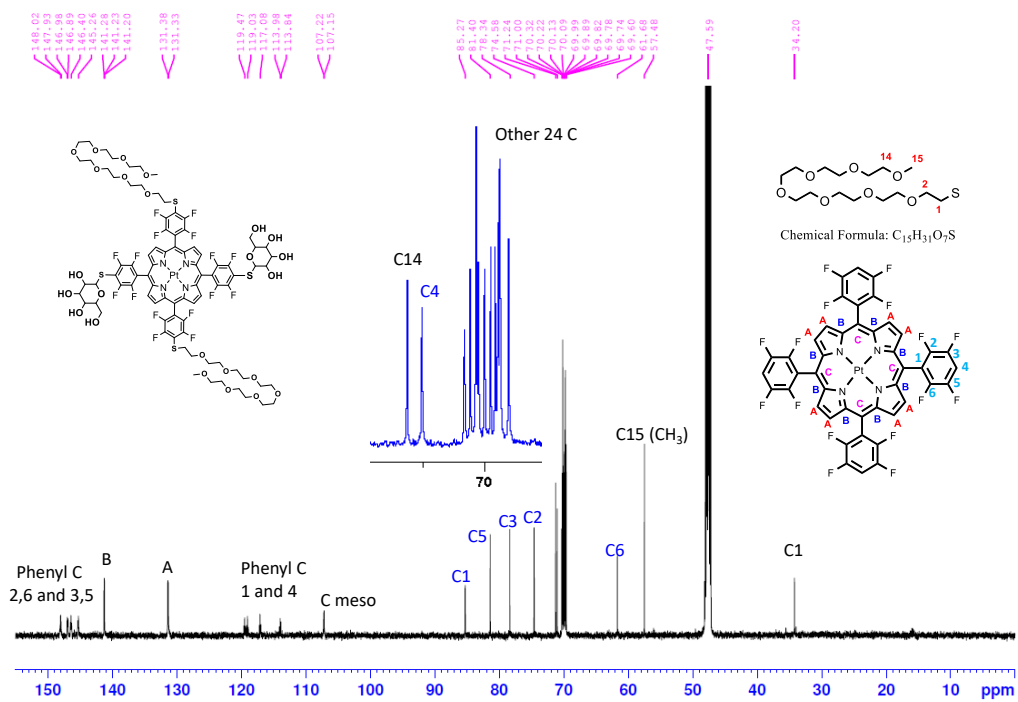
Figure 3.9: Graphical representation of the chemical reaction and structure of the final product for the synthesis of PtMPEG₂1Glc₂ (trans).



Spectrum 7: 1 H NMR of PtMPEG₂1Glc₂ (trans) in CD₃OD (600 MHz)



Spectrum 8: ^{19}F NMR of Pt(PEG)₂Glc₂ (trans) in CD₃OD (300 MHz)



Spectrum 9: ^{13}C NMR of Pt(PEG)₂Glc₂ (trans) in CD₃OD (600 MHz)

3.3.7. Chemical synthesis, NMR and MS of Pt1Glc₄

PtTFPP (8 mg, 6.85 μmol) was dissolved in 1.96 mL of DMF, mixed with thioglucose sodium salt 1Glc-S⁻Na⁺ (10.46 mg, 5 μmol) in 0.6 mL of MeOH containing TEA (9.5 μL, 68.5 μmol), incubated for 3 h at 40 °C, followed by RP-HPLC purification (10.85 mg, **yield 84.59%**) (Figure 3.10). **Purity (HPLC): 93.3%**. QToF mass spectrometry: m/z for C₆₈H₅₁F₁₆N₄O₂₀PtS₄⁻ ([M-1H]⁻) caclcd 1870.1377, found 1870.2705. **¹H NMR** ((CD₃)₂CO, 600 MHz, (CH₃)₂CO=2.07 ppm) δ ppm = 3.48-4.51 (4H, m, 4'-GlcH), 3.55-3.63 (12H, m, 2'3'5'-GlcH), 3.77 (4H, dd, J_{1,2}=11.66, 6.51, 6'-GlcH), 4.03 (4H, dd, J_{1,2}= 11.87, 2.42, 6'b-GlcH), 5.23 (4H, d, J = 8.78 Hz, 1'-GlcH), 9.24, (8H, s, β-pyrroleH). **¹⁹F NMR** (CD₃OD, 300 MHz) δ ppm = -134.86 (8F, dd, J_{1,2}= 24.89, 11.73, *meta*- 3,5- PhFGlc), -140.52 (8F, dd, J_{1,2}=24.61, 11.73, *ortho*- 2,6-PhFGlc). **¹³C NMR** ((CD₃)₂CO, 600 MHz, (CD₃)₂CO=28.96, 205.45 ppm) δ ppm = 62.3 (6'-GlcC), 70.9 (4'-GlcC), 75.06 (2'-GlcC), 78.8 (3'-GlcC), 81.53 (5'-GlcC), 84.82 (1'-GlcC), 107.35 (mesoC), 113.99 (1-PhC), 119.4 (4-PhC), 131.9 (β-pyrroleC), 141.28 (α-pyrroleC), 145.26-148.4 (3,5-PhC and 2,6-PhC). UV-vis (DMF, path length = 1cm, 25°C): λ(nm) = 393, 538, 506. PL (c = 0.2μM, DMF, path length = 1.0 cm, λ_{ex} = 390 nm, 25 °C): λ(nm) = 650, 707.

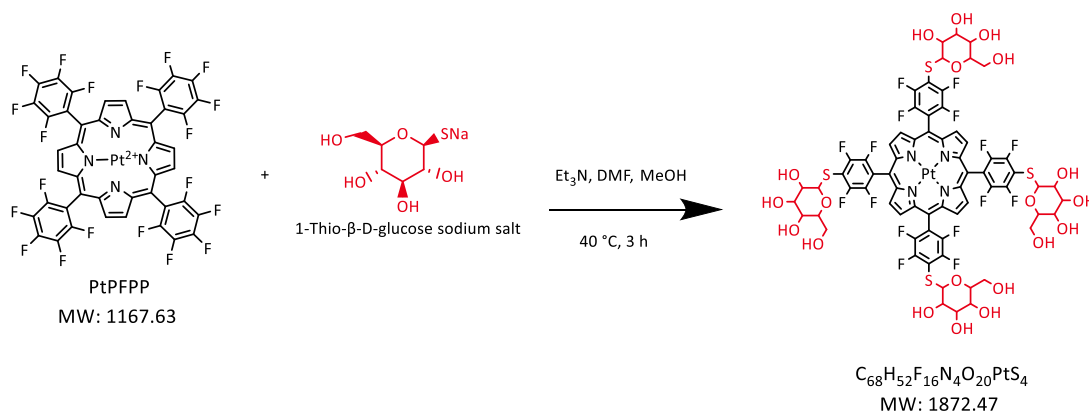
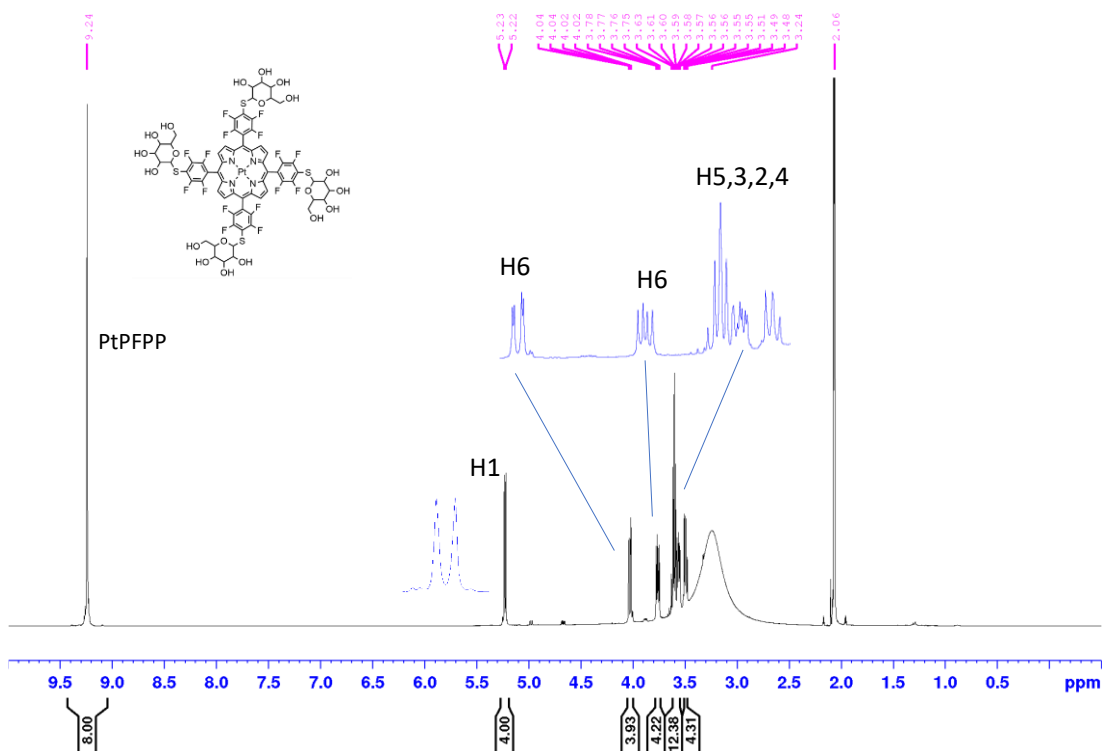
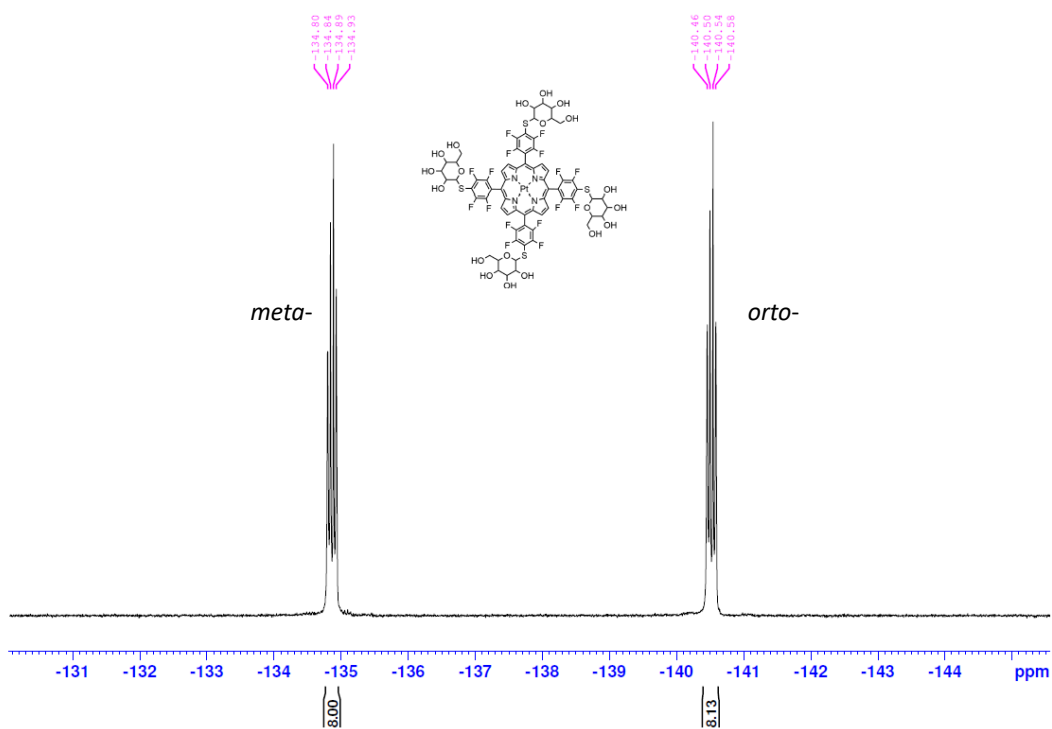


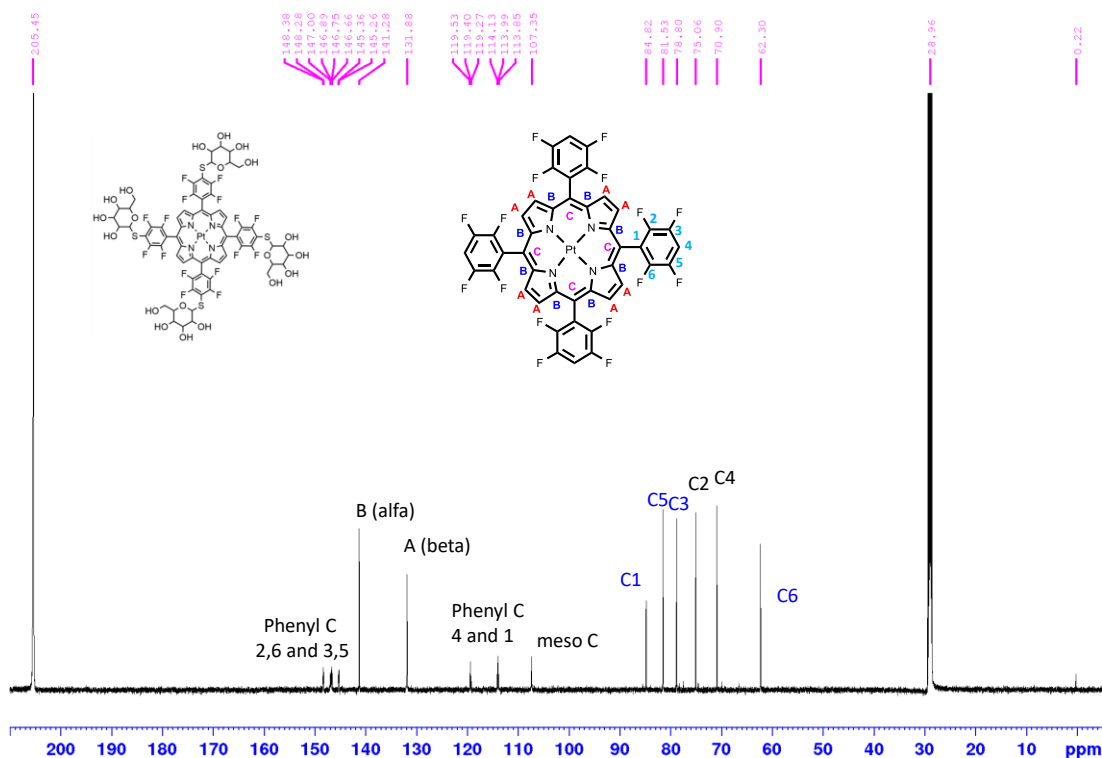
Figure 3.10: Graphical representation of the chemical reaction and structure of the final product for the synthesis of Pt1Glc₄.



Spectrum 10: ^1H NMR of Pt1Glc₄ in (CD₃)₂CO (600 MHz)



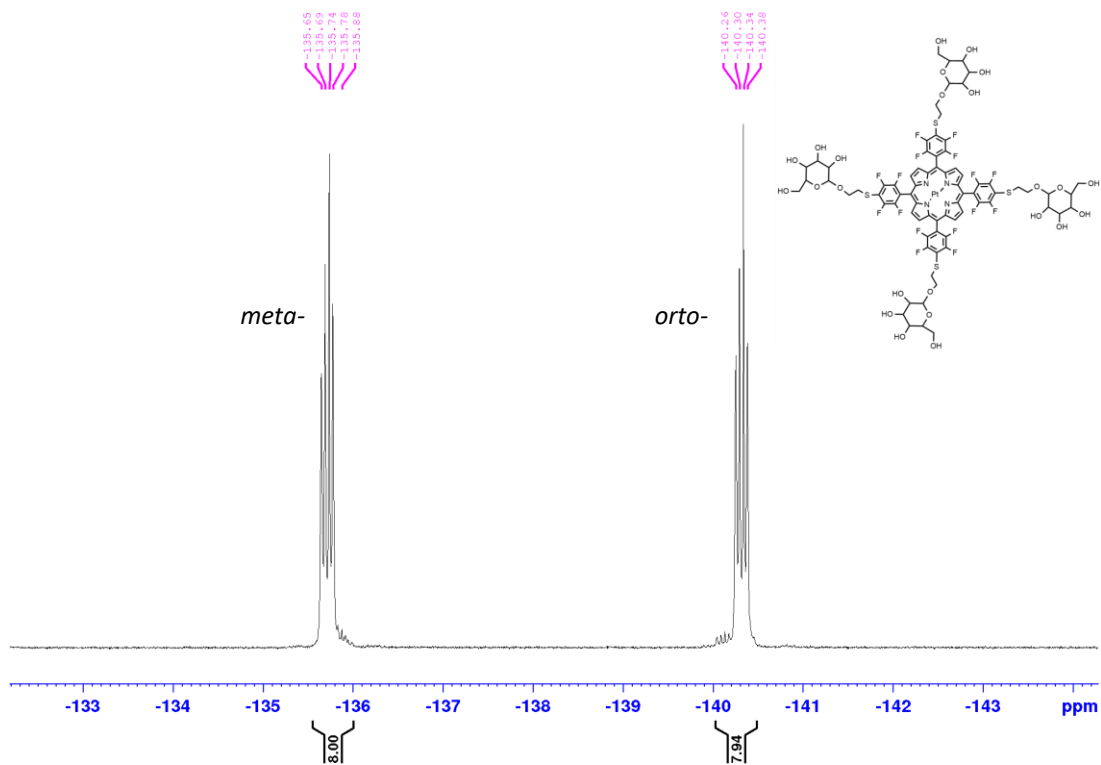
Spectrum 11: ^{19}F NMR of Pt1Glc₄ in (CD₃)₂CO (300 MHz)



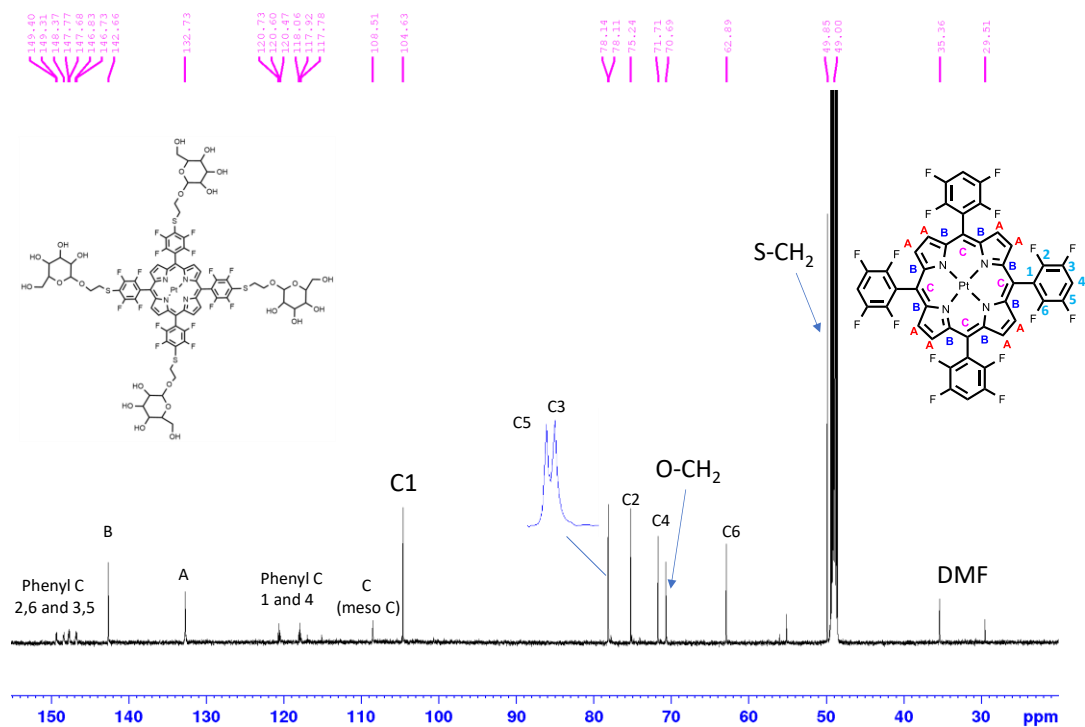
Spectrum 12: ^{13}C NMR of Pt1Glc₄ in (CD₃)₂CO (600 MHz)

3.3.8. Chemical synthesis, NMR and MS of Pt2Glc₄

PtTFPP (6mg, 5.2 μmol) dissolved in 1 mL of DMF was mixed with the thio-glucose 2Glc-SH (10 mg, 41.62 μmol) in 0.480 mL of MeOH containing TEA (7.25 μl , 52 μmol), incubated overnight at 40°C, then purified by RP-HPLC (9.39 mg, yield **88.63%**). **Purity (HPLC): 96.8%**. QToF mass spectrometry: m/z for C₇₆H₆₆F₁₆N₄O₂₄PtS₄²⁻ ([M-2H]²⁻) calcd 1023.11354, found 1023.1216. **^1H NMR** (CD₃OD, 300 MHz, CHD₂OD = 3.33 ppm) δ ppm = 3.28- 3.5 (16H, m, 4',2',3',5'-GlcH), 3.54 (2H, t, J=6.4, SCH₂CH₂-Glc), 3.75 (4H, dd, J_{1,2}=11.81, 5.25 Hz, 6'-GlcH), 3.94-3.98 (4H, m, 6'-GlcH), 4.08 (4H, dt, J =17.1, 6.42 Hz, SCH₂CH₂-Glc), 4.33 (4H, dt, J = 16.9, 6.42 Hz, SCH₂CH₂-Glc), 4.47 (4H, d, J=7.73 Hz, 1'-GlcH), 9.1 (8H, s, β -pyrroleH). **^{19}F NMR** (CD₃OD, 300 MHz) δ ppm = -135.71 (8F, dd, J_{1,2}= 24.32, 11.52, *meta*- 3,5-PhFGlc), -140.32 (8F, dd, J_{1,2}=24.61, 11.73, *ortho*-2,6-PhFGlc). **^{13}C NMR** (CD₃OD, 600 MHz, CD₃OD=49.0 ppm) δ ppm = 49.85 (S-CH₂), 62.89 (6'-GlcC), 70.69 (S-CH₂CH₂), 71.71 (4'-Glc-C), 75.24 (2'-Glc-C), 78.11 (3'-GlcC), 78.14 (5'-GlcC), 104.63 (1'-GlcC), 108.51 (mesoC), 117.92 (1-PhC), 120.6 (4-PhC), 132.73 (β -pyrroleC), 142.66 (α -pyrroleC), 146.73-149.4 (3,5-PhC and 2,6-PhC). UV-



Spectrum 14: ^{19}F NMR of Pt_2Glc_4 in CD_3OD (300 MHz)



Spectrum 15: ^{13}C NMR of Pt_2Glc_4 in CD_3OD (600 MHz)

3.3.9. Chemical synthesis, NMR and MS of PtcPEG₄

PtTFPP (0.585 mg, 500 nmol) dissolved in 1.5 mL of DMF was mixed with cPEG7-SH (2.3 mg, 5 μ mol), or mPEG7-SH (1.78 mg, 5 μ mol), in presence of TEA (1.63 μ L, 10 μ moles), and incubated 5 h at 40 °C, then purified by RP-HPLC (1.39mg, yield 95.4%).

Purity (HPLC): 94.9%. QToF mass spectrometry: m/z for C₁₂₀H₁₅₄F₁₆N₄O₄₀PtS₄²⁻ ([M - 2H]²⁻) caclcd 1459.4229, found 1459.1919. **¹H NMR** (600 MHz, (CDCl₃, CHCl₃ = 7.2 ppm) δ ppm = 2.5 (8H, t, J=6.12 Hz, CH₂-COOH), 3.38 (8H, t, J=5.96 Hz, S-CH₂), 3.5-3.7 (120H, m, O-(CH₂)₆₀), 3.87 (8H, t, J=5.95, SCH₂-CH₂), 8.79 (8H, s, β -pyrroleH). **¹⁹F NMR** (300 MHz, CDCl₃) δ ppm = -133.54 (8F, dd, J_{1,2}= 25.22, 12.03, *meta*- 3,5-PhF-PEG), -137.06 (8F, dd, J_{1,2}=24.65, 11.75, *ortho*- 2,6-PhF-PEG). **¹³C NMR** (600 MHz, CDCl₃, CHCl₃ =77.04) δ ppm = 34.42 (S-CH₂), 34.98 (COOH-CH₂), 66.52 (COOH-CH₂CH₂), 70.21 (S-CH₂CH₂), 70.21-70.74 (PEG-C chain), 107.15 (mesoC), 116.82 (1-PhC), 129.3 (4-PhC), 131.15 (β - pyrroleC), 141 (α -pyrroleC), 145.14-147.59 (3,5-PhC and 2,6-PhC), 174.33 (-C=OOH). UV-vis (DMF, path length = 1.0 cm, 25°C): λ (nm) = 393, 538, 506. PL (c = 0.2 μ M, DMF, path length = 1.0 cm, λ_{ex} = 390 nm, 25 °C): λ (nm) = 651, 701.

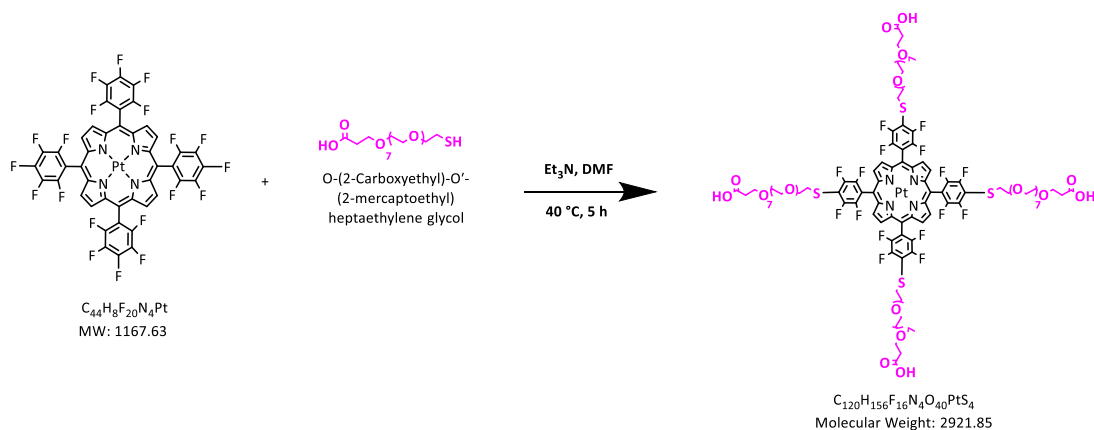
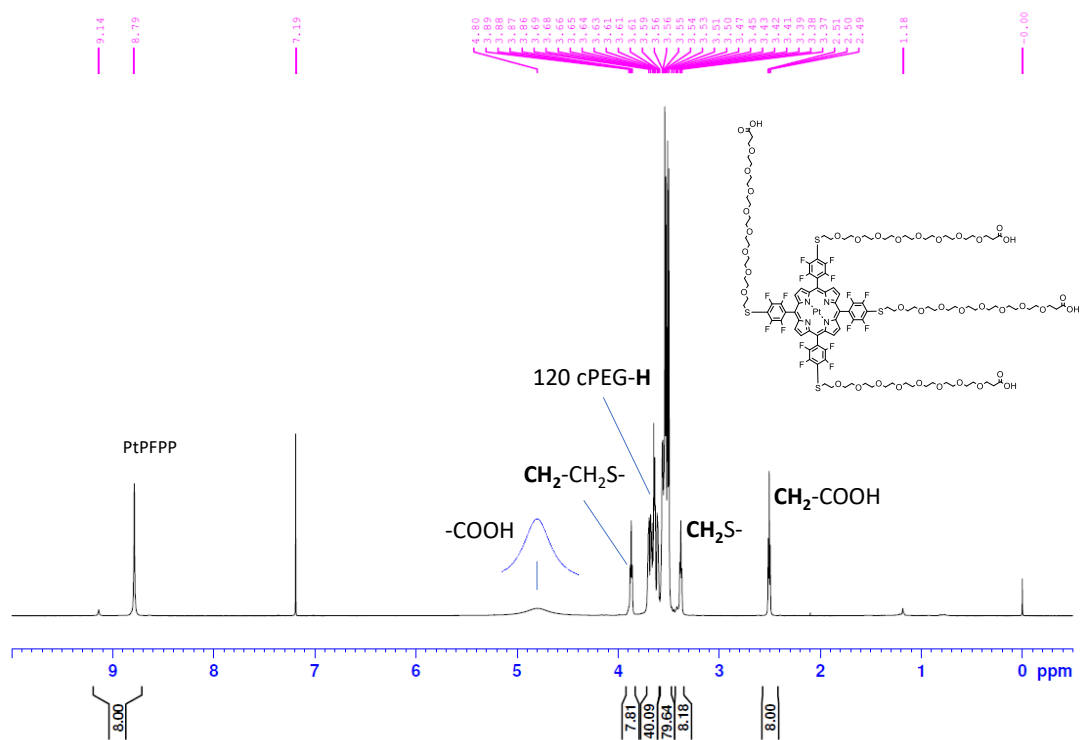
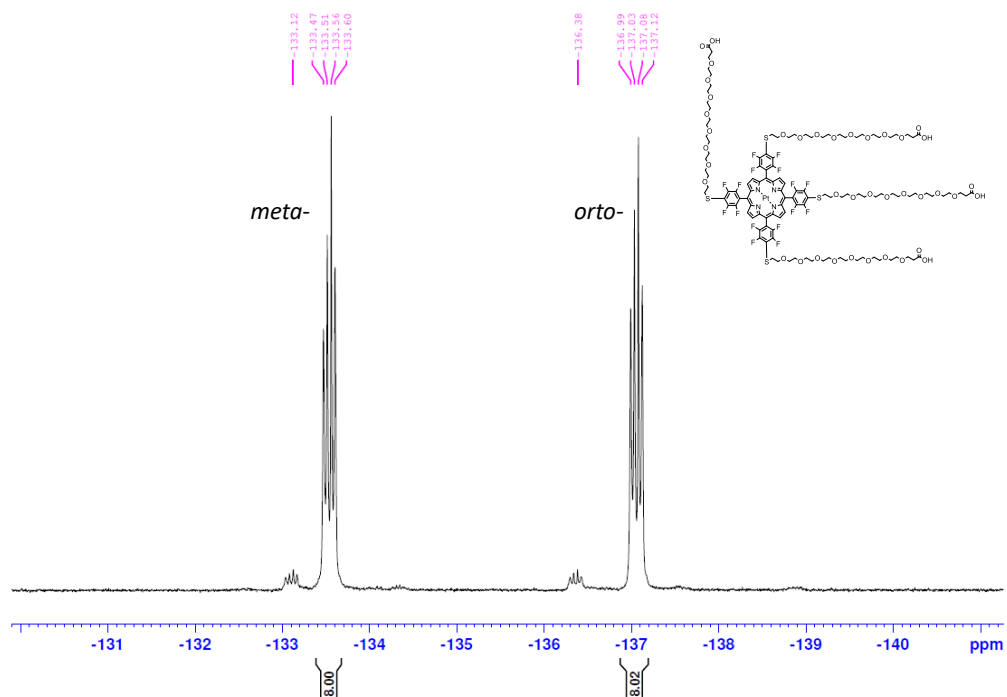


Figure 3.11: Graphical representation of the chemical reaction mixture and structure of the final product for the synthesis of PtcPEG₄



Spectrum 16: ¹H NMR PtcPEG₄ in CDCl₃ (600 MHz)



Spectrum 17: ¹⁹F NMR PtcPEG₄ in CDCl₃ (300 MHz)

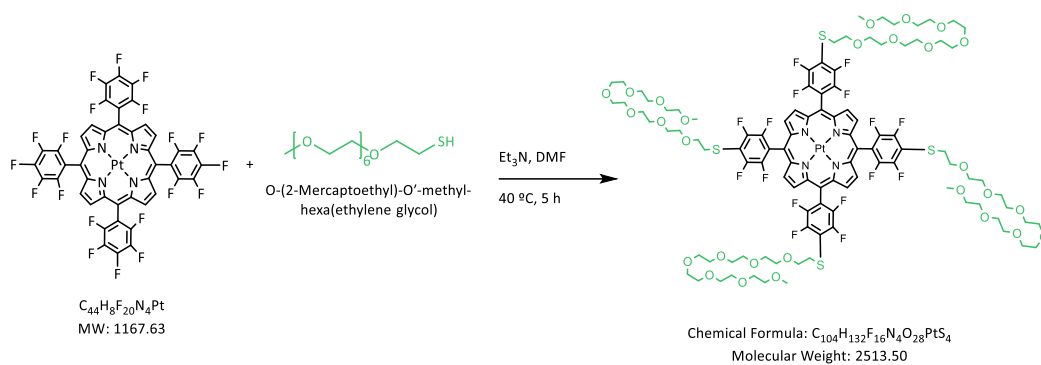
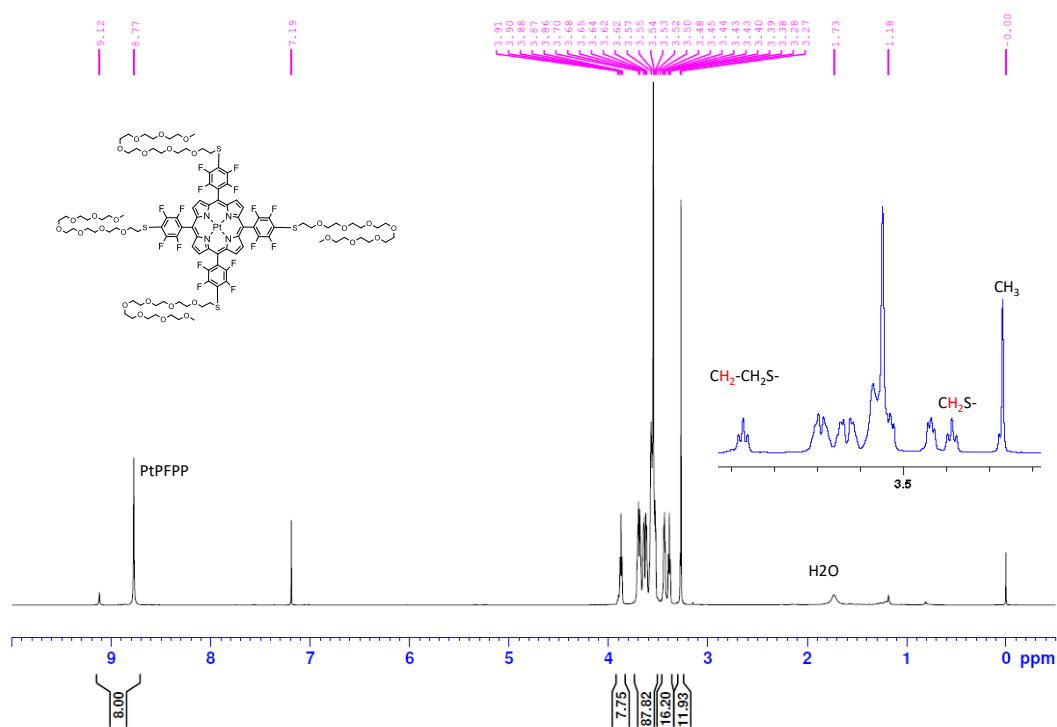
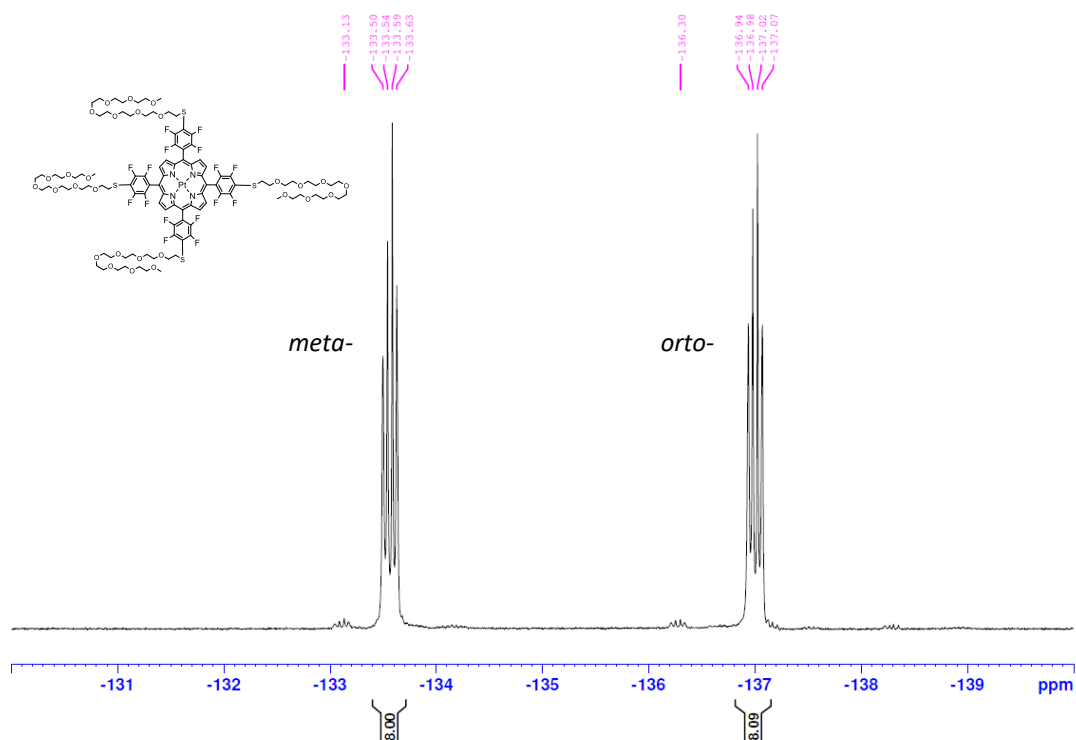


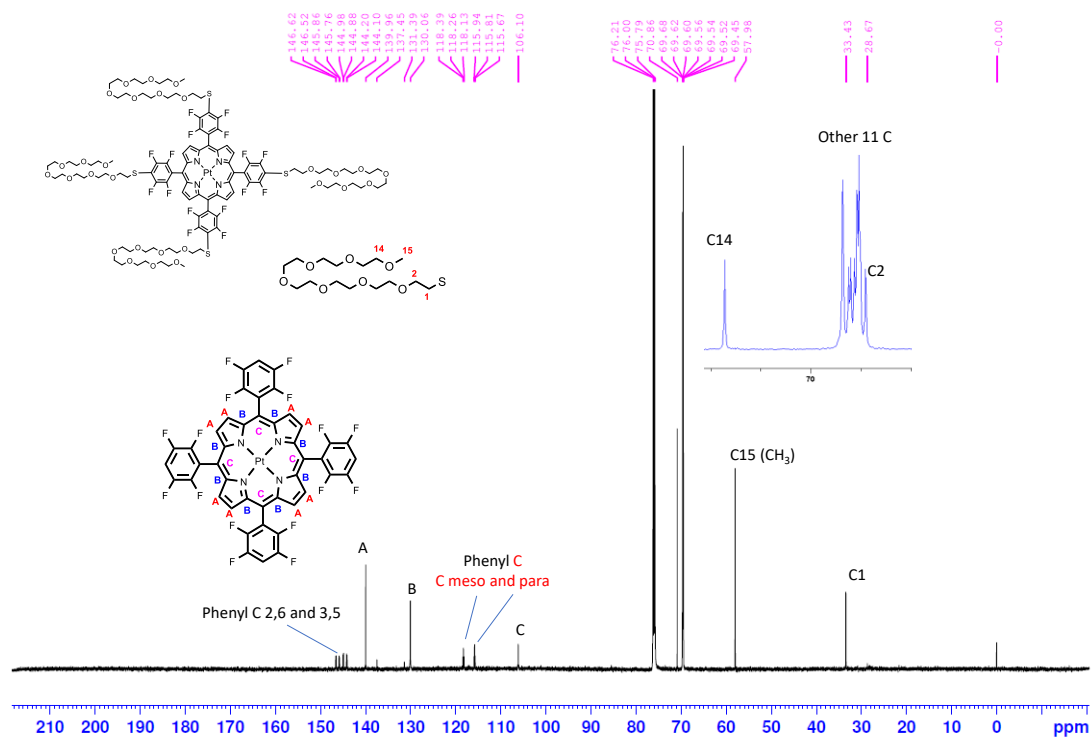
Figure 3.12: Graphical representation of the chemical reaction and structure of the final product for the synthesis of PtmPEG₄.



Spectrum 19: 1H NMR PtmPEG₄ in $CDCl_3$ (600 MHz)



Spectrum 20: ¹⁹F NMR PtMPEG₄ in CDCl₃ (300 MHz)



Spectrum 21: ¹³C NMR PtMPEG₄ in CDCl₃ (600 MHz)

When necessary, the residual TFA salt was subsequently removed by incubating the final product with an equivalent amount of HCl in methanol for 30 min at RT. The

chemical structure and purity of all these new compounds were confirmed by RP-HPLC, HR-MS, and ^1H , ^{19}F , and ^{13}C NMR spectra (Figure 3.8 and 3.9). The synthetic reaction was monitored by analytical RP-HPLC (Figure 3.4), and fractions of interest were purified by preparative RP-HPLC (see methods). Their main characteristics are summarized in Table 4. Mass spectra can be found in the S.I of (256).

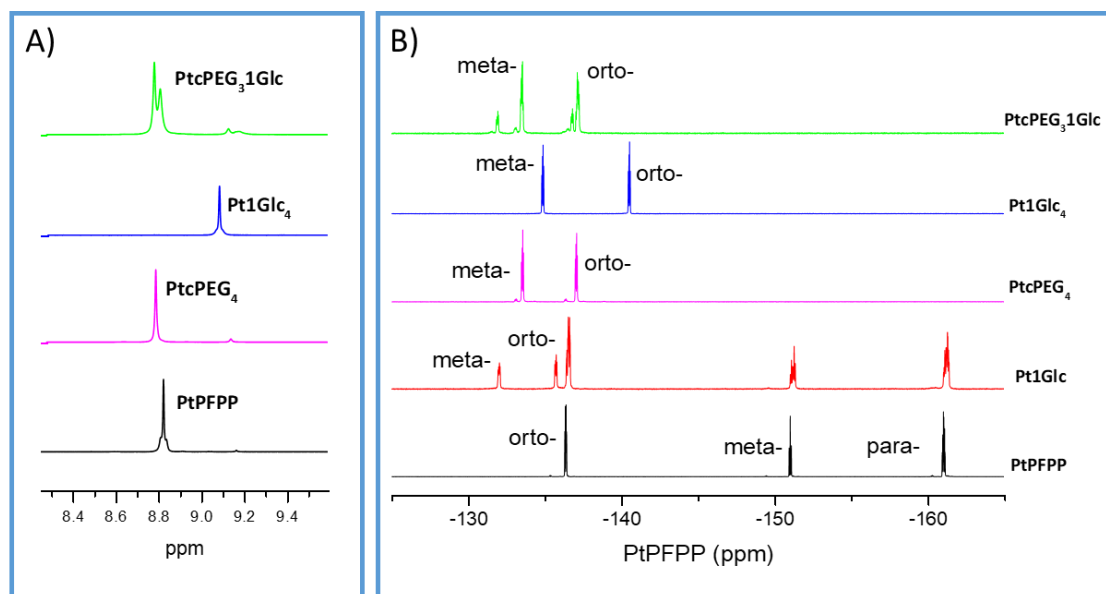


Figure 3.8: Effects of the symmetric or asymmetric substitution on the PtPFPP ^1H peak splitting pattern (A) and on the ^{19}F pattern (B).

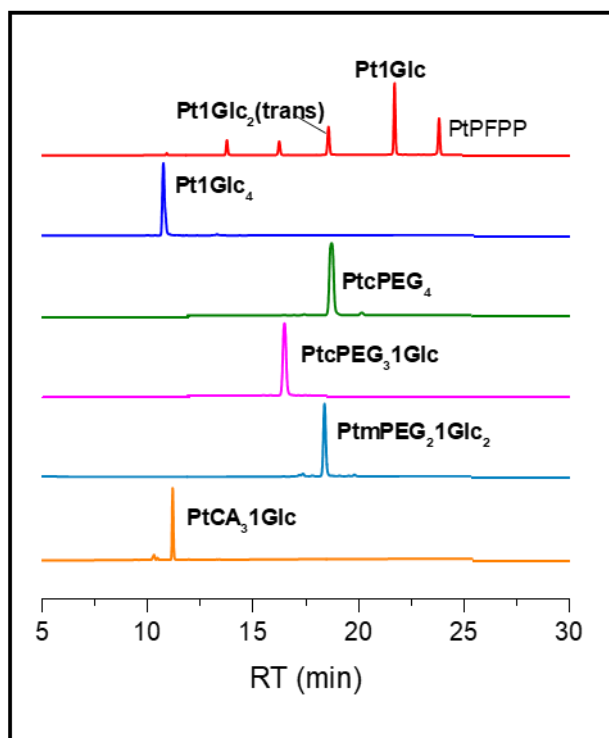


Figure 3.9: Comparison of the retention times (RT) of some of the derivatives and RP-HPLC chromatogram of the reaction mixtures at the end of each synthetic reaction (40 min gradient 0 → 100% of acetonitrile in aqueous 0.1% TFA)

Table 4. List of the newly synthesized PtPFPP derivatives and their physical characteristics

Conjugate	Yield	Mol Charge	MW g/mol	RT min
Pt1Glc₄	84.59%	0	1872.47	10.8
Pt2Glc₄	88.63%	0	2048.68	14.0
PtcPEG₄	95.4%	- 4	2921.85	18.8
PtmPEG₄	81.76%	0	2513.50	20.9
PtcPEG₃1Glc	97.5%	- 3	2659.51	16.6
PtmPEG₃1Glc	65.15%	0	2353.24	18.7
PtcPEG ₃ 2Glc	93.9%	- 3	2703.56	16.8
PtmPEG ₃ 2Glc	71.76%	0	2397.29	19.6
PtCA₃1Glc	36.8%	+ 3	1557.34	11.2
PtCA ₃ 2Glc	35.18%	+ 3	1601.39	13.2
Pt1Glc ₂ (trans)	23.71%	0	1520.05	20.9
PtmPEG₂1Glc₂ (trans)	49.12%	0	2192.98	18.4

Notes: retention time (RT) is based on 40 min gradient 0 → 100% of acetonitrile in aqueous 0.1% TFA and a flow rate of 0.63 mL/min on a YMC-Actus Triart C18, 150 × 4.5 mm I.D. RP column (YMC). The fully characterized derivatives which were selected for cell culture testing are highlighted in bold.

3.4. Photophysical and O₂-Sensing Properties of the new compounds

The newly synthesized compounds (Table 4) were subjected to spectroscopic, photophysical, and O₂-sensing characterization in aqueous media that model the physiological environment. Absorption and emission spectra, phosphorescence lifetimes, and specific brightness (phosphorescent emission normalized to the absorption) were measured for each compound in different buffers without and with protein addition (5% fetal bovine serum (FBS)), in air-saturated and deoxygenated conditions (addition of Sulfite (S) solution: 5 mg/mL KH₂PO₄, 5 mg/mL Na₂SO₃). Protein and surfactant additives are known to prevent aggregation of porphyrins in aqueous solutions and influence their self-quenching and quenching by O₂ (254). After the initial assessment of solubility, photochemistry, and testing on cultured cells, we focused on 7 of the 10 new structures that were deemed promising for sensing applications. Their characteristics are presented in Table 5 and Figure 3.10 and Figure S1 (appendix).

In our case, all of the new conjugates in DMF exerted the typical UV–vis absorbance spectra of PtPFPP, with a prominent peak at 393 nm (Soret band) and two small Q bands in the 500–550 nm region (Figure 3.10 A and S1 of the appendix). This small shift of the Soret band is likely due to altered electronic distribution by the conjugation. At the same time, broadened absorption and emission bands were observed in aqueous media, caused by partial aggregation and stacking, which were reduced after the addition of serum (273, 274). As described, tri- and tetra-PEGylation of porphyrin compounds, while decreasing hydrophobicity, also increases the tendency of aggregation in aqueous solutions (254).

Table 5. Photophysical characteristics of the derivatives synthesized in the study

Conjugate	ϵ_{DMF} $\text{M}^{-1}\text{cm}^{-1}$	Buffer	Abs (λ_{max}) [$3\mu\text{M}$]	Ip (λ_{max}) [$0.5\mu\text{M}$]	Ip/Abs [$0.5\mu\text{M}$]	LT (μs) 37°C	Relative QY Φ
PtPFPP	257,000 (395) *	PBS+1%TX-100 PBS+1%TX- 100+S	/	/	1593.3 16937.3	60 (CH_2Cl_2) **	0.088 (CH_2Cl_2) **
Pt1Glc ₄	227,130 (393)	PBS PBS+Sulfite PBS+5%FBS PBS+5%FBS+S	***	56.17 (657) 71.93 (656) 829.34 (650) 1353.82 (652)	956.2 1528.5 9261.4 17685.1	9.14 30.75 15.48 37.34	0.0050 0.0079 0.0481 0.0919
Pt2Glc ₄	256,187 (393)	PBS PBS+Sulfite PBS+5%FBS PBS+5%FBS+S	0.32 (404) / 0.36 (400) /	22.51 (658) 26.8 (657) 126.7 (653) 546.9 (652)	691.7 1209.2 2184.4 8312.2	9.15 20.15 14.34 36.72	0.0036 0.0063 0.0113 0.0432
PtcPEG ₄	291,143 (393)	PBS PBS+Sulfite PBS+5%FBS PBS+5%FBS+S	0.28 (392) / 0.31 (396) /	35.81 (653) 90.5 (653) 288.48 (651) 559.64 (651)	705.6 2152.9 4878.6 11599.4	8.08 25.94 11.75 36.1	0.0037 0.0112 0.0253 0.0603
PtmPEG ₄ [2.5 - 0.25 μM]	280,000 (393)	PBS PBS+Sulfite PBS+5%FBS PBS+5%FBS+S	0.23 (408) / 0.26 (406) /	29.88 (651) 23.04 (652) 50.75 (653) 119.27 (651)	NA	7.56 28.06 11.34 39.94	NA
PtcPEG ₃ 1Glc	222,427 (393)	PBS PBS+Sulfite PBS+5%FBS PBS+5%FBS+S	0.4 (392) / 0.54 (396) /	44.05 (652) 91.70 (651) 486.44 (651) 747.7 (650)	546.8 1320.3 4904.5 8379.4	8.19 31.01 11.7 34.67	0.0028 0.0069 0.0255 0.0435
PtmPEG ₃ 1Glc [2.5 - 0.25 μM]	232,000 (393)	PBS PBS+Sulfite PBS+5%FBS PBS+5%FBS+S	0.22 (407) / 0.23 (403) /	32.51 (652) 32.34 (651) 40.04 (655) 95.74 (651)	NA	8.27 29.07 12.45 38.53	NA
PtCA ₃ 1Glc	230,710 (393)	PBS PBS+Sulfite PBS+5%FBS PBS+5%FBS+S	0.34 (395) / 0.44 (395) /	15.34 (656) 24.59 (661) 229.05 (651) 506.33 (652)	250.1 443.3 3025.5 6399.4	10.96 34.8 16.57 38.6	0.0013 0.0023 0.0157 0.0332
PtmPEG ₂ 1Glc ₂ (trans) [5 - 0.25 μM]	222,252 (393)	PBS PBS + Sulfite PBS + 5%FBS PBS + 5%FBS + S	0.33 (401) / 0.59 (396) /	35.4 (652) 49.3 (652) 275.4 (651) 468.1 (651)	3763.9 5729 6525.1 11842.6	7.04 15.31 16.83 43.97	NA

Notes: PBS = Phosphate Buffer Saline. FBS = Fetal Bovine Serum. S = 10% of Sulfite (5 mg/mL KH_2PO_4 , 5 mg/mL Na_2SO_3) was added to deoxygenate the buffer and measure corresponding lifetimes values in air saturated and deoxygenated conditions. Molar extinction coefficients (ϵ) were calculated according to the Lambert-Beer Law. Relative Quantum Yields (Φ) were calculated in relation to PtPFPP. Absorption and emission of the reference dye were measured in deoxygenated aqueous media assuming its quantum yield as 0.088. *(275)**(130)*** (160).

Lifetimes recorded in buffered media (PBS) at 37 °C were similar for all the analysed compounds (Table 5), ranging from ~8 to 11 μ s in air saturated conditions, and from ~20 to 35 μ s upon addition of Sulfite (S). Upon addition of 5% FBS, LT values range between ~11 to 16 μ s, and ~36 to 39 μ s in deoxygenated conditions. Slightly lower values were found for the PEG derivatives, while Pt1Glc₄ and CA derivatives showed the longer LT values, reflecting their higher solubility in aqueous media. In PBS with 5% FBS, the brightness of most derivatives increased almost five-fold compared to PBS but still remained considerably lower (~2 fold) than that of Pt1Glc₄ (Figure 3.10 B).

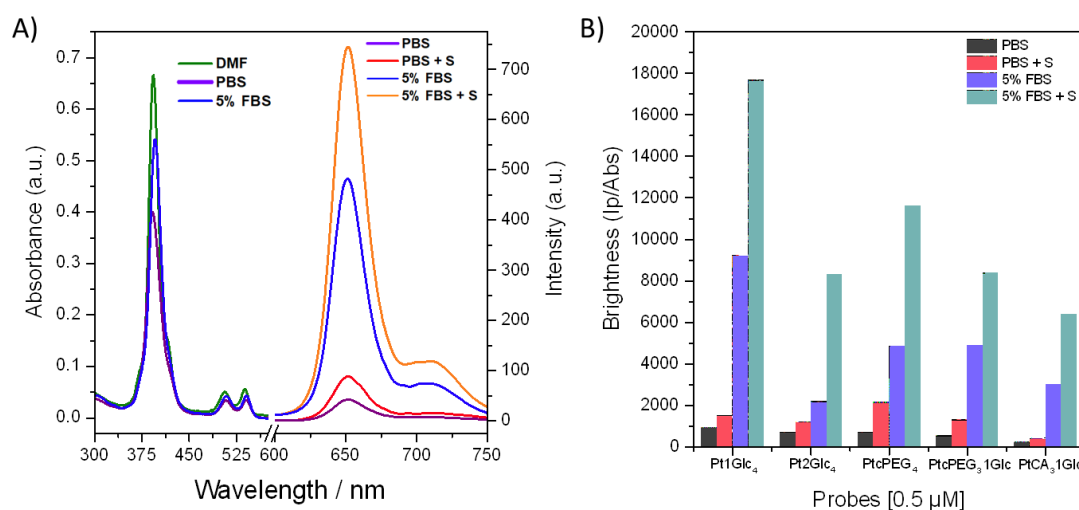


Figure 3.10: (A) Absorption and emission spectra of PtcPEG₃1Glc in the different buffers, under air-saturated or deoxygenated conditions, at 3 μ M and 0.5 μ M, respectively. (B) Relative brightness of selected PtPFPP derivatives in solution, calculated as sample phosphorescence intensity normalized for its absorbance. PBS, phosphate buffer saline; FBS, fetal bovine serum; and PBS+S, PBS with added 5 mg/mL of KH₂PO₄ and 5 mg/mL of Na₂SO₃.

The chosen PEG moieties, although not very long, can potentially interact with the porphyrin core and reduce its brightness compared to the symmetrical Pt1Glc₄, in which the thiol-glucose has less freedom of movement. This can also explain the poor photochemistry of Pt2Glc₄, in which the 2-carbon linker connects the benzene ring with the rest of the glucose moiety.

3.4.1. *trans*-di-substituted derivatives of PtPFPP

Absorption and emission spectra and phosphorescent lifetimes of the new *trans*-hetero-substituted derivative Pt_mPEG₂1Glc₂ (*trans*) (Figure 3.11 A) and its intermediate Pt1Glc₂ (*trans*) (Figure 3.11 B), were measured in different buffers, both in air-saturated and chemically deoxygenated conditions (5 mg/mL KH₂PO₄, 5 mg/mL Na₂SO₃) (Figure 3.11. C, D). The specific values are summarized in Table 5. Similar spectral characteristics to previously described PtPFPP hetero-substituted derivatives were found. As expected, the intermediate Pt1Glc₂ (*trans*) showed marked aggregation in PBS, producing a broad absorption peak at around 400 nm (Figure 3.11.D). A slightly red-shifted absorption (401 nm, in PBS 1% DMSO) was recorded for the *trans*-PEGylated derivative, which could be caused by a rearrangement of the porphyrin forming J-type aggregates (head-to-tail alignment). This feature of substituted porphyrins has been described by Villari et al. (276) for PEGylated uncharged tetrakis(*p*-hydroxyphenyl)porphyrin. Depending on the substituents' position around the porphyrin core, the photo-physical characteristics were influenced, especially their ability to self-assemble into either H-type (face-to-face alignment) or J-type aggregates. The relative brightness of Pt_mPEG₂1Glc₂ (*trans*), in PBS was approximately 6-times higher than that of Pt1Glc₂ (*trans*), and 2,5- times higher upon addition of 5% fetal bovine serum (FBS) (Figure 3.11).

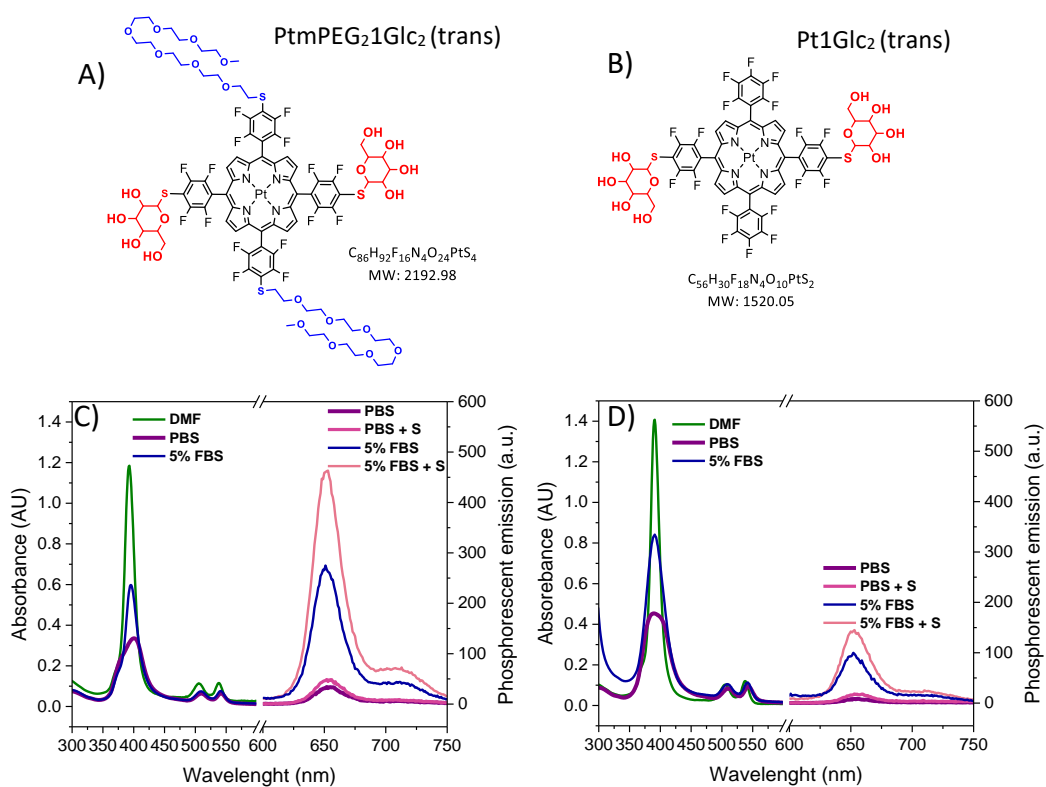


Figure 3.11: Chemical structures of the 2:2 PtPFPP derivative A) PtmPEG₂1Glc₂ (trans) and B) its intermediate Pt1Glc₂ (trans) and their corresponding absorption and emission spectra: C) PtmPEG₂1Glc₂ (trans) and D) its intermediate Pt1Glc₂ (trans) measured at probes concentrations of 5 μ M (Abs) and 0.25 μ M (Emission) respectively, at room temperature.

3.5. Conclusions

An expanded panel of hydrophilic hetero-functionalized derivatives of the PtPFPP dye was synthesized using thiol-click modification, incorporating low molecular weight PEGs or cysteamine (CA), along with one or two glucose moieties. Tetra-PEGylated and Tetra-glucosylated derivatives were also synthesised as benchmarking. The optimization of reaction and purification conditions generated high yields (70–95%) and purities (>90%). The chemical structures were confirmed by NMR and HR-MS. UV-Vis and luminescence spectroscopy revealed typical meso-substituted metalloporphyrin absorption spectra. In aqueous buffer, derivatives showed broad peaks, indicating partial aggregation. In particular, the symmetric trans-di-substituted derivative PtmPEG₂Glc₂ exhibited a red-shifted absorption, suggesting the formation of J-type aggregates. Emission maxima were consistent, and brightness calculations identified Pt1Glc₄ as the brightest probe, attributed to its higher solubility and symmetrical chemical structure.

Chapter 4: Cell staining behaviour of the new derivatives in mammalian cell cultures

4.1. Cellular uptake and toxicity of the 3:1 derivatives

Cell staining efficiency of the new derivatives was initially analysed on Murine Embryonic Fibroblasts (MEF) cells, measuring their phosphorescence intensity signals on a Victor 2 reader in TRF mode. The cells were stained for 3 and 18 h with probe concentrations between 5 μM and 20 μM (Figure 4.1.). The cellular uptake was significantly lower for the derivatives bearing three and four PEG moieties compared to the symmetric Pt1Glc₄ and Pt2Glc₄. This can be explained by the flexible corona shell and negative charges provided by the multiple carboxy-PEG moieties, which prevent probe interaction with the cell membrane and translocation inside the cell (254).

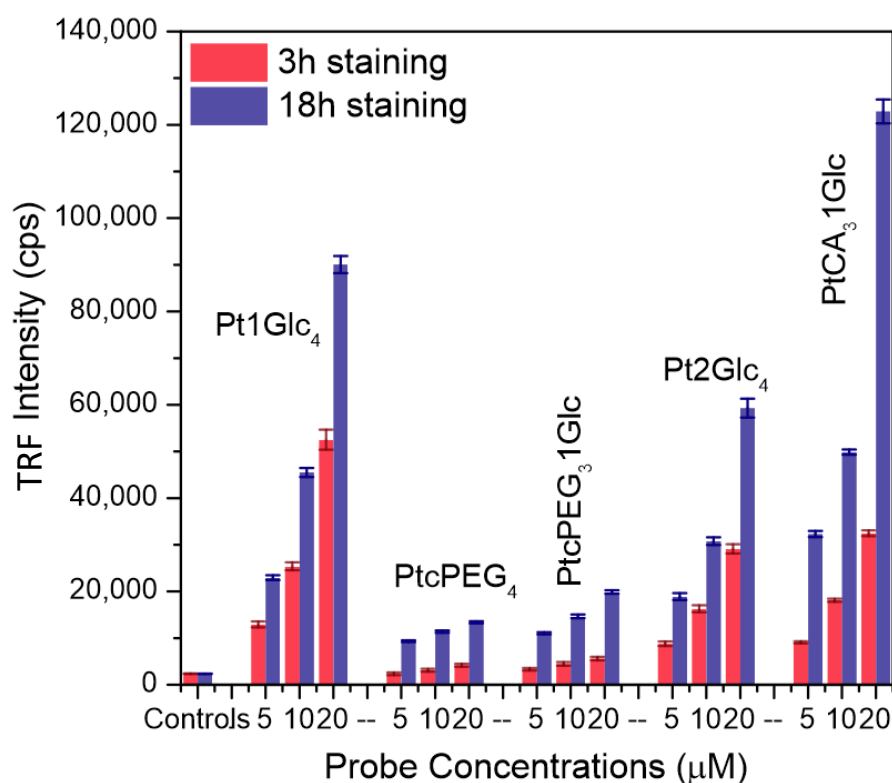


Figure 4.1: Comparison of 3 and 18 h cell staining on MEF cells using a range of dye concentrations. Data are expressed as mean of three biological replicates, confirmed over three technical replicates.

The neutral mPEG derivatives PtmPEG₄ and PtmPEG₃1Glc showed behaviour similar to the carboxy-PEG (Figure 4.2. A). This suggests that, other than the molecular charge, the ability of PEG chains to adsorb water molecules and increase the effective molecular size of the probe in aqueous solution, prevents their cellular uptake (269). Overall, the amphiphilic nature and lack of cellular receptors/targets for the PEG chains prevent their passive transport through the lipid layer. On the other hand, the cysteamine derivative PtCA₃1Glc showed good cell penetration, similar to or even higher than Pt1Glc₄. This can be explained by the positive charge of the amino group, which facilitates cell penetration through attractive interactions (128, 277).

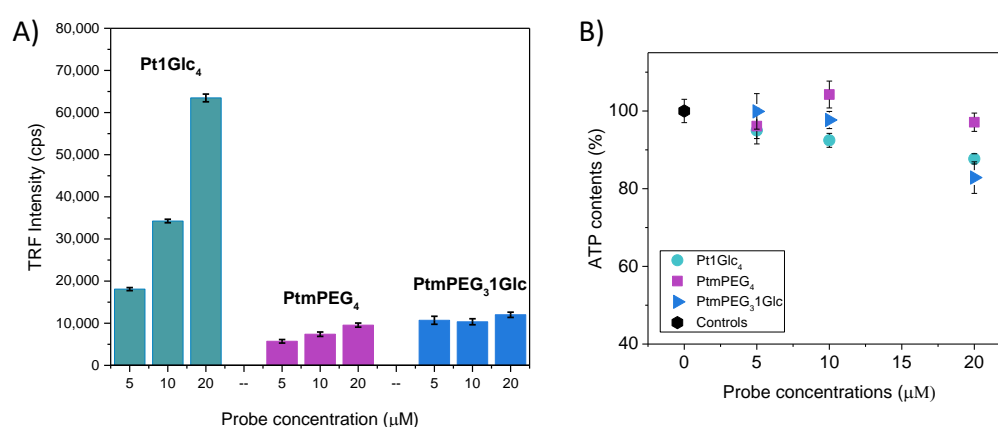


Figure 4.2: A) TRF intensity signal produced by PtmPEG₄ and PtmPEG₃1Glc after 3h staining of MEF cells using a range of dye concentrations (5-20 µM) and B) its effect on the cell viability, measured via total ATP contents (% of controls). Data are expressed as mean of three biological replicates, confirmed over two technical replicates.

The cytotoxicity of each conjugate was assessed by measuring changes in total ATP in MEF cells upon 3h or 18 h incubation with the probes (Figure 4.3. A, B). No significant cytotoxicity was seen for all the conjugates at all of the concentrations and incubation times tested. Only PtCA₃1Glc showed a drop in cell viability at concentrations >20 µM. We initially attributed this effect to the residual TFA in the sample (278-280), however, after further neutralization TFA from the purified compounds the same result was obtained. So, we attributed such toxicity to the disruption of the cell membrane mediated by the strong electrostatic attraction

between the positively charged probe and the negatively charged lipid bilayer (277, 281), which could be especially relevant at higher concentrations (i.e. > 20 μM) and long exposures (18h or more). Other possible cytotoxic mechanisms are partial nuclear penetration causing DNA binding due to the positive charge, as well as mitochondrial swelling and consequent disruption of the respiratory chain inducing apoptosis (282). In fact, as can be seen from the confocal images (Section 4.3, Fig. 4.8.D), rounded cells are observed at 10 μM concentration and 18 h incubation with PtCA₃1Glc. This could explain why this cytotoxic effect did not correlate with the TRF signals at the tested concentrations.

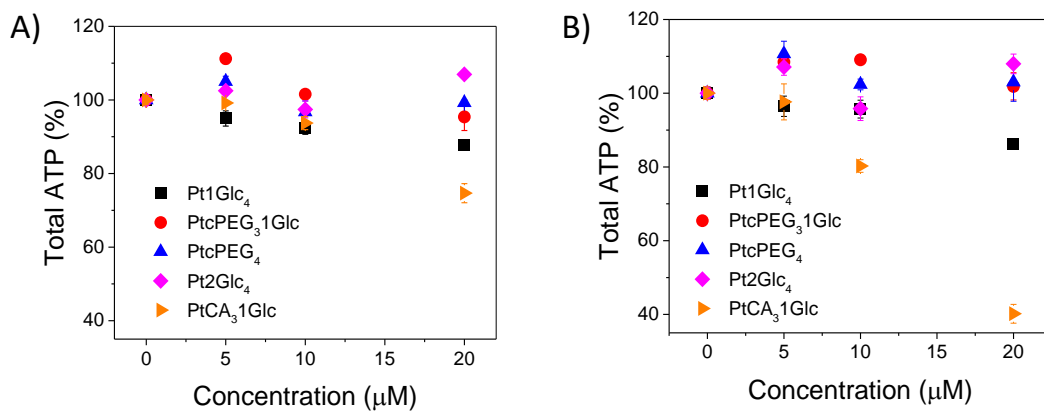


Figure 4.3: Effects of 3 h (A) and 18 h (B) staining time on the cell viability of MEFs, measured via total ATP content. Data are expressed as mean of three biological replicates, confirmed over three technical replicates.

The comparison of probes' cell staining efficiency on the human colorectal carcinoma (HCT116) cell line WT and $SCO_2^{-/-}$ showed similar results (Figure 4.4. A, B), suggesting GLUTs as potentially one of the main pathways of cellular uptake (160). $SCO_2^{-/-}$ is a highly glycolytic and non-respiring human cancer cell line, modified by disruption of both alleles of the SCO_2 gene, which encodes the homonymous protein fundamental for mitochondrial respiration (283). Such mutant cells undergo a metabolic switch to glycolysis, which upregulates the expression of glucose transporters (284). Particularly, the HCT116 cell line expresses mainly the GLUT1 subtype (285). However, other pathways of internalization cannot be ruled out.

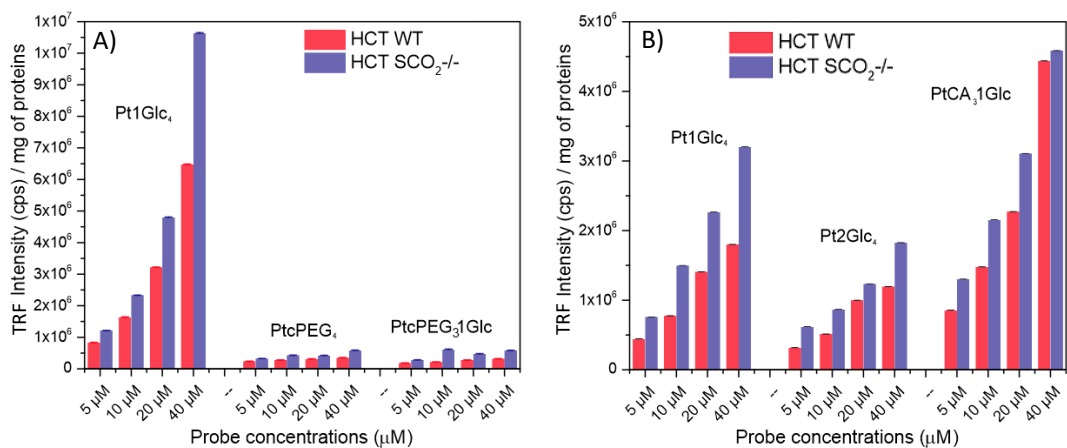


Figure 4.2: The intensity of phosphorescence signal normalized for protein content describing the effect of 3 h staining on HCT116 WT and $SCO_2^{-/-}$ cells (A, B). The Pt1Glc₄ probe was used as a reference. Data are expressed as mean of three biological replicates (one technical replicate was assessed).

As previously demonstrated, chelation of extracellular Ca^{2+} by ethylene glycol tetraacetic acid (EGTA) causes a rapid transient increase in oxygen consumption, which can be monitored by the kinetic measurement of the phosphorescence lifetime of an O_2^- sensitive probe on a TRF reader (264). Calculated lifetime values can then be converted into iO_2 concentration and plotted over time to evaluate fluctuations in cellular respiration (286). At high cell density, changes in local oxygenation can be linked to cellular respiratory activity.

In the absence of full oxygen calibrations for the new probes, only traces of TRF intensity and LT signals are shown in Figure 4.5. A, B. One can see that upon cell stimulation with EGTA in the galactose(+) medium, a marked spike in the intensity and lifetime signal was detected (286). Inhibition of the response by antimycin A (AntiA), a potent inhibitor of mitochondrial respiration and cellular O₂ consumption (224, 286, 287) was also evident.

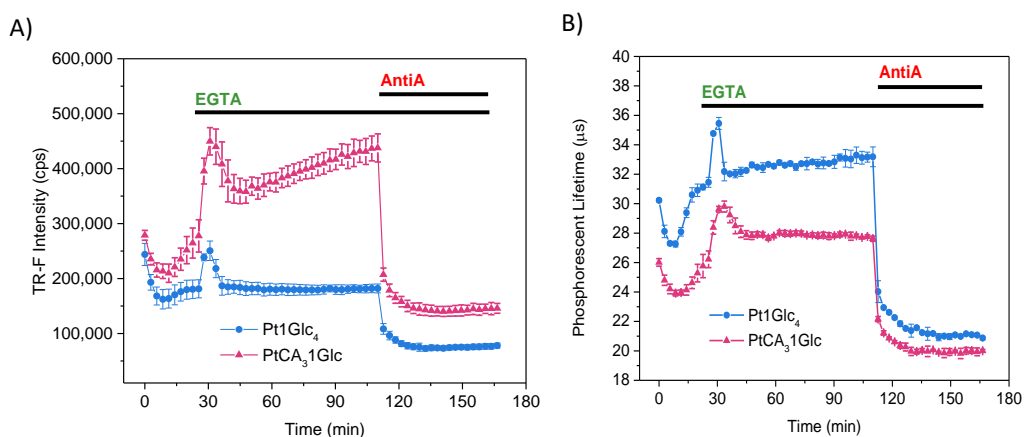


Figure 4.5: Respiration profiles. TRF Intensity (A) and lifetime (B) signals produced by the intracellular probes Pt1Glc₄ and PtCA₃1Glc on MEF adherent cells stained at 5 µM for 3 h, measured in galactose (+) respiration medium upon iCa²⁺ depletion (EGTA treatment) followed by respiratory inhibition by Ant A. Data are expressed as mean of three biological replicates, confirmed over three technical replicates.

Finally, the analysis of O₂ gradients was carried out on undifferentiated PC12 cells grown in suspension, to evaluate the usability of the new cell impermeable derivatives (288) (Figure 4.6. A-D). The graphs include blanks or negative controls (probe alone, no cells), resting cells (positive control), and cells stimulated with metabolic effectors EGTA (Ca²⁺ chelator), AntiA (mitochondrial complex III inhibitor) and FCCP (mitochondrial uncoupler).

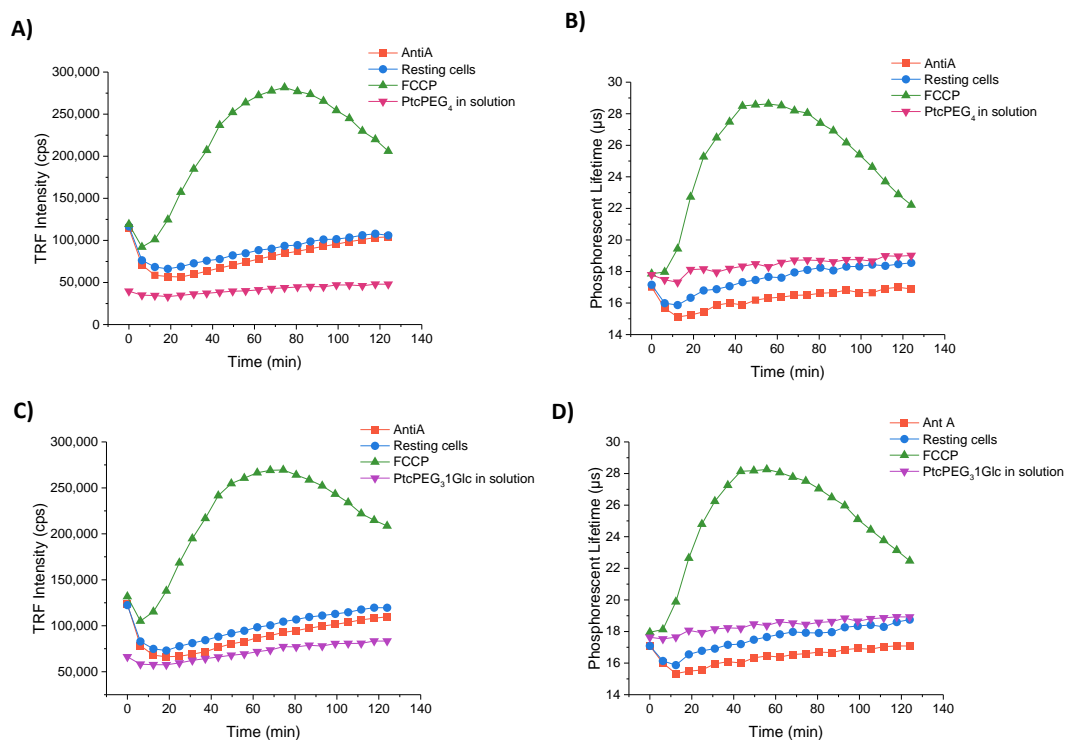


Figure 4.6: Respiration profiles. Phosphorescent emission and corresponding calculated lifetimes produced by the extracellular probes PtcPEG₄ (A and B, 5 µM) and PtcPEG₃1Glc (C and D, 5 µM), in glucose(+) medium. PC12 suspension cells were treated with 2 µM AntiA or 0.25 µM FCCP. Data are expressed as mean of three biological replicates, confirmed over three technical replicates.

We also included the well-established extracellular probe MitoXpress (Figure 4.7. A,B), and the intracellular Pt1Glc₄ (Figure 4.7. C,D) as standard references (106). The brighter probe, Pt1Glc₄, gave a smaller response to FCCP treatment (uncoupler of mitochondrial respiration that increases glycolysis and oxidative phosphorylation rates (224, 286, 287)) than the tetra- and tri-PEGylated derivatives. The latter probes also showed similar respiration profiles with the MitoXpress probe.

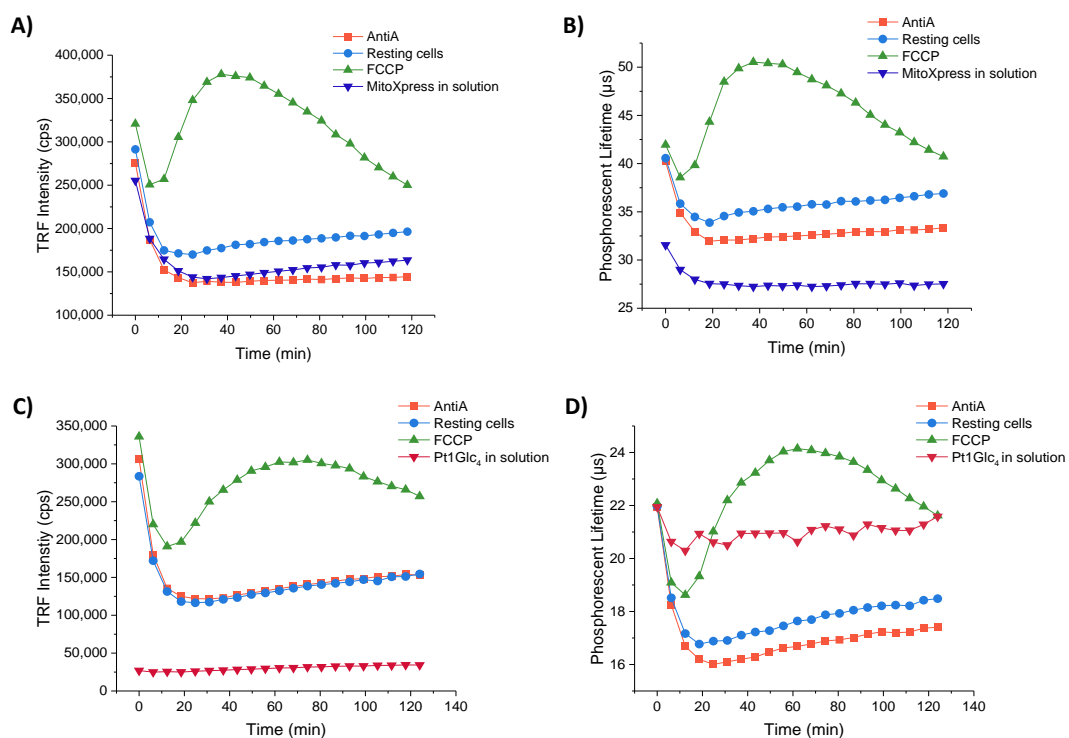


Figure 4.7: Respiration profiles. Phosphorescent emission and corresponding calculated lifetimes produced by the extracellular probe MitoXpress®-Xtra (A and B, 0.3 μ M) and the intracellular probe Pt1Glc4 (C and D, 1 μ M), in glucose (+) medium. PC12 suspension cells were treated with 2 μ M Ant A or 0.25 μ M FCCP. Data are expressed as mean of three biological replicates, confirmed over two technical replicates.

Thus, the new PEGylated derivatives can be used as extracellular probes for the detection of cellular oxygen consumption rates. However, reduced brightness, shorter lifetimes, and the tendency for aggregation make their analytical performance not as good as that of the MitoXpress probe.

4.2. Cellular uptake and toxicity of the *trans*- 2:2 derivative

To evaluate the ability of the new hetero-substituted *trans*- derivative to stain mammalian cells, we measured the TRF intensity signals of respiring MEF cells incubated with the probes Pt1Glc₂mPEG₂ (*trans*), and Pt1Glc₂ (*trans*) at 3 different concentrations, for 3 and 18 hours, at 37°C. Their staining efficiency was then compared with that of the published Pt1Glc₄. Figure 4.8 A shows that a similar intensity was obtained from cells stained with the new probe, however its intermediate is showing approximately 6-fold lower intensity signals. This can be due to Pt1Glc₂ (*trans*) having higher hydrophobicity, and lower brightness. Moreover, since its signal was lower than 30,000 count per second (cps), it cannot be used for respirometry or oxygen sensing applications (177).

Next, we investigated the effects of the probes on cell viability measuring total ATP content (% of control) under the same conditions. After incubation of cells with the probes in the dark, no significant impairment of cell viability was found (Figure 4.8. B). However, after 40 min of the TRF measurements cell viability was decreased below 70% for Pt1Glc₂ (*trans*) at 20 μM, (Figure 4.8. C). The phototoxicity of the probe at 20 μM was also confirmed by the phase contrast images of MEF cells: after cell staining in the dark, the cell layer was mostly intact (Figure 4.8. D), whereas after the exposure to light cells were detaching from the surface and spots without cells were produced (Figure 4.8. E). All this makes the *trans*-di-glycosylated intermediate unusable as an O₂ sensing probe. This is consistent with the literature data on porphyrin carbohydrate derivatives: *trans*-conformation was superior for PDT applications, due to its greater yield of hydroxy radicals ($\cdot\text{OH}$) which provide enhanced cytotoxicity(272).

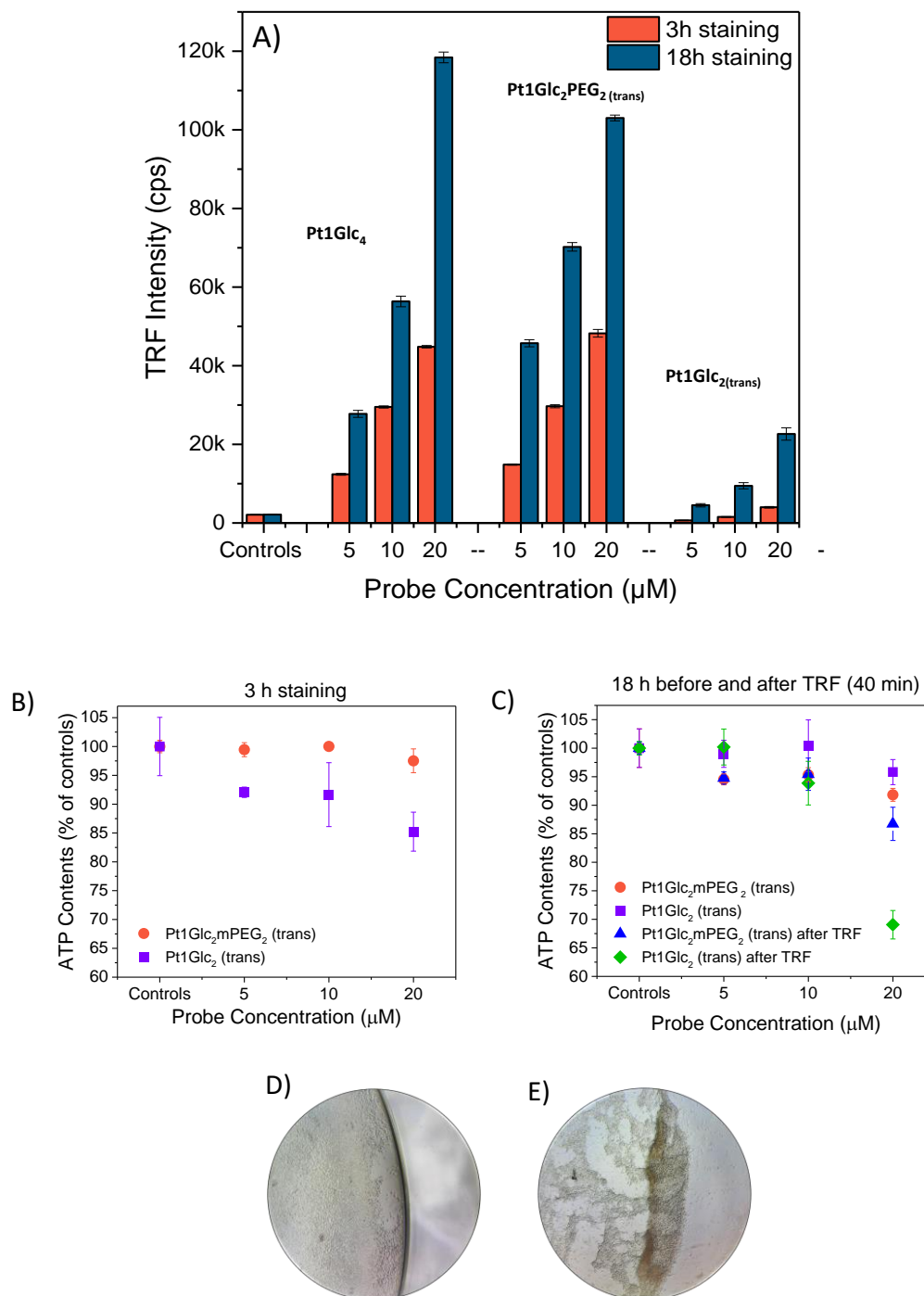


Figure 4.8: (A) Intensity signals measured in TRF mode produced by MEF cells after 3h and 18 h incubation with the probes at 5, 10, and 20 μM . Total ATP content after (B) 3 h and (C) 18 h of incubation of MEF cells with the probes at specified concentrations. Phase-contrast images of the wells containing MEF cells incubated with 20 μM Pt1Glc₂ (trans) (D) before and (E) after TRF analysis (40 min intermittent exposure to Xe lamp excitation, 2 s integration time). Data are expressed as mean of three biological replicates, confirmed over three technical replicates.

We tested the ability of PtmPEG₂1Glc₂ (trans) to trace the changes in intracellular O₂ concentration (icO₂) in respiring MEF cells induced by the addition of activator (EGTA) or inhibitor (AntiA) of respiration at atmospheric pO₂. EGTA is an extracellular Ca²⁺ chelator, which has been shown to alter Na⁺ and H⁺ concentrations in the mitochondria, leading to transient increase in O₂ consumption (264). On the other hand, AntiA inhibits cell respiration by disrupting the electron transport chain, causing the O₂ concentration to increase (286). Indeed, the effects of these modulators were seen as changes of the probe intensity and, most of all, lifetime signals of the probes over time (Figure 4.9. A and B).

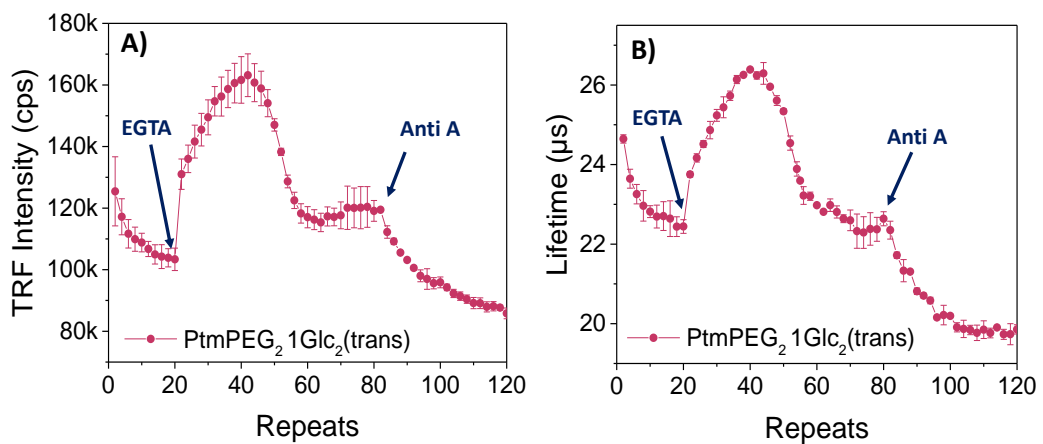


Fig. 4.9: Phosphorescence intensity (A) and lifetime (B) profiles produced by PtmPEG₂1Glc₂ (trans) upon activation of respiration of MEF cells by EGTA (2.5 mM) and inhibition by AntiA (5 μM). MEF cells were stained for 18 hours with the probe at 10 μM, and the signal was recorded in Gal(+)/Glc(-) respiration medium. Arrows indicate the time of effector addition. Data are expressed as mean of three biological replicates, confirmed over three technical replicates.

4.3. Microscopy analysis of intracellular distribution

Confocal microscopy was performed to investigate intracellular staining and subcellular localization of the IC probes. Intensity images of 2D cultures of MEF cells stained for 18 h and counter stained with calcein green, confirmed the IC or EC nature of the new derivatives. Pt1Glc₄ was previously shown to efficiently stain mammalian cells, mainly accumulating at the perinuclear level, without penetrating the nucleus (Figure 4.10. A and B) (160). PtCA₃1Glc was seen to localize similarly to Pt1Glc₄, producing even and efficient staining at 5 μM with minor nuclear staining (Figure 4.10. C). However, when the concentration is increased to 10 μM, it started to show cyto-toxicity, with cells appearing rounder and smaller (Figure 4.10. D). The PEGylated structures PtcPEG₄ and PtcPEG₃1Glc did not produce meaningful phosphorescence intensity images, confirming that they were not accumulated in cells and thus are not suitable for intracellular bioimaging applications.

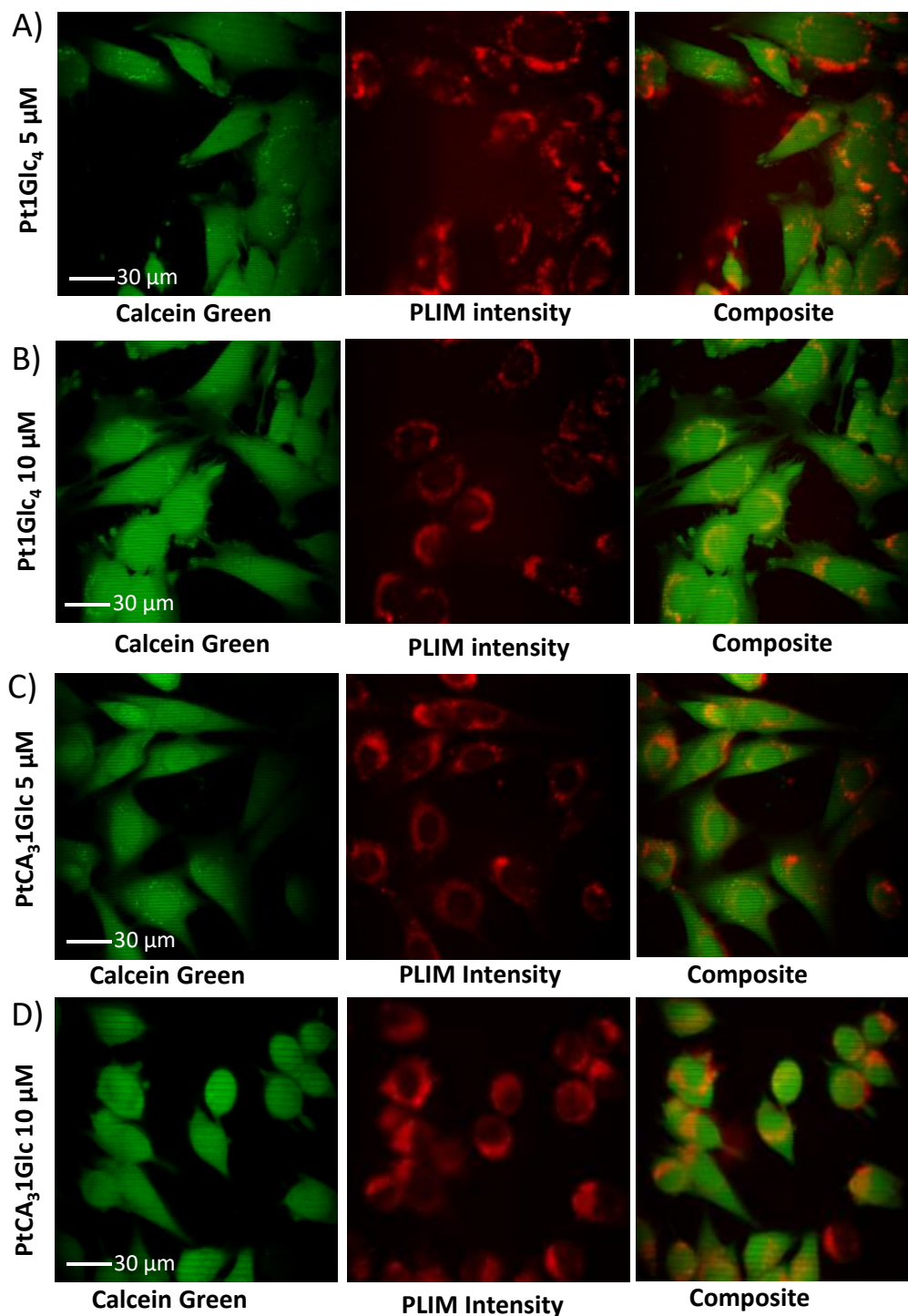


Figure 4.10: Intracellular staining and localization of the probes, visualized on a confocal microscope. Emission intensity images of MEF cells after 18 h incubation with the probes and counter stained with Calcein green. MEF cells stained with Pt1Glc₄ at A) 5 μM and B) 10 μM. MEF cells stained with PtCA₃-1Glc at C) 5 μM or D) 10 μM. Calcein green was excited at 488 nm, and probes were excited at 405 nm.

Intensity images of MEF cells stained for 18 h with 10 μ M of PtmPEG₂1Glc₂ (trans) show localization in the cytosol and minimal nuclear staining. Compared to the previously described glycosylated PtPFPP derivatives(256), it uniformly stained the entire cell in a punctated pattern (Figure 4.11).

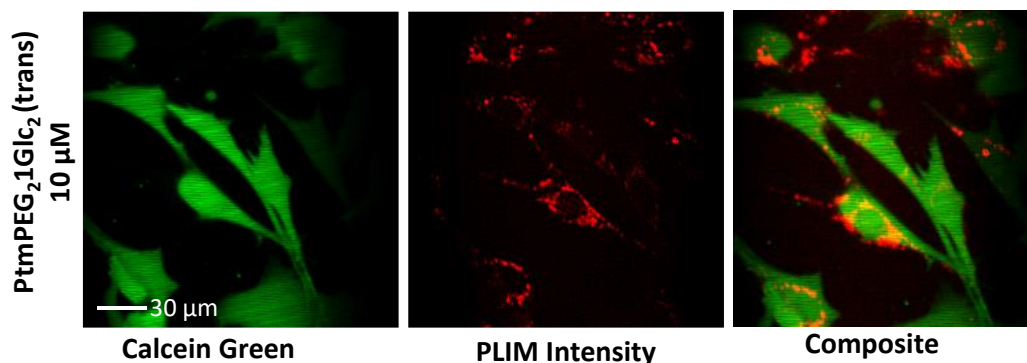


Figure 4.11: MEF cells stained with PtmPEG₂1Glc₂ (trans) at 10 μ M. All images were recorded using an immersion lens at 63x magnification. Calcein green was excited at 488 nm, and probes were excited at 405 nm.

This highlighted sign of mitochondrial staining which was also seen for the *trans*-bis-glycosylated derivatives and HeLa cells described by Hiroara et al. (250). Thus, to evaluate the mitochondrial staining of the PtmPEG₂1Glc₂ (trans) derivative, we co-stained MEF cells with the probe and 50 nM of MitoTraker Green (MTG) for 30 min and compared the recorded intensity images. Pt1Glc₄ did not show any significant overlap with the MTG staining, and mostly localized around the nucleus (Figure 4.12. A). On the other hand, PtmPEG₂1Glc₂ (trans) showed partial overlap with the mitochondrial staining, however it did not stain mitochondria in a selective manner (Figure 4.12. B). PtCA₃1Glc was also tested at 10 μ M concentration for mitochondrial staining, however its cytotoxic effect causing rounding of the cells (data not shown) did not allow the evaluation of its subcellular localization.

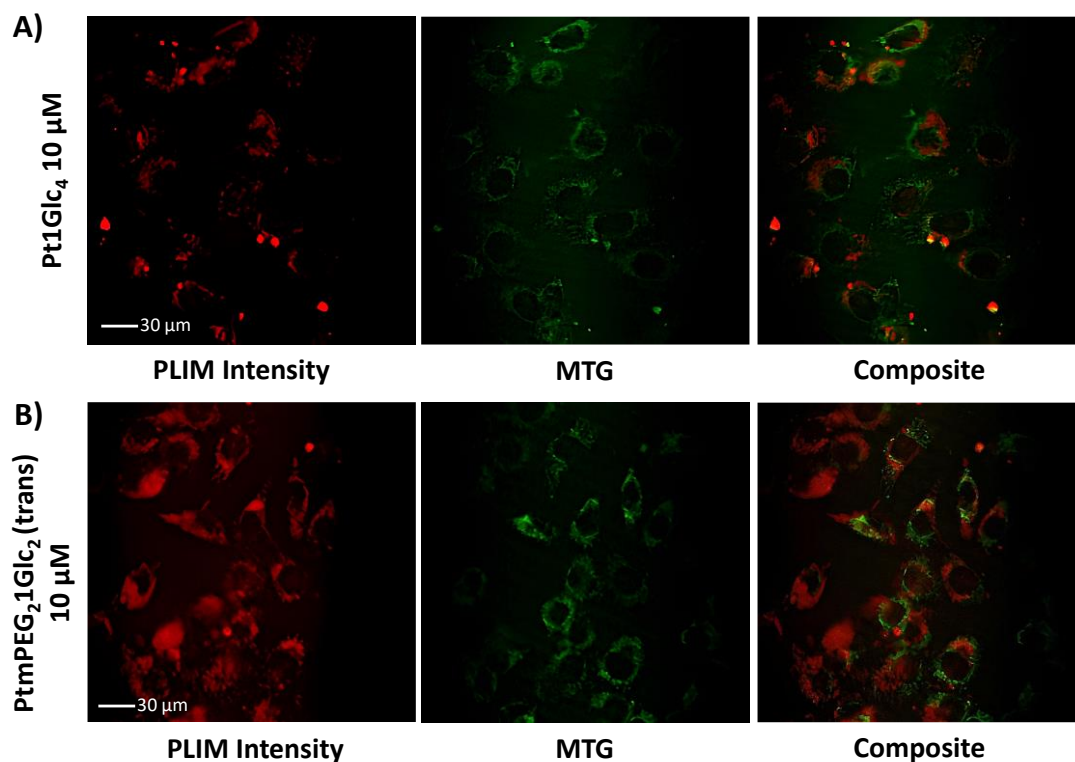


Figure 4.12: Images of MEF cells co-stained with 50 nM of Mito Tracker Green (MTG) 50 nM for 30 min and the probes at 10 μM for 18 h. Images were recorded using an immersion lens at 20x magnification. MTG was excited at 488 nm, and probes were excited at 405 nm.

4.4. Involvement of GLUTs transporters in probe uptake

In the previous study of Pt1Glc₄ it was found that its uptake depends on the GLUT transporters, however the mechanism of internalization was not studied in detail (160). We evaluated the involvement of GLUTs in the cell internalization of the symmetric Pt1Glc₄ and PtmPEG₂1Glc₂ (trans) derivatives by blocking GLUT1 (the main isoform expressed in MEF cells) by BAY-876 (289). This small molecule competitively inhibits GLUT1 with high potency and selectivity over the other GLUT isoforms.

First, we determined the inhibition efficacy of BAY-876 at 10 μM by treating MEF cells simultaneously with the inhibitor and rotenone at 5 μM (290). Rotenone is a potent inhibitor of the Complex I in the mitochondrial respiratory chain (291). This leads to a decrease in ATP production through OxPhos, thereby elevating the cell's glycolytic activity. If both BAY-876 and Rotenone are present at effective concentrations, the

cells should drastically reduce their ATP production as both glycolysis and respiration are significantly reduced. For this assay, MEF cells were grown in standard DMEM overnight, then washed and starved for 2 h with glucose-free medium (10%FBS) followed by 1 h incubation with 10 μ M BAY-876 and 5 μ M Rotenone. Prior ATP measurements, 10 mM glucose was added to the medium to induce activation of GLUT1. After 30 min cells were washed and ATP levels were measured using the assay kit. Cells treated only with BAY-876 and only Rotenone were also analysed showing 15% and 60% decreased ATP levels, respectively. The co-treatment caused complete death of the cells, confirming the inhibitory activity of BAY-876 at 10 μ M (Figure 4.13. A).

We then investigated the inhibitory effect of BAY-876 on the intracellular uptake of Pt1Glc₄ and PtmPEG₂1Glc₂ (*trans*) in Glc (+) medium and Glc (-) medium after 2 h of glucose starvation (to prevent potential competitive interactions of BAY and Glc at the receptor level). Cells were inhibited for 1 h (with or without starvation), then stained with 10 μ M of the probes in the presence of the inhibitor for 3 h, washed three times and measured on the TRF plate reader. When using Glc containing DMEM (10 mM – standard growth conditions), if GLUTs are inhibited, the uptake of Pt1Glc₄ was reduced, while PtmPEG₂1Glc₂ uptake remained unchanged. However, in glucose free medium, the *trans*- derivative increased its uptake, while Pt1Glc₄ uptake was reduced by the same amplitude. This effect could be due to the recognition of the Glc moieties present on the hetero-substituted derivative which promotes its internalization via endocytic and non-endocytic pathways (292). From this experiment it can be concluded that the fully glucosylated derivative is more dependent on GLUT1 internalization than the *trans*-di-PEGylated-di-glucosylated derivative. However, for Pt1Glc₄ other internalization pathways cannot be ruled out.

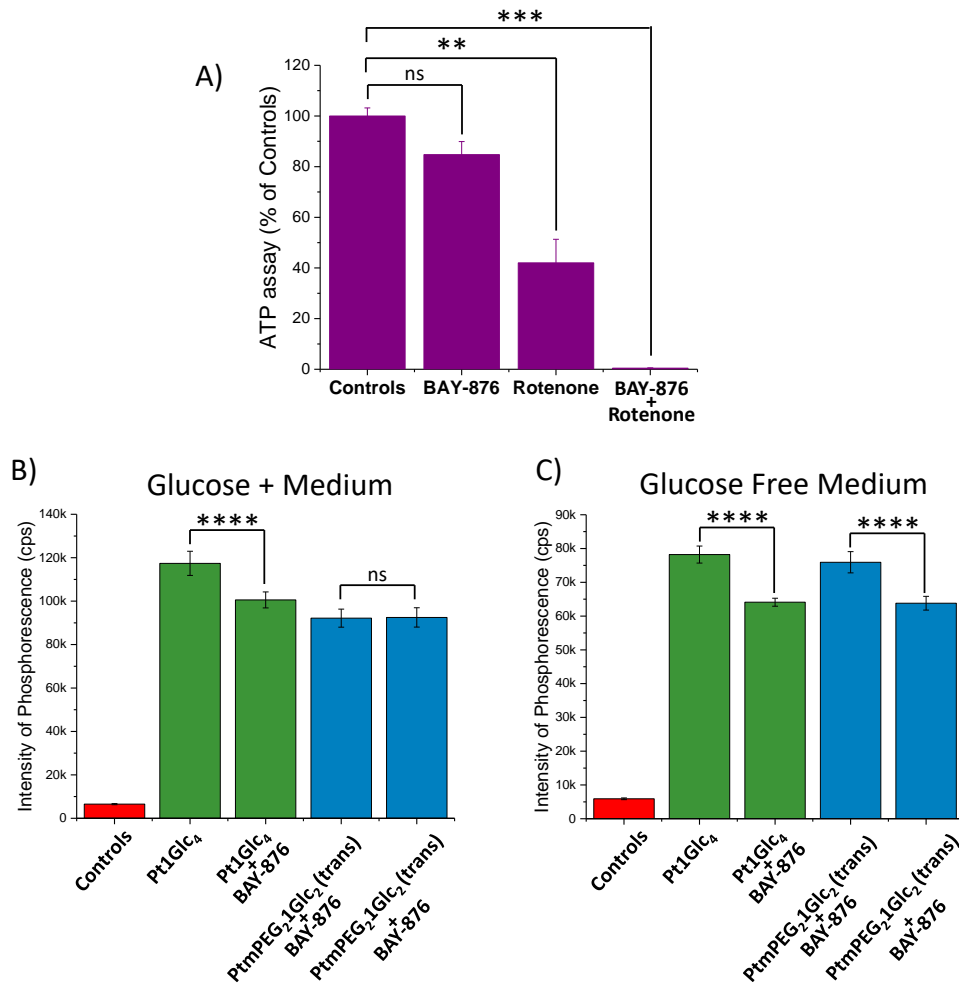


Figure 4.13: A) ATP assay of BAY-876 inhibitory activity on GLUT1 transporter. MEF cells were starved for 2 h in glucose-free DMEM in the presence of 10% FBS, then incubated for 1 h at 37 °C with 5 μ M Rotenone and 10 μ M BAY-876. GLUT1 were then activated by adding 10 mM of glucose for 30 min followed by ATP levels measurements. 3h staining of MEF cells with 10 μ M Pt1Glc₄ and PtmPEG₂1Glc₂ (trans) with and without GLUT1 inhibitor (10 μ M BAY-876, 1 h) in B) Glucose (+) and C) Glucose free (with 2 h starvation) media. (**P<0.01, ***P<0.001, ****P<0.0001 vs. positive controls; One-way ANOVA with Bonferroni's multiple comparisons test). Data are expressed as mean of three biological replicates, confirmed over three technical replicates.

4.5. Conclusions

This biological study aimed to explore the potential cell analysis applications of newly synthesized derivatives, focusing on their cellular uptake and toxicity profiles. Initial screening on MEF cells helped identify promising derivatives, which were then compared with the reference probes Pt1Glc₄. Derivatives with three and four PEG oligomers exhibited lower cellular uptake due to negative charges hindering interaction with the cell membrane. Neutral mPEG derivatives behaved similarly, suggesting reduced uptake due to increased molecular size. However, these hetero- and tetra-PEGylated derivatives proved effective as extracellular O₂ probes. In contrast, PtCA₃1Glc showed enhanced cell penetration and intracellular staining, attributed to its positive charge, which is also the cause of its higher cell toxicity. The 2:2 derivative PtmPEG₂1Glc₂ (trans) demonstrated staining efficiency comparable to Pt1Glc₄, indicating the importance of conformation and aggregation behaviour. Its intermediate Pt1Glc₂ (trans) displayed insufficient cellular uptake on MEF cells and elevated phototoxicity, rendering it unsuitable as an O₂ sensing probe. The GLUT1 dependent cellular uptake study suggested that Pt1Glc₄ uptake is more dependent on GLUT1 internalization than the *trans*-di-PEGylated-di-glucosylated derivative, although alternative internalization pathways for Pt1Glc₄ cannot be ruled out.

Chapter 5: Applications of the New Probes with Bacterial Cell Cultures

5.1. Introduction

E. coli cells represent a classical model for bacterial cell-based assays. They are frequently used as a reference in non-selective assays such as the total aerobic viable counts (TVCs) on solid media (293), and in conventional assays with selective media used to cultivate and identify certain bacterial species, such as coliforms, Enterobacteriaceae (294, 295), or pathogenic strains (296, 297). *E. coli* cells have been extensively validated in O₂ sensor based respirometric assays, e.g. rapid TVC tests performed in liquid media (234, 237, 298) with both non-selective and selective media (263).

The MitoXpress probe (Agilent) is routinely used in this platform, due to its convenient spectral characteristics, good sensitivity, low S/N, and stable and calibration-free phosphorescence lifetime-based O₂ sensing. It has been validated in various bioanalytical applications and is regarded as the gold standard in micro-respirometry. This O₂ sensor demonstrated good analytical performance and usability in simple growth media, such as nutrient broth (NB) (234). MitoXpress is especially suitable for detection on standard time-resolved fluorescence (TRF) readers, thanks to its convenient luminescence lifetime (LT) values and spectral characteristics (excitation at 360-400 nm and emission at 640-670 nm). These readers typically use a Xe-flash lamp for excitation with a pulse duration of approximately 15-20 μs, coupled with time-gated emission detection using a photon counting PMT (photomultiplier tube) detection system. This measurement setup ensures high-intensity signals and a favourable signal-to-noise (S/N) ratio, facilitating the rapid and accurate determination of MitoXpress LT values through the rapid lifetime determination (RLD) method (217, 299).

However, a recent study compared the performance of the micro-respirometry assay and the MitoXpress probe vs a macro-respirometry platform with a solid-state sensor

coating, when using more complex media (263). The first platform showed significant susceptibility of the liquid probe to interferences caused by some of the media ingredients, while the second platform was able to maintain a good response. In fact, these selective growth media can contain indicator dyes, chromogenic substrates, surfactants, other additives for the enrichment of certain bacteria (300) which can interfere with the signal response and stability.

5.2. Performance of the small molecule probes in respirometric bacterial assays using complex media

In this study, we investigated the performance of four different water-soluble O₂ sensing probes, three of which are based on Pt-porphyrin phosphors (NanO₂, Pt1Glc₄, PtmPEG₄), along with the benchmark MitoXpress probe (PtCP-BSA), in the micro-respirometry assays with *E. coli* cells and five growth media having complex composition. The main goals were to identify the best performing probes for such applications and to have a better understanding of possible interferences on the phosphorescent signals and respiration profiles generated by the O₂ probes.

We tested five media that were used in the previous study(263): nutrient broth (NB), McConkey (MC), Rapid Coliform ChromoSelect (RCC), M-Lauryl Sulfate (MLS), and Minerals Modified Glutamate (MMG) media. The media have complex and rather different composition, containing basic nutrient and special additives such as indicator dyes, metabolites, surfactants, vitamins, substrates, etc. The roles of these components are to promote growth of target microorganisms while suppressing unwanted species, or to report the presence of target microorganisms by colour changes in the media or other means. Due to the different composition and optical properties of the media (Figure 5.1), they are expected to act differently on the different O₂ probes and respirometric assays.



Figure 5.1: Photographs of 96-well plates with the different media and *E. coli* loads (zero, 10^4 or 10^6 CFU/mL): before (left) and after (right) overnight incubation or assay, at 37 °C.

5.2.1. Selection and general comparison of the O_2 probes

In micro-respirometry assays with mammalian or bacterial cells (127, 234), the MitoXpress probe is normally used at a working concentration of 0.3 μ M with respect to the dye (Table 6). It comprises a macromolecular structure produced by covalent linkage of an amino-reactive phosphor, PtCP-NCS, to a water-soluble polypeptide carrier, BSA (Figure 5.2. A) (106, 127). PtCP phosphor has high emission yield ($\Phi = \sim 0.4$, unquenched) and specific brightness ($\epsilon \cdot \Phi = 34,000 \text{ M}^{-1}\text{cm}^{-1}$) (67), however upon conjugation to BSA its brightness in aqueous buffers decreases several-fold due to static quenching caused by porphyrin-BSA interactions(301). Nonetheless, when measured in time-resolved fluorescence mode, MitoXpress probe produces sufficiently high phosphorescence intensity signals and stable lifetime values, generating smooth and meaningful respiration profiles in simple media.

The other three probes comprise the PtPFPP phosphor embedded in different micro-environment: an amphiphilic polymer for the nanoparticulate NanO2 probe, and aqueous medium for the other two small molecule probes (Figure 5.2). While PtPFPP dye is hydrophobic and has ~ 5 times lower brightness than PtCP (free unquenched state) (84), it is readily available, inexpensive and amenable to modifications by thiol chemistries (130, 251, 252, 271). Unlike the MitoXpress probe, the three other probes studied here have not been assessed in detail in micro-respirometry assays.

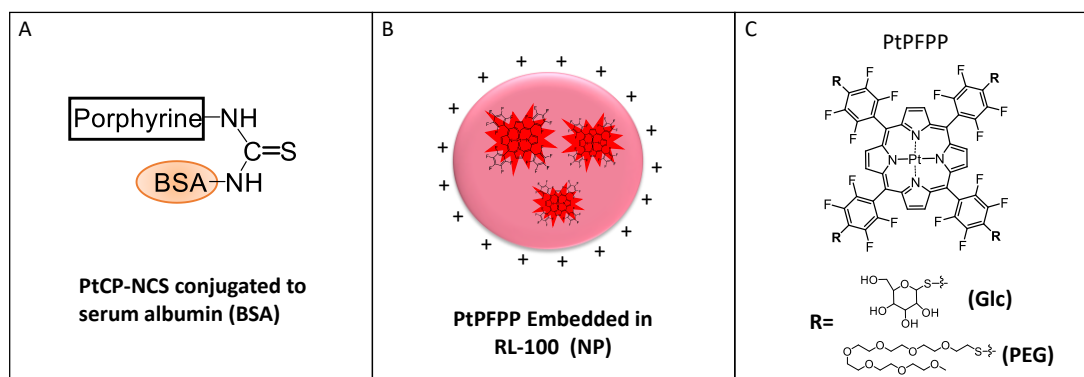


Figure 5.2: Schematic representation of the O_2 probes used in the study: A) The MitoXpress probe comprising a macromolecular conjugate of Bovine Serum Albumin (BSA) with PtCP-NCS phosphor. B) NanO₂ probe comprising core-shell nanoparticles of a cationic hydrogel, RL-100 with embedded PtPFPP molecules. C) Small molecule probes: tetra-PEGylated, PtmPEG₄, and tetra-glucosylated, Pt1Glc₄, derivatives of PtPFPP phosphor.

NanO₂ probe was developed for sensing intracellular O_2 and phosphorescence lifetime imaging microscopy (PLIM) applications on mammalian cells (177). It comprises an aqueous dispersion of cationic nanoparticles of an amphiphilic polymer, RL-100 hydrogel, with PtPFPP molecules physically trapped in the hydrophobic core (Figure 5.2B, Table 6). Thus, the polymer ‘shields’ the dye from the external environment eliminating undesirable quenching interferences from ions, hydrophilic and large molecules, and providing optimal quenching and O_2 sensitivity. The nanoparticles, with an average size of 35-40 nm have positive surface charge, they can penetrate and stain various mammalian cells and tissue samples by simple incubation of the cells in a media containing the probe (177). NanO₂ is extremely stable and can be stored for many years in concentrated aqueous stocks, at 4°C, however its colloidal and structural stability in different chemical environments has not been studied in detail. Pt1Glc₄ is a hydrophilic small-molecule probe, also with cell-penetrating ability, designed for intracellular use, deep tissue staining and mapping of O_2 concentration by PLIM. It is produced by click-modification of the hydrophobic PtPFPP scaffold with four β -D-thio-glucose moieties (Figure 5.2.C, Table 6) (160). Compared to MitoXpress and NanO₂, Pt1Glc₄ probe shows a high degree of internal quenching of the core phosphor, PtPFPP (256).

PtmPEG₄ is another small molecule derivative of PtPFPP with four thiolated hexa-PEG peripheral chains (Figure 5.2. C, Table 6). Compared to Pt1Glc₄, PtmPEG₄ is less hydrophilic and cell-impermeable (256).

Table 6: The O₂ probes used in this study and their characteristic features.

Probe	Porphyrin Phosphor	Working conc.	Probe Type	Special features
MitoXpress	PtCP	0.3 μM	Macromolecular conjugate	Protein based, cell-impermeable
NanO2	PtPFPP	0.3 μM	Nanoparticle	Polymeric core-shell NPs, shielded, cell-permeable*
Pt1Glc ₄	Modified PtPFPP	3 μM	Small molecule	Cell-permeable*
PtmPEG ₄	Modified PtPFPP	3 μM	Small molecule	Cell-impermeable*

* Assessed mostly with mammalian cells and tissues.

5.2.2. Basal and maximal phosphorescent signals of the probes in the *E. coli* assays

In standard non-selective growth media, such as NB, MitoXpress produces stable baseline with mean basal LT signal of ~22 μs, which increases to ~75 μs upon sample deoxygenation caused by bacterial growth (Table 7).

The NanO2 probe, used at the same working concentration as MitoXpress (0.3 μM), produced 6-times higher TRF intensity signals in NB media (1.7M cps vs 280k cps) and similar LT signals: 27 μs and 71 μs in air-saturated and deoxygenated conditions, respectively (Table 7). Its long LT is attributed to the rigid micro-environment of PtPFPP molecules inside the nanoparticles, which decreases non-radiative quenching from vibronic coupling (67).

Pt1Glc₄ produced reduced phosphorescence intensity signals and LT values compared to the previous probes: 160k cps and 10.3 μs in air-saturated and 750k cps and only 17.1 μs in deoxygenated conditions (Table 7) at 3 μM concentration, i.e. 10-times higher than MitoXpress and NanO2 (Table 6).

PtmPEG₄ also shows significant signal quenching: at 3 μM concentration, its TRF intensity and LT signals in NB are: 36k cps and 12 μs in air-saturated and 180k cps and 29 μs in deoxygenated conditions, respectively (Table 7).

Table 7. Basal and maximal phosphorescence signals of the probes in the different media.

Probe	Medium	I _{base} (cps)	I _{max} (cps)	LT _{base} (μs)	LT _{max} (μs)	Comments
MitoXpress [0.3 μM]	NB	279k	2.4M	22.1	74.6	Normal sigmoid and stable signals
	MC	110k	715k	25.2	65.3	Altered sigmoids
	RCC	14k	908k	15.6	40.5	Almost normal sigmoid
	MMG	56.9k	424k	19.6	46.7	Bell shaped Int, Sigmoidal LT profiles
	MLS	22k	120k	18.8	35.0	Bell shaped signals
NanO2 [0.3 μM]	NB	1.7M	13.8M	27.1	70.6	Normal sigmoid and stable signals
	MC	717k	6.5M	22.4	62.8	Almost sigmoidal signals
	RCC	738k	9.1M	21.8	57.7	Almost sigmoidal signals
	MMG	259k	2.1M	14.7	32.9	Sigmoidal signals with shorter LT _{max}
	MLS	530k	2.9M	26.4	62.5	Altered sigmoid with downward trend
Pt1Glc₄ [3 μM]	NB	164k	756k	10.3	17.1	Bell shaped Int, sigmoidal LT up-drifting
	MC	86k	397k	8.7	18.5	Altered profiles with two signal growth
	RCC	75k	1.7M	13.3	22.6	Signal drop followed by a plateau
	MMG	36k	230k	11.3	17.3	Altered sigmoid with upward trend
	MLS	29k	43k	9.2	12.1	Signal quenching
PtmPEG₄ [0.3 μM]	NB	36k	178k	11.9	29.1	Almost sigmoidal signals
	MC	69k	133k	8.8	18.5	Double Int increase and altered LT profile
	RCC	53k	303k	13.1	27.5	Bell shaped Int and almost sigmoidal LT
	MMG	17k	66k	10.9	20.9	Almost sigmoidal, smaller amplitude
	MLS	41k	109k	8.2	11.8	Signal quenching

I_{base}= basal intensity; I_{max}= maximal intensity; Cps= count per second; LT or τ = Lifetime (μs). Maximal signals were obtained at [*E. coli*] = 10⁶ (CFU/mL). Questionable signals are shown in bold red.

In the more complex RCC and MLS media, MitoXpress basal Int signals (highlighted in red) are largely quenched, dropping below the acceptable levels for this instrument (>30k cps(302)). The corresponding LT signals are also quenched considerably, which would necessitate the use of customised LT thresholds for the determination of TT values. Overall, maximal Int signals remain high and easy to measure in all the media, however, the efficiency and usability of the MitoXpress probe in RCC and MLS is questionable.

The NanO₂ probe retained high basal and very high maximal Int signals in all the media, despite their 3-6 folds quenching in MMG and MLS. Its LT signals also remained stable, being moderately quenched in MMG, which is the only problematic media for the NanO₂.

The Pt1Glc₄ and PtmPEG₄ probes, due to their lower brightness and shorter lifetimes, were measured at 25 μ s and 50 μ s delay times instead of the standard delay times (30 μ s and 70 μ s for t_1 and t_2 respectively) to prevent loss of Int signals. Nonetheless, they produced much lower basal Int signals across all media, and basal LT signals all below 13 μ s. Although these derivatives have similar chemical structures, Pt1Glc₄ probe produced much higher maximal Int signals than PtmPEG₄, in accordance to their specific brightness (Table 5). Further reduction of delay times would increase the background signals and further reduce the S/N ratio, while using higher concentrations would increase probe consumption and assay costs. Ultimately, under these respirometric assay settings, both Pt1Glc₄ and PtmPEG₄ probes are barely usable in all the media.

5.2.3. Full respiration profiles of *E. coli* produced with the different media and probes

Phosphorescent signals of an O₂ sensor have reciprocal relationship with sample O₂ concentration, described by the Stern-Volmer equation (1, 143). As a result, in respirometric bacterial assays, O₂ probes produce characteristic sigmoidal profiles of the intensity (Int, cps) and corresponding calculated lifetime (LT, μ s) signals. Initially, the signal produces a flat baseline, which corresponds to air-saturated conditions in the sample with maximal quenching of the probe by O₂. Then, at a certain time, the signal undergoes a steep transition from its low baseline to high plateau levels. This reflects the change from oxygenated conditions to deoxygenation of the sample due to rapid exponential bacterial growth and increased cell density. The time of this transition depends on the initial concentration of bacteria in the sample, the type of growth media and assay conditions used (233, 234). Bacterial cell respirometry usually monitors primary sensor signals (Int or LT). LT based mode provides reliable determination of TT values (h) for respiring samples. This, in turn, allows the

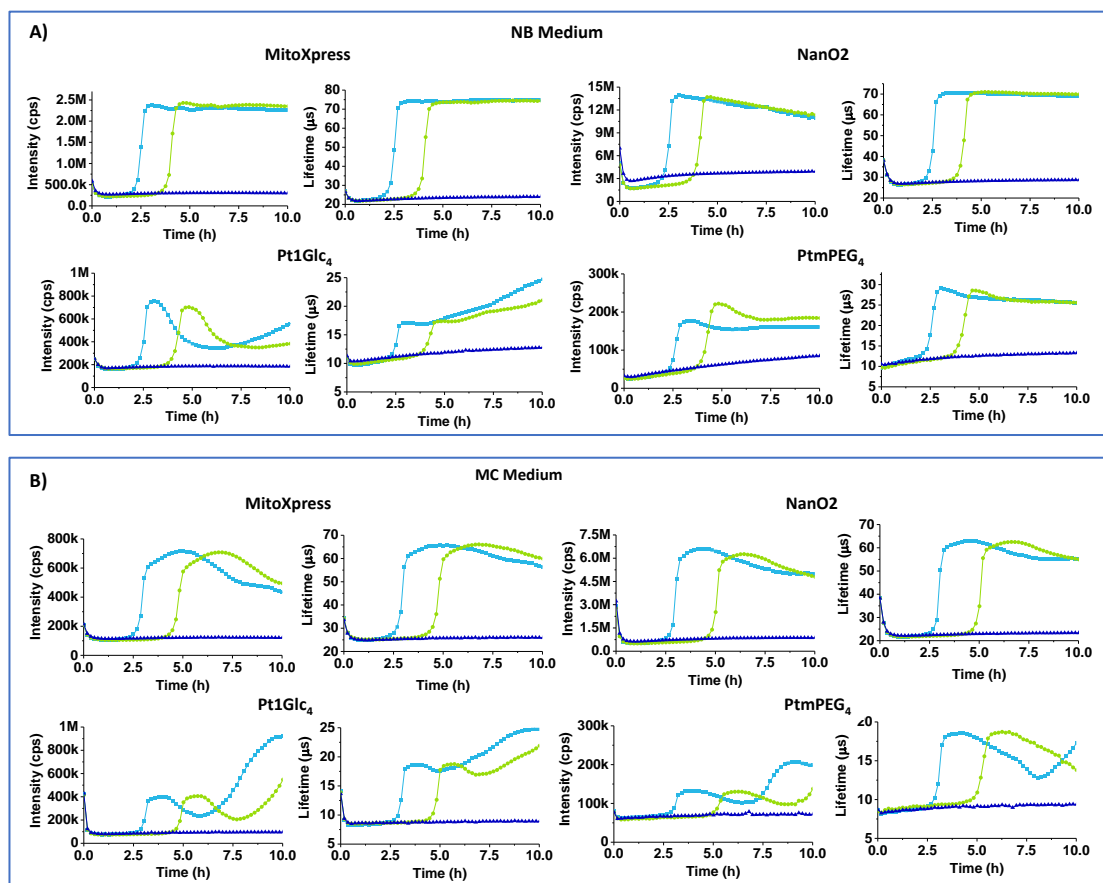
enumeration of aerobic bacteria in unknown samples: adding the sample to growth medium, monitoring its respiration profile, and determining the time to reach signal threshold (TT, hours) which is set above the baseline. Then measured TT values are converted into cell concentrations (CFU/mL or CFU/g) by applying a known calibration equation (303). However, this basic theory does not account for possible optical effects and interferences that may be caused by the medium, cells or probe being used.

Full respiration profiles of *E. coli* for the different probes in simple non-selective NB medium are shown in Figure 5.3. A. It appears that classical respiration profiles are recognisable in NB only for the MitoXpress (Int and LT) and NanO2 (LT) probes. The Int signal of NanO2 showed a downward drift in the plateau region and a small upward drift of the baseline, which can be attributed to probe binding to surfaces or media components, and gradual precipitation or decomposition. Nonetheless, NanO2 provides reliable and accurate determination of TT values, so it remains usable. Conversely, Pt1Glc₄ and PtmPEG₄ probes produced unusual (bell-shaped) Int profiles and non-classical LT profiles, with marked upward drifts of the Int baseline and unstable LT baseline. We attribute these effects to the low LT values and S/N ratio, which make these respirometric assays susceptible to interferences and changes in sample optical properties (absorbance, scattering) overtime.

In MC medium Int signals for all the probes were 1.5-2 times lower than in NB. Again, PtmPEG₄ and Pt1Glc₄ showed unacceptably low baseline Int and LT (<15 μ s) signals (Table 7) and distorted respiration profiles (Figure 5.3.B).

In RCC medium, basal, and maximal LT signals of the NanO2 were close to normal, but some odd spikes occurred at the start of the plateau region. MitoXpress showed very low basal intensity signals, reduced basal and maximal LT signals. Small molecule probes showed oddly shaped profiles and unstable LT signals (Table 2, Figure 5.3. C). Response to sample deoxygenation and TT values were detectable, though with difficulties for some of the probes.

Figure 5.3.D shows Int and LT profiles of *E. coli* cells in MMG medium. Only NanO2 probe showed close to normal sigmoidal profiles of Int and LT signals, but its LT baseline was reduced to 15 μs and maximal LT - to 33 μs (Table 7). LT profiles of MitoXpress were close to sigmoidal, but Int profiles were bell-shaped. As for the small molecule derivatives, PtmPEG₄ also showed bell-shaped Int with upward drift and complex LT profiles. Still, response to sample deoxygenation was visible for all the probes, except for Pt1Glc₄. Overall, basal and maximal Int signals of all the probes are reduced 3-6 folds, with PtmPEG₄ baseline Int below the acceptable threshold for respirometry (>30k cps) (304).



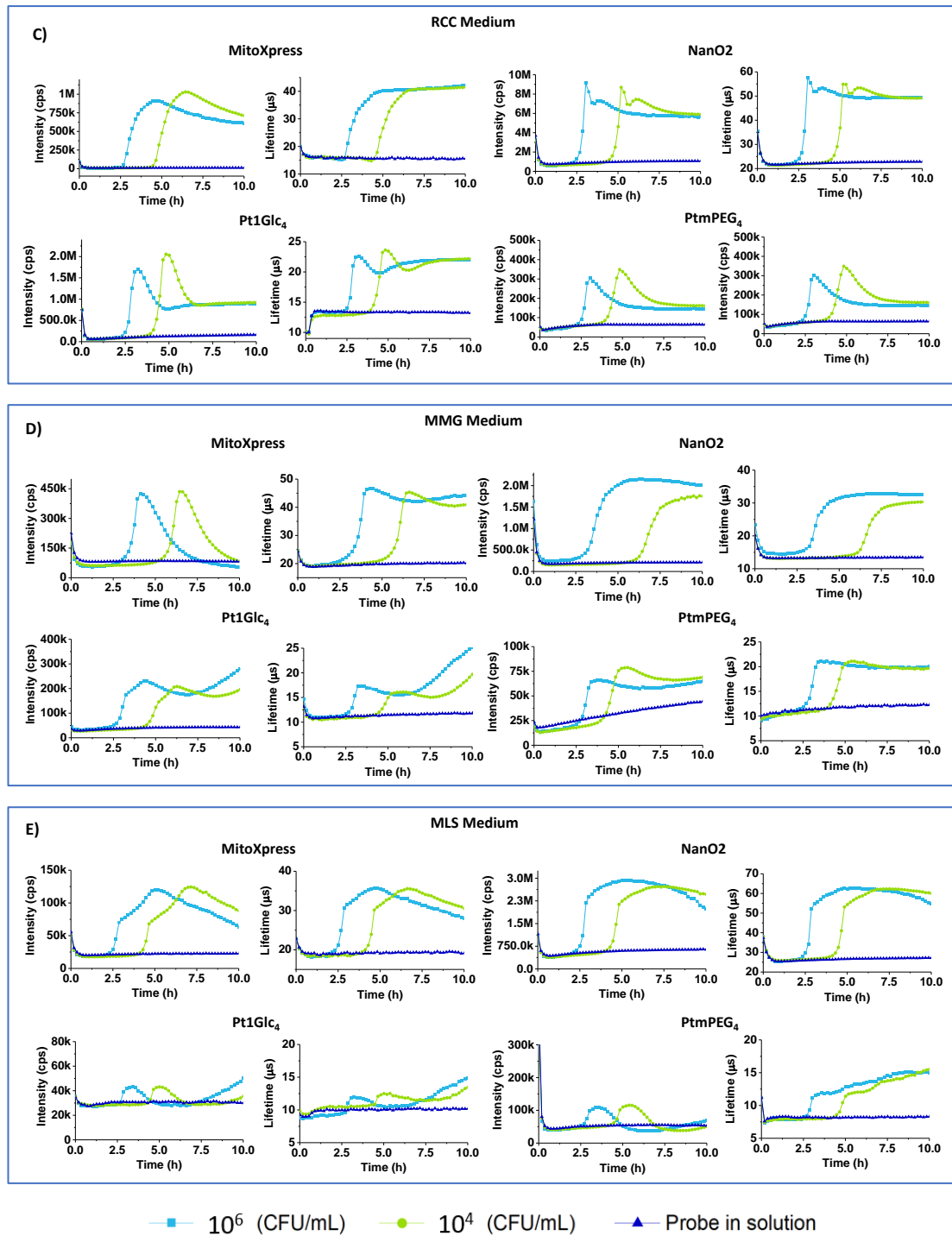


Figure 5.3: TRF intensity (cps) and LT (μ s) profiles of MitoXpress (0.3 μ M), NanO2 (0.3 μ M), Pt1Glc₄ (3 μ M), PtmPEG₄ (3 μ M), in A) NB, B) MC, C) RCC, D) MMG, and E) MLS media with 10^4 and 10^6 *E. coli* cells/mL, at 37 °C. Positive controls containing only the probe solubilised in the sterile media (without cells) are also shown. Data are expressed as mean of three biological replicates, confirmed over two technical replicates.

In MLS medium, only NanO2 retained sufficient brightness and acceptable LT amplitude, with almost sigmoidal profiles. From its lifetime signal it was possible to calculate TT value, however these signals are not stable overtime. MitoXpress probe produced extremely low Int signals and quenched LT, making difficult to use in respirometric assays. Similarly, Pt1Glc₄ and PtmPEG₄ signals were also quenched and unusable in MLS. (Table 7, Figure 5.3. E).

5.2.4. Analysis of individual media components for interferences

Effects on the probe signals and respirometric profiles of *E. coli* cells in the different media can be due to the inner filter effects (IFE), static and dynamic quenching by media components (66).

NB medium is non-selective, and it contains only NaCl, peptone (source of organic nitrogen, amino acids and long chain fatty acids) and yeast extract (source of carbohydrates, vitamins, other organic nitrogen compounds and salts), a refined meat extract (Lab-Lemco) and no other additives (269).

MC medium resembles NB, with yeast extract replaced by bile salts and lactose and added neutral red indicator (pKa=6.9) which changes colour from orange to magenta (Figure 5.1).

MMG medium contains an Fe²⁺ salt, essential vitamins (pantothenic acid), aromatic compounds (thiamine, nicotinic acid), and bromocresol purple (pH indicator) which, when incubated overnight with *E. coli*, turns the medium colour from light purple to pale yellow (269) (Figure 5.1).

RCC medium is almost colourless, it contains peptone, sorbitol and salts, sodium lauryl sulphate (anionic surfactant, 0.1 g/L) and UV chromogenic substrates X-Gal and MUG.

MLS medium contains 1 g/L of SLS surfactant (i.e. 10 times higher than RCC) and phenol red indicator (pKa=8.0) which changes colour from red to orange (Figure 5.1).

The complex composition of the selective media (263) points to possible interfering action by some components on the probe signals, depending on the type of the O₂ probe. We therefore aimed at identifying the interfering components present in the media and their mode of action on the different probes (see supplementary table S1).

For this, we carried out fluorometric titrations of the three probes (MitoXpress, NanO₂ and Pt1Glc₄, at working concentrations in 5.0 g/L NaCl, with individual components of the media. Absorbance spectra and changes in probe Int and LT signals upon addition of the compound were measured in a cuvette, and % of signal change at the concentrations used in the media were calculated (supplementary Table S2).

As expected, simple media components, such as salts (NaCl, phosphates), small-molecule metabolites (saccharides, vitamins, etc.) did not show any significant interference on the probes (data not shown). On the other hand, some of the more complex ingredients (peptone, yeast extract), coloured or chromogenic components (pH indicators, enzyme substrates) and special additives (surfactants, metal ions) did have an effect.

The component *bromocresol purple*, present in MMG, produced Int and LT quenching of all the probes, especially affecting MitoXpress (86% and 32% respectively), pointing to dynamic quenching or solution FRET (305). It is also worth mentioning that BCP, other than a pH indicator, is also used for the determination of serum albumin: it tends to bind quantitatively generating a stable complex with strong absorption at 600 nm. This could explain the belle shaped Int signals of MitoXpress in MMG (306). *Peptone* and *yeast extract* showed significant absorbance at 390 nm and enhancement on Pt1Glc₄ intensity signal by up to 436%, and MitoXpress up to 116%, without affecting their LT values. Since the 'shielded' NanO₂ probe was the least affected, we attribute these effects to binding interactions between the probe phosphor and lipophilic components present in peptone and yeast extract, which can also prevent stacking interactions and/or phosphor aggregation in aqueous solution. The latter hypothesis is supported by the effect of *bile salts* (lipophilic derivatives of

cholesterol), which largely enhanced the Int signals of Pt1Glc₄ (826%), MitoXpress (62%) and NanO₂ (31%) probes, with little effect on the LT. In fact, bile salts are known to form micelles and solubilise hydrophobic molecules (307).

Sodium lauryl sulphate, an anionic surfactant, especially concentrated in the MLS medium (1 g/l), also caused a large enhancement of Int signal of Pt1GlcPt1Glc₄ (268%) and 50% quenching of its LT. MitoXpress Int and LT were moderately quenched (21% and 24% respectively). We attribute these effects to phosphor solubilisation by the SLS and to denaturation of BSA polypeptide, thus changing phosphor's micro-environment and *K_{sv}*. Only marginal effect on NanO₂ probe.

Ferric ammonium citrate showed minor Int and LT quenching of Pt1Glc₄ (9/7%) and MitoXpress (4/12%), while NanO₂ was barely affected. This could be due to the paramagnetic effects of the Fe³⁺ ions (305), combined with the tendency of phenyl groups to co-ordinate Fe³⁺ (307).

MUG (4-methylumbelliferyl-β-D-glucuronide) is a fluorogenic substrate for β-glucuronidase; when hydrolysed, it produces blue fluorescence. *X-Gal* (5-bromo-4-chloro-3-indolyl-β-D-galacto-pyranoside) is a cell-permeable chromogenic substrate of β-galactosidase; when hydrolysed it produces a blue precipitate (λ_{max} 615 nm) and fluorescence at 600-700 nm. Both X-Gal and MUG are present in the RCC medium. They showed quenching of the Int of all the probes 16-17% by MUG and 33-45% by X-Gal), with a minor quenching of the LT by MUG (3-7%), but not by X-Gal.

Two problematic components were the chromogenic *phenol red* (present in MLS) and *neutral red* (in MC) which both strongly absorb at 395 (0.5 and > 3 AbsU respectively) and caused IFE, impeding the measurements of the probes' signals.

All the other compounds, including thiamine (vitamin B1, co-factor for essential enzymes), pantothenic acid (vitamin B5, required for fatty acid biosynthesis) and nicotinic acid (growth factor) were seen to alter probe signals only marginally (Table S2).

5.2.5. Analysis of blank signals and spectroscopic effects of the media

The unusual signal profiles could have instrumental (light scattering, high blanks, low S/N, inaccurate LT calculation, etc.), biological (metabolic switching, changes of cell

density, growth rate), or chemical origin. To elaborate this, we first measured blank Int signals for the samples containing different media with or without cells and no probe, under the settings used in the respirometry. Such blanks appeared to be rather high, ranging from ~3k cps for the MMG to ~7k for the MLS and ~15k cps for the MC when measured at 30-70 μ s (Figure 5.4 A, B). Particularly high background signals were found when measuring at reduced gating time (25 - 50 μ s), which did not allow the signal correction for some of the weakest profiles (Figure 5.4 C, D).

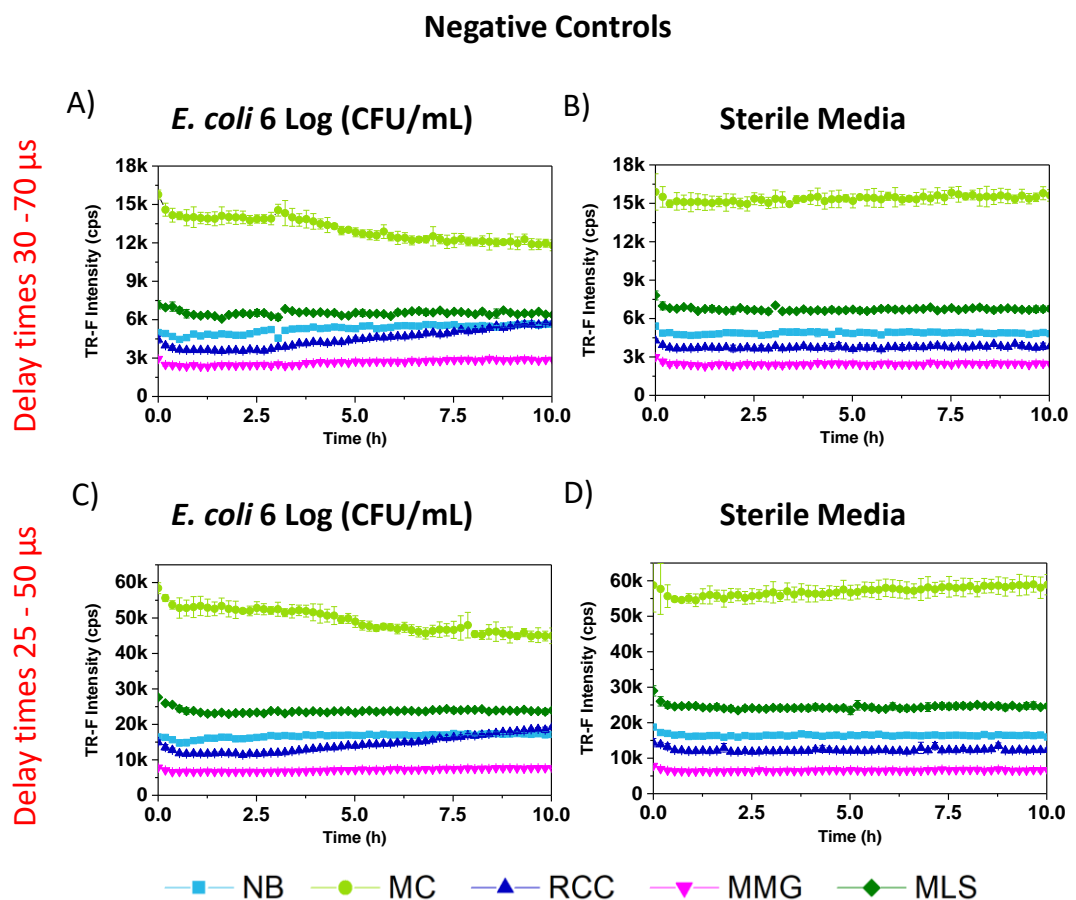


Figure 5.4: Profiles of blank Int signals (no probe) for the different media, recorded at delay times 30 and 70 μ s (A, B), or 25 and 50 μ s (C, D), with 10^6 *E. coli* CFU/mL (A, C) and without *E. coli* (B, D).

The flat profiles of blank signals suggest that cell density (largely increases over 10 h), and sample oxygenation state which occurs at ~2.5 h (Table 8, TT_R) do not significantly alter the Int signal produced by the media itself. So, high blanks do not explain the unusual effects on the respiration profiles of some probes and media. Blank-

correction of Int signals is expected to provide more accurate and stable LT and TT calculation, especially for the probes and media producing low Int signals (308). However, in our case, no improvements were seen.

Table 8. Main parameters of the densitometry profiles (A_{405} and A_{600}) of *E. coli* cells in the different media at 37°C, and comparison of its TT values with respirometry.

Media	Registration wavelength	A_0	A_{max}	TT_D , h	TT_R , h
NB	λ_{405}	0.12	0.26	2.18	2 - 2.2
	λ_{600}	0.04	0.15	2.83	
MC	λ_{405}	0.52	0.88	4.13	2.5 – 2.9
	λ_{600}	0.15	0.51	4.13	
RCC	λ_{405}	0.15	0.32	3.15	2.2 – 2.9
	λ_{600}	0.04	0.21	3.48	
MMG	λ_{405}	0.18	0.33	3.48	2.1 – 2.7
	λ_{600}	0.27	0.13	5.10	
MLS	λ_{405}	>3	n.m.	n.m.	2.2 – 2.9
	λ_{600}	0.25	0.42	4.13	

A - Absorbance (AU), TT_D - Treshold Time for densitometry profiles; TT_R - Treshold Time for respirometry profiles (Figure 3), obtained with *E. coli* at 10^6 CFU/mL. (n.m. = not mesurable).

Next, we carried out analysis of optical densitometry (OD) of the same samples as in O_2 respirometry, measuring absorbance profiles at 405 nm and 600 nm (Figure 5.5). The first wavelength is close to the excitation band (390 nm) of the probes, while the second - to their emission (650 nm). Such measurements were expected to reveal the effects of changing cell density and light scattering during the assay, as well as colour changes in the media induced by metabolising cells. OD600 is commonly used for enumeration of bacteria (309, 310).

The A_{405} profiles of *E. coli* in the different media revealed rather low absorbance values (0.12-0.3 AU) for the NB, MMG and RCC, moderate for MC (0.5-0.9 AU) and very high and practically unusable for MLS ($A_{405} >3$ AU). This data explains the large attenuation of probe Int signals in MLS and moderate attenuation in MC, due to prominent inner filter effect in these media. A_{405} growth profiles are all sigmoidal, however a clear stationary phase is recognizable only in MMG and RCC at 10^6 , while bi-phasic shape is observed in NB and MC.

Compared to the corresponding respiration profiles, signal onset (TT) occurred later in the densitometry, with an approximate delay of 1-2 h in every medium except NB (Figure 5.5, Table 8. TT_D).

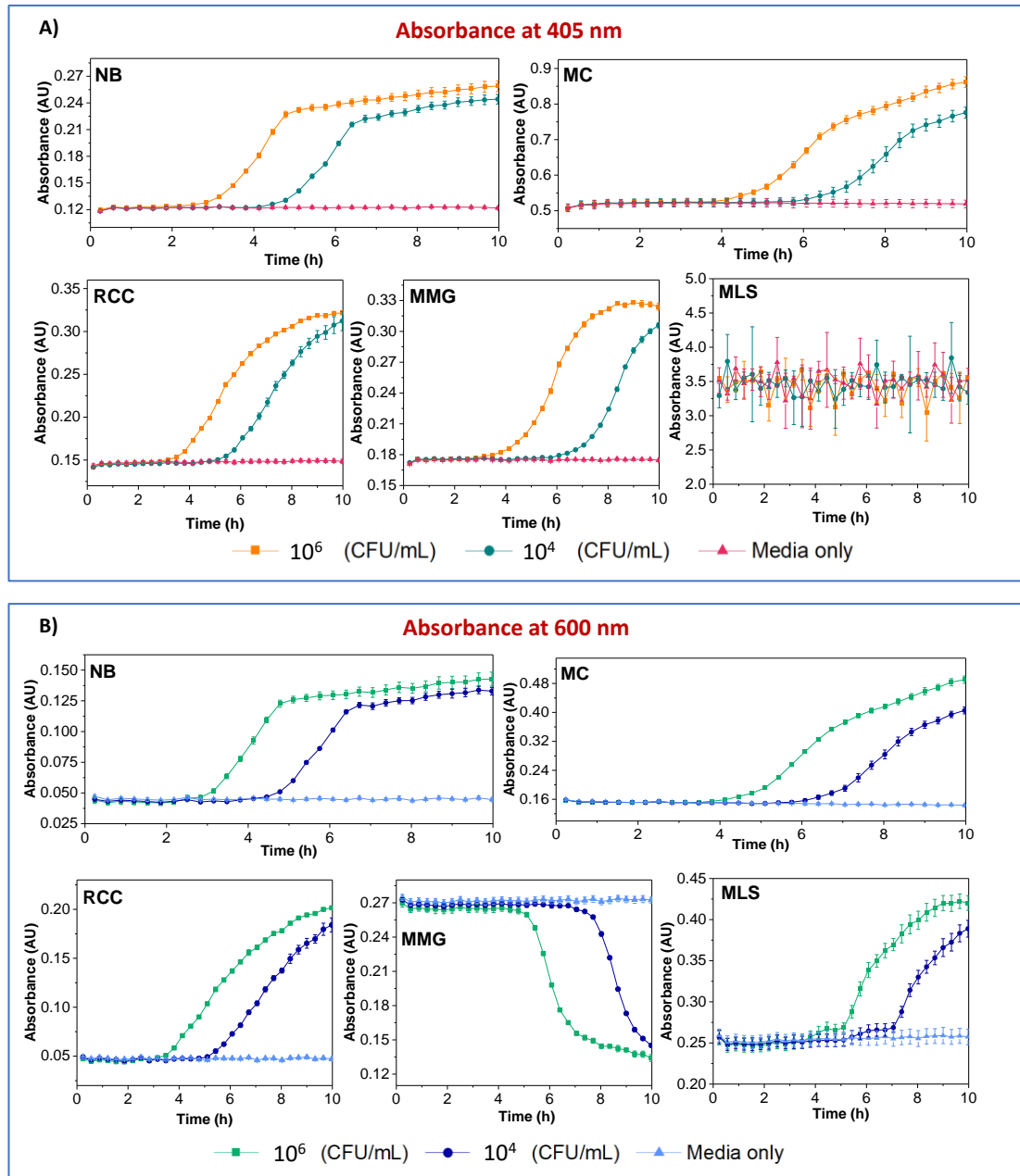


Figure 5.5: Densitometry profiles at 405 nm (A) and 600 nm (B) for the different media and *E. coli* concentrations (zero, 10⁶ and 10⁴ CFU/mL) measured over 10 h period at 37 °C in kinetic mode.

The A₆₀₀ profiles were similar in shape to A₄₀₅ in every media, except for MMG which had inverted shape with no changes occurring in the first 5 h. This could be reflecting the colour change happening in the medium, rather than in the biomass and light scattering. Notably, A₆₀₀ profiles in MLS were measurable, they had sigmoidal shape

and long TT values (>4 h). The observed differences with respirometry data are understandable. While both assays report on cell growth and bacterial cell number, their measured parameters - dissolved O₂ for respirometry and light scattering and absorption for densitometry – have different relationship with cell numbers (237).

5.3. Staining ability of the probes with *E. coli* cells

NanO₂ and Pt1Glc₄ are regarded as cell permeable on mammalian cells, as they can stain cells by simply adding them to the medium with cells and incubating for several hours, thus allowing sensing and imaging of intracellular O₂ concentrations and gradients (160, 177). In contrast, MitoXpress and PtmPEG₄ are instead regarded as cell-impermeable as they poorly stain mammalian cells(106, 256). Phosphorescent cell staining of bacterial cells, such as *E. coli*, has not been studied in detail for all these probes. However, cell-penetrating behaviour of an O₂ probe determined with mammalian cells cannot be simply extrapolated to bacterial cells, which have very different membrane composition, transport mechanisms, growth rates, etc.

Using confocal fluorescence microscopy (311), we performed phosphorescent staining (3 h incubation with suspension of *E. coli* (10⁶ CFU/mL) in NB at 37 °C) and imaging experiments with *E. coli* cells and determined cell-staining behaviour of the probes in conditions of respirometric assays. Phosphorescence intensity images in Figure 5.6 reveals that only NanO₂ probe can efficiently stain *E. coli* cells. The other probes showed no cell staining (MitoXpress) or very few stained cells in the field of view (more cells for PtmPEG₄ than for Pt1Glc₄). We can therefore conclude that only NanO₂ probe can stain *E. coli* cells.

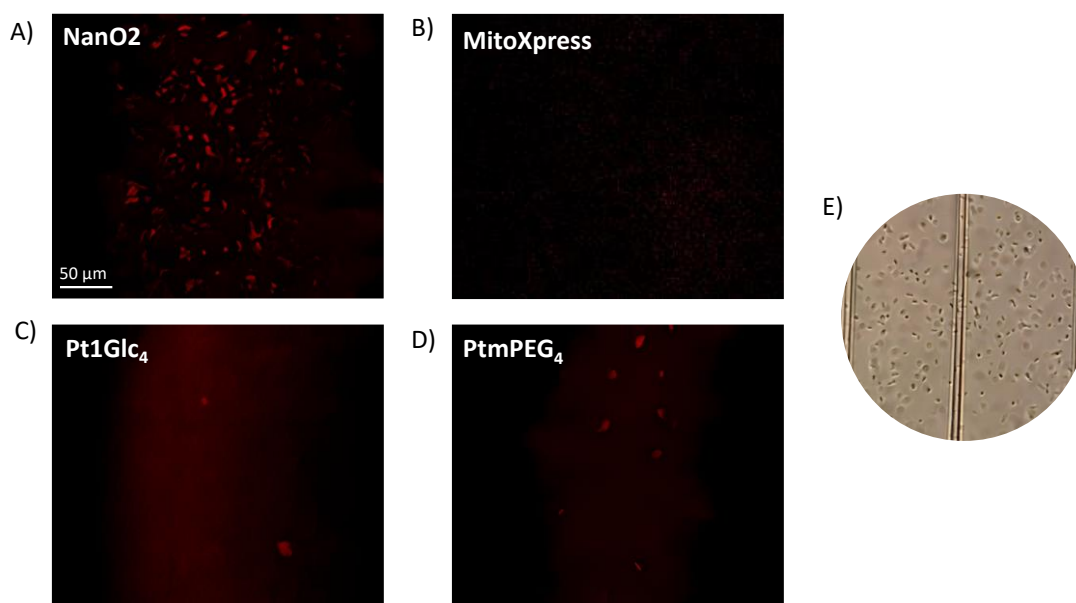


Figure 5.6: Phosphorescence intensity images of a suspension of *E. coli* cells in NB broth, pre-incubated for 3 h at 37 °C with the (A)NanO₂, (B)MitoXpress, (C)Pt1Glc₄, and (D)PtmPEG₄ probes at the working concentrations, measured on a confocal fluorescence microscope. E) Transmission image of *E. coli* in a haemocytometer of a suspension of *E. coli* cells in NB broth.

5.4. Overall comparison and ranking of the probes

The above results reveal that a number of components present in the selected media can influence probe signals and respiration profiles. Moreover, if a medium contains several such components, the overall effect will be additive. While MitoXpress and NanO₂ are able to withstand better such interferences, the small molecular probes PtmPEG₄ and Pt1Glc₄ are more affected due to low S/N and low sensitivity. As a result, such probes produce unusual profiles in this micro-respirometry assay, making them unreliable for quantification of bacteria via TT determination (263).

On the other hand, such quenching interferences and attenuation of O₂ probe Int signals in such assays can potentially be counteracted by i) using a higher probe concentration; ii) choosing brighter probes, such as NanO₂; iii) excluding the main interfering components, provided they are not critical for the intended action of the medium; iv) choosing alternative or new media with different composition but similar

selectivity and lower interferences. Clearly, these strategies have their own limitations (e.g. probe/media availability, assay costs).

Based on their behaviour and analytical performance by comparative analysis of the respiration profiles in the different media, background signals and densitometry, we were able to identify the most resilient and robust probes for use in such media and assay (Table 9). NanO₂ showed consistently lower interferences than the other probes, and it operated reliably in the four out of five complex media, including the most challenging RCC and MLS media. The superiority of NanO₂ is due to its 'shielded' core-shell structure, in which the phosphor molecules sit in the hydrophobic core of the nanoparticle and are not exposed to the aqueous media. Cell-penetrating ability of the NanO₂ in bacterial respirometry applications is also beneficial, as the cell further shields the probe from interfering compounds in the media.

Table 9. A summary of general usability of the probes in the different growth media.

Probe	NB	MC	RCC	MMG	MLS
MitoXpress	+	+	-	+/-	-
NanO ₂	+	+	+/-	+	+
PtmPEG ₄	+/-	-	+/-	-	-
Pt1Glc ₄	-	-	+/-	+/-	-

The benchmark probe MitoXpress, although working reliably in NB and MC, failed to work in RCC and MLS, and to some degree in MMG. Finally, Pt1Glc₄ and PtmPEG₄, although used at 10-times higher concentrations, both performed poorly. Pt1Glc₄ still worked, but with some problems, only in RCC and MMG, while PtmPEG₄ somewhat worked only in NB and RCC. Major limiting features of PtmPEG₄ and Pt1Glc₄ small molecular probes were their short lifetimes, below the instrument temporal resolution, low brightness, and hydrophilicity.

5.5. Conclusions

General usability and performance of the four different types of soluble O₂ probes in respirometric bacterial assays were assessed using *E. coli* cells and five complex media designed for selective bacterial assays. The detailed spectroscopic analysis of this model has revealed multiple interfering and limiting factors, which include high blank signals, low S/N due to light scattering and short-lived autofluorescence combined with the limited temporal resolution limited by the Xe-flashlamp pulse duration (afterglow) (294, 295). This especially affects the probes with short LT values (<15 μs), leading to large measurement errors and inaccurate determination of probe LT by the TRF/RLD method (294). The optical effects of complete media were mainly due to broad absorption bands of the different indicator dyes and spectral changes taking place during the assay (246). All these elements combined caused the 'dim' Pt1Glc₄ and PtmPEG₄ probes to generate unstable LT measurements, and respiration profiles of unusual shape. The asynchronous changes in sample absorbance, light scattering, and probe Int signal, especially when combined with low S/N, may also result in weird bumps and respiration profiles for some probes and media. Moreover, a number of individual media components were seen to interfere with the probes' signals in a probe-specific manner. Coloured substances, such as pH indicators, chromogenic substrates (MUG, X-gal), other UV absorbers, were acting via IFE or solution FRET. Surfactants and lipophilic molecules (e.g. SLS, bile acids) can denature protein-based probes, solubilise the phosphor in small molecules or disturb the nanoparticle structures, thus changing the phosphor's micro-environment and O₂ sensitivity, seen as quenching or enhancement of probe signals. Compounds containing heavy atoms (X-Gal, Ferric ammonium citrate) may cause dynamic or static quenching. Finally, reducing, or oxidizing agents can modify phosphor's structure and its environment. The study aimed to find resilient probes for bacterial micro-respirometry in selective media. The 'shielded' NanO₂ probe showed consistently lower interferences and operated reliably in the four out of five complex media, showing some weakness only in RCC, finishing on top of the list. The 'gold standard' MitoXpress probe was ranked second, as it was usable only in 2-3 out of five media. As for the small molecule probes Pt1Glc₄ and PtmPEG₄ were ranked the least usable,

being hampered by their low brightness, low basal LT signals, and stronger interactions with media components.

Thus, comparative analysis of respiration profiles produced by the different probes and media, allows ranking the probes, based on their ruggedness and operational performance. Overall, the order of performance is: NanO₂ > MitoXpress > Pt1Glc₄ = PtmPEG₄. Therefore, we regard NanO₂ as a viable alternative to MitoXpress probe for bacterial cell micro-respirometry. Similarly, the five media can also be ranked based on their 'harshness' with respect to the O₂ probes, as follows: MLS > MMG > RCC > MC > NB. Considering these factors is crucial for selecting appropriate probes and media for new applications and developing improved O₂ respirometry probes.

OVERALL DISCUSSION

This thesis project aimed at elaborating the SARs for a novel family of hetero-substituted PtPFPP derivatives as phosphorescent O₂ soluble probes. These probes are designed to reduce non-specific binding, increase hydrophilicity, and provide targeted cell recognition. Depending on their molecular charge, size, surface chemistry and aggregation behaviour they provide insight into intra- or extra-cellular respiration and oxygenation status using advanced multi-parametric TRF Intensity and lifetime readouts.

A series of hetero-functionalized PtPFPP derivatives bearing three low molecular weight PEGs or CA moieties, and one glucose moiety have been synthesized via thiol-click covalent modification of the peripheral fluorine atoms of PtPFPP. Overall, this synthetic work generated *six hetero-substituted derivatives*: *PtcPEG₃1Glc*, *PtmPEG₃1Glc*, *PtCA₃1Glc*, and their *2Glc counterparts*, as well as *one symmetric hetero-substituted PtmPEG₂1Glc₂ trans-* derivative. In addition, *three new tetra-substituted derivatives* were also produced: *Pt2Glc₄*, *PtcPEG₄*, and *PtmPEG₄*. The published Pt1Glc₄ (160) was also synthesised and used as a reference compound throughout the study. By optimizing the reaction and purification conditions, we produced 5–10 mg quantities of each compound and intermediates in high yield (70–95% w.r.t. mono-substituted PtPFPP), and purity (>90% by RP-HPLC). As expected, higher glycosylation of the porphyrin core decreased the retention time (RT) on the RP-HPLC and increased hydrophilicity of the probes in the order: PtGlc₄ > PtGlc₃ > PtGlc₂ *cis-* > PtGlc₂ *trans-* > PtGlc₁ > PtPFPP (271). PEGylation had a similar effect, however it provided a lower water solubility, which resulted in a higher tendency to aggregate in aqueous media. Functionalization with Cysteamine also provided high water solubility due to the positive molecular charge.

All the chemical structures, substitution type and symmetry were confirmed by means of ¹H, ¹⁹F and ¹³C NMR and HR-MS. The identification of the *cis-* or *trans-* orientation was based on the literature data (271). UV-Vis and luminescence spectroscopy were utilized to measure absorption and emission spectra, and to determine emission QY (relative to PtPFPP), brightness (emission intensity /

absorption) and phosphorescence LT of the different O₂ probe structures. All the new derivatives show a typical meso-substituted metalloporphyrin Abs spectra with Soret band at 393 nm in DMF and two Q bands. When measured in aqueous buffer (PBS) all derivatives show broad peaks, indicating partial aggregation. In particular, red-shifted absorption maxima at around 400 nm were seen for Pt2Glc₄ and PtmPEG₂1Glc₂ (trans). Red-shifted Soret bands are typical for peripherally crowded non-planar porphyrins, arising from destabilization of the molecular orbitals (HOMO > LUMO). Alternatively, it could be due to the overlap of the aryl substituents with the π-system of the porphyrin macrocycle(312). With regards to the trans-disubstituted derivative PtmPEG₂1Glc₂ (trans), the red-shifted absorption might indicate the formation of a specific J-type of aggregates, due to the symmetry of the substituents which drives the rearrangement of the aggregate into a head-to-tail stacking configuration as the least sterically hindered(276). Emission maxima were all in the typical range 650-652 nm in deoxygenated conditions. Brightness calculations and relative QYs measured in DMF, confirmed that Pt1Glc₄ is the brightest probe among the list thanks to its higher solubility in buffered aqueous media and symmetric chemical structure, preventing potential bending of the macrocycle or bond interference.

To gain insights into potential cell analysis applications of the newly synthesized derivatives, we investigated their cellular uptake and toxicity profiles. An initial screening of the cellular staining efficiency on MEF cells allowed us to select promising derivatives and compare their performance with the reference probe, Pt1Glc₄. These probe structures were further evaluated in biological media assessing intracellular staining, oxygenation profiles, oxygen consumption rates (OCR) of the cells and responses to metabolic stimulation, measured on adherent and suspension cells using four different mammalian cell lines.

The results demonstrated that derivatives bearing three and four PEG oligomers exhibited a much lower cellular uptake compared to the symmetric fully glucosylated Pt1Glc₄ and Pt2Glc₄. The negative charges provided by the carboxy-PEG moieties also prevented efficient interaction with the cell membrane and translocation inside the cell. However, the neutral mPEG derivatives (PtmPEG₄ and PtmPEG₃1Glc) exhibited

behaviour like carboxy-PEG. This suggests that, beyond molecular charge, the diminished uptake is likely caused by their higher molecular size upon H₂O molecules coordination in the aggregate structure (254). Moreover, the amphiphilic nature of PEG chains and lack of cellular targets hindered their passive transport through the lipid layer. Nonetheless, this still allows the use of 3:1 hetero- and tetra-PEGylated derivatives as extracellular O₂ probes.

In contrast, the PtCA₃1Glc derivative demonstrated high cell penetration and intracellular staining ability, facilitated by the positive charge of the amino group, enabling effective interaction with the cell membrane and consequently intracellular bioimaging. Our findings further elucidate that the substitution with 2-Thioethyl- β -D-glucopyranoside (2Glc-SH) leads to a diminished cell staining capability of Pt2Glc₄. This observed reduction is ascribed to the influence of a more flexible corona shell, resulting in compromised photochemistry and increased aggregation tendencies.

Cytotoxicity assessments revealed that, overall, the conjugates did not induce significant impairment of cell viability at the tested concentrations and incubation times, except for PtCA₃1Glc at concentrations exceeding 20 μ M. The observed cytotoxic effects, including rounded cell morphology, suggest partial nuclear penetration, mitochondrial swelling or possible cell membrane disruption due to the strong electrostatic attraction between the positively charged derivative and the negatively charged lipid bilayer.

The intriguing findings with the 2:2 derivative Pt_mPEG₂1Glc₂ (trans), which demonstrated a staining efficiency comparable to Pt1Glc₄, suggest the importance of the conformation and aggregation behaviour of the derivative. This finding is in agreement with the literature (276). The PEGylation of the trans-di-glucosylated PtPFPP intermediate, produced a biocompatible, intracellular O₂ sensing probe, with potential for oxygen bioimaging.

Moreover, when assessing the impact on cell viability, the intermediate Pt1Glc₂ (trans) did not significantly impair cell viability after 3 and 18 hours of incubation. However, prolonged exposure to light during TRF measurements decreased cell viability, indicating phototoxicity at higher concentrations. This phototoxic effect was confirmed by phase-contrast images revealing cell detachment and areas devoid of cells. Thus, Pt1Glc₂ (trans) is deemed unsuitable as an O₂ sensing probe, aligning with

literature findings that *trans*-conformation in porphyrin carbohydrate derivatives favour PDT applications (271, 272). In the same study, the *trans-bis*-glucosylated derivative was reported to be internalized more efficiently than the tetra-glucosylated derivative. Our findings show the opposite, along with increased internalization upon addition of two PEG moieties. However, the different cell lines and methods of analysis used could explain this discrepancy.

The involvement of glucose transporters (GLUTs) in cellular internalization was evaluated using the competitive inhibitor BAY-876 specific for GLUT1, the main isoform expressed in MEF cells. The results indicated that Pt1Glc₄ uptake is more dependent on GLUT1 internalization than the *trans*-di-PEGylated-di-glucosylated derivative. However, other internalization pathways cannot be ruled out for Pt1Glc₄.

The final chapter focuses on the evaluation of the usability and performance of two small molecule probes described in the previous chapters (Pt1Glc₄ and PtmPEG₄) in respirometric bacterial assays, using *E. coli* cells and five complex media. Their respiration profiles and photophysical behaviour was analysed in parallel with two other established soluble probes: MitoXpress (PtCP-BSA conjugate) and the nanoparticle NanO₂.

The detailed spectroscopic analysis of this model has revealed multiple interfering factors, which relate to the instrumentation used, probe structure and photophysical characteristics, and action of particular media components on the probes.

The study identified challenges in oxygen respirometry assays, including high blank signals, low signal-to-noise ratio (S/N) due to light scattering and autofluorescence, and limited temporal resolution. Probes with short phosphorescence lifetimes were particularly affected, leading to measurement errors.

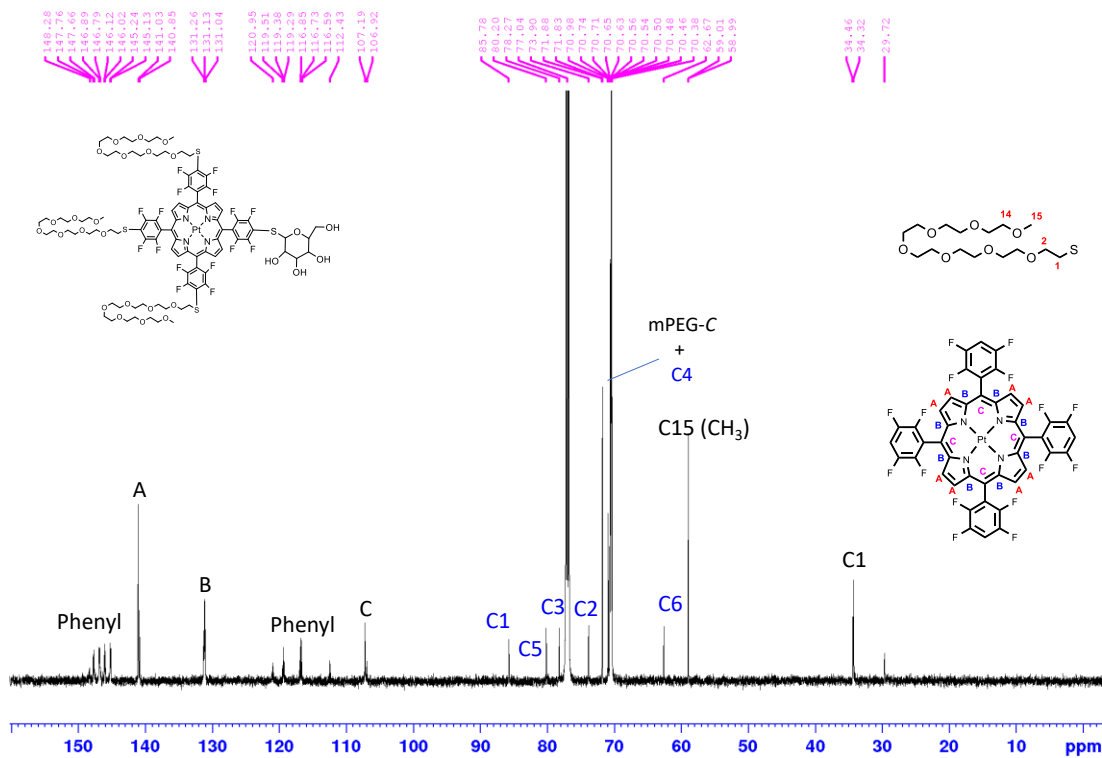
Moreover, media components, including pH indicators and lipophilic molecules, interfered with the probe signals in a probe-specific manner. The purpose of our study was to identify the most resilient and robust probes for use in the described selective media and bacterial micro-respirometry assay. The NanO₂ probe demonstrated lower interferences and reliability across most media, outperforming the 'gold standard' MitoXpress probe, suggesting NanO₂ as a viable alternative.

On the other hand, the small molecule probes Pt1Glc₄ and PtmPEG₄ did not generate acceptable signals and profiles due to lower brightness, shorter lifetimes, and higher degree of interactions with media components. The performance order was NanO₂ > MitoXpress > Pt1Glc₄ = PtmPEG₄. Media were ranked based on their 'harshness' with respect to O₂ probes as MLS > MMG > RCC > MC > NB.

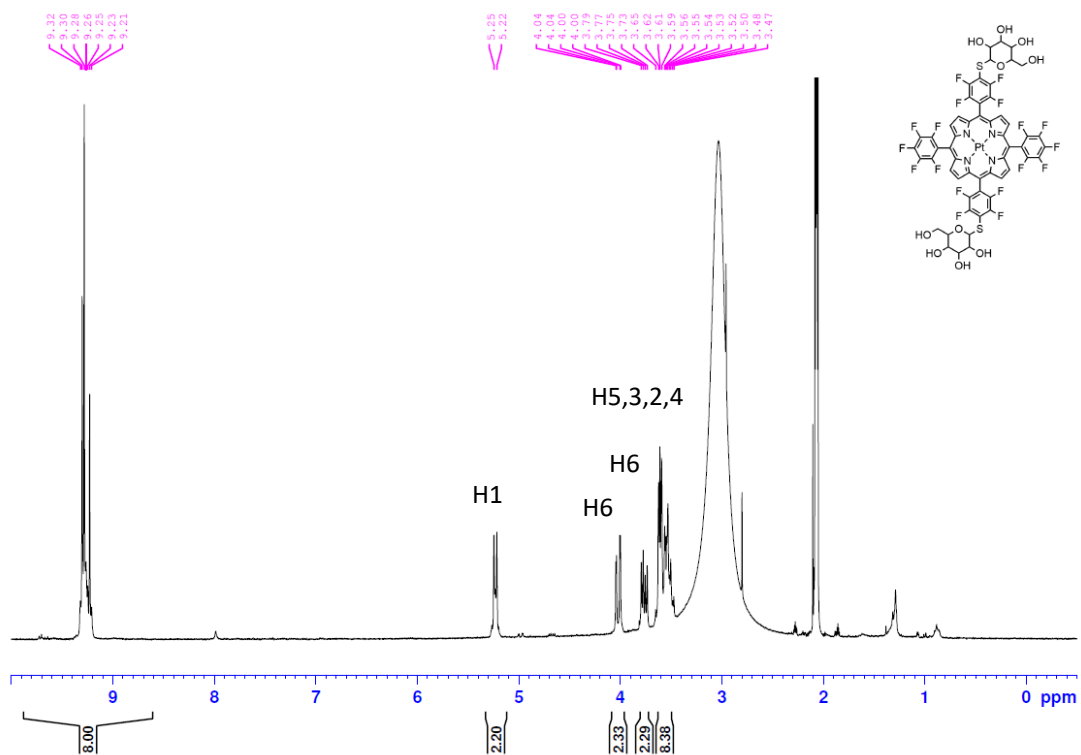
Consideration of these effects and sample/media components is necessary for selecting optimal and appropriate probes and/or media for such applications, and development of new improved probes for O₂ respirometry.

In summary, the comprehensive analysis of the 3:1 and 2:2 derivatives underscore their varying cellular uptake efficiencies, biocompatibility, and involvement of GLUTs in their internalization. The SARs revealed in this study demonstrate how intracellular delivery can be tuned by simple structural modification of the PtPFPP core. However, limitations of this type of small molecule probes were also identified, particularly their shorter lifetimes, reduced sensitivity to O₂ compared to the other porphyrin based O₂ sensing probes, and the lack of shielding from the external environment and potential interfering agents.

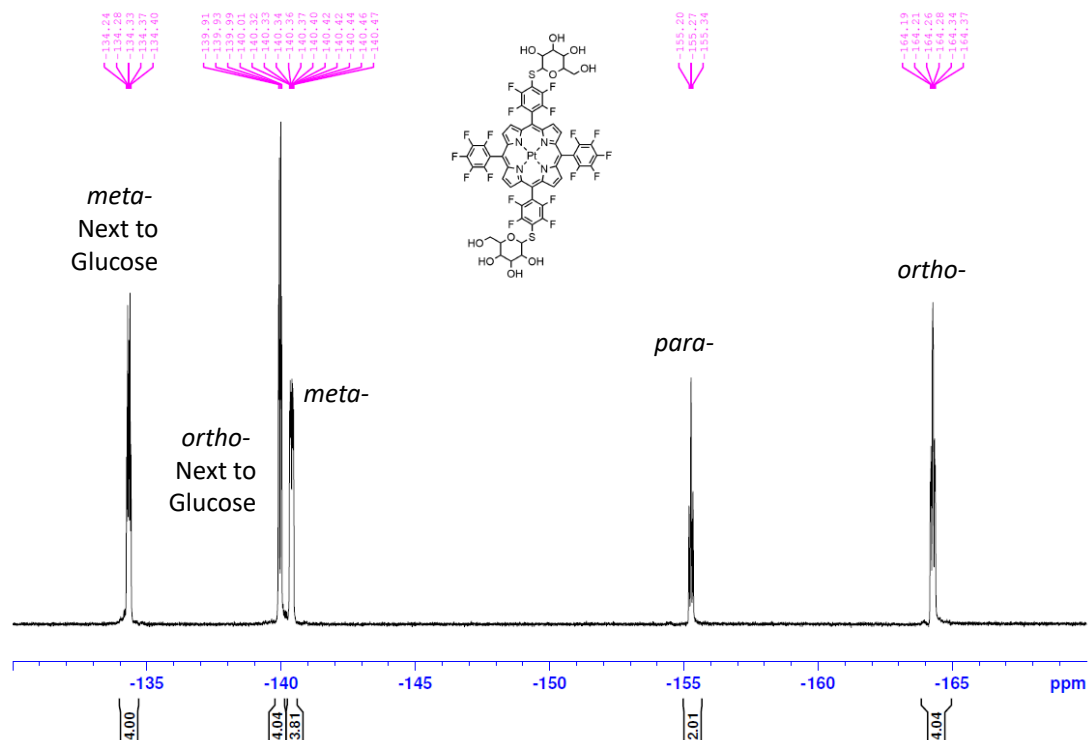
Overall, this probe design produced new soluble small molecule probes with targeted cell delivery, for IC or EC O₂ sensing and cell analysis.



Spectrum S3: ^{13}C NMR Pt mPEG₃₁Glc in CDCl_3 (600 MHz)



Spectrum S4: ^1H NMR Pt1Glc₂ (trans) in $(\text{CD}_3)_2\text{CO}$ (600 MHz)



Spectrum S5: ^{19}F NMR Pt1Glc₂ (trans) in $(\text{CD}_3)_2\text{CO}$ (300 MHz)

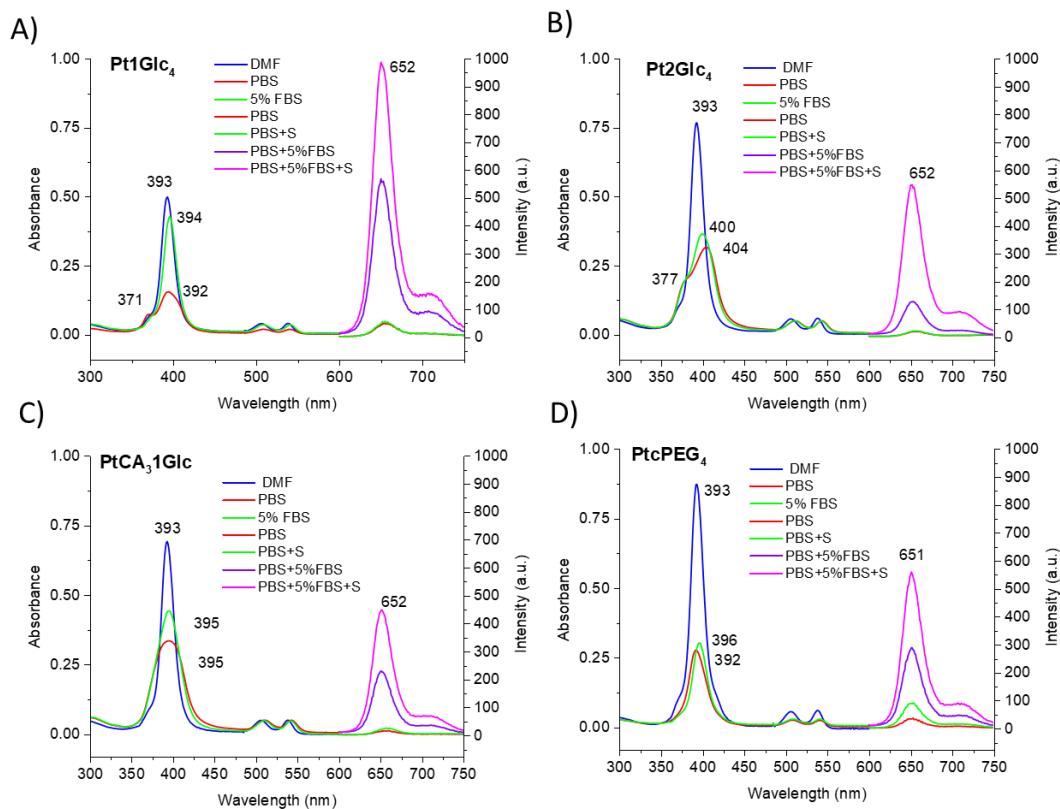


Figure S1: Absorbance and phosphorescence spectra of the synthesized derivatives in DMF, PBS, and 5%FBS in oxygenated and deoxygenated (S) conditions. A) Pt1Glc₄,

B) Pt2Glc₄, C) PtCA₃1Glc, D) PtcPEG₄. Data are expressed as mean of three technical replicates

Table S1. Composition of the different media.

Selective Media	Ingredient	Concentration
Nutrient Broth (NB)	“Lab-lemco” Powder	1.0 g/L
	Peptone	5.0 g/L
	Sodium chloride	5.0 g/L
	yeast extract	2.0 g/L
MacConkey (MC)	Bile salts	5.0 g/L
	neutral red	0.075 g/L
	Peptone	20.0 g/L
	Sodium chloride	5.0 g/L
M-Lauryl Sulfate (MLS)	phenol red	0.2 g/L
	sodium lauryl sulfate	1 g/L
	yeast extract	6 g/L
	lactose	30 g/L
Rapid Coliform ChromoSelect (RCC)	X-gal	0.08 g/L
	MUG (4-Methylumbelliferyl a	0.05 g/L
	IPTG	0.1 g/L
	Peptone	5 g/L
	dipotassium hydrogen phosphate	2.7 g/L
	potassium dihydrogen phosphate	2 g/L
	sodium lauryl sulfate	0.1 g/L
	sorbitol	1 g/L
	sodium chloride	5 g/L
Minerals Modified Glutamate (MMG)	bromocresol purple	0.02 g/L
	ferric ammonium citrate	0.02 g/L
	magnesium sulfate	0.2 g/L
	nicotinic acid	0.002 g/L
	lactose	20 g/L
	pantothenic acid	0.002 g/L
	sodium formate	0.5 g/L
	calcium chloride	0.02 g/L
	L-cystine	0.04 g/L
	dipotassium phosphate	1.8 g/L
	L-arginine	0.04 g/L
	L-aspartic acid	0.048 g/L
	thiamine	0.002 g/L

Table S2. Effects of the different components of the media on the O₂ probes.

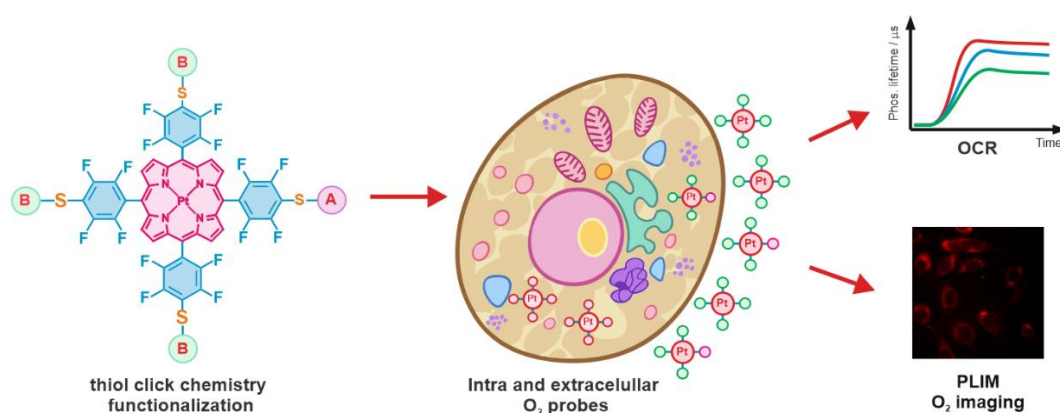
Ingredient	Concentration & Media used	Changes in A ₃₉₀ /A ₆₅₀ %/% at 1x	Quenching of Probe Int and LT signals % /% at 1x		
			NanO2	MitoXpress	Pt1Glc ₄
Lactose	MMG – 20 g/L MLS – 30 g/L	0/0	9.1/3.9	-13.7/0	-25.7/0
L-cystine	MMG - 0.04 g/L	0/0	1.5/0	-1.0/4.5	0.9/0
Thiamine	MMG - 0.002 g/L	0/0	6.5/3.9	0/0	0.6/5.6
Pantothenic acid	MMG - 0.002 g/L	0/0	8.1/3.7	-1.8/4.3	2.3/0
Nicotinic acid	MMG - 0.002 g/L	0/0	-1.4/4	0/0	5.3/0
Bile salts	MC - 5.0 g/L	0/0	-31.1/0	-62.0/4.8	-825/55
Ferric ammonium citrate	MMG - 0.02 g/L	<0.1/0	3.9/0	3.9/12	8.8/6.7
Lab-lemco	NB - 1.0 g/L	0.02/0	-16.3/0	-6.6/0	-17.9/0
Peptone	NB - 5.0 g/L MC - 20 g/L RCC - 5.0 g/L	0.15/0	-1.6/0	-54.4/0	-281/20
Yeast extract	NB - 2.0 g/L MLS - 6g/L	0.5/0	6.1/3.5	-116/4.8	-436/6.3
Sodium lauryl sulphate	MLS - 1 g/L RCC – 0.1 g/L	0/0	3.5/16	21.0/23.8	-268/50
X-gal	RCC - 0.08 g/L	0/0	33.2/3.5	42.9/0	45.0/0
MUG	RCC - 0.05 g/L	0/0	15.9/3.7	17.5/4.2	-16.1/6.7
IPTG	RCC - 0.1 g/L	0/0	6.2/0	-8.4/8.3	1.7/6.7
neutral red	MC - 0.075 g/L	0.5/0.9	n.m. (IFE)	?	?
phenol red	MLS - 0.2 g/L	>3.0/0	n.m. (IFE)	n.m. (IFE)	n.m. (IFE)
bromocresol purple	MMG - 0.02 g/L	0.5/0	47.8/12.0	85.9/31.8	44.7/12.5

n.m. – not measurable; IFE – inner filter effect; * - signal enhancement; Significant effects are shown in red (negative values correspond to signal enhancement).

Thesis Outcomes

Peer reviewed papers:

Chiara Zanetti, Rafael Di Lazaro Gaspar, Alexander V. Zhdanov, Nuala M. Maguire, Susan A. Joyce, Stuart G. Collins, Anita R. Maguire, and Dmitri B. Papkovsky. "Heterosubstituted Derivatives of Ptpfpp for O₂ Sensing and Cell Analysis: Structure–Activity Relationships." *Bioconjugate Chemistry* 33, no. 11 (2022/11/16 2022): 2161-69.



Chiara Zanetti, Liang Li, Rafael Di Lazaro Gaspar, Elisa Santovito, Sophia Elisseeva, Stuart G. Collins, Anita R. Maguire, Dmitri B. Papkovsky. "Susceptibility of the different oxygen-sensing probes to interferences in respirometric bacterial assays with complex media". *Sensors (Basel)*. (2024/01/02): 24(1):267.

Conference proceeding:

Chiara Zanetti, Eimear Larkin, Anita R. Maguire, Dmitri B. Papkovsky. "Hetero-Substituted Derivative of Ptpfpp for Intracellular O₂ Sensing of Mammalian Cells." Paper presented at the Optical Sensors 2023.

Bibliography

1. Papkovsky DB, Kerry JP. Oxygen Sensor-Based Respirometry and the Landscape of Microbial Testing Methods as Applicable to Food and Beverage Matrices. *Sensors (Basel)*. 2023;23(9).
2. Ramamoorthy R, Dutta PK, Akbar SA. Oxygen sensors: Materials, methods, designs and applications. *Journal of Materials Science*. 2003;38(21):4271-82.
3. Bartz RR, Piantadosi CA. Clinical review: Oxygen as a signaling molecule. *Critical Care*. 2010;14(5):234.
4. Brand MD, Nicholls DG. Assessing mitochondrial dysfunction in cells. *Biochem J*. 2011;435(2):297-312.
5. Papkovsky DB, Zhdanov AV. Phosphorescence based O₂ sensors – Essential tools for monitoring cell and tissue oxygenation and its impact on metabolism. *Free Radical Biology and Medicine*. 2016;101:202-10.
6. Semenza GL. Life with oxygen. *Science*. 2007;318(5847):62-4.
7. Karuppanapandian T, Moon J-C, Kim C, Manoharan K, Kim W. Reactive oxygen species in plants: their generation, signal transduction, and scavenging mechanisms. *Australian Journal of Crop Science*. 2011;5(6):709-25.
8. Li Z, Xu X, Leng X, He M, Wang J, Cheng S, Wu H. Roles of reactive oxygen species in cell signaling pathways and immune responses to viral infections. *Arch Virol*. 2017;162(3):603-10.
9. Kulkarni AC, Kuppusamy P, Parinandi N. Oxygen, the lead actor in the pathophysiologic drama: enactment of the trinity of normoxia, hypoxia, and hyperoxia in disease and therapy. *Antioxidants & redox signaling*. 2007;9(10):1717-30.
10. Papkovsky DB, Dmitriev RI. Biological detection by optical oxygen sensing. *Chem Soc Rev*. 2013;42(22):8700-32.
11. Dmitriev RI, Papkovsky DB. Optical probes and techniques for O₂ measurement in live cells and tissue. *Cell Mol Life Sci*. 2012;69(12):2025-39.
12. Coleman ML, Ratcliffe PJ. Oxygen sensing and hypoxia-induced responses. *Essays in biochemistry*. 2007;43:1-15.
13. Berra E, Ginouvès A, Pouyssegur J. The hypoxia-inducible-factor hydroxylases bring fresh air into hypoxia signalling. *EMBO reports*. 2006;7(1):41-5.
14. Azimzadeh M, Khashayar P, Amereh M, Tasnim N, Hoorfar M, Akbari M. Microfluidic-Based Oxygen (O₂) Sensors for On-Chip Monitoring of Cell, Tissue and Organ Metabolism. *Biosensors*. 2022;12(1):6.
15. Khan N, Williams BB, Hou H, Li H, Swartz HM. Repetitive tissue pO₂ measurements by electron paramagnetic resonance oximetry: current status and future potential for experimental and clinical studies. *Antioxidants & redox signaling*. 2007;9(8):1169-82.
16. Mirabello V, Cortezon-Tamarit F, Pascu SI. Oxygen Sensing, Hypoxia Tracing and in Vivo Imaging with Functional Metalloprobes for the Early Detection of Non-communicable Diseases. *Frontiers in Chemistry*. 2018;6(27).
17. dos Santos AIF, de Almeida DQ, Terra LF, Baptista McS, Labriola L. Photodynamic therapy in cancer treatment-an update review. *J cancer metastasis Treat*. 2019;5(25):10.20517.
18. Nam J, Son S, Park KS, Zou W, Shea LD, Moon JJ. Cancer nanomedicine for combination cancer immunotherapy. *Nature Reviews Materials*. 2019;4(6):398-414.
19. Yu W-D, Sun G, Li J, Xu J, Wang X. Mechanisms and therapeutic potentials of cancer immunotherapy in combination with radiotherapy and/or chemotherapy. *Cancer letters*. 2019;452:66-70.

20. Battino R, Rettich TR, Tominaga T. The Solubility of Oxygen and Ozone in Liquids. *Journal of Physical and Chemical Reference Data*. 1983;12:163-78.
21. Wang X-d, Wolfbeis OS. Optical methods for sensing and imaging oxygen: materials, spectroscopies and applications. *Chemical Society Reviews*. 2014;43(10):3666-761.
22. Arnoudse PB, Pardue HL, Bourland JD, Miller R, Geddes LA. Instrumentation for the breath-by-breath determination of oxygen and carbon dioxide based on nondispersive absorption measurements. *Anal Chem*. 1992;64(2):200-4.
23. Golterman HL, editor *The Winkler Determination. Polarographic Oxygen Sensors*; 1983 1983//; Berlin, Heidelberg: Springer Berlin Heidelberg.
24. HOWARD RO, RICHARDSON DW, SMITH MH, PATTERSON Jr JL. Oxygen consumption of arterioles and venules as studied in the Cartesian diver. *Circulation Research*. 1965;16(3):187-96.
25. Van Slyke DD, Neill JM. The determination of gases in blood and other solutions by vacuum extraction and manometric measurement. I. *Journal of Biological Chemistry*. 1924;61(2):523-73.
26. Swinnerton JW, Linnenbom V, Cheek C. Determination of Dissolved Gases in Aqueous Solutions by Gas Chromatography. *Analytical Chemistry*. 1962;34(4):483-5.
27. Wei Y, Jiao Y, An D, Li D, Li W, Wei Q. Review of Dissolved Oxygen Detection Technology: From Laboratory Analysis to Online Intelligent Detection. *Sensors*. 2019;19(18):3995.
28. Marassi V, Giordani S, Kurevija A, Panetta E, Roda B, Zhang N, et al. The Challenges of O₂ Detection in Biological Fluids: Classical Methods and Translation to Clinical Applications. *Int J Mol Sci*. 2022;23(24).
29. Clark JR LC, Wolf R, Granger D, Taylor Z. Continuous recording of blood oxygen tensions by polarography. *Journal of applied physiology*. 1953;6(3):189-93.
30. Roussakis E, Li Z, Nichols AJ, Evans CL. Oxygen-sensing methods in biomedicine from the macroscale to the microscale. *Angewandte Chemie International Edition*. 2015;54(29):8340-62.
31. Melnikov PV, Alexandrovskaya AY, Naumova AO, Arlyapov VA, Kamanina OA, Popova NM, et al. Optical Oxygen Sensing and Clark Electrode: Face-to-Face in a Biosensor Case Study. *Sensors*. 2022;22(19):7626.
32. Carpenter JH. The accuracy of the winkler method for dissolved oxygen analysis 1. *Limnology and Oceanography*. 1965;10(1):135-40.
33. Sinex JE. Pulse oximetry: Principles and limitations. *The American Journal of Emergency Medicine*. 1999;17(1):59-66.
34. Aoyagi T. Pulse oximetry: its invention, theory, and future. *Journal of anesthesia*. 2003;17:259-66.
35. Ferrari M, Mottola L, Quaresima V. Principles, Techniques, and Limitations of Near Infrared Spectroscopy. *Canadian Journal of Applied Physiology*. 2004;29(4):463-87.
36. Pellicer A, Bravo MdC. Near-infrared spectroscopy: A methodology-focused review. *Seminars in Fetal and Neonatal Medicine*. 2011;16(1):42-9.
37. Wahr JA, Tremper KK, Samra S, Delpy DT. Near-Infrared spectroscopy: Theory and applications. *Journal of Cardiothoracic and Vascular Anesthesia*. 1996;10(3):406-18.
38. Rosenberger C, Rosen S, Paliege A, Heyman SN. Pimonidazole Adduct Immunohistochemistry in the Rat Kidney: Detection of Tissue Hypoxia. In: Becker GJ, Hewitson TD, editors. *Kidney Research: Experimental Protocols*. Totowa, NJ: Humana Press; 2009. p. 161-74.
39. Varia MA, Calkins-Adams DP, Rinker LH, Kennedy AS, Novotny DB, Fowler WC, Raleigh JA. Pimonidazole: A Novel Hypoxia Marker for Complementary Study of Tumor Hypoxia and Cell Proliferation in Cervical Carcinoma. *Gynecologic Oncology*. 1998;71(2):270-7.

40. Ruiz-Cabello J, Barnett BP, Bottomley PA, Bulte JWM. Fluorine (¹⁹F) MRS and MRI in biomedicine. *NMR in Biomedicine*. 2011;24(2):114-29.
41. Hare RD, Smith AM, Forster BB, MacKay AL, Whittall KP, Kiehl KA, Liddle PF. Functional magnetic resonance imaging: the basics of blood-oxygen-level dependent (BOLD) imaging. *Canadian Association of Radiologists Journal*. 1998;49(5):320-9.
42. Ogawa S, Lee TM, Nayak AS, Glynn P. Oxygenation-sensitive contrast in magnetic resonance image of rodent brain at high magnetic fields. *Magn Reson Med*. 1990;14(1):68-78.
43. Bobko AA, Dhimitruka I, Eubank TD, Marsh CB, Zweier JL, Khramtsov VV. Trityl-based EPR probe with enhanced sensitivity to oxygen. *Free Radical Biology and Medicine*. 2009;47(5):654-8.
44. Fan AP, An H, Moradi F, Rosenberg J, Ishii Y, Nariai T, et al. Quantification of brain oxygen extraction and metabolism with [¹⁵O]-gas PET: A technical review in the era of PET/MRI. *NeuroImage*. 2020;220:117136.
45. Fleming IN, Manavaki R, Blower PJ, West C, Williams KJ, Harris AL, et al. Imaging tumour hypoxia with positron emission tomography. *British Journal of Cancer*. 2015;112(2):238-50.
46. Vanderkooi JM, Wilson DF. A New Method for Measuring Oxygen Concentration in Biological Systems. In: Longmuir IS, editor. *Oxygen Transport to Tissue VIII*. Boston, MA: Springer US; 1986. p. 189-93.
47. Lübbers D, Opitz N. Quantitative fluorescence photometry with biological fluids and gases. *Oxygen Transport to Tissue—II*. 1976:65-8.
48. Borisov SM. Fundamentals of Quenched Phosphorescence O₂ Sensing and Rational Design of Sensor Materials. In: Papkovsky DB, Dmitriev RI, editors. *Quenched-phosphorescence Detection of Molecular Oxygen: Applications in Life Sciences: The Royal Society of Chemistry*; 2018. p. 0.
49. Charlesworth JM. Optical sensing of oxygen using phosphorescence quenching. *Sensors and Actuators B: Chemical*. 1994;22(1):1-5.
50. Wolfbeis OS. Luminescent sensing and imaging of oxygen: Fierce competition to the Clark electrode. *BioEssays*. 2015;37(8):921-8.
51. Damborský P, Švitel J, Katrlík J. Optical biosensors. *Essays in Biochemistry*. 2016;60(1):91-100.
52. Madsen PL, Secher NH. Near-infrared oximetry of the brain. *Progress in Neurobiology*. 1999;58(6):541-60.
53. Hamaoka T, McCully KK, Niwayama M, Chance B. The use of muscle near-infrared spectroscopy in sport, health and medical sciences: recent developments. *Philos Trans A Math Phys Eng Sci*. 2011;369(1955):4591-604.
54. Macnab AJ, Gagnon RE, Gagnon FA, LeBlanc JG. NIRS monitoring of brain and spinal cord — detection of adverse intraoperative events. *Spectroscopy*. 2003;17:607654.
55. Cheung A, Tu L, Macnab A, Kwon BK, Shadgan B. Detection of hypoxia by near-infrared spectroscopy and pulse oximetry: a comparative study. *J Biomed Opt*. 2022;27(7).
56. Liu J, Qu R, Ogura M, Shibata T, Harada H, Hiraoka M. Real-time imaging of hypoxia-inducible factor-1 activity in tumor xenografts. *Journal of radiation research*. 2005;46(1):93-102.
57. Mason RP, Ran S, Thorpe PE. Quantitative assessment of tumor oxygen dynamics: molecular imaging for prognostic radiology. *Journal of Cellular Biochemistry*. 2002;87(S39):45-53.
58. Liu S, Shah SJ, Wilmes LJ, Feiner J, Kodibagkar VD, Wendland MF, et al. Quantitative tissue oxygen measurement in multiple organs using ¹⁹F MRI in a rat model. *Magnetic resonance in medicine*. 2011;66(6):1722-30.

59. Baudelet C, Gallez B. How does blood oxygen level-dependent (BOLD) contrast correlate with oxygen partial pressure (pO₂) inside tumors? *Magnetic Resonance in Medicine: An Official Journal of the International Society for Magnetic Resonance in Medicine*. 2002;48(6):980-6.
60. Howe F, Robinson S, McIntyre D, Stubbs M, Griffiths J. Issues in flow and oxygenation dependent contrast (FLOOD) imaging of tumours. *NMR in Biomedicine: An International Journal Devoted to the Development and Application of Magnetic Resonance In Vivo*. 2001;14(7-8):497-506.
61. Kmiec MM, Tse D, Mast JM, Ahmad R, Kuppusamy P. Implantable microchip containing oxygen-sensing paramagnetic crystals for long-term, repeated, and multisite in vivo oximetry. *Biomedical Microdevices*. 2019;21:1-16.
62. Chapman JD, Schneider RF, Urbain JL, Hanks GE. Single-photon emission computed tomography and positron-emission tomography assays for tissue oxygenation. *Semin Radiat Oncol*. 2001;11(1):47-57.
63. Rumsey WL, Vanderkooi JM, Wilson DF. Imaging of phosphorescence: a novel method for measuring oxygen distribution in perfused tissue. *Science*. 1988;241(4873):1649-51.
64. Quaranta M, Borisov SM, Klimant I. Indicators for optical oxygen sensors. *Bioanal Rev*. 2012;4(2-4):115-57.
65. Dmitriev RI, Papkovsky DB. Optical probes and techniques for O₂ measurement in live cells and tissue. *Cellular and Molecular Life Sciences*. 2012;69(12):2025-39.
66. Dmitriev RI, Papkovsky DB. *Quenched-phosphorescence Detection of Molecular Oxygen: Applications in Life Sciences: Royal Society of Chemistry; 2018.*
67. Lakowicz J. Lakowicz JR (2006) *Principles of fluorescence spectroscopy*, 3rd edn. Springer, New York, 20062006.
68. Borisov S, Vasil ev V. Formation of singlet oxygen photosensitized by water-soluble metalloporphyrins. *RUSSIAN JOURNAL OF PHYSICAL CHEMISTRY C/C OF ZHURNAL FIZICHESKOI KHIMII*. 2001;75(11):1890-5.
69. Djurovich PI, Murphy D, Thompson ME, Hernandez B, Gao R, Hunt PL, Selke M. Cyclometalated iridium and platinum complexes as singlet oxygen photosensitizers: quantum yields, quenching rates and correlation with electronic structures. *Dalton Transactions*. 2007(34):3763-70.
70. Ogilby PR, Foote CS. Chemistry of singlet oxygen. 36. Singlet molecular oxygen (1. DELTA. g) luminescence in solution following pulsed laser excitation. Solvent deuterium isotope effects on the lifetime of singlet oxygen. *Journal of the American Chemical Society*. 1982;104(7):2069-70.
71. Sies H, de Groot H. Role of reactive oxygen species in cell toxicity. *Toxicology Letters*. 1992;64-65:547-51.
72. Feng Y, Cheng J, Zhou L, Zhou X, Xiang H. Ratiometric optical oxygen sensing: a review in respect of material design. *Analyst*. 2012;137(21):4885-901.
73. Lakowicz JR, editor *Principles of fluorescence spectroscopy*1983.
74. Papkovsky DB. *Methods in Optical Oxygen Sensing: Protocols and Critical Analyses. Methods in Enzymology*. 381: Academic Press; 2004. p. 715-35.
75. Wahba M, El-Enany N, Belal F. Application of the Stern–Volmer equation for studying the spectrofluorimetric quenching reaction of eosin with clindamycin hydrochloride in its pure form and pharmaceutical preparations. *Analytical methods*. 2015;7(24):10445-51.
76. Wu Y, Sutton GD, Halamicek MD, Xing X, Bao J, Teets TS. Cyclometalated iridium-coumarin ratiometric oxygen sensors: improved signal resolution and tunable dynamic ranges. *Chemical Science*. 2022;13(30):8804-12.

77. Hartmann P, Leiner MJP, Lippitsch ME. Response characteristics of luminescent oxygen sensors. *Sensors and Actuators B: Chemical*. 1995;29(1):251-7.
78. Carraway ER, Demas JN, DeGraff BA, Bacon JR. Photophysics and photochemistry of oxygen sensors based on luminescent transition-metal complexes. *Analytical Chemistry*. 1991;63(4):337-42.
79. Demas JN, DeGraff B, Xu W. Modeling of luminescence quenching-based sensors: comparison of multisite and nonlinear gas solubility models. *Analytical Chemistry*. 1995;67(8):1377-80.
80. Tang Y, Tehan EC, Tao Z, Bright FV. Sol-Gel-Derived Sensor Materials That Yield Linear Calibration Plots, High Sensitivity, and Long-Term Stability. *Analytical Chemistry*. 2003;75(10):2407-13.
81. Xu H, Aylott JW, Kopelman R, Miller TJ, Philbert MA. A real-time ratiometric method for the determination of molecular oxygen inside living cells using sol-gel-based spherical optical nanosensors with applications to rat C6 glioma. *Analytical chemistry*. 2001;73(17):4124-33.
82. Larsen M, Borisov SM, Grunwald B, Klimant I, Glud RN. A simple and inexpensive high resolution color ratiometric planar optode imaging approach: application to oxygen and pH sensing. *Limnology and Oceanography: Methods*. 2011;9(9):348-60.
83. Yoshihara T, Yamaguchi Y, Hosaka M, Takeuchi T, Tobita S. Ratiometric molecular sensor for monitoring oxygen levels in living cells. *Angewandte Chemie International Edition*. 2012;51(17):4148-51.
84. Quaranta M, Borisov SM, Klimant I. Indicators for optical oxygen sensors. *Bioanalytical reviews*. 2012;4:115-57.
85. Kostov Y, Rao G. Ratio measurements in oxygen determinations: wavelength ratiometry, lifetime discrimination, and polarization detection. *Sensors and Actuators B: Chemical*. 2003;90(1):139-42.
86. Kostov Y, Van Houten KA, Harms P, Pilato RS, Rao G. Unique Oxygen Analyzer Combining a Dual Emission Probe and a Low-Cost Solid-State Ratiometric Fluorometer. *Applied Spectroscopy*. 2000;54(6):864-8.
87. Neugebauer U, Pellegrin Y, Devocelle M, Forster RJ, Signac W, Moran N, Keyes TE. Ruthenium polypyridyl peptide conjugates: membrane permeable probes for cellular imaging. *Chemical communications*. 2008(42):5307-9.
88. O'Riordan TC, Zhdanov AV, Ponomarev GV, Papkovsky DB. Analysis of intracellular oxygen and metabolic responses of mammalian cells by time-resolved fluorometry. *Anal Chem*. 2007;79(24):9414-9.
89. Sharman KK, Periasamy A, Ashworth H, Demas J. Error analysis of the rapid lifetime determination method for double-exponential decays and new windowing schemes. *Analytical Chemistry*. 1999;71(5):947-52.
90. Yoshihara T, Hirakawa Y, Hosaka M, Nangaku M, Tobita S. Oxygen imaging of living cells and tissues using luminescent molecular probes. *Journal of Photochemistry and Photobiology C: Photochemistry Reviews*. 2017;30:71-95.
91. Birch DJ, Imhof RE. Time-domain fluorescence spectroscopy using time-correlated single-photon counting. *Topics in Fluorescence Spectroscopy: Techniques*; Springer; 1991. p. 1-95.
92. Enderlein J, Erdmann R. Fast fitting of multi-exponential decay curves. *Optics Communications*. 1997;134(1):371-8.
93. Chelushkin PS, Tunik SP. Phosphorescence Lifetime Imaging (PLIM): State of the Art and Perspectives. In: Yamanouchi K, Tunik S, Makarov V, editors. *Progress in Photon Science: Recent Advances*. Cham: Springer International Publishing; 2019. p. 109-28.
94. Suhling K, French PM, Phillips D. Time-resolved fluorescence microscopy. *Photochemical & Photobiological Sciences*. 2005;4(1):13-22.

95. Baggaley E, Weinstein JA, Williams JAG. Time-Resolved Emission Imaging Microscopy Using Phosphorescent Metal Complexes: Taking FLIM and PLIM to New Lengths. In: Lo KK-W, editor. *Luminescent and Photoactive Transition Metal Complexes as Biomolecular Probes and Cellular Reagents*. Berlin, Heidelberg: Springer Berlin Heidelberg; 2015. p. 205-56.
96. Neurauter G, Klimant I, Wolfbeis OS. Fiber-optic microsensors for high resolution pCO₂ sensing in marine environment. *Fresenius' journal of analytical chemistry*. 2000;366:481-7.
97. Tobita S, Yoshihara T. Intracellular and in vivo oxygen sensing using phosphorescent iridium(III) complexes. *Current Opinion in Chemical Biology*. 2016;33:39-45.
98. König K. Multiphoton microscopy in life sciences. *Journal of microscopy*. 2000;200(2):83-104.
99. Zhong W, Urayama P, Mycek M-A. Imaging fluorescence lifetime modulation of a ruthenium-based dye in living cells: the potential for oxygen sensing. *Journal of Physics D: Applied Physics*. 2003;36(14):1689.
100. Alford PC, Cook MJ, Lewis AP, McAuliffe GS, Skarda V, Thomson AJ, et al. Luminescent metal complexes. Part 5. Luminescence properties of ring-substituted 1, 10-phenanthroline tris-complexes of ruthenium (II). *Journal of the Chemical Society, Perkin Transactions 2*. 1985(5):705-9.
101. Cook MJ, Lewis AP, McAuliffe GS, Skarda V, Thomson AJ, Glasper JL, Robbins DJ. Luminescent metal complexes. Part 1. Tris-chelates of substituted 2, 2'-bipyridyls with ruthenium (II) as dyes for luminescent solar collectors. *Journal of the Chemical Society, Perkin Transactions 2*. 1984(8):1293-301.
102. Borisov SM, Klimant I. Ultrabright Oxygen Optodes Based on Cyclometalated Iridium(III) Coumarin Complexes. *Analytical Chemistry*. 2007;79(19):7501-9.
103. Zhang KY, Gao P, Sun G, Zhang T, Li X, Liu S, et al. Dual-phosphorescent iridium (III) complexes extending oxygen sensing from hypoxia to hyperoxia. *Journal of the American Chemical Society*. 2018;140(25):7827-34.
104. Chen Y, Rees TW, Ji L, Chao H. Mitochondrial dynamics tracking with iridium(III) complexes. *Current Opinion in Chemical Biology*. 2018;43:51-7.
105. Koren K, Borisov SM, Saf R, Klimant I. Strongly Phosphorescent Iridium(III)-Porphyrins – New Oxygen Indicators with Tuneable Photophysical Properties and Functionalities. *European Journal of Inorganic Chemistry*. 2011;2011(10):1531-4.
106. O'Riordan TC, Soini AE, Papkovsky DB. Monofunctional derivatives of coproporphyrins for phosphorescent labeling of proteins and binding assays. *Anal Biochem*. 2001;290(2):366-75.
107. Önal E, Ay Z, Yel Z, Ertekin K, Gürek AG, Topal SZ, Hirel C. Design of oxygen sensing nanomaterial: synthesis, encapsulation of phenylacetylide substituted Pd (II) and Pt (II) meso-tetraphenylporphyrins into poly (1-trimethylsilyl-1-propyne) nanofibers and influence of silver nanoparticles. *RSC advances*. 2016;6(12):9967-77.
108. Sommer JR, Shelton AH, Parthasarathy A, Ghiviriga I, Reynolds JR, Schanze KS. Photophysical Properties of Near-Infrared Phosphorescent π -Extended Platinum Porphyrins. *Chemistry of Materials*. 2011;23(24):5296-304.
109. Amao Y, Miyashita T, Okura I. Optical oxygen detection based on luminescence change of metalloporphyrins immobilized in poly (isobutylmethacrylate-co-trifluoroethylmethacrylate) film. *Analytica Chimica Acta*. 2000;421(2):167-74.
110. Borchert NB, Ponomarev GV, Kerry JP, Papkovsky DB. O₂/pH multisensor based on one phosphorescent dye. *Anal Chem*. 2011;83(1):18-22.
111. Hyland MA, Morton MD, Brückner C. meso-Tetrakis(pentafluorophenyl)porphyrin-Derived Chromene-Annulated Chlorins. *The Journal of Organic Chemistry*. 2012;77(7):3038-48.

112. Papkovsky DB, Ponomarev GV, Trettnak W, O'Leary P. Phosphorescent complexes of porphyrin ketones: optical properties and application to oxygen sensing. *Analytical chemistry*. 1995;67(22):4112-7.
113. Sahu A, Dash D, Mishra K, Mishra SP, Yadav R, Kashyap P. Properties and Applications of Ruthenium. 2018.
114. Wang X-y, Del Guerso A, Schmeihl RH. Photophysical behavior of transition metal complexes having interacting ligand localized and metal-to-ligand charge transfer states. *Journal of Photochemistry and Photobiology C: Photochemistry Reviews*. 2004;5(1):55-77.
115. Bansal AK, Holzer W, Penzkofer A, Tsuboi T. Absorption and emission spectroscopic characterization of platinum-octaethyl-porphyrin (PtOEP). *Chemical Physics*. 2006;330(1):118-29.
116. de Haas RR, van Gijlswijk RP, van der Tol EB, Zijlmans HJ, Bakker-Schut T, Bonnet J, et al. Platinum porphyrins as phosphorescent label for time-resolved microscopy. *Journal of Histochemistry & Cytochemistry*. 1997;45(9):1279-92.
117. Lai S-W, Hou Y-J, Che C-M, Pang H-L, Wong K-Y, Chang CK, Zhu N. Electronic spectroscopy, photophysical properties, and emission quenching studies of an oxidatively robust perfluorinated platinum porphyrin. *Inorganic chemistry*. 2004;43(12):3724-32.
118. Chou PT, Chi Y. Phosphorescent dyes for organic light-emitting diodes. *Chemistry—European Journal*. 2007;13(2):380-95.
119. Abayakoon P, Epa R, Petricevic M, Bengt C, Mui JW, van der Peet PL, et al. Comprehensive Synthesis of Substrates, Intermediates, and Products of the Sulfoglycolytic Embden-Meyerhoff-Parnas Pathway. *J Org Chem*. 2019;84(5):2901-10.
120. Tobita S, Yoshihara T. Intracellular and in vivo oxygen sensing using phosphorescent iridium (III) complexes. *Current opinion in chemical biology*. 2016;33:39-45.
121. Paxian M, Keller SA, Cross B, Huynh TT, Clemens MG. High-resolution visualization of oxygen distribution in the liver in vivo. *American Journal of Physiology-Gastrointestinal and Liver Physiology*. 2004;286(1):G37-G44.
122. Zhang S, Hosaka M, Yoshihara T, Negishi K, Iida Y, Tobita S, Takeuchi T. Phosphorescent light-emitting iridium complexes serve as a hypoxia-sensing probe for tumor imaging in living animals. *Cancer research*. 2010;70(11):4490-8.
123. Tsuboyama A, Iwawaki H, Furugori M, Mukaide T, Kamatani J, Igawa S, et al. Homoleptic cyclometalated iridium complexes with highly efficient red phosphorescence and application to organic light-emitting diode. *Journal of the American Chemical Society*. 2003;125(42):12971-9.
124. Yoshihara T, Hosaka M, Terata M, Ichikawa K, Murayama S, Tanaka A, et al. Intracellular and in vivo oxygen sensing using phosphorescent Ir (III) complexes with a modified acetylacetonato ligand. *Analytical chemistry*. 2015;87(5):2710-7.
125. Mei E, Vinogradov S, Hochstrasser RM. Direct observation of triplet state emission of single molecules: single molecule phosphorescence quenching of metalloporphyrin and organometallic complexes by molecular oxygen and their quenching rate distributions. *Journal of the American Chemical Society*. 2003;125(43):13198-204.
126. Papkovsky DB, O'Riordan TC. Emerging Applications of Phosphorescent Metalloporphyrins. *Journal of Fluorescence*. 2005;15(4):569-84.
127. Hynes J, Floyd S, Soini AE, O'Connor R, Papkovsky DB. Fluorescence-based cell viability screening assays using water-soluble oxygen probes. *J Biomol Screen*. 2003;8(3):264-72.
128. Dmitriev RI, Ropiak HM, Ponomarev GV, Yashunsky DV, Papkovsky DB. Cell-Penetrating Conjugates of Coproporphyrins with Oligoarginine Peptides: Rational Design and Application for Sensing Intracellular O₂. *Bioconjugate Chemistry*. 2011;22(12):2507-18.

129. Dmitriev RI, Zhdanov AV, Ponomarev GV, Yashunski DV, Papkovsky DB. Intracellular oxygen-sensitive phosphorescent probes based on cell-penetrating peptides. *Anal Biochem.* 2010;398(1):24-33.
130. Che C-M, Hou Y-J, Chan MCW, Guo J, Liu Y, Wang Y. [meso-Tetrakis(pentafluorophenyl)porphyrinato]platinum(ii) as an efficient, oxidation-resistant red phosphor: spectroscopic properties and applications in organic light-emitting diodes. *Journal of Materials Chemistry.* 2003;13(6):1362-6.
131. Lee S-K, Okura I. Photostable Optical Oxygen Sensing Material: Platinum Tetrakis(pentafluorophenyl)porphyrin Immobilized in Polystyrene. *Analytical Communications.* 1997;34(6):185-8.
132. Haber J, Matachowski L, Pamin K, Poltowicz J. The effect of peripheral substituents in metalloporphyrins on their catalytic activity in Lyons system. *Journal of Molecular Catalysis A: Chemical.* 2003;198(1-2):215-21.
133. Chizhova N, Dmitrieva O, Mamardashvili NZ. Synthesis, Structure, and Spectral Properties of Perhalogenated Metalloporphyrins. *Russian Journal of Inorganic Chemistry.* 2022;67(3):267-75.
134. Schäferling M. The art of fluorescence imaging with chemical sensors. *Angewandte Chemie International Edition.* 2012;51(15):3532-54.
135. Zhang K, Zhang H, Li W, Tian Y, Li S, Zhao J, Li Y. PtOEP/PS composite particles based on fluorescent sensor for dissolved oxygen detection. *Materials Letters.* 2016;172:112-5.
136. Penso CM, Rocha JL, Martins MS, Sousa PJ, Pinto VC, Minas G, et al. PtOEP-PDMS-based optical oxygen sensor. *Sensors.* 2021;21(16):5645.
137. Staudinger C, Borisov SM. Long-wavelength analyte-sensitive luminescent probes and optical (bio) sensors. *Methods and applications in fluorescence.* 2015;3(4):042005.
138. Vinogradov SA, Wilson DF. Metalloporphyrins. New phosphorescent probes for oxygen measurements. *Journal of the Chemical Society, Perkin Transactions 2.* 1995(1):103-11.
139. Graham KR, Yang Y, Sommer JR, Shelton AH, Schanze KS, Xue J, Reynolds JR. Extended Conjugation Platinum(II) Porphyrins for use in Near-Infrared Emitting Organic Light Emitting Diodes. *Chemistry of Materials.* 2011;23(24):5305-12.
140. Borisov SM, Nuss G, Haas W, Saf R, Schmuck M, Klimant I. New NIR-emitting complexes of platinum(II) and palladium(II) with fluorinated benzoporphyrins. *Journal of Photochemistry and Photobiology A: Chemistry.* 2009;201(2):128-35.
141. DiMarco G, Lanza M. Optical solid-state oxygen sensors using metalloporphyrin complexes immobilized in suitable polymeric matrices. *Sensors and Actuators B: Chemical.* 2000;63(1-2):42-8.
142. Xu W, McDonough RC, 3rd, Langsdorf B, Demas JN, DeGraff BA. Oxygen sensors based on luminescence quenching: interactions of metal complexes with the polymer supports. *Anal Chem.* 1994;66(23):4133-41.
143. Banerjee S, Kelly C, Kerry JP, Papkovsky DB. High throughput non-destructive assessment of quality and safety of packaged food products using phosphorescent oxygen sensors. *Trends in Food Science & Technology.* 2016;50:85-102.
144. Li L, Zhdanov AV, Papkovsky DB. Advanced multimodal solid-state optochemical pH and dual pH/O₂ sensors for cell analysis. *Sensors and Actuators B: Chemical.* 2022;371:132486.
145. Banerjee S, Kuznetsova RT, Papkovsky DB. Solid-state oxygen sensors based on phosphorescent diiodo-borondipyrromethene dye. *Sensors and Actuators B: Chemical.* 2015;212:229-34.
146. Papkovsky DB, Ovchinnikov AN, Ogurtsov VI, Ponomarev GV, Korpela T. Biosensors on the basis of luminescent oxygen sensor: the use of microporous light-scattering support materials. *Sensors and Actuators B: Chemical.* 1998;51(1-3):137-45.

147. Liu Q, Vo-Dinh T. Spectral filtering modulation method for estimation of hemoglobin concentration and oxygenation based on a single fluorescence emission spectrum in tissue phantoms. *Med Phys*. 2009;36(10):4819-29.
148. Wang X-D, Wolfbeis OS. *Fiber-Optic Chemical Sensors and Biosensors (2008–2012)*. *Analytical Chemistry*. 2013;85(2):487-508.
149. Kocincova AS, Borisov SM, Krause C, Wolfbeis OS. Fiber-Optic Microsensors for Simultaneous Sensing of Oxygen and pH, and of Oxygen and Temperature. *Analytical Chemistry*. 2007;79(22):8486-93.
150. Braun RD, Lanzen JL, Snyder SA, Dewhirst MW. Comparison of tumor and normal tissue oxygen tension measurements using OxyLite or microelectrodes in rodents. *American Journal of Physiology-Heart and Circulatory Physiology*. 2001;280(6):H2533-H44.
151. Griffiths J, Robinson S. The OxyLite: a fibre-optic oxygen sensor. *The British journal of radiology*. 1999;72(859):627-30.
152. Wu W, Ji S, Wu W, Guo H, Wang X, Zhao J, Wang Z. Enhanced luminescence oxygen sensing property of Ru(II) bispyridine complexes by ligand modification. *Sensors and Actuators B: Chemical*. 2010;149(2):395-406.
153. Koren K, Borisov SM, Klimant I. Stable optical oxygen sensing materials based on click-coupling of fluorinated platinum (II) and palladium (II) porphyrins—A convenient way to eliminate dye migration and leaching. *Sensors and Actuators B: Chemical*. 2012;169:173-81.
154. Tian Y, Shumway BR, Meldrum DR. A new cross-linkable oxygen sensor covalently bonded into poly (2-hydroxyethyl methacrylate)-co-polyacrylamide thin film for dissolved oxygen sensing. *Chemistry of Materials*. 2010;22(6):2069-78.
155. Borisov SM, Lehner P, Klimant I. Novel optical trace oxygen sensors based on platinum (II) and palladium (II) complexes with 5, 10, 15, 20-meso-tetrakis-(2, 3, 4, 5, 6-pentafluorophenyl)-porphyrin covalently immobilized on silica-gel particles. *Analytica Chimica Acta*. 2011;690(1):108-15.
156. Toncelli C, Arzhakova OV, Dolgova A, Volynskii AL, Kerry JP, Papkovsky DB. Phosphorescent oxygen sensors produced by spot-crazing of polyphenylenesulfide films. *Journal of Materials Chemistry C*. 2014;2(38):8035-41.
157. Toncelli C, Arzhakova OV, Dolgova A, Volynskii AL, Bakeev NF, Kerry JP, Papkovsky DB. Oxygen-sensitive phosphorescent nanomaterials produced from high-density polyethylene films by local solvent-crazing. *Analytical chemistry*. 2014;86(3):1917-23.
158. Kelly C, Yusufu D, Okkelman I, Banerjee S, Kerry JP, Mills A, Papkovsky DB. Extruded phosphorescence based oxygen sensors for large-scale packaging applications. *Sensors and Actuators B: Chemical*. 2020;304:127357.
159. Yusufu D, Han R, Mills A. 3D printed O₂ indicators. *Analyst*. 2020;145(12):4124-9.
160. Dmitriev R, Kondrashina A, Koren K, Klimant I, Zhdanov A, Pakan J, et al. Small molecule phosphorescent probes for O₂ imaging in 3D tissue models. *Biomaterials Science*. 2014;2.
161. Fercher A, Ponomarev GV, Yashunski D, Papkovsky D. Evaluation of the derivatives of phosphorescent Pt-coproporphyrin as intracellular oxygen-sensitive probes. *Analytical and bioanalytical chemistry*. 2010;396:1793-803.
162. Ji J, Rosenzweig N, Jones I, Rosenzweig Z. Novel fluorescent oxygen indicator for intracellular oxygen measurements. *Journal of biomedical optics*. 2002;7(3):404-9.
163. Koren K, Borisov SM, Saf R, Klimant I. Strongly phosphorescent iridium (III)–porphyrins—new oxygen indicators with tuneable photophysical properties and functionalities. *Wiley Online Library*; 2011.
164. Dunphy I, Vinogradov SA, Wilson DF. Oxyphor R2 and G2: phosphors for measuring oxygen by oxygen-dependent quenching of phosphorescence. *Analytical Biochemistry*. 2002;310(2):191-8.

165. Vinogradov SA, Lo L-W, Wilson DF. Dendritic Polyglutamic Porphyrins: Probing Porphyrin Protection by Oxygen-Dependent Quenching of Phosphorescence. *Chemistry – A European Journal*. 1999;5(4):1338-47.
166. Ceroni P, Lebedev AY, Marchi E, Yuan M, Esipova TV, Bergamini G, et al. Evaluation of phototoxicity of dendritic porphyrin-based phosphorescent oxygen probes: an in vitro study. *Photochemical & Photobiological Sciences*. 2011;10(6):1056-65.
167. Lebedev AY, Cheprakov AV, Sakadzic S, Boas DA, Wilson DF, Vinogradov SA. Dendritic phosphorescent probes for oxygen imaging in biological systems. *ACS applied materials & interfaces*. 2009;1(6):1292-304.
168. Lebedev AY, Cheprakov AV, Sakadžić S, Boas DA, Wilson DF, Vinogradov SA. Dendritic Phosphorescent Probes for Oxygen Imaging in Biological Systems. *ACS Applied Materials & Interfaces*. 2009;1(6):1292-304.
169. Koo Lee Y-E, Ulbrich EE, Kim G, Hah H, Strollo C, Fan W, et al. Near Infrared Luminescent Oxygen Nanosensors with Nanoparticle Matrix Tailored Sensitivity. *Analytical Chemistry*. 2010;82(20):8446-55.
170. Sumner JP, Westerberg NM, Stoddard AK, Fierke CA, Kopelman R. Cu⁺- and Cu²⁺-sensitive PEBBLE fluorescent nanosensors using DsRed as the recognition element. *Sensors and Actuators B: Chemical*. 2006;113(2):760-7.
171. Cywinski PJ, Moro AJ, Stanca SE, Biskup C, Mohr GJ. Ratiometric porphyrin-based layers and nanoparticles for measuring oxygen in biosamples. *Sensors and Actuators B: Chemical*. 2009;135(2):472-7.
172. Kondrashina AV, Dmitriev RI, Borisov SM, Klimant I, O'Brien I, Nolan YM, et al. A phosphorescent nanoparticle-based probe for sensing and imaging of (intra) cellular oxygen in multiple detection modalities. *Advanced Functional Materials*. 2012;22(23):4931-9.
173. Borisov SM, Mayr T, Mistlberger G, Waich K, Koren K, Chojnacki P, Klimant I. Precipitation as a simple and versatile method for preparation of optical nanochemosensors. *Talanta*. 2009;79(5):1322-30.
174. Buck SM, Koo Y-EL, Park E, Xu H, Philbert MA, Brasuel MA, Kopelman R. Optochemical nanosensor PEBBLEs: photonic explorers for bioanalysis with biologically localized embedding. *Current opinion in chemical biology*. 2004;8(5):540-6.
175. Clark HA, Hoyer M, Philbert MA, Kopelman R. Optical nanosensors for chemical analysis inside single living cells. 1. Fabrication, characterization, and methods for intracellular delivery of PEBBLE sensors. *Analytical chemistry*. 1999;71(21):4831-6.
176. Koo Y-EL, Cao Y, Kopelman R, Koo SM, Brasuel M, Philbert MA. Real-Time Measurements of Dissolved Oxygen Inside Live Cells by Organically Modified Silicate Fluorescent Nanosensors. *Analytical Chemistry*. 2004;76(9):2498-505.
177. Fercher A, Borisov SM, Zhdanov AV, Klimant I, Papkovsky DB. Intracellular O₂ sensing probe based on cell-penetrating phosphorescent nanoparticles. *ACS Nano*. 2011;5(7):5499-508.
178. Kondrashina AV, Dmitriev RI, Borisov SM, Klimant I, O'Brien I, Nolan YM, et al. A Phosphorescent Nanoparticle-Based Probe for Sensing and Imaging of (Intra)Cellular Oxygen in Multiple Detection Modalities. *Advanced Functional Materials*. 2012;22(23):4931-9.
179. Wang X-H, Peng H-S, Chang Z, Hou L-L, You F-T, Teng F, et al. Synthesis of ratiometric fluorescent nanoparticles for sensing oxygen. *Microchimica Acta*. 2012;178:147-52.
180. Ashokkumar P, Adarsh N, Klymchenko AS. Ratiometric nanoparticle probe based on FRET-amplified phosphorescence for oxygen sensing with minimal phototoxicity. *Small*. 2020;16(32):2002494.
181. Kitagawa S. Metal-organic frameworks (MOFs). *Chemical Society Reviews*. 2014;43(16):5415-8.

182. Lu K, Aung T, Guo N, Weichselbaum R, Lin W. Nanoscale metal–organic frameworks for therapeutic, imaging, and sensing applications. *Advanced Materials*. 2018;30(37):1707634.
183. Xu R, Wang Y, Duan X, Lu K, Micheroni D, Hu A, Lin W. Nanoscale Metal–Organic Frameworks for Ratiometric Oxygen Sensing in Live Cells. *Journal of the American Chemical Society*. 2016;138(7):2158-61.
184. Dou Z, Yu J, Cui Y, Yang Y, Wang Z, Yang D, Qian G. Luminescent Metal–Organic Framework Films As Highly Sensitive and Fast-Response Oxygen Sensors. *Journal of the American Chemical Society*. 2014;136(15):5527-30.
185. Barrett SM, Wang C, Lin W. Oxygen sensing via phosphorescence quenching of doped metal–organic frameworks. *Journal of Materials Chemistry*. 2012;22(20):10329-34.
186. Qi X, Shen N, Al Othman A, Mezentssev A, Permyakova A, Yu Z, et al. Metal-Organic Framework-Based Nanomedicines for the Treatment of Intracellular Bacterial Infections. *Pharmaceutics*. 2023;15(5):1521.
187. Linnane E, Haddad S, Melle F, Mei Z, Fairen-Jimenez D. The uptake of metal–organic frameworks: A journey into the cell. *Chemical Society Reviews*. 2022.
188. Lan G, Ni K, You E, Wang M, Culbert A, Jiang X, Lin W. Multifunctional Nanoscale Metal–Organic Layers for Ratiometric pH and Oxygen Sensing. *Journal of the American Chemical Society*. 2019;141(48):18964-9.
189. Pan T, Yang C, Shi J, Hao C, Qiao Y, Li J, et al. Dual pH and oxygen luminescent nanoprobes based on graft polymers for extracellular metabolism monitoring and intracellular imaging. *Sensors and Actuators B: Chemical*. 2019;291:306-18.
190. Fercher A, Ponomarev GV, Yashunski D, Papkovsky D. Evaluation of the derivatives of phosphorescent Pt-coproporphyrin as intracellular oxygen-sensitive probes. *Analytical and Bioanalytical Chemistry*. 2010;396(5):1793-803.
191. Dolan C, Moriarty RD, Lestini E, Devocelle M, Forster RJ, Keyes TE. Cell uptake and cytotoxicity of a novel cyclometalated iridium(III) complex and its octaarginine peptide conjugate. *Journal of Inorganic Biochemistry*. 2013;119:65-74.
192. Schmäzlín E, Van Dongen JT, Klimant I, Marmodée B, Steup M, Fisahn J, et al. An optical multifrequency phase-modulation method using microbeads for measuring intracellular oxygen concentrations in plants. *Biophysical Journal*. 2005;89(2):1339-45.
193. Wang X-d, Stolwijk JA, Lang T, Sperber M, Meier RJ, Wegener J, Wolfbeis OS. Ultra-small, highly stable, and sensitive dual nanosensors for imaging intracellular oxygen and pH in cytosol. *Journal of the American Chemical Society*. 2012;134(41):17011-4.
194. Zhdanov AV, Okkelman IA, Collins FW, Melgar S, Papkovsky DB. A novel effect of DMOG on cell metabolism: direct inhibition of mitochondrial function precedes HIF target gene expression. *Biochimica et Biophysica Acta (BBA)-Bioenergetics*. 2015;1847(10):1254-66.
195. Summerton JE. Endo-Porter: a novel reagent for safe, effective delivery of substances into cells. *Ann N Y Acad Sci*. 2005;1058:62-75.
196. O'Riordan TsC, Fitzgerald K, Ponomarev GV, Mackrill J, Hynes J, Taylor C, Papkovsky DB. Sensing intracellular oxygen using near-infrared phosphorescent probes and live-cell fluorescence imaging. *American Journal of Physiology-Regulatory, Integrative and Comparative Physiology*. 2007;292(4):R1613-R20.
197. O'Riordan TC, Fitzgerald K, Ponomarev GV, Mackrill J, Hynes J, Taylor C, Papkovsky DB. Sensing intracellular oxygen using near-infrared phosphorescent probes and live-cell fluorescence imaging. *Am J Physiol Regul Integr Comp Physiol*. 2007;292(4):R1613-20.
198. Murase T, Yoshihara T, Tobita S. Mitochondria-specific oxygen probe based on iridium complexes bearing triphenylphosphonium cation. *Chemistry Letters*. 2012;41(3):262-3.

199. Ballut S, Makky A, Chauvin B, Michel J-P, Kasselouri A, Maillard P, Rosilio V. Tumor targeting in photodynamic therapy. From glycoconjugated photosensitizers to glycodendrimeric one. Concept, design and properties. *Organic & Biomolecular Chemistry*. 2012;10(23):4485-95.
200. Chen X, Hui L, Foster DA, Drain CM. Efficient synthesis and photodynamic activity of porphyrin-saccharide conjugates: targeting and incapacitating cancer cells. *Biochemistry*. 2004;43(34):10918-29.
201. Komatsu H, Yoshihara K, Yamada H, Kimura Y, Son A, Nishimoto Si, Tanabe K. Ruthenium complexes with hydrophobic ligands that are key factors for the optical imaging of physiological hypoxia. *Chemistry—A European Journal*. 2013;19(6):1971-7.
202. Kersemans V, Cornelissen B. Targeting the Tumour: Cell Penetrating Peptides for Molecular Imaging and Radiotherapy. *Pharmaceuticals*. 2010;3(3):600-20.
203. Dmitriev RI, Ropiak HM, Yashunsky DV, Ponomarev GV, Zhdanov AV, Papkovsky DB. Bactenecin 7 peptide fragment as a tool for intracellular delivery of a phosphorescent oxygen sensor. *Febs j*. 2010;277(22):4651-61.
204. Yoshihara T, Murayama S, Masuda T, Kikuchi T, Yoshida K, Hosaka M, Tobita S. Mitochondria-targeted oxygen probes based on cationic iridium complexes with a 5-amino-1, 10-phenanthroline ligand. *Journal of Photochemistry and Photobiology A: Chemistry*. 2015;299:172-82.
205. Mašek J, Bartheldyová E, Korvasová Z, Škrabalová M, Koudelka Š, Kulich P, et al. Immobilization of histidine-tagged proteins on monodisperse metallochelation liposomes: Preparation and study of their structure. *Analytical biochemistry*. 2011;408(1):95-104.
206. Soh N. Selective chemical labeling of proteins with small fluorescent molecules based on metal-chelation methodology. *Sensors*. 2008;8(2):1004-24.
207. Dmitriev RI, O'Donnell N, Papkovsky DB. Metallochelate Coupling of Phosphorescent Pt-Porphyrins to Peptides, Proteins, and Self-Assembling Protein Nanoparticles. *Bioconjugate Chemistry*. 2016;27(2):439-45.
208. Glymenaki E, Kandyli M, Apostolidou CP, Kokotidou C, Charalambidis G, Nikoloudakis E, et al. Design and Synthesis of Porphyrin–Nitrilotriacetic Acid Dyads with Potential Applications in Peptide Labeling through Metallochelate Coupling. *ACS omega*. 2022;7(2):1803-18.
209. Borisov SM, Pommer R, Svec J, Peters S, Novakova V, Klimant I. New red-emitting Schiff base chelates: Promising dyes for sensing and imaging of temperature and oxygen via phosphorescence decay time. *Journal of Materials Chemistry C*. 2018;6(33):8999-9009.
210. Esipova TV, Barrett MJP, Erlebach E, Masunov AE, Weber B, Vinogradov SA. Oxyphor 2P: A High-Performance Probe for Deep-Tissue Longitudinal Oxygen Imaging. *Cell Metabolism*. 2019;29(3):736-44.e7.
211. Liu H, Yang H, Hao X, Xu H, Lv Y, Xiao D, et al. Development of Polymeric Nanoprobes with Improved Lifetime Dynamic Range and Stability for Intracellular Oxygen Sensing. *Small*. 2013;9(15):2639-48.
212. Tsytsarev V, Arakawa H, Borisov S, Pumbo E, Erzurumlu RS, Papkovsky DB. In vivo imaging of brain metabolism activity using a phosphorescent oxygen-sensitive probe. *Journal of Neuroscience Methods*. 2013;216(2):146-51.
213. Bhatti JS, Bhatti GK, Reddy PH. Mitochondrial dysfunction and oxidative stress in metabolic disorders—A step towards mitochondria based therapeutic strategies. *Biochimica et Biophysica Acta (BBA)-Molecular Basis of Disease*. 2017;1863(5):1066-77.
214. Picard M, Taivassalo T, Gouspillou G, Hepple RT. Mitochondria: isolation, structure and function. *The Journal of physiology*. 2011;589(18):4413-21.
215. Schmidt CA, Fisher-Wellman KH, Neuffer PD. From OCR and ECAR to energy: Perspectives on the design and interpretation of bioenergetics studies. *Journal of Biological Chemistry*. 2021;297(4).

216. Brand MD, Nicholls DG. Assessing mitochondrial dysfunction in cells. *Biochemical Journal*. 2011;435(2):297-312.
217. Will Y, Hynes J, Ogurtsov VI, Papkovsky DB. Analysis of mitochondrial function using phosphorescent oxygen-sensitive probes. *Nature Protocols*. 2006;1(6):2563-72.
218. Cantor JR. The Rise of Physiologic Media. *Trends Cell Biol*. 2019;29(11):854-61.
219. Herst PM, Tan AS, Scarlett D-JG, Berridge MV. Cell surface oxygen consumption by mitochondrial gene knockout cells. *Biochimica et Biophysica Acta (BBA) - Bioenergetics*. 2004;1656(2):79-87.
220. Kondrashina AV, Ogurtsov VI, Papkovsky DB. Comparison of the three optical platforms for measurement of cellular respiration. *Analytical biochemistry*. 2015;468:1-3.
221. Hynes J, Marroquin LD, Ogurtsov VI, Christiansen KN, Stevens GJ, Papkovsky DB, Will Y. Investigation of Drug-Induced Mitochondrial Toxicity Using Fluorescence-Based Oxygen-Sensitive Probes. *Toxicological Sciences*. 2006;92(1):186-200.
222. Ferrick DA, Neilson A, Beeson C. Advances in measuring cellular bioenergetics using extracellular flux. *Drug discovery today*. 2008;13(5-6):268-74.
223. Hynes J, Natoli Jr E, Will Y. Fluorescent pH and oxygen probes of the assessment of mitochondrial toxicity in isolated mitochondria and whole cells. *Current protocols in toxicology*. 2009;40(1):2.16. 1-2.. 22.
224. Zhdanov A, Favre C, O'Flaherty L, Adam J, O'Connor R, Pollard P, Papkovsky D. Comparative bioenergetic assessment of transformed cells using a cell energy budget platform. *Integrative Biology*. 2011;3(11):1135-42.
225. Papkovsky DB. Optochemical sensor-based systems for the analysis of cell metabolism and bioenergetics: an overview. *Optical Sensors 2023*. 2023;12572:90-5.
226. Kondrashina AV, Papkovsky DB, Dmitriev RI. Measurement of cell respiration and oxygenation in standard multichannel biochips using phosphorescent O₂-sensitive probes. *Analyst*. 2013;138(17):4915-21.
227. Papkovsky D, Zhdanov AV, Fercher A, Dmitriev RI, Hynes J. *Phosphorescent oxygen-sensitive probes: Springer Science & Business Media; 2012*.
228. Beeson CC, Beeson GC, Schnellmann RG. A high-throughput respirometric assay for mitochondrial biogenesis and toxicity. *Analytical Biochemistry*. 2010;404(1):75-81.
229. Nadanaciva S, Rana P, Beeson GC, Chen D, Ferrick DA, Beeson CC, Will Y. Assessment of drug-induced mitochondrial dysfunction via altered cellular respiration and acidification measured in a 96-well platform. *Journal of Bioenergetics and Biomembranes*. 2012;44(4):421-37.
230. Zhdanov AV, Dmitriev RI, Hynes J, Papkovsky DB. Chapter Ten - Kinetic Analysis of Local Oxygenation and Respiratory Responses of Mammalian Cells Using Intracellular Oxygen-Sensitive Probes and Time-Resolved Fluorometry. In: Galluzzi L, Kroemer G, editors. *Methods in Enzymology*. 542: Academic Press; 2014. p. 183-207.
231. Zhdanov AV, Ogurtsov VI, Taylor CT, Papkovsky DB. Monitoring of cell oxygenation and responses to metabolic stimulation by intracellular oxygen sensing technique. *Integrative Biology*. 2010;2(9):443-51.
232. Hoehler TM, Jørgensen BB. Microbial life under extreme energy limitation. *Nature Reviews Microbiology*. 2013;11(2):83-94.
233. O'Mahony FC, O'Donovan C, Hynes J, Moore T, Davenport J, Papkovsky DB. Optical Oxygen Microrespirometry as a Platform for Environmental Toxicology and Animal Model Studies. *Environmental Science & Technology*. 2005;39(13):5010-4.
234. Elisseeva S, Kelly C, Cruz-Romero M, Zhdanov AV, Kerry JP, Papkovsky DB. The use of optical oxygen sensing and respirometry to quantify the effects of antimicrobials on common food spoilage bacteria and food samples. *Sensors and Actuators B: Chemical*. 2020;322:128572.

235. Papkovsky DB, Kerry JP. Oxygen Sensor-Based Respirometry and the Landscape of Microbial Testing Methods as Applicable to Food and Beverage Matrices. *Sensors*. 2023;23(9):4519.
236. Papkovsky D, Hynes J, Fernandes R. Optical oxygen sensing systems for drug discovery applications: Respirometric Screening Technology (RST): SPIE; 2005.
237. O'Mahony FC, Papkovsky DB. Rapid High-Throughput Assessment of Aerobic Bacteria in Complex Samples by Fluorescence-Based Oxygen Respirometry. *Applied and Environmental Microbiology*. 2006;72(2):1279-87.
238. Stitt DT, Nagar MS, Haq TA, Timmins MR. Determination of growth rate of microorganisms in broth from oxygen-sensitive fluorescence plate reader measurements. *Biotechniques*. 2002;32(3):684-9.
239. Santovito E, Elisseeva S, Bukulin A, Kerry JP, Papkovsky DB. Facile biosensor-based system for on-site quantification of total viable counts in food and environmental swabs. *Biosensors and Bioelectronics*. 2021;176:112938.
240. Dufort S, Sancey L, Coll J-L. Physico-chemical parameters that govern nanoparticles fate also dictate rules for their molecular evolution. *Adv Drug Deliv Rev*. 2012;64(2):179-89.
241. Alexis F, Pridgen E, Molnar LK, Farokhzad OC. Factors Affecting the Clearance and Biodistribution of Polymeric Nanoparticles. *Molecular Pharmaceutics*. 2008;5(4):505-15.
242. Esipova TV, Karagodov A, Miller J, Wilson DF, Busch TM, Vinogradov SA. Two new "protected" oxyphors for biological oximetry: properties and application in tumor imaging. *Analytical chemistry*. 2011;83(22):8756-65.
243. Pham TD, Wallace DC, Burke PJ. Microchambers with solid-state phosphorescent sensor for measuring single mitochondrial respiration. *Sensors*. 2016;16(7):1065.
244. Chu C-S, Lo Y-L, Sung T-W. Enhanced oxygen sensing properties of Pt (II) complex and dye entrapped core-shell silica nanoparticles embedded in sol-gel matrix. *Talanta*. 2010;82(3):1044-51.
245. Qiao Y, Pan T, Li J, Yang C, Wen J, Zhong K, et al. Extracellular oxygen sensors based on PtTFPP and four-arm block copolymers. *Applied Sciences*. 2019;9(20):4404.
246. Li J, Qiao Y, Pan T, Zhong K, Wen J, Wu S, et al. Amphiphilic Fluorine-Containing Block Copolymers as Carriers for Hydrophobic PtTFPP for Dissolved Oxygen Sensing, Cell Respiration Monitoring and In Vivo Hypoxia Imaging with High Quantum Efficiency and Long Lifetime. *Sensors*. 2018;18(11):3752.
247. Yang C. *Applying Luminescent Oxygen Sensors in Hydrogels*: Johns Hopkins University; 2021.
248. Dmitriev RI, Borisov SM, DÜssmann H, Sun S, Müller BJ, Prehn J, et al. Versatile Conjugated Polymer Nanoparticles for High-Resolution O₂ Imaging in Cells and 3D Tissue Models. *ACS Nano*. 2015;9(5):5275-88.
249. Zhao Q, Pan T, Xiang G, Mei Z, Jiang J, Li G, et al. Highly efficient ratiometric extracellular oxygen sensors through physical incorporation of a conjugated polymer and PtTFPP in graft copolymers. *Sensors and Actuators B: Chemical*. 2018;273:242-52.
250. Becer CR, Hoogenboom R, Schubert US. Click chemistry beyond metal-catalyzed cycloaddition. *Angew Chem Int Ed Engl*. 2009;48(27):4900-8.
251. Koren K, Borisov SM, Klimant I. Stable optical oxygen sensing materials based on click-coupling of fluorinated platinum(II) and palladium(II) porphyrins-A convenient way to eliminate dye migration and leaching. *Sens Actuators B Chem*. 2012;169(5):173-81.
252. Hoyle CE, Lowe AB, Bowman CN. Thiol-click chemistry: a multifaceted toolbox for small molecule and polymer synthesis. *Chemical Society Reviews*. 2010;39(4):1355-87.
253. Greenwald RB, Choe YH, McGuire J, Conover CD. Effective drug delivery by PEGylated drug conjugates. *Adv Drug Deliv Rev*. 2003;55(2):217-50.
254. Sibrian-Vazquez M, Jensen TJ, Vicente MG. Synthesis and cellular studies of PEG-functionalized meso-tetraphenylporphyrins. *J Photochem Photobiol B*. 2007;86(1):9-21.

255. Pinto SMA, Almeida SFF, Tomé VA, Prata AD, Calvete MJF, Serpa C, Pereira MM. Water soluble near infrared dyes based on PEGylated-Tetrapyrrolic macrocycles. *Dyes and Pigments*. 2021;195:109677.
256. Zanetti C, Gaspar RDL, Zhdanov AV, Maguire NM, Joyce SA, Collins SG, et al. Heterosubstituted Derivatives of PtPFPP for O₂ Sensing and Cell Analysis: Structure–Activity Relationships. *Bioconjugate Chemistry*. 2022;33(11):2161-9.
257. Asayama S, Mizushima K, Nagaoka S, Kawakami H. Design of Metalloporphyrin–Carbohydrate Conjugates for a New Superoxide Dismutase Mimic with Cellular Recognition. *Bioconjugate Chemistry*. 2004;15(6):1360-3.
258. Maillard P, Guerquin-Kern JL, Huel C, Momenteau M. Glycoconjugated porphyrins. 2. Synthesis of sterically constrained polyglycosylated compounds derived from tetraphenylporphyrins. *The Journal of Organic Chemistry*. 1993;58(10):2774-80.
259. Chen X, Hui L, Foster DA, Drain CM. Efficient synthesis and photodynamic activity of porphyrin-saccharide conjugates: targeting and incapacitating cancer cells. *Biochemistry*. 2004;43(34):10918-29.
260. Samaroo D, Soll CE, Todaro LJ, Drain CM. Efficient Microwave-Assisted Synthesis of Amine-Substituted Tetrakis(pentafluorophenyl)porphyrin. *Organic Letters*. 2006;8(22):4985-8.
261. Chen X, Drain CM. Photodynamic Therapy using Carbohydrate Conjugated Porphyrins. *Drug Design Reviews - Online*. 2004;1(3):215-34.
262. Zheng X, Pandey RK. Porphyrin-Carbohydrate Conjugates: Impact of Carbohydrate Moieties in Photodynamic Therapy (PDT). *Anti-Cancer Agents in Medicinal Chemistry- Anti-Cancer Agents*. 2008;8(3):241-68.
263. Elisseeva S, Santovito E, Linehan E, Kerry JP, Papkovsky DB. Performance assessment of the two oxygen sensor based respirometric platforms with complex media and in selective bacterial assays. *Sensors and Actuators B: Chemical*. 2023;383:133582.
264. Zhdanov AV, Ward MW, Taylor CT, Souslova EA, Chudakov DM, Prehn JHM, Papkovsky DB. Extracellular calcium depletion transiently elevates oxygen consumption in neurosecretory PC12 cells through activation of mitochondrial Na⁺/Ca²⁺ exchange. *Biochimica et Biophysica Acta (BBA) - Bioenergetics*. 2010;1797(9):1627-37.
265. Pasetto P, Chen X, Drain CM, Franck RW. Synthesis of hydrolytically stable porphyrin C- and S-glycoconjugates in high yields. Electronic supplementary information (ESI) available: experimental details. See <http://www.rsc.org/suppdata/cc/b0/b008489l>. *Chemical Communications*. 2001(1):81-2.
266. Walker DB, Joshi G, Davis AP. Progress in biomimetic carbohydrate recognition. *Cellular and Molecular Life Sciences*. 2009;66(19):3177-91.
267. Masayuki T, Hideomi K, Itaru H, Seiji S. A Novel Sugar Sensing System Designed with a Cooperative Action of a Boronic-Acid-Appended Zinc Porphyrin and a 3-Pyridylboronic Acid Axial Ligand. *Bulletin of the Chemical Society of Japan*. 1997;70(3):699-705.
268. Rusin O, Hub M, Král Vr. Novel water-soluble porphyrin-based receptors for saccharide recognition. *Materials Science and Engineering: C*. 2001;18(1):135-40.
269. Vandegriff KD, McCarthy M, Rohlfes RJ, Winslow RM. Colloid osmotic properties of modified hemoglobins: chemically cross-linked versus polyethylene glycol surface-conjugated. *Biophysical Chemistry*. 1997;69(1):23-30.
270. Sibrian-Vazquez M, Jensen TJ, Vicente MGH. Synthesis and cellular studies of PEG-functionalized meso-tetraphenylporphyrins. *Journal of Photochemistry and Photobiology B: Biology*. 2007;86(1):9-21.
271. Hirohara S, Nishida M, Sharyo K, Obata M, Ando T, Tanihara M. Synthesis, photophysical properties and photocytotoxicity of mono-, di-, tri- and tetra-glucosylated fluorophenylporphyrins. *Bioorg Med Chem*. 2010;18(4):1526-35.

272. Hirohara S, Sharyo K, Kawasaki Y, Totani M, Tomotsuka A, Funasako R, et al. trans-Bisglycoconjugation is an Efficient and Robust Architecture for PDT Photosensitizers Based on 5,10,15,20-Tetrakis(pentafluorophenyl)porphyrin Derivatives. *Bulletin of the Chemical Society of Japan*. 2013;86(11):1295-308.
273. Cohen S, Margalit R. Binding of porphyrin to human serum albumin. Structure-activity relationships. *Biochem J*. 1990;270(2):325-30.
274. Moan J, Rimington C, Evensen JF, Western A. Binding of Porphyrins to Serum Proteins. In: Kessel D, editor. *Methods in Porphyrin Photosensitization*. Boston, MA: Springer US; 1985. p. 193-205.
275. Dmitriev R. Multi-Parametric Live Cell Microscopy of 3D Tissue Models 2017.
276. Villari V, Mineo P, Scamporrino E, Micali N. Spontaneous self-assembly of water-soluble porphyrins having poly (ethylene glycol) as branches: Dependence of aggregate properties from the building block architecture. *Chemical Physics*. 2012;409:23-31.
277. Goodman CM, McCusker CD, Yilmaz T, Rotello VM. Toxicity of Gold Nanoparticles Functionalized with Cationic and Anionic Side Chains. *Bioconjugate Chemistry*. 2004;15(4):897-900.
278. Cornish J, Callon KE, Lin CQ, Xiao CL, Mulvey TB, Cooper GJ, Reid IR. Trifluoroacetate, a contaminant in purified proteins, inhibits proliferation of osteoblasts and chondrocytes. *Am J Physiol*. 1999;277(5):E779-83.
279. Kaiser E, Rohrer J. Determination of residual trifluoroacetate in protein purification buffers and peptide preparations by ion chromatography. *Journal of Chromatography A*. 2004;1039(1):113-7.
280. Abedini A, Cao P, Raleigh DP. Detection of Helical Intermediates During Amyloid Formation by Intrinsically Disordered Polypeptides and Proteins. In: Eliezer D, editor. *Protein Amyloid Aggregation: Methods and Protocols*. New York, NY: Springer New York; 2016. p. 55-66.
281. Fernández-Ponce C, Muñoz-Miranda JP, de los Santos DM, Aguado E, García-Cozar F, Litrán R. Influence of size and surface capping on photoluminescence and cytotoxicity of gold nanoparticles. *Journal of Nanoparticle Research*. 2018;20(11):305.
282. Fröhlich E. The role of surface charge in cellular uptake and cytotoxicity of medical nanoparticles. *International journal of nanomedicine*. 2012:5577-91.
283. Matsumoto T, Wang P-Y, Ma W, Sung HJ, Matoba S, Hwang PM. Polo-like kinases mediate cell survival in mitochondrial dysfunction. *Proc Natl Acad Sci U S A*. 2009;106(34):14542-6.
284. Matoba S, Kang J-G, Patino WD, Wragg A, Boehm M, Gavrilova O, et al. p53 Regulates Mitochondrial Respiration. *Science*. 2006;312(5780):1650-3.
285. Maddalena F, Lettini G, Gallicchio R, Sisinni L, Simeon V, Nardelli A, et al. Evaluation of Glucose Uptake in Normal and Cancer Cell Lines by Positron Emission Tomography. *Mol Imaging*. 2015;14:490-8.
286. Zhdanov AV, Ward MW, Prehn JHM, Papkovsky DB. Dynamics of Intracellular Oxygen in PC12 Cells upon Stimulation of Neurotransmission*. *Journal of Biological Chemistry*. 2008;283:5650 - 61.
287. Zhdanov AV, Aviello G, Knaus UG, Papkovsky DB. Cellular ROS imaging with hydro-Cy3 dye is strongly influenced by mitochondrial membrane potential. *Biochimica et Biophysica Acta (BBA) - General Subjects*. 2017;1861(2):198-204.
288. Dmitriev RI, Zhdanov AV, Jasione G, Papkovsky DB. Assessment of cellular oxygen gradients with a panel of phosphorescent oxygen-sensitive probes. *Anal Chem*. 2012;84(6):2930-8.
289. Siebeneicher H, Cleve A, Rehwinkel H, Neuhaus R, Heisler I, Müller T, et al. Identification and optimization of the first highly selective GLUT1 inhibitor BAY-876. *ChemMedChem*. 2016;11(20):2261-71.

290. Reckzeh ES, Waldmann H. Development of glucose transporter (GLUT) inhibitors. *European journal of organic chemistry*. 2020;2020(16):2321-9.
291. Xiong N, Long X, Xiong J, Jia M, Chen C, Huang J, et al. Mitochondrial complex I inhibitor rotenone-induced toxicity and its potential mechanisms in Parkinson's disease models. *Critical reviews in toxicology*. 2012;42(7):613-32.
292. Hamilton KE, Bouwer MF, Louters LL, Looyenga BD. Cellular binding and uptake of fluorescent glucose analogs 2-NBDG and 6-NBDG occurs independent of membrane glucose transporters. *Biochimie*. 2021;190:1-11.
293. Standardization IOF. *Microbiology of the Food Chain: Horizontal Method for the Enumeration of Microorganisms--Part 1: Colony Count at 30° C by the Pour Plate Technique: International Organization for Standardization*; 2022.
294. Blood RM, Curtis G. Media for 'total' Enterobacteriaceae, coliforms and *Escherichia coli*. *Progress in industrial microbiology*. 1995;34:163-85.
295. Rompre A, Servais P, Baudart J, De-Roubin M-R, Laurent P. Detection and enumeration of coliforms in drinking water: current methods and emerging approaches. *Journal of microbiological methods*. 2002;49(1):31-54.
296. Yousef AE. Detection of bacterial pathogens in different matrices: Current practices and challenges. *Principles of bacterial detection: biosensors, recognition receptors and Microsystems*. 2008:31-48.
297. Váradi L, Luo JL, Hibbs DE, Perry JD, Anderson RJ, Orenge S, Groundwater PW. Methods for the detection and identification of pathogenic bacteria: past, present, and future. *Chemical Society Reviews*. 2017;46(16):4818-32.
298. Qiu W, Nagl S. Automated miniaturized digital microfluidic antimicrobial susceptibility test using a chip-integrated optical oxygen sensor. *ACS sensors*. 2021;6(3):1147-56.
299. O'Riordan TC, Zhdanov AV, Ponomarev GV, Papkovsky DB. Analysis of intracellular oxygen and metabolic responses of mammalian cells by time-resolved fluorometry. *Analytical chemistry*. 2007;79(24):9414-9.
300. Bonnet M, Lagier JC, Raoult D, Khelaifia S. Bacterial culture through selective and non-selective conditions: the evolution of culture media in clinical microbiology. *New Microbes New Infect*. 2020;34:100622.
301. O'Riordan TC, Hynes J, Yashunski D, Ponomarev GV, Papkovsky DB. Homogeneous assays for cellular proteases employing the platinum(II)-coproporphyrin label and time-resolved phosphorescence. *Analytical Biochemistry*. 2005;342(1):111-9.
302. Papkovsky DB, Zhdanov AV, Fercher A, Dmitriev RI, Hynes J, Zhdanov AV, et al. O₂ Analysis on a Fluorescence Spectrometer or Plate Reader. Phosphorescent oxygen-sensitive probes. 2012:29-69.
303. Hempel A, Borchert N, Walsh H, Choudhury KR, Kerry J, Papkovsky D. Analysis of total aerobic viable counts in raw fish by high-throughput optical oxygen respirometry. *Journal of food protection*. 2011;74(5):776-82.
304. Zhdanov AV, Hynes J, Dmitriev RI, Papkovsky DB. O₂ Analysis on a Fluorescence Spectrometer or Plate Reader. In: Papkovsky DB, Zhdanov AV, Fercher A, Dmitriev RI, Hynes J, editors. *Phosphorescent Oxygen-Sensitive Probes*. Basel: Springer Basel; 2012. p. 29-69.
305. Poulin BA, Ryan JN, Aiken GR. Effects of iron on optical properties of dissolved organic matter. *Environmental science & technology*. 2014;48(17):10098-106.
306. Doumas BT, Peters Jr T. Serum and urine albumin: a progress report on their measurement and clinical significance. *Clinica Chimica Acta*. 1997;258(1):3-20.
307. Kim H, Koo B. Iron (III) Sensors Based on the Fluorescence Quenching of Poly(phenylene ethynylene)s and Iron-Detecting PDMS Pads. *Macromolecular Research*. 2021;29(5):360-4.

308. Sen R, Li L, Zhdanov AV, Gaspar RD, Papkovsky DB. Phosphorescence lifetime measurements with sensor materials: Comparison of the four different detection platforms. *Sensors and Actuators B: Chemical*. 2022;371:132496.
309. Mallette M. Chapter XV evaluation of growth by physical and chemical means. *Methods in microbiology*. 1: Elsevier; 1969. p. 521-66.
310. Zhang H, Zhao Y, He X, Gao P. A novel approach for assessing the susceptibility of *Escherichia coli* to antibiotics. *Science China Life Sciences*. 2010;53:1346-55.
311. Nie S, Chiu DT, Zare RN. Probing individual molecules with confocal fluorescence microscopy. *Science*. 1994;266(5187):1018-21.
312. Haddad RE, Gazeau S, Pécaut J, Marchon J-C, Medforth CJ, Shelnutz JA. Origin of the red shifts in the optical absorption bands of nonplanar tetraalkylporphyrins. *Journal of the American Chemical Society*. 2003;125(5):1253-68.